universität wien

DISSERTATION / DOCTORAL THESIS

Titel der Dissertation /Title of the Doctoral Thesis

„Density functional theory
for the random-phase approximation“

verfasst von / submitted by

Stefan Riemelmoser, BSc MSc

angestrebter akademischer Grad / in partial fulfilment of the requirements for the degree of

Doktor der Naturwissenschaften (Dr. rer. nat.)

Wien, 2023 / Vienna 2023

Studienkennzahl lt. Studienblatt / degree programme code as it appears on the student record sheet:	A 796 605 411
Dissertationsgebiet lt. Studienblatt / field of study as it appears on the student record sheet:	Physik
Betreut von / Supervisor:	Univ.-Prof. Dipl.-Ing. Dr. Georg Kresse

Abstract / Zusammenfassung

Abstract

The random-phase approximation (RPA) is a high-level electronic structure theory that seamlessly accounts for exchange interactions as well as for dispersion and van der Waals interactions. Despite being a decades-old theory, the RPA has only recently been applied to real materials. The reason is the large computational cost associated with numerical RPA calculations. In particular, RPA calculations slowly converge with respect to the basis set size. Further, it is very challenging to perform RPA calculations in a self-consistent way.

In this work, we apply density functional theory to speed up RPA calculations. In a first approach, we use a range-separation framework to identify the plane wave basis set incompleteness error as short-range contributions to the RPA. We device two plane wave basis set correction methods based on the homogeneous electron gas model, and show that both methods become exact in the limit of large plane wave cutoffs. The basis set correction methods are applied to calculate the lattice constants of 6 prototypical solids.

In a second approach, we replace the RPA entirely by a machine learning (ML) substitute model. The machine learning model is constructed as a non-local extension to the common gradient approximation of density functional theory. The optimized effective potential method is used to supply derivative information for the training process. To benchmark the RPA optimized effective potentials, we have calculating band gaps and dielectric constants for 15 semiconductors and insulators. Through bypassing the RPA optimized effective potential equation, our machine learning approach allows also for self-consistent calculations. This enables the seamless calculation of forces and stresses, which is otherwise challenging for the RPA. We train an RPA substitute functional for diamond surfaces and liquid water, and show that our ML method enables RPA-level calculations at a larger scale.

Zusammenfassung

Die sogenannte random-phase approximation (RPA, Näherung der zufälligen Phase) ist eine hochentwickelte Theorie der elektronischen Struktur, die in nahtloser Weise sowohl Austausch-Wechselwirkungen als auch Dispersion und van der Waals Wechselwirkungen beschreibt. Obwohl die RPA Theorie bereits Jahrzehnte alt ist, wurde sie erst kürzlich auf realistische Materialien angewandt. Der Grund ist der hohe Rechenaufwand, welcher mit numerischen RPA Berechnungen einhergeht. Insbesondere konvergieren RPA Rechnungen sehr langsam mit der Größe des Basissatzes. Weiters sind selbstkonsistente RPA Rechnungen besonders herausfordernd.

Im Rahmen dieser Arbeit wenden wir Dichtefunktionaltheorie an, um RPA Rechnungen zu beschleunigen. In einem ersten Ansatz trennen wir die RPA Energie in lang- und kurzreichweitige Anteile auf, und identifizieren den Basissatz-Fehler (innerhalb eines Basissatzes von ebenen Wellen) als kurzreichweitige Beiträge zur RPA. Wir konstruieren zwei Korrekturmethoden für den Basissatz-Fehler basierend auf einem homogenen Elektronengasmodell, und beweisen die Exaktheit dieser Methoden im Grenzfall hoher Energien. Wir wenden die Basissatz-Korrekturmethoden an, um die Gitterkonstanten 6 prototypischer Festkörper zu berechnen.

In einem zweiten Ansatz ersetzen wir die RPA vollständig durch ein machine learning (ML, maschinelles Lernen) Modell. Das ML Modell ist als nicht-lokale Erweiterung zur üblichen Gradientenkorrektur der Dichtefunktionaltheorie konstruiert. Die Methode der optimierten effektiven Potentiale wird benutzt, um Gradienteninformation für den Trainingsprozess zu liefern. Als Vergleichstest für die optimierten effektiven Potentiale der RPA haben wir Bandlücken und dielektrische Konstanten von 15 Halbleitern und Isolatoren berechnet. Indem die Gleichung der RPA optimierten effektiven Potentiale überbrückt wird, ermöglicht unser ML Ansatz auch selbstkonsistente Rechnungen. Das erlaubt die nahtlose Berechnung von Kräften und Stresstensoren, was für die RPA ansonsten herausfordernd ist. Wir trainieren ein ML Funktional, das die RPA für Diamantoberflächen und flüssiges Wasser substituiert, und wir zeigen, dass unsere ML Methode ermöglicht, Rechnungen mit RPA Niveau auf größerer Skala durchzuführen.

Acknowledgements

First of all, I would like to extend sincere thanks to Georg Kresse, who has been my supervisor since my bachelor studies all up to now. In countless discussions, Georg has provided me with invaluable insight about electronic structure, materials physics and science in general. He has strongly supported my research efforts, and he has encouraged me to take on challenging problems. I also thank Georg for providing me with the opportunity to present our work at several international conferences.

Next, I would like to thank Merzuk Kaltak and Carla Verdi for their much appreciated scientific contributions. Merzuk's deep insight into mathematics and the VASP code and Carla's expert machine learning knowledge have greatly benefited our joint research projects. Furthermore, I would like to thank Doris Hecht-Aichholzer, Christine Schrempf, Michael Pöltl, and many more nice members of the CMP group for providing a wonderful working environment. Special thanks also to Menno Bokdam for his helpful advice and mentoring.

I also want to acknowledge the administrative and teaching staff at the University of Vienna. In particular, I want to thank Prof. Neumann for his great courses in computational physics and further Profs. Rumpf, Hoang and Neufeld whose lectures have instilled me with awe for theoretical physics. Moreover, I want to express my admiration for J. C. Slater, J. P. Perdew, and many more legends of electronic structure theory - they are the giants upon whose shoulders I humble stand.

Last not least, I want to thank both my Austrian and Serbian families for emotional support. I extend my heartfelt gratitude and appreciation to my loving wife Biljana, for being the source of my inspiration and ambition. Furthermore, I thank my brother Markus for serving as best man at the wedding, and my parents for enabling my studies in the first place.

Contents

Chapter 1

Introduction

Kohn-Sham density functional theory (DFT) is the standard first principles method for electronic structure calculations. The central unknown in DFT is the exchange-correlation energy E_{xc}, which accounts for quantum electron-electron interactions. The eminent success of DFT is deeply tied to that of its canonical (semi)-local approximations for E_{xc}. In the local density approximation (LDA), E_{xc} is approximated to be locally that of the homogeneous electron gas with the same density. In the GGA (generalized gradient approximation), E_{xc} depends also on the local density gradient. The (semi-)local approximations, however, miss important long-range exchange and correlation effects. The random-phase approximation (RPA) can capture such non-local interactions by explicitly including information from both occupied and unoccupied electronic orbitals. Especially the dependence on unoccupied orbitals is, however, associated with overwhelming computational cost. This has held back large scale applications of the RPA for many decades. In recent years, important progress was made by Kaltak *et al.*[1,2] who reduced the cost of RPA calculations via algorithmic developments, see also Refs. [3, 4].

Furthermore, RPA calculations are usually performed in a many-body perturbation theory (post Kohn-Sham DFT) framework. That is, RPA calculations are not done self-consistently, but rather one evaluates $E_{\mathrm{xc}}^{\mathrm{RPA}}$ using orbitals from a baseline LDA or GGA calculation. Not only is this approximation somewhat unsatisfying from a theoretical viewpoint, there are also practical issues involved. Namely, the Hellmann-Feynman theorem does no longer apply, which necessitates the inclusion of complicated correction terms for RPA forces and stresses.[5] In principle, the RPA can be brought within the Kohn-Sham DFT framework via the optimized effective potential (OEP) method.[6–8] However, self-consistent RPA-OEP calculations are rarely carried out, since OEP raises the computational cost of standard RPA calculations by typically one to two orders of magnitude.

In this work, we reduce the computational cost of the RPA using basis set corrections and machine learning. The machine learning approach also speeds up self-consistent RPA calculations. The main results presented in Chaps. 4-6 have also been published in three papers.[9–11]

In Chap. 4, we use range-separation to analyze the errors for RPA correlation energies due to incomplete plane wave basis sets. In the short-range limit corresponding to large plane wave cutoff energies, these basis set incompleteness errors become strictly local. We use this exact limit to construct two basis set correction methods based on the homogeneous electron gas. First, the RPA basis set errors are directly approximated via short-range LDA functionals. Second, we perform an implicit basis set extrapolation by modifying the Coulomb kernel. That is, to make up for its truncation at large wave vectors, this "squeezed Coulomb kernel" is enhanced at intermediate wave vectors in return. We use the basis set correction methods to calculate lattice constants of prototypical solids. We find that both methods work

well for Si and C-diamond. However, the examples of Kr and Pd show that the underlying homogeneous electron gas model is not always sufficiently accurate.

In Chap. 5, we perform self-consistent RPA-OEP calculations for 15 semiconductors and insulators. We find that Kohn-Sham band gaps in the RPA are somewhat larger than band gaps obtained using the GGA. Moreover, dielectric constants obtained by self-consistent RPA-OEP calculations are in better agreement with experiment than dielectric constants obtained using the GGA. Further, we investigate dynamical screening effects in form of the quasiparticle approximation. Our theoretical analysis of the quasiparticle approximation for simple model systems provides a satisfactory interpretation for the calculated numerical effects that the quasiparticle approximation introduces for the band gaps and dielectric constants.

In Chap. 6, we develop a machine learning (ML) scheme that bypasses the RPA-OEP equation, substituting the RPA with a ML density functional. The ML-RPA functional can be interpreted as a non-local extension of the GGA. ML-RPA also exhibits the favorable GGA scaling behavior with respect to system size. We fit an ML-RPA functional for diamond, its surfaces and liquid water. The ML-RPA predictions for the formation energies of 28 diamond surfaces are in excellent agreement with RPA reference data. For water, however, ML-RPA is less accurate and seems to miss some crucial non-local interactions. Since ML-RPA can be applied self-consistently like any other DFT functional, forces and stresses are readily available. As demonstration, we apply ML-RPA to calculate diamond phonons in large supercells and to perform long MD simulations for liquid water.

The rest of this thesis is structured as follows. In Part I, we give a brief theoretical introduction to density function theory and the random-phase approximation. Results are presented in Part II and summed up in Part III. Finally, Part IV collects the appendices.

Part I

Theory

Chapter 2

Density functional theory

2.1 Historical background: exchange-only theories

In the following, we will present fundamentals in density functional theory from a historical perspective. The discussion mainly follows the reviews of Becke[12] and Jones,[13] as well as the book of Martin[14] (Chaps. 5-8). Throughout, we will use Hartree atomic units, where $\hbar = m_e = e = 4\pi/\epsilon_0 = 1$. The discussion is mainly restricted to the spin-non-polarized case, and electronic spin is taken into account via factors of 2 where appropriate.

2.1.1 Born-Oppenheimer Hamiltonian

Within the Born-Oppenheimer approximation, the time-independent Schrödinger equation for N_e electrons moving in an external potential v_{ext} reads

$$\begin{aligned} &H\Psi(\mathbf{r}_1\sigma_1, ..., \mathbf{r}_{N_e}\sigma_{N_e}) = E\Psi(\mathbf{r}_1\sigma_1, ..., \mathbf{r}_{N_e}\sigma_{N_e}) \\ &H = -\sum_i \frac{1}{2}\nabla_i^2 + \sum_i v_{\text{ext}}(\mathbf{r}_i) + \frac{1}{2}\sum_{i\neq j}\frac{1}{|\mathbf{r}_i - \mathbf{r}_j|}, \end{aligned} \tag{2.1}$$

where the $\mathbf{r}_i$ and σ_i are spatial and spin coordinates of the electrons. The ground state energy E has the following contributions

$$E = \langle\Psi|H|\Psi\rangle = T + E_{\text{ext}} + E_{ee}. \tag{2.2}$$

The first term (T) accounts for the kinetic energy of the electrons, the last term (E_{ee}) for Coulombic electron-electron interactions. Further, v_{ext} typically describes electrostatic interactions between electrons and atomic nuclei (located at fixed positions R_A, with charges Z_A),

$$v_{\text{ext}}(\mathbf{r}) = \sum_A \frac{-Z_A}{|\mathbf{r}_i - \mathbf{R}_A|}. \tag{2.3}$$

The associated external energy E_{ext} can be further rewritten as

$$\begin{aligned} E_{\text{ext}} &= \langle\Psi|\sum_i v_{\text{ext}}(\mathbf{r}_i)|\Psi\rangle \\ &= \int \mathrm{d}\mathbf{r}\, n(\mathbf{r}) v_{\text{ext}}(\mathbf{r}), \end{aligned} \tag{2.4}$$

where $n(\mathbf{r})$ is the electronic density, that is the probability to find an electron at $\mathbf{r}$,

$$n(\mathbf{r}) = \langle\Psi|\sum_{i,\sigma}\delta(\mathbf{r} - \mathbf{r}_i)|\Psi\rangle\,. \tag{2.5}$$

From the normalization of the wave function $\langle\Psi|\Psi\rangle = 1$, it follows that $n(\mathbf{r})$ fulfills the sum rule

$$\int \mathrm{d}\mathbf{r}\, n(\mathbf{r}) = N_e. \tag{2.6}$$

Eq. (2.4) also shows that v_{ext} is formally linked to E_{ext} via a functional derivative, $v_{\mathrm{ext}}(\mathbf{r}) = \delta E_{\mathrm{ext}}/\delta n(\mathbf{r})$. An additional energy term has to account for electrostatic interactions between nuclei,

$$E_{nn} = \frac{1}{2}\sum_{A\neq B}\frac{Z_A Z_B}{|\mathbf{R}_A - \mathbf{R}_B|}, \tag{2.7}$$

but we neglect E_{nn} in the following, since it is only a constant from the perspective of the electronic structure.

Equation (2.1) could be written down immediately after the invention of quantum mechanics in the 1920s. However, it was soon realized that the direct numerical solution in terms of the many-body electronic wave function $\Psi(\mathbf{r}_1\sigma_1, ..., \mathbf{r}_{N_e\sigma_{N_e}})$ is hopeless except for simple cases. This problem was tackled soon thereafter, and around 1930 two iconic independent particle methods were formulated: the Hartree approximation and Hartree-Fock theory.

2.1.2 Independent particle approximation

Within the independent particle approximation, one seeks to replace the complicated many-body electron-electron interaction by a mean-field potential v_{eff}, which accounts for the electron-electron interactions in an effective (averaged) way. For the moment, we consider the simpler (Hartree-like) case, where $v_{\mathrm{eff}}(\mathbf{r})$ is a local multiplicative potential like $v_{\mathrm{ext}}(\mathbf{r})$. The solution of one N_e-body problem (2.1) is then replaced by solving N_e one-body problems,

$$\begin{aligned} h_\sigma(\mathbf{r})\phi_{i,\sigma}(\mathbf{r}) &= \varepsilon_{i,\sigma}\phi_{i,\sigma}(\mathbf{r}) \\ h_\sigma(\mathbf{r}) &= -\frac{1}{2}\nabla^2 + v_{\mathrm{ext}}(\mathbf{r}) + v_{\mathrm{eff},\sigma}(\mathbf{r}). \end{aligned} \tag{2.8}$$

The IP wavefunction Ψ^{IP} is constructed from the lowest energy one-electron orbitals ϕ_i. The electron are placed in these orbitals in form of a single Slater determinant,

$$\begin{aligned} &\Psi(\mathbf{r}_1\sigma_1, ..., \mathbf{r}_{N_e}\sigma_{N_e}) \approx \Psi^{\mathrm{IP}}(\mathbf{r}_1\sigma_1, ..., \mathbf{r}_{N_e}\sigma_{N_e}) \\ &= \frac{1}{\sqrt{N!}}\sum_P (-1)^P \phi_{1,\sigma_1}(\mathbf{r}_{P(1)})\cdot\phi_{2,\sigma_2}(\mathbf{r}_{P(2)})\cdot ... \cdot \phi_{N_e,\sigma_{N_e}}(\mathbf{r}_{P(N_e)}). \end{aligned} \tag{2.9}$$

This determinant form respects the proper fermionic antisymmetry, that is Ψ^{IP} changes its sign under exchange of two coordinates $\mathbf{r}_i$ and $\mathbf{r}_j$. From now on, we will drop the spin indices σ_i and specify the spin-non-polarized case, where $N_e/2$ orbitals are occupied twice ("spin up, spin down"). Including a factor 2 that accounts for spin multiplicity, the IP Hamiltonian is then just the sum of the one-electron Hamiltonians h

$$H \approx H^{\mathrm{IP}} = 2\sum_i^{\mathrm{occ}} h(\mathbf{r}_i), \tag{2.10}$$

and the total energy E^{IP} is given by

$$E \approx E^{\mathrm{IP}} = \langle \Psi^{\mathrm{IP}} | \, H^{\mathrm{IP}} \, | \Psi^{\mathrm{IP}} \rangle = T^{\mathrm{IP}} + E_{\mathrm{ext}} + E_{\mathrm{eff}}. \tag{2.11}$$

Here, T^{IP} is the IP kinetic energy,

$$T^{\mathrm{IP}} = 2 \sum_{i}^{\mathrm{occ}} \langle \phi_i | -\frac{1}{2} \nabla_i^2 | \phi_i \rangle \,, \tag{2.12}$$

and E_{eff} is the energy term corresponding to the mean-field potential, $v_{\mathrm{eff}}(\mathbf{r}) = \delta E_{\mathrm{eff}} / \delta n(\mathbf{r})$. Within the independent particle ansatz [Eq. (2.9)], the electronic density is simply given by the sum of the probabilities to find an electron in orbital ϕ_i,

$$n \approx n^{\mathrm{IP}}(\mathbf{r}) = 2 \sum_{i}^{\mathrm{occ}} \phi_i^*(\mathbf{r}) \phi_i(\mathbf{r}). \tag{2.13}$$

The independent particle approximation immensely simplifies the electronic structure problem, but how should one choose the mean-field potential? One can try to fit $v_{\mathrm{eff}}(\mathbf{r})$ to experimental data, material by material, but a good theoretical model should be able to calculate $v_{\mathrm{eff}}(\mathbf{r})$ from first principles. The interaction energy between classical charges, the so-called Hartree energy, is given by

$$E_{\mathrm{H}} = \frac{1}{2} \int \mathrm{d}\mathbf{r} \, \mathrm{d}\mathbf{r}' \frac{n(\mathbf{r}) n(\mathbf{r}')}{|\mathbf{r} - \mathbf{r}'|}, \tag{2.14}$$

and a charge $n(\mathbf{r})$ feels the corresponding Hartree potential

$$v_{\mathrm{H}}(\mathbf{r}) = \frac{\delta E_{\mathrm{H}}}{\delta n(\mathbf{r})} = \int \mathrm{d}\mathbf{r}' \frac{n(\mathbf{r}')}{|\mathbf{r} - \mathbf{r}'|}. \tag{2.15}$$

Combining this with Eq. (2.8), we obtain the Hartree approximation

$$\left[-\frac{1}{2} \nabla_i^2 + v_{\mathrm{ext}}(\mathbf{r}) + v_{\mathrm{H}}(\mathbf{r}) \right] \phi_i(\mathbf{r}) = \varepsilon_i \phi_i(\mathbf{r}). \tag{2.16}$$

Note that this is a non-linear problem as v_{H} depends on $\phi_i(\mathbf{r})$ via Eq. (2.13). The usual solution is linearizing and iterating, thus one starts with initial guesses for $\phi_i^{(0)}$ or $n^{(0)}$ (for example, superposition of atomic densities). Then, one calculates $\phi_i^{(1)}$ via Eq. (2.16). Further iterations are carried out until some convergence criteria is met,

$$\left[-\frac{1}{2} \nabla_i^2 + v_{\mathrm{ext}}(\mathbf{r}) + v_{\mathrm{H}}^{(n)}(\mathbf{r}) \right] \phi_i^{(n+1)}(\mathbf{r}) = \varepsilon_i^{(n+1)} \phi_i^{(n+1)}(\mathbf{r}). \tag{2.17}$$

This iterative process is called the *electronic self-consistency cycle*.

2.1.3 Hartree-Fock approximation

The Hartree approximation is not very useful, however. Through the Hartree potential, an electron in orbital ϕ_i interacts not only with all other electrons in orbitals $\phi_j (j \neq i)$, but also with itself $(j = i)$, which is clear when we rewrite Eq. (2.14) as

$$E_{\mathrm{H}} = 2 \int \mathrm{d}\mathbf{r} \, \mathrm{d}\mathbf{r}' \sum_{ij}^{\mathrm{occ}} \frac{\phi_i^*(\mathbf{r}) \phi_i(\mathbf{r}) \phi_j^*(\mathbf{r}') \phi_j(\mathbf{r}')}{|\mathbf{r} - \mathbf{r}'|}. \tag{2.18}$$

In Hartree-Fock theory, this spurious self-interaction is canceled by adding the following "exchange energy" (swapping two indices in the above expression)

$$E_{\mathrm{x}} = -\int \mathrm{d}\mathbf{r}\,\mathrm{d}\mathbf{r}' \sum_{ij}^{\mathrm{occ}} \frac{\phi_i^*(\mathbf{r})\phi_j(\mathbf{r})\phi_j^*(\mathbf{r}')\phi_i(\mathbf{r}')}{|\mathbf{r}-\mathbf{r}'|}. \tag{2.19}$$

The missing factor of two compared to the Hartree energy accounts for the fact that only electrons of equal spin feel the exchange energy (a manifestation of the Pauli exclusion principle). As in Hartree theory one solves a mean-field equation that contains an exchange term Σ_{x} next to the Hartree potential,

$$\left[-\frac{1}{2}\nabla_i^2 + v_{\mathrm{ext}}(\mathbf{r}) + v_{\mathrm{H}}(\mathbf{r}) + \Sigma_{\mathrm{x}}\right]\phi_i(\mathbf{r}) = \varepsilon_i\phi_i(\mathbf{r}), \tag{2.20}$$

and this equation is likewise meant to be solved self-consistently. An important difference between the Hartree and Hartree-Fock theories, however, is the fact that the Hartree potential v_{H} is a local, one-electron potential that is the same for all orbitals ϕ_i [Eq. (2.16)]. In contrast, the corresponding operator Σ_{x} in Hartree-Fock theory is non-local and acts differently on the ϕ_i,

$$\begin{aligned} \Sigma_{\mathrm{x}}(\mathbf{r},\mathbf{r}') &= -\sum_{j}^{\mathrm{occ}} \frac{\phi_j(\mathbf{r})\phi_j^*(\mathbf{r}')}{|\mathbf{r}-\mathbf{r}'|} \\ \Sigma_{\mathrm{x}}\phi_i(\mathbf{r}) &= \int \mathrm{d}\mathbf{r}'\, \Sigma_{\mathrm{x}}(\mathbf{r},\mathbf{r}')\phi_i(\mathbf{r}'). \end{aligned} \tag{2.21}$$

The exchange energy (2.19) is recovered by taking the expectation value

$$E_{\mathrm{x}} = \int \mathrm{d}\mathbf{r} \sum_{i}^{\mathrm{occ}} \phi_i^*(\mathbf{r})\Sigma_{\mathrm{x}}\phi_i(\mathbf{r}). \tag{2.22}$$

Hartree-Fock theory is a lot more useful than Hartree theory, and for many decades, it was the standard of quantum chemistry. For simple systems such as the hydrogen atom, Hartree-Fock theory even becomes exact. However, the numerical evaluation of the exchange term scales as $\mathcal{O}(N^4)$ with respect to the system size N. This makes Hartree-Fock theory significantly more expensive than Hartree theory, which scales only as $\mathcal{O}(N^3)$.

2.1.4 Xα method

At the beginning of the 1950s, Slater therefore proposed a cheaper (Hartree-like) approximation to Hartree-Fock.[15] Multiplying and dividing Eq. (2.21) by $\phi_i^*(\mathbf{r})\phi_i(\mathbf{r})$ yields

$$\Sigma_{\mathrm{x}}\phi_i(\mathbf{r}) = \left[-\int \mathrm{d}\mathbf{r}' \sum_{j}^{\mathrm{occ}} \frac{1}{\phi_i^*(\mathbf{r})\phi_i(\mathbf{r})} \frac{\phi_i^*(\mathbf{r})\phi_j(\mathbf{r})\phi_j^*(\mathbf{r}')\phi_i(\mathbf{r}')}{|\mathbf{r}-\mathbf{r}'|}\right]\phi_i(\mathbf{r}). \tag{2.23}$$

Slater than took an orbital average in both the nominator and the denominator to obtain

$$\begin{aligned}\Sigma_{\mathrm{x}}\phi_i(\mathbf{r}) &\approx \left[-\frac{2}{n(\mathbf{r})}\int \mathrm{d}\mathbf{r}' \sum_{ij}^{\mathrm{occ}} \frac{\phi_i^*(\mathbf{r})\phi_j(\mathbf{r})\phi_j^*(\mathbf{r}')\phi_i(\mathbf{r}')}{|\mathbf{r}-\mathbf{r}'|}\right]\phi_i(\mathbf{r}) \\ &= \left[-\frac{2}{n(\mathbf{r})}\int \mathrm{d}\mathbf{r}' \frac{|\sum_i^{\mathrm{occ}} \phi_i^*(\mathbf{r})\phi_i(\mathbf{r}')|^2}{|\mathbf{r}-\mathbf{r}'|}\right]\phi_i(\mathbf{r}) \\ &= v_{\mathrm{x}}^{\mathrm{Slater}}(\mathbf{r})\phi_i(\mathbf{r}).\end{aligned} \tag{2.24}$$

where $v_{\mathrm{x}}^{\mathrm{Slater}}$ is a local one-electron potential that acts the same on all orbitals, mimicking the non-local exchange operator Σ_{x}. This "Slater potential" is an important precursor to the optimized effective potential method (see Chap. 5). Slater noticed that $v_{\mathrm{x}}^{\mathrm{Slater}}(\mathbf{r})$ is the Coulomb potential of an exchange density ("exchange hole") $n_x(\mathbf{r},\mathbf{r}')$,

$$n_{\mathrm{x}}(\mathbf{r},\mathbf{r}') = -\frac{4}{n(\mathbf{r})}|\sum_i^{\mathrm{occ}} \phi_i^*(\mathbf{r})\phi_i(\mathbf{r}')|^2, \tag{2.25}$$

and this exchange hole has the properties

$$\begin{aligned} n_{\mathrm{x}}(\mathbf{r},\mathbf{r}) &= -n(\mathbf{r}) \\ \int \mathrm{d}\mathbf{r}'\; n_{\mathrm{x}}(\mathbf{r},\mathbf{r}') &= -1. \end{aligned} \tag{2.26}$$

These two relations can be understood again as manifestations of the Pauli principle. From the definition (2.25), it is also obvious that n_{x} is non-positive,

$$n_{\mathrm{x}}(\mathbf{r},\mathbf{r}') \leq 0. \tag{2.27}$$

Furthermore, the exchange energy can be understood as an interaction of the density with the exchange hole in analogy to the Hartree interaction (2.14),

$$E_{\mathrm{x}} = \frac{1}{2}\int \mathrm{d}\mathbf{r}\; n(\mathbf{r}) \int \mathrm{d}\mathbf{r}'\; \frac{n_{\mathrm{x}}(\mathbf{r},\mathbf{r}')}{|\mathbf{r}-\mathbf{r}'|}, \tag{2.28}$$

where the factor $1/2$ likewise accounts for doubling counting.

Next, Slater proposed a further approximation to Eq. (2.24). In what is nowadays called "local density approximation" (LDA), the exchange energy density is approximated to be locally that of the homogeneous electron gas (HEG),

$$E_{\mathrm{x}} \approx E_{\mathrm{x}}^{\mathrm{LDA}} = \int \mathrm{d}\mathbf{r}\; n(\mathbf{r})\varepsilon_{\mathrm{x,HEG}}[n(\mathbf{r})]. \tag{2.29}$$

The HEG is a simple theoretical system (an idealized metal) whose electronic density n is per definition constant throughout space. The value of n, or equivalently the Wigner-Seitz radius $r_{\mathrm{s}} = (3/4\pi n)^{1/3}$ completely characterizes the HEG. That is, the HEG exchange energy per electron $\varepsilon_{\mathrm{x,HEG}}$ *is simply a function of* r_{s}, which Dirac derived to be

$$\varepsilon_{\mathrm{x,HEG}}(r_{\mathrm{s}}) = -\frac{3}{4\pi}\left(\frac{9\pi}{4}\right)^{1/3}\frac{1}{r_{\mathrm{s}}}. \tag{2.30}$$

The corresponding LDA exchange potential is

$$v_{\mathrm{x}}^{\mathrm{LDA}}(\mathbf{r}) = \frac{\delta E_{\mathrm{x}}^{\mathrm{LDA}}}{\delta n(\mathbf{r})} = \frac{4}{3}\varepsilon_{\mathrm{x,HEG}}[n(\mathbf{r})]. \tag{2.31}$$

The original work of Slater included an additional factor $\alpha = 3/2$ in Eq. (2.29) ("Xα method"),

$$E_{\mathrm{x}}^{\mathrm{X}\alpha} = \alpha E_{\mathrm{x}}^{\mathrm{LDA}} = \alpha \int \mathrm{d}\mathbf{r}\, n(\mathbf{r}) \varepsilon_{\mathrm{x,HEG}}[n(\mathbf{r})], \tag{2.32}$$

but after some discussion it was agreed that $\alpha = 1$ is preferable from a theoretical standpoint. However, values of $\alpha > 1$ gave better agreement with experimental data, which was later explained by the fact that, roughly speaking, the LDA underestimates the exchange energy of inhomogeneous systems. This possibility of optimizing the α parameter, or even adjusting it in order to fit different materials individually, foreshadowed both the promise and the conundrum of semi-empirical density functional theory.

In summation, the LDA exchange has a simple interpretation. In accordance with the Pauli principle, electrons carve out an exchange hole n_{x} around themselves, which integrates to minus one electron. The exchange energy is given by the interaction between the electronic density and the exchange hole. In the LDA, the exchange hole is further approximated to depend only on the local density, and its form is approximated to be spherically symmetric. It is interesting to note that the Dirac expression (2.30) can be re-derived easily by imposing these simple properties for the exchange-hole.[13]

Missing from the exchange-only theories (Hartree-Fock, Xα) are so-called correlation effects. That is, per definition, correlation accounts for quantum effects beyond exchange,

$$\begin{aligned} E &= T + E_{\mathrm{ext}} + E_{\mathrm{H}} + E_{\mathrm{xc}} \\ E_{\mathrm{c}} &= E_{\mathrm{xc}} - E_{\mathrm{x}}. \end{aligned} \tag{2.33}$$

The importance of correlation is immediately clear for the HEG, where Hartree-Fock predicts a vanishing density of states at the Fermi level.[16] This is of course fairly disturbing given that the HEG is supposed to simulate an ideal metal. In contrast to the Hartree-Fock result, the HEG density of states predicted by LDA is simply a free-electron one (Hartree approximation). That is, $v_{\mathrm{x,HEG}}$ is just a constant in space and can therefore only shift the energy spectrum, but not change the dispersion. The added exchange dispersion is averaged out when replacing $\Sigma_{\mathrm{x}} \to v_{\mathrm{x}}^{\mathrm{LDA}}$. This does not detract from the fact that $E_{\mathrm{x}}^{\mathrm{LDA}}$ is exactly equivalent to the exact exchange energy E_{x} for the HEG (by construction).

Physically, this failure of Hartree-Fock can be attributed to the long-range $1/r$ asymptotic behavior of the Coulomb potential (IR divergence). That is, a non-vanishing density of states can be restored, if one dampens the Coulomb potential in Eq. (2.19) (see Chap. 17 in Ref. [17]),

$$\frac{1}{r} \to \frac{e^{-r/r_{\mathrm{TF}}}}{r}. \tag{2.34}$$

This can be interpreted as a collective correlation of electrons that effectively screens the Coulomb interaction beyond $r \gtrsim r_{\mathrm{TF}}$. The characteristic screening length in the HEG ("Thomas-Fermi length") is given by

$$r_{\mathrm{TF}} = \left(\frac{\pi}{12}\right)^{1/3} r_{\mathrm{s}}^{1/2}. \tag{2.35}$$

Thomas-Fermi screening is discussed further in Chap. 3, and more sophisticated treatment of the HEG dispersion is given in App. D.

Overall, such screening effects and other collective electronic correlations lower

the Hartree-Fock energy ($E_c \leq 0$). Analogously to the exchange hole [Eq. (2.28)], one can define a correlation hole n_c,

$$E_c = \frac{1}{2}\int \mathrm{d}\mathbf{r}\, n(\mathbf{r}) \int \mathrm{d}\mathbf{r}'\, \frac{n_c(\mathbf{r},\mathbf{r}')}{|\mathbf{r}-\mathbf{r}'|}, \tag{2.36}$$

which fulfills[18]

$$\begin{aligned} n_c(\mathbf{r},\mathbf{r}) &\leq 0 \\ \int \mathrm{d}\mathbf{r}' n_c(\mathbf{r},\mathbf{r}') &= 0. \end{aligned} \tag{2.37}$$

Furthermore, when taking a system average and spherical average,[18]

$$\langle n_{x,c}(u)\rangle = \frac{1}{N_e}\int \mathrm{d}\mathbf{r}\, n(\mathbf{r}) \int \frac{\mathrm{d}\Omega_{\mathbf{u}}}{4\pi} n_{x,c}(\mathbf{r},\mathbf{r}+\mathrm{u}), \tag{2.38}$$

$\langle n_x\rangle$ increases quadratically with the electron-electron separation $u = |\mathbf{r}'-\mathbf{r}|$, but $\langle n_c\rangle$ increases only linearly,

$$\begin{aligned} \langle n_x(u)\rangle &\approx \langle n_x(u=0)\rangle + \mathcal{O}(u^2) \\ \langle n_c(u)\rangle &\approx \langle n_c(u=0)\rangle + \mathcal{O}(u). \end{aligned} \tag{2.39}$$

This interesting property of the correlation hole is connected to the electronic cusp condition,[19] that is further discussed in Chap. 4.

2.2 Kohn-Sham density functional theory

In the 1960s, Kohn and Sham[20] proposed the combined LDA for exchange and correlation

$$E_{xc}^{LDA} = \int \mathrm{d}\mathbf{r}\, n(\mathbf{r}) \varepsilon_{xc,HEG}[n(\mathbf{r})]. \tag{2.40}$$

Per definition, the correlation energy density of the HEG is given by

$$\varepsilon_{c,HEG}(r_s) = \varepsilon_{xc,HEG}(r_s) - \varepsilon_{x,HEG}(r_s), \tag{2.41}$$

however, $\varepsilon_{c,HEG}(r_s)$ cannot be as easily derived and written down analytically as $\varepsilon_{x,HEG}(r_s)$. For many years, simple interpolation formulas such as the one by Wigner were used instead,

$$\varepsilon_{c,HEG}^{Wigner}(r_s) = -\frac{0.44}{r_s + 7.8}. \tag{2.42}$$

In the 1960s, some progress was made by treating the HEG problem with methods from many-body perturbation theory (RPA[21] and GW,[22] this is further discussed in Chaps. 4 and 5, respectively). In the 1980s, numerically exact results for the HEG were obtained via Quantum Monte Carlo simulations,[23] solving the search for $\varepsilon_c^{LDA}(r_s)$ once and for all. Fig. 2.1 compares the exact exchange-correlation energy to the Dirac, Wigner and RPA approximations. Note that the HEG exchange dominates for high densities (small r_s), and for small densities (large r_s) correlation becomes more important. For metallic densities ($r_s \sim 2-5$), the Wigner formula can roughly approximate the exact correlation energy, whereas RPA overestimates it by a fairly constant amount (about 500 meV per electron $\approx$ 0.018 Ha per electron). In

summation, the Kohn-Sham LDA equations read

$$\left[-\frac{1}{2}\nabla_i^2 + v_{\rm ext}(\mathbf{r}) + v_{\rm H}(\mathbf{r}) + v_{\rm xc}^{\rm LDA}(\mathbf{r})\right]\phi_i(\mathbf{r}) = \varepsilon_i\phi_i(\mathbf{r})$$
$$v_{\rm xc}^{\rm LDA} = \frac{\delta E_{\rm xc}^{\rm LDA}}{\delta n(\mathbf{r})}. \tag{2.43}$$

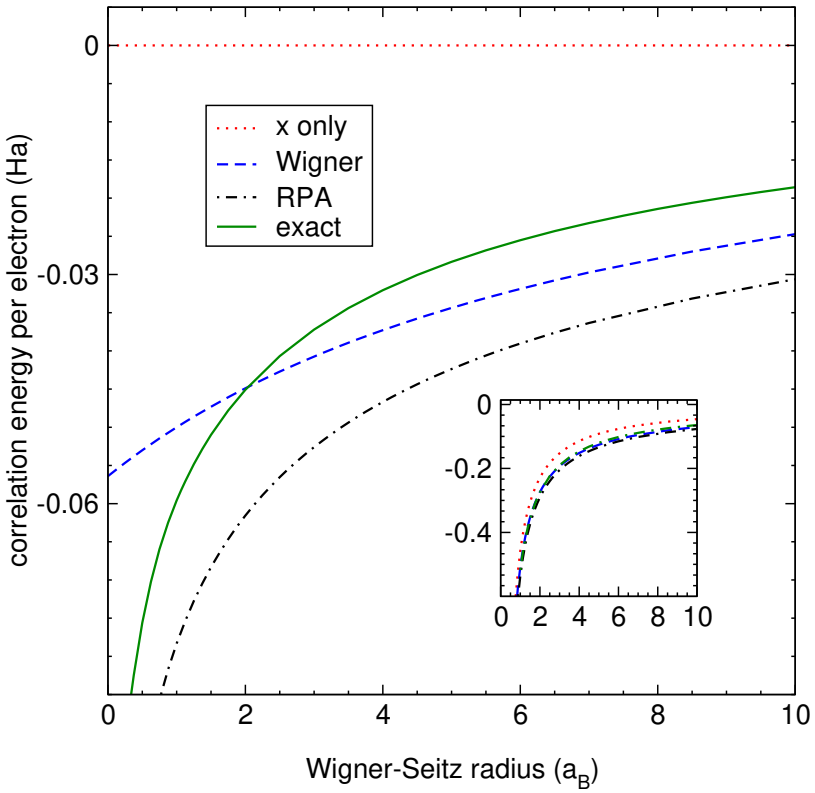

FIGURE 2.1: Correlation energy for the homogeneous electron gas [see Eq. (2.41)]. Next to the exact result,[23] we show also the Wigner [Eq. (2.42)] and RPA (see Chap. 4) approximations. Inset diagram: full exchange-correlation energy, $\varepsilon_{\rm xc,HEG} = \varepsilon_{\rm x,HEG} + \varepsilon_{\rm c,HEG}$ [see Eq. (2.30) for the exchange part].

2.2.1 Hohenberg-Kohn theorems

Two theorems derived earlier by Hohenberg and Kohn[24] provided a firm theoretical basis for the LDA of Kohn and Sham. The first Hohenberg-Kohn theorem states that there is a one-to-one relation between the ground state density and the external potential,

$$n \Leftrightarrow v_{\rm ext}. \tag{2.44}$$

More precisely, n determines $v_{\rm ext}$ only up to a constant, but the addition of a constant to $v_{\rm ext}$ is insignificant from the perspective of the electronic structure. For a given number of electrons, $v_{\rm ext}$ completely determines the Hamiltonian (2.1). Therefore, it is clear that $v_{\rm ext}$ determines in principle all electronic properties through solution of the Schrödinger equation. This includes the ground state density, thus we trivially have $v_{\rm ext} \Rightarrow n$. In contrast, the other direction in Eq. (2.44) is a very powerful

statement, as it implies that all electronic properties are also functionals of n,

$$n \Rightarrow v_{\text{ext}} \Rightarrow \textit{everything}! \tag{2.45}$$

The proof of the Hohenberg-Kohn theorem (2.44) proceeds via *reductio ad absurdum*, and assumes a non-degenerate ground state (see Chaps. 6-7 in the book of Martin[14] for extensions to the degenerate and spin-polarized cases). We assume that there is a second external potential v'_{ext} that differs from v_{ext} by more than a constant and that yields the same ground state density as v_{ext}. Since Ψ and Ψ' are the ground state wave functions of the corresponding Hamiltonians H and H', we have the inequality

$$E = \langle \Psi | \, H \, | \Psi \rangle < \langle \Psi' | \, H \, | \Psi' \rangle \, . \tag{2.46}$$

Adding and subtracting H' to H and plugging in Eq. (2.4) yields

$$E < E' + \int \mathrm{d}\mathbf{r} \, n(\mathbf{r}) [v_{\text{ext}}(\mathbf{r}) - v'_{\text{ext}}(\mathbf{r})]. \tag{2.47}$$

An analogous inequality holds for E' (swapping the indices),

$$E' < E + \int \mathrm{d}\mathbf{r} \, n(\mathbf{r}) [v'_{\text{ext}}(\mathbf{r}) - v_{\text{ext}}(\mathbf{r})], \tag{2.48}$$

and subtracting this from Eq. (2.47) leads to the contradiction

$$E - E' < E' - E. \tag{2.49}$$

Therefore, H cannot have the same ground state density as H', and Eq. (2.44) holds. Next to the electronic cusp [Eq. (2.39)], there is also a nuclear cusp condition,[19] which plays a central role in the "Wilson interpretation" of the Hohenberg-Kohn theorem (2.44).[13] The nuclear cusps are located at the positions of the electronic nuclei $\mathbf{R}_A$, and the shape of the cusps are connected to the nuclear charges Z_A. Further, integrating the electronic density gives N_e [Eq. (2.6)], so the external potential (2.3) is completely determined!

Next, we define the energy functional

$$\begin{aligned} E[n] &= F[n] + \int \mathrm{d}\mathbf{r} \, n(\mathbf{r}) v_{\text{ext}}(\mathbf{r}) \\ F[n] &= T[n] + E_{ee}[n], \end{aligned} \tag{2.50}$$

where T and E_{ee} are the kinetic energy and electron-electron interaction of the fully interacting system [Eq. (2.1)]. T and E_{ee} are functionals of n, since Ψ is a functional of n. Furthermore, $F[n]$ is independent of v_{ext}, which makes it a "universal density functional". The second Hohenberg-Kohn theorem states that $E[n]$ is minimized by the exact ground state density, if one constraints possible densities n' such that they integrate to N_e. Hohenberg and Kohn[24] proved this for densities n' that belong to external potentials v'_{ext} via Eq. (2.44), and again, the v'_{ext} differ from v_{ext} by more than a constant. These n' correspond to ground state wave functions $\Psi' \neq \Psi$, but Ψ minimizes $E(\Psi[n])$, and therefore

$$\begin{aligned} E[n'] &= F[n'] + \int \mathrm{d}\mathbf{r} \, n'(\mathbf{r}) v_{\text{ext}}(\mathbf{r}) \\ &> F[n] + \int \mathrm{d}\mathbf{r} \, n(\mathbf{r}) v_{\text{ext}}(\mathbf{r}). \end{aligned} \tag{2.51}$$

Strictly speaking, only a subset of all possible densities are represented via Eq. (2.44), but the proof can be extended to a wider range of densities (see Chap. 6 in the book of Martin[14]).

The central ansatz of Kohn and Sham[20] was to link the energy functional $E[n]$ to a system of N_e independent particles with the same ground state density,

$$E[n] = T^{\mathrm{IP}}[n] + E_{\mathrm{H}}[n] + E_{\mathrm{xc}}[n] + \int \mathrm{d}\mathbf{r}\, n(\mathbf{r}) v_{\mathrm{ext}}(\mathbf{r}), \tag{2.52}$$

where T^{IP} is the kinetic energy of the independent particles [Eq. (2.12)] and E_{H} is the Hartree energy [Eq. (2.14)]. By comparing with Eq. (2.50), we see that this formally defines the exchange-correlation functional as

$$\begin{aligned} E_{\mathrm{xc}}[n] &= F[n] - T^{\mathrm{IP}}[n] - E_{\mathrm{H}}[n] \\ &= T[n] - T^{\mathrm{IP}}[n] + E_{ee}[n] - E_{\mathrm{H}}[n]. \end{aligned} \tag{2.53}$$

When the exact exchange-correlation functional is plugged into Eq. (2.43) instead of $E_{\mathrm{xc}}^{\mathrm{LDA}}$, and the calculations are performed self-consistently, this yields the exact ground state density. Further, the ground state energy and other ground state properties are exact as well. In this sense, the framework of Kohn-Sham density functional theory (DFT) is a theoretical justification of the independent particle ansatz.[25] Exited state properties, however, are generally not exact in Kohn-Sham DFT. An illuminating example is the HEG, where LDA is the exact exchange-correlation functional, but yields a free-electron density of states.

Both $F[n]$ and $E_{\mathrm{xc}}[n]$ have a generally complicated, non-local, and unknown form. However, much is gained in practice by subtracting out $T^{\mathrm{IP}}[n]$ and $E_{\mathrm{H}}[n]$, which are explicitly known in terms of the IP wave functions and IP density. That is, $E_{\mathrm{xc}}[n]$ is a much smaller contribution to the total energy functional than $F[n]$, and therefore $E_{\mathrm{xc}}[n]$ is a better target for simple approximations such as the LDA. Kohn and Sham[20] proved that the LDA becomes (i) exact in the limit of weakly varying densities, and (ii) exact also in the high density limit (where the kinetic energy dominates). It is noteworthy that the LDA also fullfils the sum rules for n_{x} and n_{c} exactly [Eqs. (2.26) and (2.36)], since the HEG is a theoretically possible system. However, unlike Hartree-Fock, LDA does exhibit self-interaction error. The LDA self-interaction error is present for both the exchange and correlation parts, this is evident for example for the hydrogen atom (where LDA fails to reproduce the exact results $E_{\mathrm{x}} = -E_{\mathrm{H}}$, $E_{\mathrm{c}} = 0$).

2.2.2 The LDA in practice

For almost 30 years, the LDA (in the Kohn-Sham or Xα variants) was by far the dominant use of DFT, and these expressions were used almost interchangeably.[13] During this initial DFT era, the LDA was applied to a wide range of different systems (see Jones and Gunnarsson[26] for a review), and its performance exceeded by far the humble expectations of Kohn and Sham.[20] Analysis comparing the LDA to higher level theories showed that the success of the LDA stems in part from systematic error cancellation. That is, the LDA tends to underestimate exchange effects and overestimate correlation effects, such that the combined LDA exchange-correlation energy is more accurate than either LDA exchange energy or LDA correlation energy alone. Another error cancellation effect occurs through the fact that the exchange and correlation energies depend only on the averages $\langle n_{\mathrm{x}} \rangle$ and $\langle n_{\mathrm{c}} \rangle$. That is, even

though the exchange-correlation holes of real systems can deviate strongly from the ones predicted by LDA, the respective spherical averages of the holes tend to be in much better agreement,[26] and the system average deemphasizes regions where the LDA is less accurate (such as nuclear regions or tails of the electronic density).[18]

Nevertheless, the LDA exhibits clear model errors, such as a pronounced tendency for overbinding. That is, typically the LDA bond lengths are too small, the LDA binding energies are too large, and the LDA overly favors close-packed structures. Further, there is the problem of spurious self-interaction, which prevents LDA for example to bind certain anions.[27] This can be understood by the fact that the LDA exchange potential falls off too quickly in the far-field limit. Namely, $n(\mathbf{r})$ decays exponentially, and so does $v_{\mathrm{x}}^{\mathrm{LDA}}$ via Eq. (2.31). Instead, the exchange potential should fall off as $1/r$ in order to cancel the corresponding self-interaction term of the Hartree potential. Together with the electron-ion term, this leaves an attractive $[(N_e - 1) - Z_A]/r$ long-range interaction tail which can bind the far-out electron. That is, the electron sees "sees" an ionic charge $(N_e - 1) - Z_A$ rather than $N_e - Z_A$ (for a neutral atom, $N_e = Z_A$). In other words, such an electron that is far removed from its atom does no longer contribute to the overall atomic charge. Generally, the lack of exchange interactions leads to overly delocalized orbitals. LDA can even transfer spurious charge fragments between two spatially separated systems. A clear example is the drastic failure for the binding curve of H_2^+,[28] where LDA incorrectly stabilizes a state with $1/2$ electron at each H atom. This also leads to an unphysical maximum in the binding curve. This spurious charge transfer is also connected to the "band gap problem".[29] That is, LDA notoriously yields gaps that are much smaller than the experimental gaps. However, the band gap issue is only in part a failure of the LDA. Since gaps are excited state properties, even the exact DFT gap differs from the experimental one,[30,31] see also Chap. 5.

2.2.3 Generalized gradient approximation

An idea that goes back to the origins of DFT[20,24] is the so-called gradient expansion. That is, one considers a gas of almost constant density,

$$n(\mathbf{r}) \approx n + \sum_{\alpha} \nabla_\alpha r_\alpha n + \frac{1}{2} \sum_{\alpha,\beta} r_\alpha r_\beta \nabla_\alpha \nabla_\beta n + \ldots, \tag{2.54}$$

and calculates correction terms to $E_{\mathrm{xc}}^{\mathrm{LDA}}$. As there is no "direction" in the HEG, linear contributions vanish, and second order contributions proportional $\nabla_\alpha \nabla_\beta$ vanish for $\alpha \neq \beta$ (see also App. F for a related discussion). Further, second order contributions proportional to $\nabla^2 n$ can be recast as contributions $|\boldsymbol{\nabla} n|^2$ via integration by parts.[18] One then obtains the so-called gradient expansion approximation (GAE), whose exchange part is

$$\begin{aligned} E_{\mathrm{x}}^{\mathrm{GEA}} &= \int \mathrm{d}\mathbf{r}\, n(\mathbf{r}) \varepsilon_{\mathrm{x,HEG}}[n(\mathbf{r})] F_{\mathrm{x}}^{\mathrm{GAE}}[n(\mathbf{r}), |\boldsymbol{\nabla} n(\mathbf{r})|] \\ F_{\mathrm{x}}^{\mathrm{GAE}} &= 1 + \mathrm{const} \times \left[n^{4/3}(\mathbf{r}) |\boldsymbol{\nabla} n(\mathbf{r})| \right]^2 + \ldots \end{aligned} \tag{2.55}$$

Here, F_{x} is called the enhancement factor, and the gradient correction for the correlation part can be obtained similarly. However, the GAE turned out to be generally unsuccessful, its exchange potential contains an unphysical divergence for finite systems, and the GAE correlation energy has even the wrong sign. Progress was made in the 1980s, when Langreth *et al.*[32,33] truncated the GAE at small wave

vectors to remove spurious gradient corrections. Interestingly, these wave vector decomposition schemes partly relied on the random-phase approximation (see also Chap 4). Later, it was suggested to perform a truncation in real space rather than in Fourier space.[34,35] It had been recognized that the GAE (2.55) violates exact constraints for the exchange hole, specifically the sum rule (2.26) and non-positivity condition (2.27). To fix this issue, Perdew and Wang[34] proposed a "generalized gradient correction" (GGA), where the enhancement factor F_x is modified to conform with the exact constraints. Subsequently, they developed GGA functionals for correlation as well. This work culminated in the development of the Perdew-Burke-Ernzerhof (PBE) functional,[36] which includes several exact constraints in an elegant fashion. There also exist semi-empirical gradient corrections such as the "BLYP" functional (Becke exchange[35] combined with Lee-Yang-Par correlation[37]). In this approach, the enhancement factors for exchange and correlation assume parameterized functional forms. As for the Xα method, the parameters can be adjusted to reproduce higher level theory or experimental data.

GGA alleviates the overbinding problem of LDA to large extend. Furthermore, it improves both the accuracy of individual exchange and correlation parts, as well as the combined overall accuracy. Starting in the 1990, the success of GGA lead to widespread applications of DFT in solid state physics as well as chemistry. This even culminated in a Nobel prize in chemistry for DFT that was awarded to Kohn in 1998[25] (shared with Pople).

2.2.4 Beyond the GGA

Despite large progresses made, the GGA shares some of the LDA limitations. Most importantly, the theory remains fundamentally nearsighted, depending only on the (semi-)local quantities $n(\mathbf{r})$ and $|\boldsymbol{\nabla} n(\mathbf{r})|$. It is therefore not surprising that the GGA fundamentally fails to reproduce the correct long-range asymptotics required for a description of dispersion and van der Waals (vdW) interactions. Hartree-Fock, which lacks the corresponding correlation effects, fails as well. For atomic and molecular dimers, the asymptotics are of the London form (R^{-6}). A simple and effective approach is to add an explicit dispersion correction of this type as an extra correlation energy term,

$$E_c^{\text{disp}} = -\sum_{AB}^{\text{atoms}} f(R_{\text{AB}}, A, B) C_6^{\text{AB}} / R_{AB}^6. \tag{2.56}$$

The crucial part of this method are the coefficients C_6^{AB}, which can be either simply fit to experimental data or higher level theory, or constructed via more sophisticated schemes that take atomic environments into account.[38,39] Furthermore, some cut-off function $f(R_{\text{AB}})$ truncates the dispersion interaction for smaller distances R_{AB}.[40] One can also include higher order terms ($R^{-8}, R^{-10}, ...$) as well as three-body and higher-body contributions. While there are more elaborate vdW methods (see Refs. [41] and [42]), one appealing feature of the scheme (2.56) is the fact that the computational overhead of calculating E_c^{vdW} is generally small. Strictly speaking, a C_6 approach leaves Kohn-Sham DFT, since E_c^{disp} depends explicitly on the atomic positions. Furthermore, the dispersion correction (2.56) involves (few) semi-empirical parameters, which need to be adapted to each GGA base functional specifically.

Next to the dispersion problem, the GGA also exhibits self-interaction. Although self-interaction errors are generally improved quantitatively with respect to the LDA, the GGA exhibits some of the same qualitative failures such as H_2^+ and the

anions. Again, this is connected to the fundamentally nearsighted nature of the theory. Importantly, the self-interaction errors mostly reside in the exchange part. For instance, the asymptotic $1/r$ decay is captured by the Slater potential, and Hartree-Fock is exact for H_2^+. This inspired Becke and others to create so-called "hybrid functionals", where one admixes a fraction of Hartree-Fock exchange to a DFT base functional. While Becke's initial "half-and-half" hybrid was still based on the LDA, he later introduced the following three-parameter hybrid form[43]

$$E_{\mathrm{xc}}^{\mathrm{hybrid}} = E_{\mathrm{xc}}^{\mathrm{LDA}} + a(E_{\mathrm{x}} - E_{\mathrm{x}}^{\mathrm{LDA}}) + b(E_{\mathrm{x}}^{\mathrm{GGA}} - E_{\mathrm{x}}^{\mathrm{LDA}}) + c(E_{\mathrm{c}}^{\mathrm{GGA}} - E_{\mathrm{c}}^{\mathrm{LDA}}) \tag{2.57}$$

The widely used "B3LYP" hybrid functional is based on the BLYP functional and uses the parameters $\{a = 0.20, b = 0.72, c = 0.81\}$.[44] Perdew *et al.*[45] created a hybrid based on the PBE functional and invoked theoretical reasoning to obtain the parameters $\{a = 1/4, b = 1 - a = 3/4, c = 1\}$. This functional is called "PBE0" and completely eliminates the contribution from $E_{\mathrm{xc}}^{\mathrm{LDA}}$ along with the b and c parameters. However, even with such a single-parameter hybrid it is unavoidable that the optimal amount of exact exchange (the a parameter) depends on the specific material. Furthermore, the optimal hybrid parameters depend in principle also on the GGA base functional. Even though hybrid functionals leave Kohn-Sham DFT, the approach was later given a sound theoretical framework ("generalized Kohn-Sham theory").[46] Hybrid functionals can improve on the accuracy of the GGA, however, the calculations are also significantly more expensive (especially for extended systems). In the meantime, some schemes have been developed to alleviate computational cost.[47,48]

Hybrid DFT is immensely popular, and together with the GGA it builds the backbone of modern DFT calculations.[49] Later, more heavily parametrized hybrid functionals were created,[50] and some also include explicit vdW corrections.[51] Such functionals can achieve astounding accuracy for systems resembling those included in their respective training sets. In recent years, the path of data-driven functional development has been taken further, eventually leading to the construction of machine learned density functionals (see Chap. 6).

Chapter 3

Random-phase approximation

As discussed above, the inclusion of fractions of exact exchange and dispersion corrections can cure the failings of semi-local DFT to a certain amount. However, hybrids and vdW functionals generally contain semi-empirical parameters which are fitted to specific (classes of) materials and applications. It is therefore highly desirable to validate the parameters used by comparing predictions with higher-level theories that are parameter-free. Within DFT, such higher-level theories can be constructed systematically via the adiabatic connection formalism, and the simplest and most popular of the adiabatic connection theories is the random-phase approximation (RPA). In the following, we first introduce the random-phase approximation for the response function, and then show how the adiabatic connection formalism translates this into an approximation for the exchange-correlation energy. The discussion mainly follows the reviews of Ren *et al.*[52] and Olsen *et al.*[53] as well as the thesis of Harl.[54]

3.1 The RPA response function

Per definition, χ describes the linear response of the density to a small variation of the external v_{ext},

$$\chi(\mathbf{r}, \mathbf{r}', t - t') = \theta(t - t') \frac{\delta n(\mathbf{r}, t)}{\delta v_{\text{ext}}(\mathbf{r}', t')}, \tag{3.1}$$

where the step function ensures causality. In contrast, the Kohn-Sham (non-interacting) response function χ_0 describes the linear density response to a small variation of the Kohn-Sham potential v_{KS},

$$\chi_0(\mathbf{r}, \mathbf{r}', t - t') = \theta(t - t') \frac{\delta n(\mathbf{r}, t)}{\delta v_{\text{KS}}(\mathbf{r}', t')}. \tag{3.2}$$

Using the chain rule and surpessing the indices, we can relate the exact and KS response functions as

$$\begin{aligned} \chi &= \frac{\delta n}{\delta v_{\text{KS}}} \frac{\delta v_{\text{KS}}}{\delta v_{\text{ext}}} \\ &= \chi_0 \left[1 + \left(\frac{\delta v_{\text{H}}}{\delta n} + \frac{\delta v_{\text{xc}}}{\delta n} \right) \frac{\delta n}{\delta v_{\text{ext}}} \right] \\ &= \chi_0 + \chi_0 (V + f_{\text{xc}}) \chi, \end{aligned} \tag{3.3}$$

where V is the bare Coulomb kernel and we have defined the exchange-correlation kernel

$$f_{\text{xc}}(\mathbf{r}, \mathbf{r}', t - t') = \frac{\delta v_{\text{xc}}(\mathbf{r}, t)}{\delta n(\mathbf{r}', t')}. \tag{3.4}$$

In the random-phase approximation, the response of an electron is taken to be that of a classical test charge. That is, one neglects exchange-correlation effects by setting $f_{\text{xc}} = 0$, yielding

$$\begin{aligned} \chi^{\text{RPA}} &= \chi_0 + \chi_0 V \chi^{\text{RPA}} \\ \leftrightarrow \chi^{\text{RPA}} &= \chi_0 / (1 - \chi_0 V). \end{aligned} \tag{3.5}$$

The RPA response function for the HEG electron gas is given in App. B ("Lindhard function"). Here, we note only that the static HEG response function reduces to the Thomas-Fermi form in the small wave vector limit,

$$\chi^{\text{TF}}_{\text{HEG}} = \chi^{\text{RPA}}_{\text{HEG}}(q \to 0, \omega = 0) = -\frac{1}{4\pi r^2_{\text{TF}}}. \tag{3.6}$$

Within this approximation, a point-like test charge obeys the Poisson equation

$$-\nabla^2 V^{\text{TF}}(\mathbf{r}) = 4\pi[\delta(\mathbf{r}) + \chi^{\text{TF}} V^{\text{TF}}(\mathbf{r})], \tag{3.7}$$

which yields the sreened interaction (2.34) when solved for V^{TF} (see Chap. 17 in Ref. [17]).

3.2 Adiabatic connection theory

The crucial idea in adiabatic connection theory is to rephrase approximations for E_{xc} as approximations for the exact response function χ. To motivate this idea, we first show that the exact exchange energy can be rewritten in a form involving the non-interacting (Kohn-Sham) response function χ_0,

$$E_{\text{x}} = -\frac{1}{2} \int \mathrm{d}\mathbf{r}\, \mathrm{d}\mathbf{r}' \frac{1}{|\mathbf{r} - \mathbf{r}'|} \left[n(\mathbf{r}) \delta(\mathbf{r} - \mathbf{r}') + 2 \int_0^\infty \frac{d\omega}{2\pi} \chi_0(\mathbf{r}, \mathbf{r}', i\omega) \right]. \tag{3.8}$$

Using perturbation theory, one can derive an explicit expression for χ_0[54]

$$\chi_0(\mathbf{r}, \mathbf{r}', i\omega) = -2 \sum_i^{\text{occ}} \sum_a^{\text{unocc}} \frac{\phi_i^*(\mathbf{r}) \phi_a(\mathbf{r}') \phi_a^*(\mathbf{r}) \phi_i(\mathbf{r}')}{i\omega - (\varepsilon_i - \varepsilon_a)} + \text{c.c.}, \tag{3.9}$$

where c.c. denotes the complex conjugate, and the factor two accounts for spin. Note further that this expression depends on unoccupied electronic orbitals next to occupied ones. Moreover, χ_0 is expressed in terms of imaginary frequencies, and we can perform the frequency integral in Eq. (3.8) using

$$\int_0^\infty \frac{\mathrm{d}\omega}{2\pi} \frac{1}{i\omega + \varepsilon_a - \varepsilon_i} + \text{c.c.} = \int_0^\infty \frac{\mathrm{d}\omega}{2\pi} \frac{2(\varepsilon_a - \varepsilon_i)}{\omega^2 + (\varepsilon_a - \varepsilon_i)^2} = \frac{1}{2}, \tag{3.10}$$

Thus, we can rewrite the second term in Eq. (3.8) as

$$\begin{aligned} &- \int \mathrm{d}\mathbf{r}\, \mathrm{d}\mathbf{r}' \frac{1}{|\mathbf{r} - \mathbf{r}'|} \int_0^\infty \frac{\mathrm{d}\omega}{2\pi} \chi_0(\mathbf{r}, \mathbf{r}', i\omega) \\ &= - \int \mathrm{d}\mathbf{r}\, \mathrm{d}\mathbf{r}' \frac{1}{|\mathbf{r} - \mathbf{r}'|} \sum_i^{\text{occ}} \sum_a^{\text{unocc}} \phi_i^*(\mathbf{r}) \phi_a(\mathbf{r}') \phi_a^*(\mathbf{r}) \phi_i(\mathbf{r}'). \end{aligned} \tag{3.11}$$

We have also used the symmetry of the integrand under exchange of integration variables ($\mathbf{r} \leftrightarrow \mathbf{r}'$). To treat the first term in Eq. (3.8), we insert Eq. (2.13) for the

electronic density and use the completeness relation

$$\delta(\mathbf{r}-\mathbf{r}') = \sum_{n}^{\text{all}} \phi_n^*(\mathbf{r})\phi_n(\mathbf{r}') = \sum_{j}^{\text{occ}} \phi_j^*(\mathbf{r})\phi_j(\mathbf{r}') + \sum_{a}^{\text{unocc}} \phi_a^*(\mathbf{r})\phi_a(\mathbf{r}'), \tag{3.12}$$

which finally recovers the Hartree-Fock expression (2.19).

Next, we consider an adiabatic switching from an (approximate) Kohn-Sham Hamiltonian (switching parameter $\lambda = 0$) to the interacting Hamiltonian ($\lambda = 1$)

$$H^\lambda = H^{\text{KS}} + \frac{\lambda}{2}\sum_{i\neq j}\frac{1}{|\mathbf{r}_i - \mathbf{r}_j|} - \sum_{i,\sigma} v_\sigma^\lambda(\mathbf{r}_i). \tag{3.13}$$

We have adapted again the more general notation used at the beginning of Chap. 2 that treats spin explicitly. The potential v^λ is not known at intermediate values of λ, but is rather *defined such that it yields a constant electronic density along the adiabatic connection path*. We write the difference between exact and KS energies as ("Pauli trick")

$$E - E^{\text{KS}} = \int_0^1 \mathrm{d}\lambda \frac{\partial E^\lambda}{\partial \lambda} = \int_0^1 \mathrm{d}\lambda \frac{\partial}{\partial\lambda}\left\langle \Psi^\lambda \right| H^\lambda \left| \Psi^\lambda \right\rangle. \tag{3.14}$$

The Hellmann-Feynman theorem tells us that only explicit variations of H with λ contribute,

$$\frac{\partial}{\partial\lambda}\left\langle \Psi^\lambda \right| H^\lambda \left| \Psi^\lambda \right\rangle = \left\langle \Psi^\lambda \right| \frac{1}{2}\sum_{i\neq j}\frac{1}{|\mathbf{r}_i - \mathbf{r}_j|} - \frac{\partial}{\partial\lambda}\sum_{i,\sigma} v_\sigma^\lambda(\mathbf{r}_i) \left| \Psi^\lambda \right\rangle. \tag{3.15}$$

Using the constant density requirement and Eq. (2.4), the second term in this expression yields

$$\begin{aligned} -\int_0^1 \mathrm{d}\lambda \left\langle \Psi^\lambda \right| \sum_{i,\sigma}\frac{\partial}{\partial\lambda} v_\sigma^\lambda(\mathbf{r}_i) \left| \Psi^\lambda \right\rangle &= -\sum_\sigma \int \mathrm{d}\mathbf{r}\, n_\sigma(\mathbf{r}) \left[v_\sigma^{\lambda=1}(\mathbf{r}) - v_\sigma^{\lambda=0}(\mathbf{r}) \right] \\ &= -(E_{\text{H}} + E_{\text{xc}}^{\text{KS}}). \end{aligned} \tag{3.16}$$

Therefore, the remaining coupling constant integral equals the sum of Hartree energy plus exact exchange-correlation energy,

$$\begin{aligned} \int_0^1 \mathrm{d}\lambda \left\langle \Psi^\lambda \right| \frac{1}{2}\sum_{i\neq j}\frac{1}{|\mathbf{r}_i - \mathbf{r}_j|} \left| \Psi^\lambda \right\rangle &= E - E^{\text{KS}} + (E_{\text{H}} + E_{\text{xc}}^{\text{KS}}) \\ &= E_{\text{H}} + E_{\text{xc}}, \end{aligned} \tag{3.17}$$

where we have also used Eq. (2.53).

Next, it is useful to define the electronic pair density $n^2(\mathbf{r},\mathbf{r}')$, that is the joint probability to find an electron at $\mathbf{r}$ and another electron at $\mathbf{r}'$ [compare Eq. (2.5)],

$$n^{2,\lambda}(\mathbf{r},\mathbf{r}') = \left\langle \Psi^\lambda \right| \sum_{i\neq j}\sum_{\sigma\sigma'} \delta(\mathbf{r}-\mathbf{r}_i)\delta_{\sigma\sigma_i}\delta(\mathbf{r}-\mathbf{r}_j)\delta_{\sigma'\sigma_j} \left| \Psi^\lambda \right\rangle, \tag{3.18}$$

which can be used to rewrite Eq. (3.17) as[18]

$$\frac{1}{2}\int_0^1 \mathrm{d}\lambda \int \mathrm{d}\mathbf{r}\,\mathrm{d}\mathbf{r}' \frac{n^{2,\lambda}(\mathbf{r}',\mathbf{r}')}{|\mathbf{r}-\mathbf{r}'|} = E_{\text{H}} + E_{\text{xc}}. \tag{3.19}$$

Comparing this result to the definition of the exchange-correlation hole n_{xc} [compare Eqs. (2.25) and (2.36)], we see that n_{xc} is related to the coupling constant integrated pair density,

$$\int_0^1 \mathrm{d}\lambda\; n^{2,\lambda}(\mathbf{r},\mathbf{r}') = n(\mathbf{r})n(\mathbf{r}') + n(\mathbf{r})n_{\mathrm{xc}}(\mathbf{r},\mathbf{r}'). \tag{3.20}$$

This relation is useful for explicit constructions of n_{xc}. The exchange hole [Eq. (2.25)] is recovered as the independent-particle limit ($\lambda = 0$). The pair density can by further expressed in terms of density fluctuations δn,

$$\delta n(\mathbf{r}) = \sum_\sigma \delta n_\sigma(\mathbf{r}) = \sum_\sigma [\sum_i \delta(\mathbf{r}-\mathbf{r}_i)\delta_{\sigma\sigma_i} - n_\sigma(\mathbf{r})]. \tag{3.21}$$

We rewrite Eq. (3.18) by adding and subtracting terms $i = j$,

$$\begin{aligned}
&\langle\Psi^\lambda|\sum_{i\neq j}\delta(\mathbf{r}-\mathbf{r}_i)\delta_{\sigma\sigma_i}\delta(\mathbf{r}'-\mathbf{r}_j)\delta_{\sigma\sigma_j}|\Psi^\lambda\rangle \\
&= \langle\Psi^\lambda|\sum_{ij}\sum_{\sigma\sigma'}\delta(\mathbf{r}-\mathbf{r}_i)\delta_{\sigma\sigma_i}\delta(\mathbf{r}'-\mathbf{r}_j)\delta_{\sigma\sigma_j} - \sum_i\sum_{\sigma'\sigma'}\delta(\mathbf{r}-\mathbf{r}_i)\delta_{\sigma\sigma_i}\delta(\mathbf{r}'-\mathbf{r}_i)\delta_{\sigma',\sigma_i}|\Psi^\lambda\rangle \\
&= \langle\Psi^\lambda|\,[\delta n(\mathbf{r}) + n(\mathbf{r})][\delta n(\mathbf{r}') + n(\mathbf{r}')]\,|\Psi^\lambda\rangle - n(\mathbf{r})\delta(\mathbf{r}-\mathbf{r}') \\
&= \langle\Psi^\lambda|\,\delta n(\mathbf{r})\delta n(\mathbf{r}')\,|\Psi^\lambda\rangle + n(\mathbf{r})n(\mathbf{r}') - n(\mathbf{r})\delta(\mathbf{r}-\mathbf{r}'),
\end{aligned} \tag{3.22}$$

where we have used that the expection value of $\delta n(\mathbf{r})$ vanishes,

$$\langle\Psi^\lambda|\,\delta n(\mathbf{r})\,|\Psi^\lambda\rangle = 0. \tag{3.23}$$

In a last step, we subtract the Hartree energy [Eq. (2.14)] and employ the fluctuation-dissipation theorem[54] [compare Eq. (3.8) for the exchange-only case],

$$\langle\Psi^\lambda|\,\delta n(\mathbf{r})\delta n(\mathbf{r}')\,|\Psi^\lambda\rangle = -2\int_0^\infty \frac{d\omega}{2\pi}\chi^\lambda(\mathbf{r},\mathbf{r}',i\omega). \tag{3.24}$$

This finally yields the so-called ACFDT expression for E_{xc} ("adiabatic connection fluctuation-dissipation theorem"),

$$E_{\mathrm{xc}} = -\frac{1}{2}\int_0^1 \mathrm{d}\lambda \int \mathrm{d}\mathbf{r}\,\mathrm{d}\mathbf{r}'\frac{1}{|\mathbf{r}-\mathbf{r}'|}\left[n(\mathbf{r})\delta(\mathbf{r}-\mathbf{r}') + 2\int_0^\infty \frac{d\omega}{2\pi}\chi^\lambda(\mathbf{r},\mathbf{r}',i\omega)\right]. \tag{3.25}$$

Subtracting the exchange energy, we can further express the exact correlation energy as

$$E_{\mathrm{c}} = -\frac{1}{2}\int_0^1 \mathrm{d}\lambda \int \mathrm{d}\mathbf{r}\,\mathrm{d}\mathbf{r}'\frac{1}{|\mathbf{r}-\mathbf{r}'|}2\int_0^\infty \frac{\mathrm{d}\omega}{2\pi}[\chi^\lambda(\mathbf{r},\mathbf{r}',i\omega) - \chi_0(\mathbf{r},\mathbf{r}',i\omega)]. \tag{3.26}$$

Inserting the RPA approximation for χ^λ [compare Eq. (3.5)] allows us to *perform the coupling constant integration analytically*,

$$\begin{aligned}\int_0^1 d\lambda \ \left(\chi^{\lambda,\mathrm{RPA}} - \chi_0\right) V &= \int_0^1 \mathrm{d}\lambda \ \chi_0 \lambda V \chi^{\lambda,\mathrm{RPA}} V \\ &= \int_0^1 \mathrm{d}\lambda \ \left(\chi_0 \lambda V \chi_0 V + \chi_0 \lambda V \chi_0 \lambda V \chi_0 V + ...\right) \\ &= \frac{1}{2}\chi_0 V \chi_0 V + \frac{1}{3}\chi_0 V \chi_0 V \chi_0 V + ... \\ &= -\ln(1 - \chi_0 V) - \chi_0 V.\end{aligned} \tag{3.27}$$

We have obtained the ACFDT-RPA correlation energy,

$$\begin{aligned}E_\mathrm{c}^\mathrm{RPA} &= \int_0^\infty \frac{\mathrm{d}\omega}{2\pi} \mathrm{Tr}\left\{\ln[1 - \chi_0(i\omega)V] + \chi_0(i\omega)V\right\} \\ \mathrm{Tr}(AB) &= \int \mathrm{d}\mathbf{r} \, \mathrm{d}\mathbf{r}' A(\mathbf{r}, \mathbf{r}') B(\mathbf{r}', \mathbf{r}).\end{aligned} \tag{3.28}$$

It is interesting that this formula can be derived also from several other approaches. Within many-body perturbation theory, the RPA can be expressed as a series of ring diagrams. This diagrammatic approach is emphasized in Chaps. 4 and 5. Moreover, the RPA can be obtained within coupled cluster theory and from a plasmon perspective, see Ref. [55]. Such alternative viewpoints are also helpful when constructing different beyond-RPA theories.

3.3 The RPA in practice

Since its development, the RPA has been used as a precise theory for long-range interactions.[21,56,57] Accordingly, a main focus point of RPA calculations has been its application to dispersion, vdW, and hydrogen bonding. That includes weakly interacting dimers,[58] rare gas solids,[59] graphite and other layered materials[60,61] as well as water and ice (see Refs. [62–64], Chap. 6). Moreover, the RPA gives a good description of covalent and metallic bonds.[65,66] This balanced account of different bonding types enables the RPA to give an unbiased characterization of different bonding geometries. Notable applications are barrier heights,[52] phase energy differences,[53] silicon defects[2] and gold clusters.[67] RPA calculations of diamond surface energies are presented in Chap. 6. Perhaps most famous is the application to molecular adsorption processes,[68,69] where the RPA predicts adsorption energies and geometries with excellent accuracy next to a good description of both the isolated surfaces and molecules.

Despite its numerous successes, the RPA is not a perfect theory, and the most glaring failure is a large overestimation of total correlation energies. That is, compared to exact references, RPA correlation energies are too negative by roughly 500 meV per electron.[53] However, most physically interesting properties are calculated from energy differences, where one can benefit from error cancellation. The fact that the RPA is so successful means that this error cancellation is astonishingly systematic. One counterexample are atomization energies, which tend to be underestimated by the RPA.[52,70]

The pronounced overcorrelation of RPA is already present for the HEG (see Fig. 2.1). This has inspired several beyond-RPA corrections. In the so-called RPA+ method,[70,71] the RPA is corrected at the level of semi-local DFT. For instance, the

most simple RPA+ correction is based on LDA,

$$E_{\mathrm{c}}^{\mathrm{RPA+}} = E_{\mathrm{c}}^{\mathrm{RPA}} + \int \mathrm{d}\mathbf{r}\, n(\mathbf{r})\{\varepsilon_{\mathrm{c,HEG}}[n(\mathbf{r})] - \varepsilon_{\mathrm{c,HEG}}^{\mathrm{RPA}}[n(\mathbf{r})]\}. \tag{3.29}$$

The idea that the RPA is defective at short-range has also been used to create (semi-empirical) range-separated RPA hybrid functionals (see Refs. [72–76], Chap. 4).

The overcorrelation can be understood by the fact that RPA correlation is not free of self-interaction. This has inspired corrections from many-body perturbation theory on the one hand, where one can add second order and higher order exchange diagrams that are missing in the RPA (SOSEX).[52,77] On the other hand, one can go beyond the RPA within the adiabatic connection framework via more elaborate approximations for f_{xc}. That is, the RPA corresponds to the Hartree approximation for f_{xc}, and a hierarchy of beyond-Hartree approximations can be constructed fairly similarly to the approximations for E_{xc} discussed in Chap. 2. The inclusion of the exact exchange kernel f_{x} tends to improve upon RPA, but this is extremely expensive (f_{x} is non-local in both space and time). Approximations for f_{xc} can be found also using semi-local DFT. The simplest kernel is the adiabatic (frequency-independent) LDA exchange kernel [compare Eq. (2.31)]

$$\begin{aligned} f_{\mathrm{x}}^{\mathrm{ALDA}}(\mathbf{r},\mathbf{r}',t-t') &= \delta(\mathbf{r}-\mathbf{r}')\delta(t-t')f_{\mathrm{x,HEG}}[n(\mathbf{r},t)] \\ f_{\mathrm{x,HEG}}(r_{\mathrm{s}}) &= -\pi\left(\frac{4}{9\pi}\right)^{2/3} r_{\mathrm{s}}^2. \end{aligned} \tag{3.30}$$

However, the use of this kernel causes a UV catastrophe, which leads the pair density to diverge at small distances.[78] Even tough this unphysical UV divergence is integrable (the correlation energy is finite), the ALDA is plagued by serious numerical problems. Olsen and Thygesen[79] eliminated this divergence by a truncation in Fourier space. Their rALDAx method ("renormalized ALDAx") has also been extended to include correlation and gradient corrections, and the recent rPBE kernel shows particularly promising results.[53]

A more subtle problem of the RPA is that one usually uses orbitals from (semi-)local DFT calculations to evaluate the RPA expression (3.28). To some extend, the RPA will "inherit" the deficiencies of the approximate DFT ground state. To that point, RPA using PBE orbitals tends to improve somewhat over RPA using LDA orbitals. However, the differences between these two is significantly smaller than the differences between the actual PBE and LDA functionals.[53] The fact that the dependence on the DFT reference state tends to be weak is indeed quite favorable and justifies the use of (semi-)local DFT orbitals for RPA calculations to some extend. However, there are cases such as the Ar dimer where the approximate DFT ground state is simply qualitatively wrong. As a remedy, Ren *et al.*[80] suggested to keep DFT orbitals for the RPA correlation energy, but evaluate the exchange energy using Hartree-Fock orbitals. From a theoretical viewpoint, the cleanest solution is clearly a self-consistency cycle, but RPA self-consistency is not as straightforward as for DFT or Hartree-Fock. In Chap. 5, we use the optimized effective potential method to perform self-consistent RPA calculations. For the sake of completeness, we note that there are also other self-consistent RPA schemes, see for example Ref. [81]. Moreover, one can cure the deficiencies of the DFT ground state by adding diagrammatic "singles" corrections to the RPA.[52,80,82]

Finally, the large computational cost associated with RPA calculations has been a major hurdle for large scale applications. At the beginning of the 2000s, Furche[83]

implemented a general purpose RPA code which scaled, however, as $\mathcal{O}(N^6)$ with respect to the system size. In the following years, the computational cost was reduced with the help of several algorithmic improvements. For instance, some speed-up has been achieved via resolution-of-the-identity techniques.[52,55] Furthermore, Kaltak *et al.*[1,2] used the space-time *GW* formalism[3,4] to bring the RPA system size scaling down to $\mathcal{O}(N^3) - \mathcal{O}(N^4)$. Another computational hurdle is that RPA correlation energies converge slowly with respect to the basis set size. Specifically, many unoccupied orbitals are needed to resolve the RPA cusp. In Chap. 4, we show how range-reparation can eliminate the cusp and therefore speed up basis set convergence. Notably, the cusp gets less pronounced when RPA is corrected via SOSEX or f_{xc}, which can also alleviate basis set convergence to some extend (however, the corrections require other computational overhead). Alternatively, the basis set problem can also be tackled via density functional perturbation theory.[52] Last, in Chap. 6 we employ machine learning to reduce the RPA system size scaling to $\mathcal{O}(N \ln N)$.

Part II

Results

Chapter 4

Plane wave basis set correction methods for RPA correlation energies

Stefan Riemelmoser, Merzuk Kaltak, and Georg Kresse

Plane wave basis set correction methods for RPA correlation energies

published in: The Journal of Chemical Physics **152** (13), 134103 (2020)
doi: https://doi.org/10.1063/5.0002246
arxiv: https://arxiv.org/abs/2001.08124

Author contribution: Conception of the project (together with coworkers), analytical derivations (together with coworkers), code implementation, numerical calculations, first paper draft, paper editing and proofreading (together with coworkers)

Electronic correlation energies from the random-phase approximation converge slowly with respect to the plane wave basis set size. We study the conditions under which a short-range local density functional can be used to account for the basis set incompleteness error. Furthermore, we propose a one-shot extrapolation scheme based on the Lindhard response function of the homogeneous electron gas. The different basis set correction methods are used to calculate equilibrium lattice constants for prototypical solids of different bonding types.

4.1 Introduction

The random-phase approximation (RPA) for the electronic correlation energy was developed during the beginnings of many-body perturbation theory in the 1950s. The detailed analytical studies of the homogeneous electron gas (HEG) in the RPA have contributed greatly to the understanding of many-body effects in solid state physics such as plasmons, screening and electronic correlation in general.[84] However, large scale practical applications of the RPA have been possible only in the last one or two decades due to increasing computer power.

In the 1970s, the RPA was formulated in the framework of density functional theory (DFT)[20,24] by Langreth and Perdew via the adiabatic connection formalism.[56,57] It can be categorized as a fifth rung functional (i.e. includes unoccupied orbitals) on Jacob's ladder.[85] In the early 2000s, renewed interest was drawn to the RPA following the work of Yan *et al.*[71] and Furche.[83] Most importantly, the RPA - unlike lower rung functionals - describes long-range effects like van der Waals - bonding and dispersion very well. Furthermore, the RPA is compatible with exact exchange and behaves well in the metallic limit, where other methods such as Møller-Plesset perturbation theory diverge.[59,65] Finally, the adiabatic connection formalism provides a natural way to construct beyond-RPA theories, see e.g. Ref. [78]. The recent development has been summarized in the review of Ren *et al.*,[52] which also includes derivations of the standard RPA expressions.

One limiting factor of the RPA, like for other methods based on many-body perturbation theory, is the slow convergence of the correlation energy with respect to the basis set size. In a canonical plane wave implementation, the RPA scales at least as N_{PW}^3 with respect to the number of plane waves N_{PW}.[1–3] On the other hand, the basis set incompleteness error decays only as $1/N_{\mathrm{PW}}$.[59,86,87] The reason for this slow convergence is connected to the electronic cusp condition,[19,88] which states that the exact many-body wave function has a kink at electron coalescence. This (integrable) UV - divergence is caused by the $1/r$ - singularity of the Coulomb potential, or equivalently by its $1/q^2$ - high momentum behavior. The cusp-related convergence problem is not limited to plane waves, but applies also to local basis sets.[83]

The most straightforward strategy to reduce the computational cost is to perform a basis set extrapolation.[59,87] Alternatively, range-separated DFT[89] circumvents the cusp condition directly by replacing the short-range part of the Coulomb interaction, which includes the singularity, by DFT. Range-separation has been applied to the RPA by Toulouse *et al.*,[72,73] Janesko *et al.*[74–76] and Bruneval,[90] who have all reported a significant reduction of computational cost.

Range-separation has possibly further advantages. The RPA has well known shortcomings in describing short- and mid-range correlation effects, such as the prediction of an unphysical bump in the dissociation curve of Be_2.[72] Unsurprisingly, it is thus possible to improve on full-range RPA by creating range-separated hybrid functionals. The price to pay is the introduction of empirical parameters into the theory. Inverse range-separation, which aims to cure IR divergences, has been applied extensively to the exchange energy, e.g. in the popular HSE hybrid functional.[47]

Range-separation schemes up to now have been based mostly on the error function. In this paper, we drop this constraint and investigate the performance of alternative long-range potentials. First, we recall the wave vector decomposition method of old[21] to study range-separated RPA based on momentum cutoffs. Second, we propose an optimized long-range potential ("squeezed Coulomb kernel") that performs an implicit basis set extrapolation.

In Sec. 4.2, we discuss our range-separation scheme, and study exacts limits for range-separation based on wave vector decomposition. Then, we use the results for the low-density HEG to construct the squeezed Coulomb kernel. In Sec. 4.3, we present numerical studies for the HEG and discuss the analytical representations of our local density functionals. In Sec. 4.4, we show test calculations for a small set of prototypical materials and compare the different basis set correction methods. Conclusions are drawn in Sec. 4.5. The discussion is restricted to the case of non-spin-polarized electrons. Unless stated otherwise, Hartree units are used throughout the work.

4.2 Theory

4.2.1 Range-separated density functional theory

Since we are interested in a simple basis set correction method for post-DFT RPA calculations, we adopt the range-separation scheme of Bruneval.[90] Generally, the Coulomb kernel is decomposed in a long-range and a complementary short-range part

$$V = V^{\mathrm{LR}}(\mu) + V^{\mathrm{SR}}(\mu), \tag{4.1}$$

where μ is a tunable range-separation parameter and cuts of the Coulomb potential at a cutoff radius $r_{\mathrm{cut}} \approx 1/\mu$. The long-range version of the RPA correlation energy $E_{\mathrm{c}}^{\mathrm{RPA,LR}}$ is obtained by replacing V by V^{LR} in the text-book expression. The short-range part is then formally defined as

$$E_{\mathrm{c}}^{\mathrm{RPA,SR}}(\mu) = E_{\mathrm{c}}^{\mathrm{RPA}} - E^{\mathrm{RPA,LR}}(\mu), \tag{4.2}$$

and is, in practice, approximated by a density functional

$$E_{\mathrm{c}}^{\mathrm{RPA}} \approx E_{\mathrm{c}}^{\mathrm{RPA,LR}}(\mu) + E_{\mathrm{c}}^{\mathrm{DFT,SR}}(\mu). \tag{4.3}$$

This scheme provides a generalized adiabatic connection[89,91] between the full-range RPA, which is obtained in the limit $\mu \to \infty$ and DFT in the limit $\mu \to 0$. As in standard DFT, the transferability of the density functional is key to the success of the method. Near the full-range limit, short-range effects are essentially localized. Thus, we can expect that the short-range part is described exactly by the local density approximation (LDA).[20] A more concrete theorem will be given further below.

In the LDA, the short-range correction required to recover the full RPA correlation energy is given by

$$E_{\mathrm{c}}^{\mathrm{LDA,SR}} = \int \mathrm{d}\mathbf{r}\, \varepsilon_{\mathrm{c,HEG}}^{\mathrm{RPA,SR}}[n(\mathbf{r})] n(\mathbf{r}), \tag{4.4}$$

where $n(\mathbf{r})$ is the local electronic density and $\varepsilon_{\mathrm{c,HEG}}^{\mathrm{RPA,SR}}$ is given by the difference between the full-range and the long-range RPA correlation energy per particle for the homogeneous electron gas

$$\varepsilon_{\mathrm{c,HEG}}^{\mathrm{RPA,SR}}(n) = \varepsilon_{\mathrm{c,HEG}}^{\mathrm{RPA}}(n) - \varepsilon_{\mathrm{c,HEG}}^{\mathrm{RPA,LR}}(n). \tag{4.5}$$

Naturally, it is also possible to use more sophisticated density functionals. For example, various gradient correction schemes were discussed by Toulouse *et al.*[92] However, in this work we will stay at the LDA level of DFT, which was also the choice of Bruneval.[90]

Nowadays, the most common way to separate the Coulomb potential in long- and short-range parts is based on the error function

$$\begin{aligned} V^{\mathrm{LR}}(r,\mu) &= \mathrm{erf}(\mu r)/r \\ V^{\mathrm{SR}}(r,\mu) &= 1/r - \mathrm{erf}(\mu r)/r. \end{aligned} \tag{4.6}$$

Besides the error function, other separation methods have been suggested. Toulouse *et al.*[89] have used a scheme based on the "erfgau interaction"

$$V^{\mathrm{LR}}_{\mathrm{erfgau}}(r,\mu) = \mathrm{erf}(c\mu r)/r - \frac{2c\mu}{\sqrt{\pi}}\exp(-c^2\mu^2 r^2/3), \tag{4.7}$$

where $c = (1+6\sqrt{3})^{1/2}$ is some scaling constant introduced in order to achieve similar cutoff radii as the error function. The erfgau interaction provides a much sharper separation between long and short-range interactions. They showed that this is manifest in the DFT limit, where both $E_{\mathrm{x}}^{\mathrm{SR}}$ and $E_{\mathrm{c}}^{\mathrm{SR}}$ were flat as a function of the range-separation parameter for the erfgau interaction, but not for the error function.[89] This means that the erfgau interaction does a better job at separating out long-range effects.

4.2.2 Wave vector decomposition

When working with a plane wave basis, it is natural to seek a range-separation scheme in Fourier space. In this section, we review the available literature on what is commonly referred to as "wave vector decomposition". We comment first on the limit of small wave vectors corresponding to the DFT limit (which is less relevant to the present work but included here for completeness) and then on the more relevant case of large wave vectors, corresponding to the full-range limit.

The error function exhibits Gaussian decay over the Coulomb potential

$$V^{\mathrm{LR}}(q,\mu) = \frac{4\pi e^{-q^2/4\mu^2}}{q^2}, \tag{4.8}$$

whereas the wave vector decomposition method is based on a hard momentum cutoff

$$V^{\mathrm{LR}}(q,Q_{\mathrm{cut}}) = \begin{cases} 4\pi/q^2 & \text{for } q \le Q_{\mathrm{cut}} \\ 0 & \text{for } q > Q_{\mathrm{cut}}. \end{cases} \tag{4.9}$$

The latter scheme was used by Nozières and Pines[21] (NP) to investigate the RPA for the HEG.

For the small wave vector limit, NP developed a series expansion for $\varepsilon_{\mathrm{c}}^{\mathrm{RPA,LR}}$ in terms of the cutoff momentum

$$\varepsilon_{\mathrm{c,HEG}}^{\mathrm{RPA,LR}}(Q_{\mathrm{cut}}) = -\frac{3\alpha}{8\pi}Q_{\mathrm{cut}}^2 r_{\mathrm{s}} + \mathcal{O}(Q_{\mathrm{cut}}^3 r_{\mathrm{s}}^{3/2}), \tag{4.10}$$

where $\alpha = (4/9\pi)^{1/3}$ and $r_{\mathrm{s}} = (\alpha k_{\mathrm{F}})^{-1}$ is the Wigner-Seitz radius. NP studied corrections to the RPA from second and higher order exchange diagrams and found that they contribute to the expansion above only at order $\mathcal{O}(Q_{\mathrm{cut}}^4)$. Thus, the contribution of small wave vectors to the correlation energy is exactly described by the RPA

$$\varepsilon_{\mathrm{c,HEG}}^{\mathrm{LR,RPA}} \to \varepsilon_{\mathrm{c,HEG}}^{\mathrm{LR}} \quad \text{for } Q_{\mathrm{cut}} \to 0. \tag{4.11}$$

The series expansion (4.10) is valid, if the relevant momentum transfers are small compared to the Thomas-Fermi wave vector $k_s = \sqrt{4k_F/\pi}$.

For large Q_{cut}, NP used second order perturbation theory for $\varepsilon^{SR}_{c,HEG}(Q_{cut})$ and then interpolated between this and the small Q_{cut} expansion (4.10). This gave the NP interpolation formula for the electronic correlation energy

$$\varepsilon^{NP}_{c,HEG}(r_s) = (0.031 \ln(r_s) - 0.115)\,\text{Rydberg}. \tag{4.12}$$

A similar interpolation method was used by Langreth and Perdew[56,57] to describe the exchange-correlation energies of metallic surfaces. However, they used local density functional theory for large momentum transfers. Hence, their method closely resembles our own wave vector decomposition scheme.

4.2.3 Approaching the full-range limit

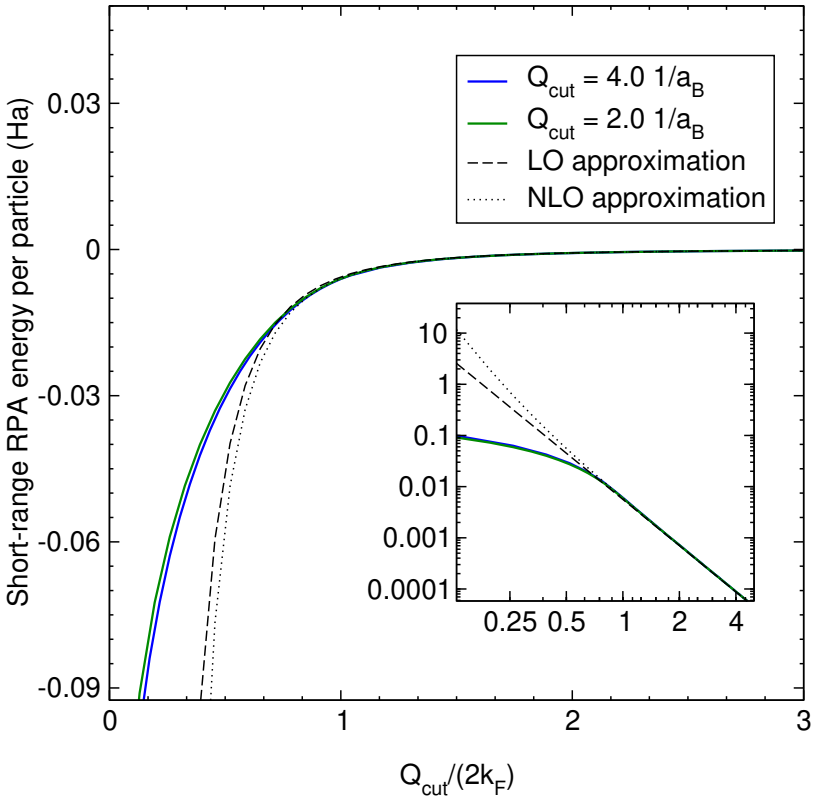

FIGURE 4.1: Short-range LDA functionals for two different cutoffs Q_{cut}. Full lines represent numerical evaluations of $\varepsilon^{RPA,SR}_{c,HEG}$ as a function of $1/k_F \propto r_s$, dashed and dotted lines represent the low density approximation (4.14) up to leading order (LO) and next-to-leading order (NLO) respectively. The latter is on this scale hardly distinguishable from $\varepsilon^{RPA,SR}_{c,HEG}$ for $Q_{cut}/(2k_F) \gtrsim 1$. Inset diagram: log-log plot of $|\varepsilon^{RPA,SR}_{c,HEG}|$.

The short-range RPA correlation energy per particle for the HEG, $\varepsilon^{RPA,SR}_{c,HEG}$, is an important quantity in our range-separation scheme [see Eq. (4.4)]. One requires to know $\varepsilon^{RPA,SR}_{c,HEG}$ as a function of the range-separation parameter Q_{cut}. As $Q_{cut} \to \infty$, V^{LR} approaches the full Coulomb potential and $E^{RPA,SR}_c$ vanishes. In Sec. 4.2.4, we will show that the large Q_{cut} limit yields important information on the plane wave basis set incompleteness error. Furthermore, knowledge of the exact limits is useful

for finding practical representations of $\varepsilon_{c,HEG}^{RPA,SR}$. Paziani *et al.*[93] have conducted studies along these lines for the error function, here we concentrate on the hard cutoff.

Numerically, $\varepsilon_{c,HEG}^{RPA,SR}$ can be evaluated with relative ease, since the Lindhard response function for the HEG in terms of imaginary frequencies $\chi_{0,HEG}(q,i\omega)$ is well known [see for example Eq. (4.8) in Ref. [94]]. For a given long-range potential and value of r_s, we first obtain $\varepsilon_{c,HEG}^{RPA,LR}(r_s)$ via (see Appendix B)

$$\varepsilon_{c,HEG}^{RPA,LR} = \frac{1}{n}\int \frac{dq}{(2\pi)^3} 4\pi q^2 \int_0^\infty \frac{d\omega}{2\pi} \left\{ \ln\left[1 - \chi_{0,HEG}(q,i\omega)V^{LR}(q)\right] + \chi_{0,HEG}(q,i\omega)V^{LR}(q) \right\}, \tag{4.13}$$

and then $\varepsilon_{c,HEG}^{RPA,SR}(r_s)$ using Eq. (4.5). We calculate $\varepsilon_{c,HEG}^{RPA,SR}$ according to this procedure and show results in Fig. 4.1 for two different cutoffs Q_{cut}.

In the low density or large Q_{cut} limit, $\varepsilon_{c,HEG}^{RPA,SR}$ behaves as (see Ref. [87], Appendix B)

$$\varepsilon_{c,HEG}^{RPA,SR}(r_s, Q_{cut}) = -\frac{1}{\pi Q_{cut}^3 r_s^3} + \mathcal{O}\left(\frac{1}{Q_{cut}^5 r_s^5}\right). \tag{4.14}$$

To estimate the validity range of the low density expansion, we have to compare Q_{cut} to some natural momentum scale. The relevant scale is the Fermi wave vector k_F, which is manifest in Eq. (4.14) ($k_F \propto 1/r_s$). Fig. 4.1 shows that the low density approximation is accurate for $Q_{cut} \gtrsim 2k_F$. Furthermore, Fig. 4.1 shows that $\varepsilon_{c,HEG}^{RPA,SR}$ is nearly scale invariant when plotted versus $Q_{cut}/2k_F$. For $Q_{cut} \to 0$, $\varepsilon_{c,HEG}^{RPA,SR}$ converges towards the full range RPA value $\varepsilon_{c,HEG}^{RPA}$, and for large Q_{cut}, the scale invariance follows from the asymptotics [Eq. (4.14)]. However, the near scale invariance at intermediate densities is not an obvious observation.

Since we will also apply range-separation to the exchange energy, we require expressions for the respective short-range LDA correction. Analogous to Eq. (4.5), the short-range exchange energy per particle for the HEG is defined as

$$\varepsilon_{x,HEG}^{SR}(n) = \varepsilon_{x,HEG}(n) - \varepsilon_{x,HEG}^{LR}(n), \tag{4.15}$$

where $\varepsilon_{x,HEG} = -3/(4\pi\alpha r_s)$ is the familiar Dirac expression for the full-range exchange energy per particle and $\varepsilon_{x,HEG}^{LR}$ is given by (see Appendix A)

$$\varepsilon_{x,HEG}^{LR}(r_s, Q_{cut}) = \begin{cases} \frac{-Q_{cut}}{\pi} + \frac{3\alpha Q_{cut}^2}{8\pi} r_s - \frac{\alpha^3 Q_{cut}^4}{64\pi} r_s^3 & \text{for } Q_{cut} < 2k_F \\ 0 & \text{for } Q_{cut} \geq 2k_F. \end{cases} \tag{4.16}$$

The constant term is connected to the normalization of the exchange hole, see Ref. [91]. As pointed out by NP, the term linear in r_s cancels the respective correlation term. This cancellation applies for the error function as well, but with linear terms $\pm 3\alpha/(2\pi)\mu^2 r_s$.[93]

4.2.4 Plane wave basis set incompleteness error

The large Q_{cut} limit of $\varepsilon_{c,HEG}^{RPA,SR}$ relates to an equation previously derived by Klimeš *et al.*,[86] as we briefly discuss in this section. To show this, one inserts the leading order term in Eq. (4.14) into Eq. (4.4) and uses $r_s = (3/4\pi n)^{1/3}$. This means we construct

a local density functional approximation for the short-range part, yielding

$$E_c^{\mathrm{RPA,SR}}(Q_{\mathrm{cut}}) \approx -\frac{4}{3Q_{\mathrm{cut}}^3}\int \mathrm{d}\mathbf{r}\, n(\mathbf{r})n(\mathbf{r}). \tag{4.17}$$

By Fourier transforming the density to reciprocal space, we obtain

$$E_c^{\mathrm{RPA,SR}}(Q_{\mathrm{cut}}) \approx -\frac{4\Omega}{3Q_{\mathrm{cut}}^3}\sum_{\mathbf{q}} |n(\mathbf{q})|^2, \tag{4.18}$$

where Ω is the system volume. This is exactly the expression that has been derived by Klimeš *et al.*[86] for the plane wave basis set incompleteness error [their definition of the latter, compare Eq. (10) in Ref. [86], corresponds to $E_c^{\mathrm{RPA,SR}}$ in our range-separation scheme].

This shows that at sufficiently high cutoffs the plane wave basis set incompleteness error is described exactly by the short-range LDA. It is important to point out that this statement contains additional information over the simple fact that $E_c^{\mathrm{RPA,LR}}(Q_{\mathrm{cut}})$ approaches the full-range value as $Q_{\mathrm{cut}} \to \infty$, since it precisely predicts the leading order correction.

The key assumption in the derivation of Klimeš *et al.*[86] was that for high energies the unoccupied orbitals can be approximated by plane waves. This is always guaranteed as the kinetic energy then dominates the Hamiltonian. Clearly, using the HEG as a reference system makes a similar assumption. An alternative proof of this theorem using the coupling constant formalism was given previously by Burke *et al.*[95] Toulouse *et al.*[89] have derived similar theorems for the error function.

Finally, we briefly discuss how these results can be extended beyond the RPA. In the RPA+SOSEX (second order screened exchange),[77,96] Eq. (4.17) is merely reduced by a factor of two for non-spin-polarized systems. This can be easily understood, as the SOSEX correction simply restores the Pauli principle in the large Q_{cut} limit, i.e. the self-interaction between electrons of same spins is exactly cancelled.[21,97] However, the exact (rather than RPA) short-range correlation energy is not simply a function of the local density alone, but also involves the on-top pair density.[89,95] Although the LDA does not generally describe the latter exactly, it is still an accurate approximation, if the ground state wave function in the weak coupling limit is well described by a single Slater determinant.[98]

4.2.5 Plane wave basis set extrapolation

Prior to the work of Klimeš *et al.*,[86] Harl and Kresse [59] provided numerical evidence that the plane wave basis set incompleteness error falls off as $1/Q_{\mathrm{cut}}^3$ and suggested a basis set extrapolation method based on

$$E_c^{\mathrm{RPA,LR}}(Q_{\mathrm{cut}}) = E_c^{\mathrm{RPA}} + \frac{A_3}{Q_{\mathrm{cut}}^3}, \tag{4.19}$$

where E_c^{RPA} and A_3 are obtained by a linear fit of $E_c^{\mathrm{RPA,LR}}(Q_{\mathrm{cut}})$ versus $1/Q_{\mathrm{cut}}^3$. Gulans [87] has calculated higher order corrections to Eq. (4.14) and suggested the extrapolation

$$E^{\mathrm{RPA,LR}}(Q_{\mathrm{cut}}) = E_c^{\mathrm{RPA}} + \frac{A_3}{Q_{\mathrm{cut}}^3} + \frac{A_5}{Q_{\mathrm{cut}}^5} + \frac{A_7}{Q_{\mathrm{cut}}^7}, \tag{4.20}$$

where A_5 and A_7 are further fit parameters. In Appendix B, we provide an analytical evaluation of A_3 - A_7 for the HEG, yielding

$$\begin{aligned} E_{\mathrm{c,HEG}}^{\mathrm{RPA,SR}}(Q_{\mathrm{cut}})/\Omega = -n^2 \left[\frac{4}{3Q_{\mathrm{cut}}^3} + \frac{8k_{\mathrm{F}}^2}{25Q_{\mathrm{cut}}^5} + \frac{288k_{\mathrm{F}}^4}{1225Q_{\mathrm{cut}}^7} + \mathcal{O}\left(\frac{1}{Q_{\mathrm{cut}}^9}\right) \right] \\ + \pi n^3 \left[\frac{32}{7Q_{\mathrm{cut}}^7} + \mathcal{O}\left(\frac{1}{Q_{\mathrm{cut}}^9}\right) \right] + \ldots, \end{aligned} \tag{4.21}$$

where n is the electronic density of the HEG [note that our coefficients differ from the ones given in Ref. [87], see discussion after Eq. (B.3)]. The terms proportional to n^2 stem from the direct MP2 diagram, compare Fig. 4.2. The terms proportional to n^3 stem from the third order ring diagram and so forth. As was pointed out by Gulans, these terms can be interpreted neatly in terms of the electronic cusp. They represent probabilities that there are two, three, ..., electrons at the same place. This interpretation suggests a beyond-LDA short-range functional based on an expansion involving the pair density. However, we do not attempt to construct such a functional here and leave it up to future work.

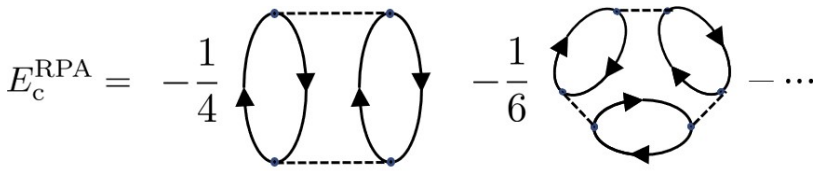

FIGURE 4.2: Representation of the RPA correlation energy in terms of Feynman diagrams. The Feynman rules can be found in Ref. [99], with prefactor convention as in Ref. [52]. The second order ring diagram is called direct MP2 diagram.

4.2.6 One-shot extrapolation method

The basis set extrapolation schemes described above require repeated evaluations of RPA correlation energies for a set of cutoff energies Q_{cut}. Since this is typically one of the bottlenecks in modern RPA implementations, the basis set extrapolation increases the computational cost. We now propose a one-shot extrapolation scheme that accounts for basis set incompleteness *a priori* via an optimized long-range potential. The Coulomb interaction is enhanced at intermediate momentum transfers $q \approx Q_{\mathrm{cut}}$ in order to make up for the cutoff at $q = Q_{\mathrm{cut}} + \Delta Q$

$$V_{\mathrm{SCK}}^{\mathrm{LR}}(q, Q_{\mathrm{cut}}) = \begin{cases} 4\pi/q^2 & \text{for } q < Q_{\mathrm{cut}} - \Delta Q \\ 4\pi f_{\mathrm{SCK}}(q)/q^2 & \text{for } Q_{\mathrm{cut}} - \Delta Q \leq q \leq Q_{\mathrm{cut}} + \Delta Q \\ 0 & \text{for } q > Q_{\mathrm{cut}} + \Delta Q. \end{cases} \tag{4.22}$$

We base the construction of this "squeezed Coulomb kernel" (SCK) on the fact that at large momentum transfers, the RPA is dominated by the direct MP2 term (see Fig. 4.2)

$$\varepsilon_{\mathrm{c,HEG}}^{\mathrm{RPA}}(q) \sim \chi_{0,\mathrm{HEG}}^2(q) V^2(q) \quad \text{for } q \to \infty, \tag{4.23}$$

where $\chi_{0,\mathrm{HEG}}(q)$ is the frequency integrated Lindhard response function, see Appendix B. In the same limit, $\chi_{0,\mathrm{HEG}}(q)$ falls off as $1/q$, which yields the leading order

term in Eq. (4.21)

$$\varepsilon_{\mathrm{c,HEG}}^{\mathrm{RPA,SR}}(Q_{\mathrm{cut}}) \sim \int_{Q_{\mathrm{cut}}}^{\infty} \mathrm{d}q\, q^2 \left[\frac{1}{q} V(q)\right]^2 \sim \frac{1}{Q_{\mathrm{cut}}^3}. \tag{4.24}$$

The SCK is constructed to make up for the loss of correlation energy by enhancing the Coulomb potential at intermediate q assuming $\chi_0 \approx \chi_{0,\mathrm{HEG}}$

$$\begin{aligned} \int_{Q_{\mathrm{cut}}-\Delta Q}^{\infty} \mathrm{d}q\, q^2 \left[\frac{1}{q} V(q)\right]^2 &\overset{!}{=} \int_{Q_{\mathrm{cut}}-\Delta Q}^{\infty} \mathrm{d}q\, q^2 \left[\frac{1}{q} V_{\mathrm{SCK}}^{\mathrm{LR}}(q, Q_{\mathrm{cut}})\right]^2 \\ &= \int_{Q_{\mathrm{cut}}-\Delta Q}^{Q_{\mathrm{cut}}+\Delta Q} \mathrm{d}q\, q^2 \left[\frac{4\pi}{q^3} f_{\mathrm{SCK}}(q)\right]^2. \end{aligned} \tag{4.25}$$

Details on the choice of $f_{\mathrm{SCK}}(q)$ and ΔQ will be given in section 4.3, where we also show that ΔQ plays only the role of a window parameter. This means that the effective cutoff momentum is located at $q = Q_{\mathrm{cut}}$, i.e. at the center of the window, rather than at $q = Q_{\mathrm{cut}} - \Delta Q$.

This approach is in spirit similar to standard ion-pseudo-potential methods, which have been employed to handle the nuclear cusp.[100] The standard pseudo-potentials are constructed such that they reproduce the electronic properties of an atomic reference. In our case, it is the low-density HEG that plays the role of the reference system.

We do not combine the SCK with a short-range LDA correction, because the SCK already describes low densities well enough. This is exactly the region where the LDA works best, while for high densities it transfers spurious long-range effects to inhomogeneous systems.[33,92]

In fact, we argue in the following that neglecting the LDA correction can be seen as an attempted effective gradient correction. In the local interaction parameter effective gradient correction of Toulouse *et al.*,[92] $\varepsilon_{\mathrm{c,HEG}}^{\mathrm{SR}}$ is reduced for small r_{s} to prevent the over-correction of correlation. This was done by choosing the range-separation parameter locally as

$$\mu_{\mathrm{eff}} = \max[\mu_1(\mathbf{r}), \mu], \tag{4.26}$$

where $\mu_1(\mathbf{r})$ is some typical correlation length, for instance $\mu_1(\mathbf{r}) = \alpha k_{\mathrm{s}}(\mathbf{r})$. This reduces the short-range correction for high densities and hence mimics a gradient correction, as

$$\varepsilon_{\mathrm{c,HEG}}^{\mathrm{RPA,SR}}(r_{\mathrm{s}}, \mu_1) < \varepsilon_{\mathrm{c,HEG}}^{\mathrm{RPA,SR}}(r_{\mathrm{s}}, \mu_2) \quad \text{if } \mu_1 > \mu_2. \tag{4.27}$$

We return now to the SCK and assume that $\varepsilon_{\mathrm{c,HEG}}^{\mathrm{RPA,SR}}$ vanishes exactly for $Q_{\mathrm{cut}} > \mu_1$. We will show in section 4.3 that this is an excellent approximation for $\mu_1 = 2k_{\mathrm{F}}$. Then, an effective gradient correction is obtained by simply neglecting the short-range LDA correction, as the assumption above implies

$$\varepsilon_{\mathrm{c,HEG,SCK}}^{\mathrm{RPA,SR}}(r_{\mathrm{s}}, \max[\mu_1, Q_{\mathrm{cut}}]) = 0 \quad \forall r_{\mathrm{s}}. \tag{4.28}$$

4.3 Computational details

In the following we present results from various numerical studies of the HEG. We argue that for the purpose of basis set correction, one can identify $\mu \approx Q_{\mathrm{cut}}$ for a fair comparison between the error function and the plane wave cutoff schemes. Since its

structure is visually more revealing, we show the long-range RPA correlation energy per particle $\varepsilon_{c,\mathrm{HEG}}^{\mathrm{RPA,LR}}$ rather than $\varepsilon_{c,\mathrm{HEG}}^{\mathrm{RPA,SR}}$ throughout. The latter can be easily obtained by subtracting $\varepsilon_{c,\mathrm{HEG}}^{\mathrm{RPA,LR}}$ from the full-range reference.

4.3.1 Smooth momentum cutoff

The discontinuous cutoff in Eq. (4.9) causes technical problems such as shell-filling effects. We follow Ref. [65] and replace the step at $q = Q_{\mathrm{cut}}$ by a smooth cosine window

$$V_{\mathrm{cos}}^{\mathrm{LR}}(q, Q_{\mathrm{cut}}) = \begin{cases} 4\pi/q^2 & \text{for } q < Q_{\mathrm{cut}} - \Delta Q \\ 4\pi f_{\mathrm{cos}}(q)/q^2 & \text{for } Q_{\mathrm{cut}} - \Delta Q \leq q \leq Q_{\mathrm{cut}} + \Delta Q \\ 0 & \text{for } q > Q_{\mathrm{cut}} + \Delta Q, \end{cases} \tag{4.29}$$

where

$$f_{\mathrm{cos}}(q) = \frac{1}{2} + \frac{1}{2}\cos\left[\frac{q^2/2 - (Q_{\mathrm{cut}} - \Delta Q)^2/2}{(Q_{\mathrm{cut}} + \Delta Q)^2/2 - (Q_{\mathrm{cut}} - \Delta Q)^2/2}\pi\right], \tag{4.30}$$

and ΔQ controls the "smoothness" of the window. For $\Delta Q \to 0$, Eq. (4.9) is recovered. Even a narrow window with $\Delta Q = 0.1 Q_{\mathrm{cut}}$ remedies the technical issues, and changes the short-range functional very little. Most notable is a slight reduction of $\varepsilon_{c,\mathrm{HEG}}^{\mathrm{RPA,LR}}$ at densities where $r_s \approx 4/Q_{\mathrm{cut}}$ [see Fig. 4.3 (solid lines)]. The choice of the window parameter ΔQ represents a trade-off between smoothness and plane wave basis set convergence, since the latter is now tied to a cutoff energy $(Q_{\mathrm{cut}} + \Delta Q)^2/2$.

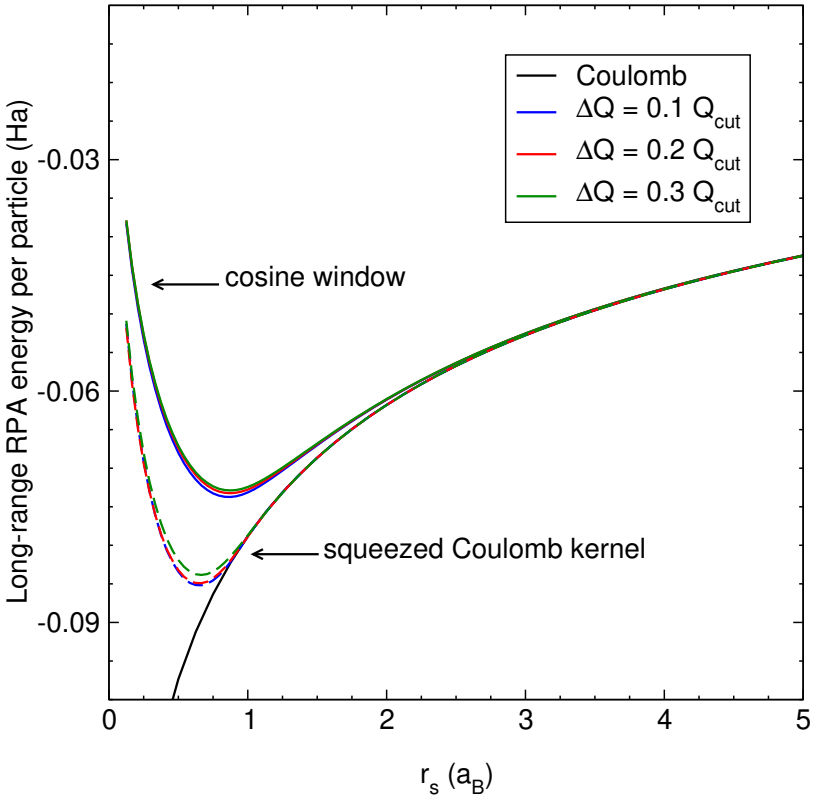

FIGURE 4.3: Long-range RPA correlation energies per particle for the HEG, $\varepsilon_{c,\mathrm{HEG}}^{\mathrm{RPA,LR}}$, for different window parameters ΔQ at fixed cutoff momentum $Q_{\mathrm{cut}} = 4.0\, a_B^{-1}$. Solid lines represent the cosine window, dashed lines the squeezed Coulomb kernel (SCK).

4.3.2 Form of the squeezed Coulomb kernel

In the construction of the SCK, we impose the following constraints: (i) it should join onto the bare Coulomb kernel at $Q_{\text{cut}} - \Delta Q$, (ii) it should vanish at $Q_{\text{cut}} + \Delta Q$, and (iii) it should be positive definite. A convenient form that satisfies the constraints (i)-(iii) as well as Eq. (4.25) is

$$f_{\text{SCK}}(q) = q^2 \frac{2\Delta Q(Q_{\text{cut}} + \Delta Q - q)}{[(Q_{\text{cut}} - \Delta Q)^2 - q(Q_{\text{cut}} - 3\Delta Q)]^2}. \tag{4.31}$$

Similar to the smooth momentum cutoff above, ΔQ controls the width of the window [see Fig. 4.3 (dashed lines)]. As the function $f_{\text{SCK}}(q)$ contains more structure than the cosine window, we use a broader window with $\Delta Q = 0.2 Q_{\text{cut}}$. The form of the SCK is displayed in Fig. 4.4. As variations in the window parameter ΔQ do not change $\varepsilon_{\text{c,HEG}}^{\text{RPA,LR}}$ significantly, the effective cutoff momentum is located at the center of the window, i.e. at $q = Q_{\text{cut}}$, as is the case for the cosine window as well.

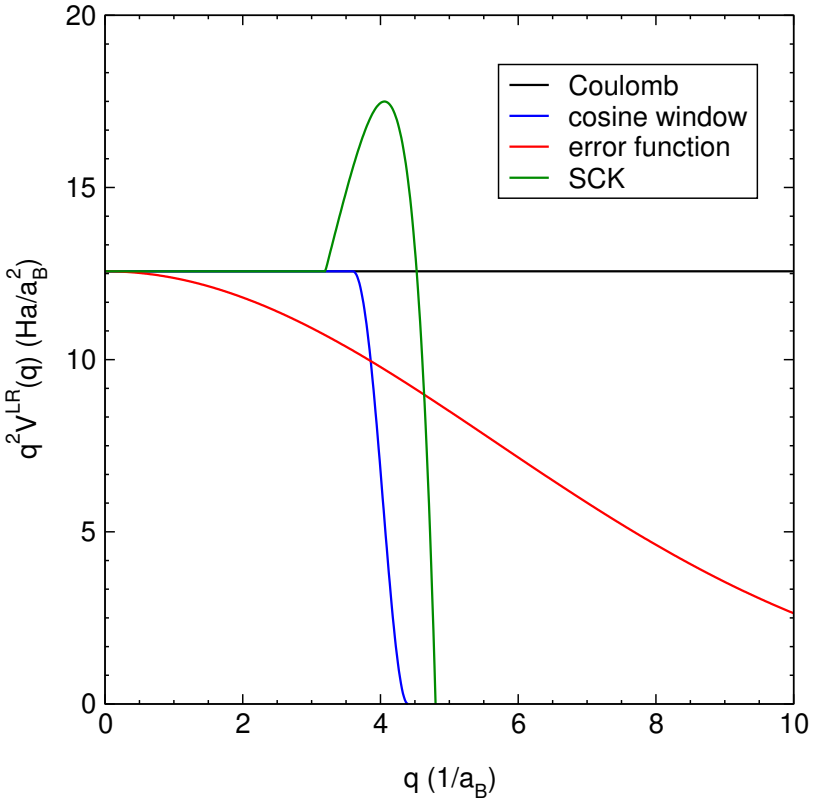

FIGURE 4.4: Fourier representation of the different long-range potentials at range-separation parameters $Q_{\text{cut}} = \mu = 4.0\, a_{\text{B}}^{-1}$. For the width of the cosine window, we use $\Delta Q = 0.1 Q_{\text{cut}}$, and for the squeezed Coulomb kernel (SCK) $\Delta Q = 0.2 Q_{\text{cut}}$.

4.3.3 Analytical representation of the short-range local density functional

Fig. 4.5 depicts $\varepsilon_{\text{c,HEG}}^{\text{RPA,LR}}$ for different long-range potentials. Generally, $\varepsilon_{\text{c,HEG}}^{\text{RPA,LR}}$ vanishes for $r_{\text{s}} \to 0$ and approaches the full-range value as $r_{\text{s}} \to \infty$, compare Eqs. (4.10) and (4.14). For each long-range potential, there is a distinct minimum at intermediate densities, which indicates a shift from the high density to the low density regime. The relevant limit for basis set correction is that of large range-separation parameters, corresponding to the low density regime. Judging from the numerical data, we

identify this regime roughly at densities given by $r_s \gtrsim 4/Q_{cut}$ and $r_s \gtrsim 4/\mu$, which corresponds to $Q_{cut} \gtrsim 2k_F$ and $\mu \gtrsim 2k_F$.

For the error function, $\varepsilon_{c,HEG}^{RPA,LR}$ approaches the full-range value only slowly as $r_s \to \infty$. Identifying $Q_{cut} \approx \mu$, the cosine window describes low densities better than the error function, but high densities worse. This means that the cosine window separates long- and short-range effects better than the error function. The SCK is exact in the low density limit per construction, and $\varepsilon_{c,HEG}^{RPA,SR} = \varepsilon_{c,HEG}^{RPA} - \varepsilon_{c,HEG}^{RPA,LR}$ vanishes rapidly for $Q_{cut} \gtrsim 2k_F$.

To parametrize $\varepsilon_{c,HEG}^{RPA,SR}(r_s)$ for both the cosine window and the error function, we choose a form similar to that used by Paziani *et al.*[93]

$$\varepsilon_{c,HEG}^{RPA,SR}(r_s) = A \frac{\ln\left(\frac{r_s + a_0 r_s^2 + a_1 r_s^3 + a_2 r_s^4}{1 + a_3 r_s + a_4 r_s^2 + a_5 r_s^3 + a_2 r_s^4}\right)}{1 + a_6 r_s + a_7 r_s^2}. \tag{4.32}$$

The a_i are determined by a non-linear least square fit for a given range-separation parameter and the constant A enforces the high density limit of Gell-Mann and Brueckner [101]

$$\begin{aligned} \varepsilon_{c,HEG}^{RPA,SR}(r_s) &\approx A \ln(r_s) \qquad \text{for } r_s \to 0 \\ A &= -\frac{\ln(2) - 1}{\pi^2}. \end{aligned} \tag{4.33}$$

This is the appropriate behavior for any reasonable LDA functional, since (i) $\varepsilon_{c,HEG}^{RPA,LR}$ vanishes for $r_s \to 0$, and (ii) the RPA becomes exact in this limit. The fit parameters a_i are given in Appendix C for selected range-separation parameters.

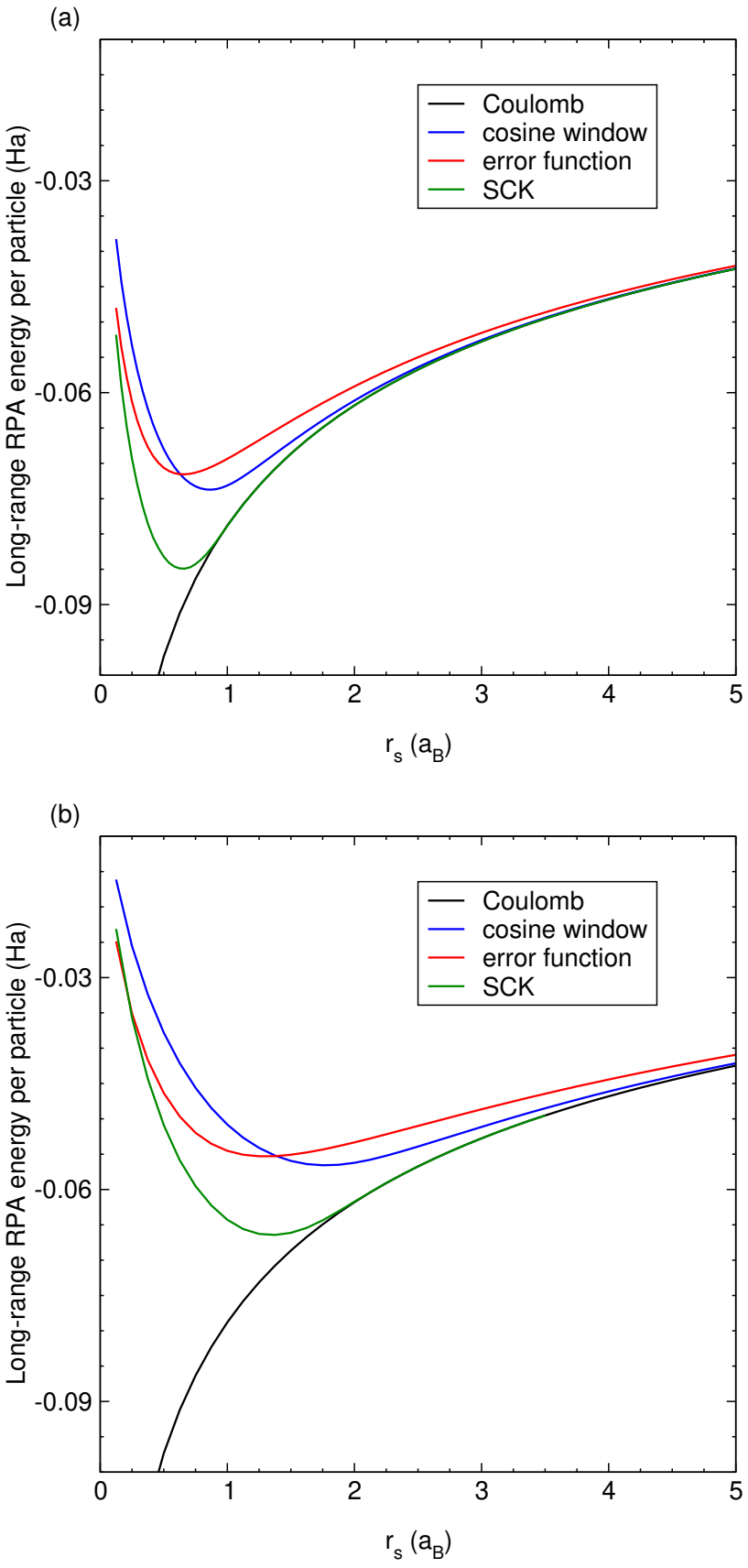

FIGURE 4.5: Long-range RPA correlation energies per particle $\varepsilon_{c,HEG}^{RPA,LR}$ for the HEG for the different long-range potentials. (a) range-separation parameters $Q_{cut} = \mu = 4.0\, a_B^{-1}$ as in Fig. 4.4, (b) $Q_{cut} = \mu = 2.0\, a_B^{-1}$.

4.4 Applications

4.4.1 Applied settings

TABLE 4.1: Chosen settings for the RPA calculations. The short-hand _sv for the PAW potentials indicates treatment of the outermost s and p core states as valence. The orbital plane wave cutoffs E_{max} are given in eV, k-point sampling is done on Γ-centered $k \times k \times k$-grids. Values for the zero point corrected experimental lattice constant a_0 (in Å) are taken from Ref. [102]. For Kr, we use the result from an accurate quantum chemistry calculation.[103] Values of $2k_{\text{F}}$ at the experimental lattice constant are given in a_{B}^{-1}.

		PAW potentials	E_{max}	k	a_0	$2k_{\text{F}}$
C	(A4)	C_GW_new	600	6	3.553	2.93
Si	(A4)	Si_GW	500	6	5.421	1.92
MgO	(B1)	Mg_sv_GW O_GW	600	6	4.189	3.13
Kr	(A1)	Kr_GW	700	8	5.598	1.88
Pd	(A1)	Pd_sv_GW	500	10	3.876	3.51
Al	(A1)	Al_sv_GW	600	10	4.018	2.88

We use the RPA implementation in the Vienna Ab Initio Simulation Package (VASP)[104] as presented in Ref. [65], which also describes the calculation of the exact exchange energy. The orbitals of the underlying DFT calculations are obtained self-consistently using the Perdew-Burke-Ernzerhof (PBE) functional.[36] The equilibrium lattice constants are found by a Murnaghan equation of state fitted to energies evaluated at seven lattice volumes centered at the experimental value, spanning a window of ±15% . If the lattice constants deviate from experiment by more than 3%, additional points are considered. In the present work we consider six prototypical materials, which are summarized in Table 4.1. Notably, we use a large plane wave cutoff energy E_{max} for the orbital basis set (`ENCUT` in VASP). This ensures sufficiently converged lattice constants for all long-range potentials. The relative errors in the lattice constants are estimated to be under 0.1%. For the response function χ_0, we use a smaller cutoff energy $E^{\chi}_{\text{max}} = 2/3\, E_{\text{max}}$ (`ENCUTGW` in VASP).

4.4.2 Convergence behavior for total energies

Fig. 4.6 compares the convergence behavior of the long-range RPA energies with respect to E^{χ}_{max} for C and Pd at the experimental lattice constant, with E_{max} fixed to the values stated in Table 4.1. For both the cosine window and the SCK, $E^{\text{RPA,LR}}$ is fully converged with respect to E^{χ}_{max} once the potentials vanish, i.e. beyond the energies $(Q_{\text{cut}} + \Delta Q)^2/2$. These cutoff energies are given in Table 4.2 for selected range-separation parameters.

This makes it possible to automatically adapt the range-separation parameter Q_{cut} to a given plane wave cutoff E^{χ}_{max} or vice versa. For the error function, however, $E_{\text{c}}^{\text{RPA,LR}}$ is in principle fully converged only at infinite cutoff energies, and this simple automatic adaption is not possible. In practice, one would have to perform additional convergence tests for each value of μ or resort to more elaborate schemes.[105] For the sake of simplicity, we omit these convergence tests throughout and use the large cutoffs $E^{\chi}_{\text{max}} = 2/3\, E_{\text{max}}$ for all values of μ, compare Table 4.1.

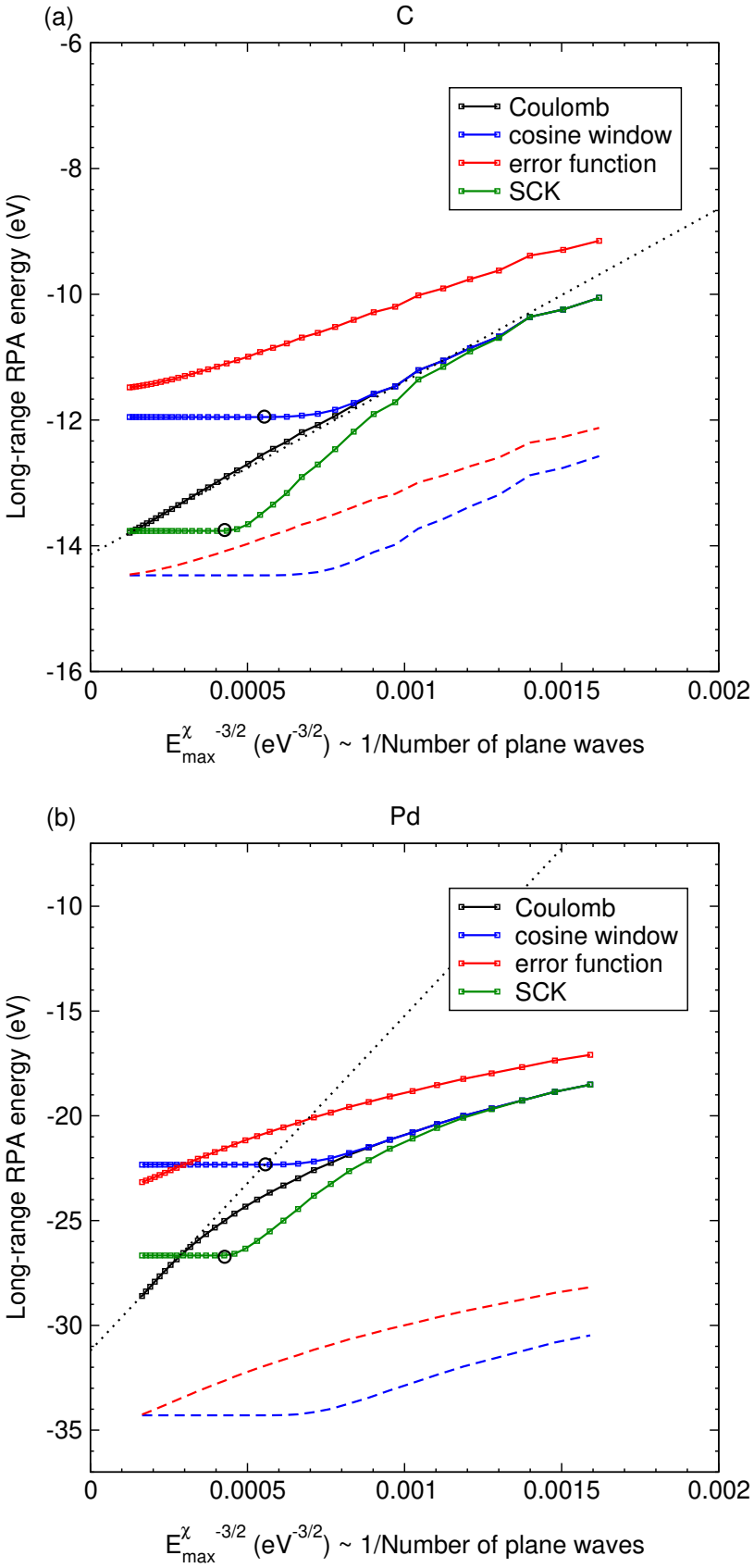

FIGURE 4.6: Convergence of $E_c^{\mathrm{RPA,LR}}$ with respect to E_{max}^{χ} for (a) C and (b) Pd at the experimental lattice volume. Range-separation parameters are set to $Q_{\mathrm{cut}} = \mu = 3.0\, a_B^{-1}$. Dotted lines represent basis set extrapolations using Eq. (4.19), fitted to the last eight data points (linear fits in this plot). For cosine window and error function, dashed lines include the short-range LDA correction. Circles indicate the energies $(Q_{\mathrm{cut}} + \Delta Q)^2/2$, where the long-range potentials vanish for the cosine window and the SCK respectively.

Fig. 4.6 shows that replacing $E_c^{RPA} \rightarrow E_c^{RPA,LR}$ generally underestimates the correlation energy, whereas including the short-range LDA correction (dashed curves) overcorrelates. Fig. 4.6 furthermore demonstrates the basis set extrapolation according to Eq. (4.19) (dotted curves, $1/N_{PW} \propto 1/Q_{cut}^3$), which provides full-range reference values in the following.

For C, the full-range data closely follows the $1/N_{PW}$ behavior that is expected from the HEG model even at smaller values of E_{max}^{χ}. In contrast, the full-range curve for Pd deviates strongly from the $1/N_{PW}$ behavior except for very large values of E_{max}^{χ}. This is due to the properties of the highly localized $4d$ - electrons of Pd. Thus, for our purposes C can be considered to be an "easy" material, and Pd a "difficult" one. Heuristically, this can also be related to the fact that for the same range-separation parameter the relative amount of short-range correlation $E_c^{RPA,SR}/(E_c^{RPA,LR} + E_c^{RPA,SR})$ is smaller for C than for Pd. Likewise, total correlation energies are better reproduced for C than for Pd.

Due to systematic error cancellation, relative energies are in general easier to converge than total energies. To obtain equilibrium lattice constants, we have to compare systems of slightly different lattice volumes. We can expect good cancellation, if the orbitals of these systems are similar. A more detailed analysis will be given in the following.

TABLE 4.2: Cutoff energies $(Q_{cut} + \Delta Q)^2/2$ for the cosine window ($\Delta Q = 0.1 Q_{cut}$) and the SCK ($\Delta Q = 0.2 Q_{cut}$). The range-separation parameters are given in a_B^{-1}, the associated cutoff energies are converted to eV.

Q_{cut}	$(Q_{cut} + 0.1Q_{cut})^2/2$	$(Q_{cut} + 0.2Q_{cut})^2/2$
2	66	78
3	148	176
4	263	313

4.4.3 Lattice constants

TABLE 4.3: Equilibrium lattice constants a_0 are given in Å, errors (in %) are given with respect to the zero point corrected experimental values, see Table 5.2. LDA and PBE calculations are performed self-consistently, full-range RPA and exact exchange are evaluated on top of self-consistent PBE orbitals.

	LDA		PBE		RPA+EXX	
	a_0	Error	a_0	Error	a_0	Error
C	3.535	-0.5	3.571	0.5	3.565	0.3
Si	5.410	-0.2	5.472	0.9	5.437	0.3
MgO	4.165	-0.6	4.256	1.6	4.210	0.5
Kr	5.336	-4.7	6.302	12.6	5.690	1.6
Pd	3.842	-0.9	3.940	1.7	3.895	0.5
Al	3.982	-0.9	4.035	0.4	4.036	0.4

Harl *et al.*[65] have studied lattice constants for solids of various bonding types and found the following general behavior: LDA overbinds in comparison to the experimental values, PBE underbinds, and the RPA (with standard PAW potentials) underbinds, but less than PBE. This trend also applies to noble gas solids, though the

(semi-)local functionals fail quite dramatically at describing van der Waals bonds with PBE yielding lattice constants that are significantly too large.[59] Table 4.3 confirms these results for the materials considered here. Slight differences to the full-range RPA lattice constants reported in the recent study of Klimeš *et al.*[82] (compare values listed as "RPA std-PAW") are due to higher cutoff energies used in the present work.

Fig. 4.7 shows that replacing $E_c^{\mathrm{RPA}} \to E_c^{\mathrm{RPA,LR}}$ typically leads to larger lattice constants (dashed lines). The lattice constants tend to be overcorrected when $E_c^{\mathrm{RPA,SR}}$ is included (solid lines). In this section, the quality of the short-range LDA correction is only judged by *whether or not it yields lattice constants that are closer to the full-range RPA base line* than their respective long-range only counterparts (dashed lines), whereas in Sec. 4.4.4, we will compare with experimental results.

The performance of the short-range LDA correction is closely linked to the performance of the standard LDA, compare Table 4.3. The short-range correction works well for C and Si, where the difference between standard LDA and full-range RPA lattice constants is also smallest. Between those two materials, convergence with respect to the range-separation parameter is faster for Si, which is attributable to a size effect, i.e. $2k_F$ is smaller for Si than for C. For the other materials, however, the short-range LDA correction strongly overcorrelates. The most extreme cases are MgO, Pd and Kr in combination with the cosine window. At $Q_{\mathrm{cut}} = 2\,a_B^{-1}$, i.e. $(Q_{\mathrm{cut}} + \Delta Q)^2/2 \approx 66$ eV, most of the relevant contributions to the correlation energy are simply disregarded in the RPA. In these cases, the LDA correction results in a quite severe underestimation of the lattice constant. The upshot is that an adequate cutoff must be at least around $Q_{\mathrm{cut}} = 3\,a_B^{-1}$.

Turning briefly to range-separation using the error function, we note that it is generally better behaved than the hard cosine cutoff, but shares similar issues as the cosine window. The uncorrected lattice constants are too large, whereas the corrected lattice constants are a little bit too small. But "stark" outliners as for the cosine window are missing. We relate this to the fact that the error function cuts off the Coulomb kernel very slowly so that for momentum transfers $q \approx \mu$ a sizeable fraction of the Coulomb kernel is still present. This also means that one must use fairly large plane wave cutoffs for the response function to recover truly converged results for the correlation energy. Hence, computational gains are small when the error function is used for range-separation.

To judge the plane wave basis set extrapolation via the SCK, we compare to the non-extrapolated plane wave cutoff scheme, i.e. cosine windows using the same effective cutoff momentum Q_{cut}. Fig. 4.8 shows that the SCK shares the good description for C and Si with the short-range LDA correction, as well as the poor description for Kr and Pd. This can be attributed to the success or failure of the HEG model, which is underlying both methods: if the correlation part that is not handled explicitly corresponds to plane wave-like contributions, both methods are reliable, otherwise the errors are sizable. Hence, as for the cosine window, results for $Q_{\mathrm{cut}} = 2\,a_B^{-1}$ are fairly unreliable.

As discussed earlier, we expect that the SCK mimics some aspects of a short-range effective gradient correction, if the long-range effects are sufficiently well described. In fact, the SCK underbinds C and Si, but overbinds the other materials. Noticeably, the MgO lattice constant is almost converged at $Q_{\mathrm{cut}} = 3\,a_B^{-1}$, and long-range correlation effects play an important role for MgO. However, the good description of MgO is maybe somewhat coincidental, as it again relies on fortuitous error cancellation, whereas the good description of C and Si also extends to total correlation energies (not shown here).

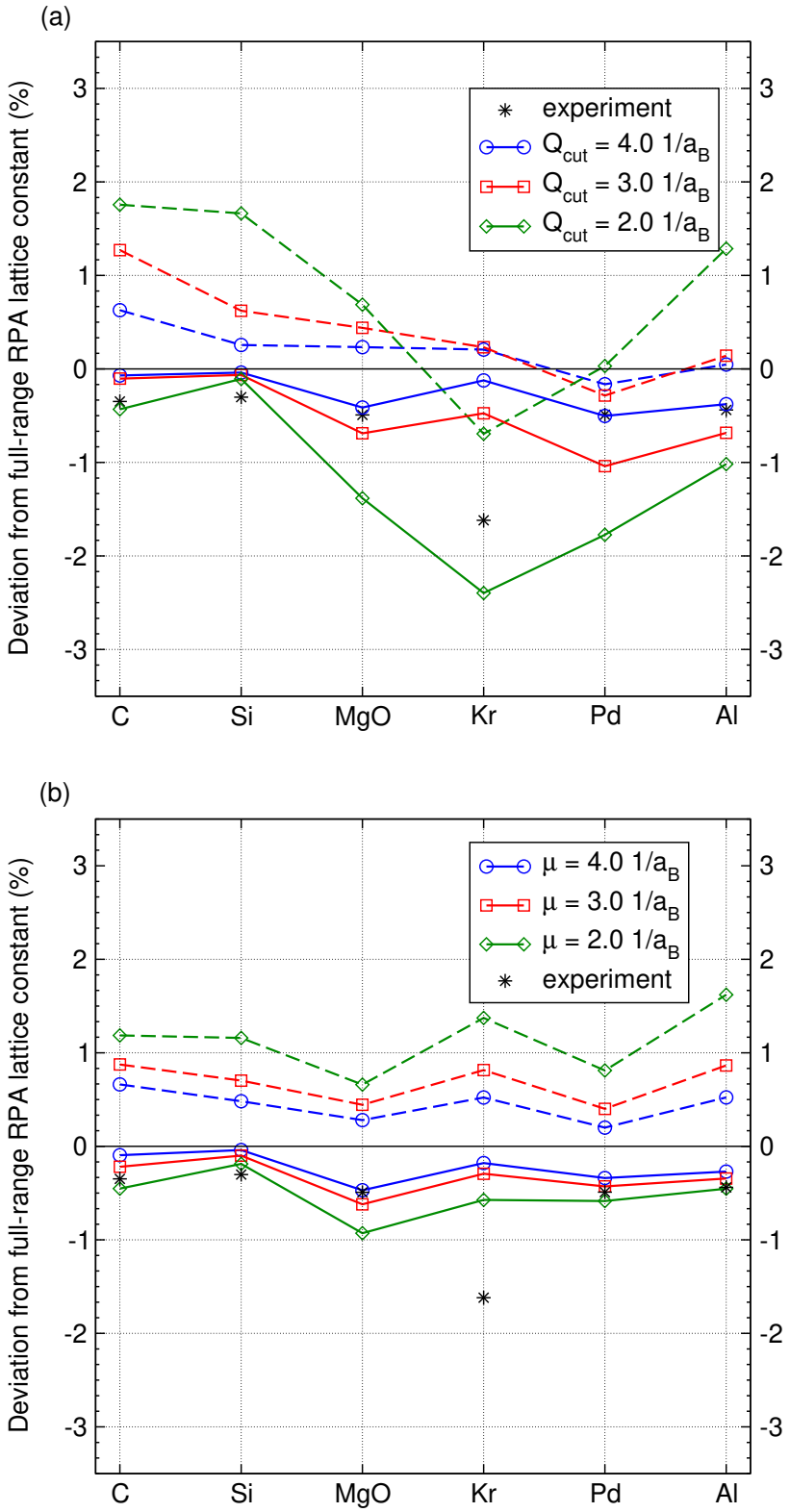

FIGURE 4.7: Equilibrium lattice constants obtained via range-separated RPA correlation energies for (a) cosine window, (b) error function. Dashed lines represent results without, and solid lines represent results with short-range LDA correction. The full-range reference values are obtained with the extrapolation scheme (4.19).

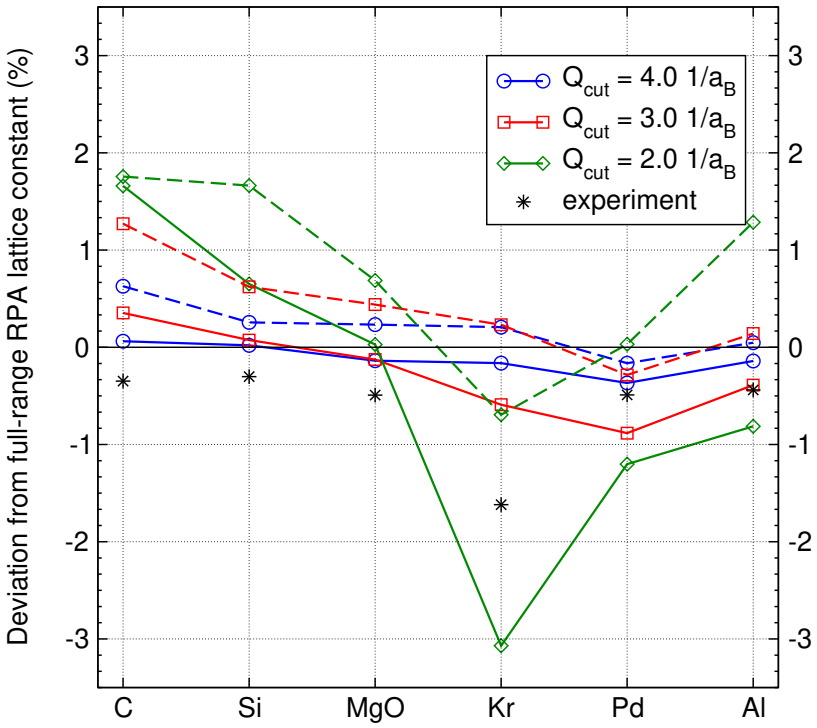

FIGURE 4.8: Equilibrium lattice constants obtained via the SCK extrapolation method. Solid lines represent extrapolated results, dashed lines non-extrapolated results [same as in figure 4.7(a)]. The full-range reference values are obtained with the extrapolation scheme (4.19).

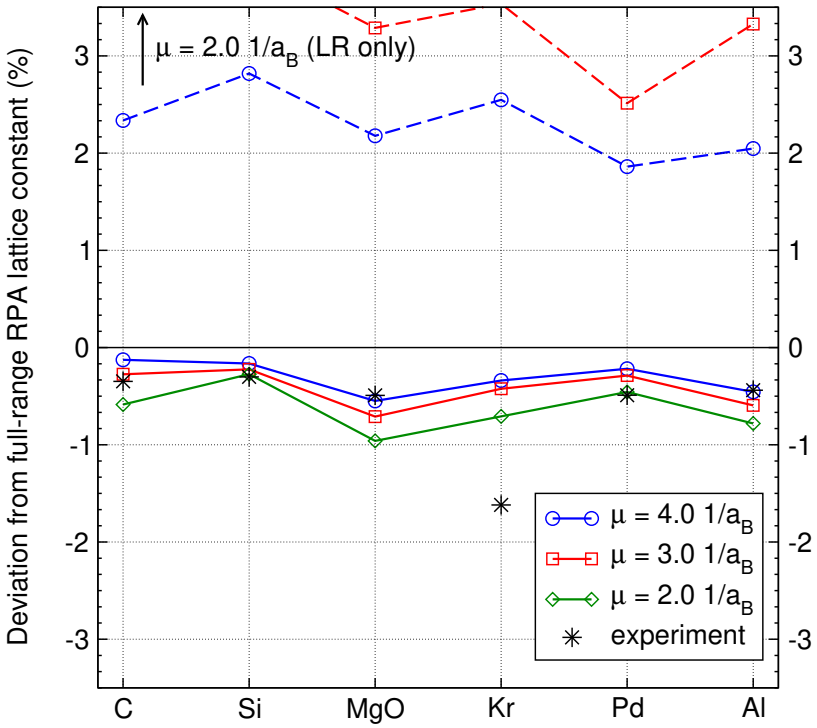

FIGURE 4.9: Equilibrium lattice constants obtained via range-separated exchange and range-separated RPA correlation energies. Dashed line represent results without, and solid lines represent results with short-range LDA correction. The full-range reference values are obtained with the extrapolation scheme (4.19).

4.4.4 Semi-empirical RPA-LDA hybrid functional

With decreasing range-separation parameter, the results for the error function change more slowly than those for the cosine window. This is because the error function mixes long- and short-range effects and does not abruptly cut off the Coulomb kernel. As discussed in Sec. 4.2, we expect similar results for both methods for $Q_{\text{cut}} = 2\mu$ in the DFT limit [compare the discussion following Eq. (4.16)]. In contrast, we identified that both methods work similar for $Q_{\text{cut}} = \mu$ near the full-range limit, hence the slower change for the error function. The slow change of the results with respect to μ for the error function is in fact advantageous for the construction of semi-empirical RPA-LDA hybrid functionals, where the optimal μ for one system should be transferable to other systems.

For every material considered here, there is an optimal range-separation parameter μ or Q_{cut} that reproduces the experimental lattice constant. This is to be expected, since (i) the range-separated functional switches between the full-range RPA and LDA. (ii) the overbinding of standard LDA is generally due to the correlation part, whereas the exchange part underbinds. (iii) LDA functionals based on the RPA instead of exact (QMC) data overbind even more than standard LDA, which can be deduced from the fact that the RPA+ correction typically increases the RPA lattice constants by 0.2-0.3%.[65]

Thus, by choosing the range-separation parameter empirically, we can improve the lattice constants upon full-range RPA. From our limited data set, we observe that the error function with $\mu \simeq 2k_{\text{F}}$ gives the best lattice constants with respect to experiment [compare Fig. 4.7(b)]. Kr seems off, though the experimental value used here is possibly about 0.5% too small.[103] For the cosine window, however, such a simple approximation does not work, since the results vary too rapidly as the cutoff changes.

In summary, we find that the error function is better suited for the construction of semi-empirical RPA-LDA hybrid functionals. Even though the mixing of long- and short-range effects is not ideal in terms of removing the cusp-related UV divergence, it leads to improved transferability with respect to the optimal range-separation parameter.

4.4.5 Range-separated exchange

To study the influence of short-range exchange, we now replace the short-range part of the exchange energy by LDA similar to the treatment of correlation as described in section 4.2,

$$\begin{aligned} E_{\text{x}} &= E_{\text{x}}^{\text{LR}} + E_{\text{x}}^{\text{SR}} \\ &\approx E_{\text{x}}^{\text{LR}} + \int \mathrm{d}\mathbf{r}\, \varepsilon_{\text{x,HEG}}^{\text{SR}}[n(\mathbf{r})]n(\mathbf{r}). \end{aligned} \tag{4.34}$$

The treatment of E_{x}^{LR} in VASP is technically elaborate, as one-center PAW terms are explicitly evaluated for exchange. Range-separated exchange has been implemented for the error function only and is rather involved for other Coulomb kernels. For details of the implementation in VASP we refer to Refs. [106] and [107]. This problem does not occur for the RPA contribution, where the all-electron density is restored on the plane wave grid (see Ref. [54]).

The error cancellation between exchange and correlation has played a central role in the success of standard LDA. This is manifest in the cancellation of the HEG terms linear in r_{s}, as discussed earlier. The importance of joint treatment of exchange and correlation was also emphasized by Langreth and Perdew [56] for their wave

vector decomposition method. Joint treatment of range-separated exchange has also been employed by most of the authors investigating range-separated RPA based on the error function,[72–76] though none of these studies have commented on the role of short-range exchange on its own.

Fig. 4.9 shows that entirely neglecting short-range exchange deteriorates the results even for large μ. However, the short-range corrected lattice constants differ only slightly from the full-range exchange counterparts, compare Fig. 4.7. Thus, we can conclude that the LDA describes short-range exchange very well, in fact much better than short-range correlation.

In the following, we will comment on the observation that the short-range correction works better for exchange than for correlation near the full-range limit. This finding is not entirely surprising, since exchange is essentially a long-range effect. The exchange hole is quadratic in r_{12} for small electronic distances r_{12} (*"no cusp for exchange"*).[89] This is drastically manifest in the wave vector analysis of the HEG, where only momentum transfers $q \leq 2k_\mathrm{F}$ contribute [compare Eq. (4.16)]. For the error function, the separation between long- and short-range effects is not as extreme. As shown in Appendix A, there is always at least a small short-range contribution [compare Eq. (A.3)]. For large μ the short-range LDA exchange correction still becomes exact, as was shown originally by Gill *et al.*,[108]

$$E_\mathrm{x}^\mathrm{SR}(\mu) = -\frac{\pi}{4\mu^2} \int \mathrm{d}\mathbf{r}\, n(\mathbf{r})^2 + \mathcal{O}\left(\frac{1}{\mu^4}\right) \tag{4.35}$$

This is analogous to our theorem (4.17) on short-range RPA correlation, see also Appendix A. But even beyond that, it seems plausible that the short-range LDA correction for exchange should work well near the full-range limit. There is no cusp for exchange, and so the short-range exchange contribution can be plane wave-like. In contrast, for correlation a large amount of plane waves is always needed to properly resolve the cusp.

It may still seem non-intuitive that the joint treatment of local exchange and local correlation is not beneficial here. However, we have focused on large μ, i.e. on short-range effects, whereas the cancellation is valid for small μ, compare Eqs. (4.10) and (4.16). Most clearly perhaps, this is seen in a real space picture. The cancellation of the HEG exchange and correlation holes pertains to the long-range parts, making the combined exchange-correlation hole more local. As for the short-range parts, we reiterate that there is a cusp for correlation but not for exchange.

Finally, the SCK method, which is designed to remove the electronic cusp explicitly, is not applicable to exchange. However, there exist similar methods for inverse range-separation, such as the cutoff scheme of Rozzi *et al.*[48]

4.5 Conclusion and Outlook

We have shed new light on the plane wave basis set incompleteness error in the RPA by relating it to range-separated density functional theory. In a gist, the plane wave basis set incompleteness error of the RPA correlation energies can be described by a complementary short-range local density functional. In the limit of large cutoff energies, this partitioning becomes even exact. Furthermore, we have introduced a one-shot basis set correction method based on an optimized long-range potential. The method modifies the Coulomb kernel at intermediate wave vectors such that the truncated and "squeezed" Coulomb kernel reproduces the RPA correlation energy of the low-density homogeneous electron gas exactly.

In practice, we find that the success of the two plane wave basis set correction methods used here is tied to that of the underlying HEG model. If the states that are removed from an explicit correlation treatment are plane wave-like, then the correction methods are successful. If the removed states are not plane wave-like, the correction methods tend to fail or are at least less accurate. Difficult materials are obviously transition metals (here Pd), oxides (here MgO), but also in van der Waals bonded solids (Kr) it is not a simple matter to develop accurate methods for correcting basis set errors.

An interesting aspect that emerged from the present study is that since the RPA tends to underbind (underestimates relative binding energies, overestimates lattice constants) and the local density approximation overbinds (overestimates relative binding energies, underestimates lattice constants), there is always one specific range-separation parameter that reproduces the experiment. Although the few data we have inspected suggest that $\mu \simeq 2k_{\mathrm{F}}$ yields the best results, also a fixed $\mu \simeq 3\, a_{\mathrm{B}}^{-1}$ seems to work remarkably well for lattice constants. More extensive tests will be required in order to tell whether such an approach will work equally well for other properties.

Somewhat surprisingly, we have found that the joint treatment of local exchange and local correlation does not improve the predicted lattice constants. As the short-range exchange correction is essentially exact for large μ, the errors introduced in the correlation cannot be compensated by errors in the exchange. This can be interpreted by the fact that there is no cusp for exchange.

Finally, we note that the extrapolation via the squeezed Coulomb kernel can be further improved by including higher order terms in the low density expansion. Moreover, it would be desirable to generalize the method towards non-locality in order to describe more strongly correlated systems better. Climbing this Jacob's ladder for the optimized long-range potential should lead to faster convergence with respect to the plane wave basis set size.

Chapter 5

Optimized effective potentials from the random-phase approximation: Accuracy of the quasiparticle approximation

Stefan Riemelmoser, Merzuk Kaltak, and Georg Kresse

Optimized effective potentials from the random-phase approximation: Accuracy of the quasiparticle approximation

published in: The Journal of Chemical Physics **154** (15), 154103 (2021)
doi: https://doi.org/10.1063/5.0045400
arxiv: https://arxiv.org/abs/2101.10009

Author contribution: Conception of the project, analytical derivations, code implementation (together with coworkers), numerical calculations, first paper draft, paper editing and proofreading (together with coworkers)

The optimized effective potential (OEP) method presents an unambiguous way to construct the Kohn-Sham potential corresponding to a given diagrammatic approximation for the exchange-correlation functional. The OEP from the random-phase approximation (RPA) has played an important role ever since the conception of the OEP formalism. However, the solution of the OEP equation is computationally fairly expensive and has to be done in a self-consistent way. So far, large scale solid state applications have therefore been performed only using the quasiparticle approximation (QPA), neglecting certain dynamical screening effects. We obtain the exact RPA-OEP for 15 semiconductors and insulators by direct solution of the linearized Sham-Schlüter equation. We investigate the accuracy of the QPA on Kohn-Sham band gaps and dielectric constants, and comment on the issue of self-consistency.

5.1 Introduction

In Kohn-Sham density functional theory (KS-DFT),[20,24] the complicated many-body problem of interacting electrons in a solid is mapped to a fictitious system of non-interacting particles in an effective local, one-body potential. The mapping is such that the densities of the interacting and non-interacting systems agree, and so do other ground state properties, for example total energies. The effective potential, called KS potential, is uniquely determined from the electronic density (up to a constant). It consists of the external potential, a classical Coulomb term as well as an "everything else" exchange-correlation term, $v_{\mathrm{xc}} = \delta E_{\mathrm{xc}}/\delta n$.

The exchange-correlation energy E_{xc} is a generally unknown non-local density functional, and the initial success of KS-DFT was grounded in large part in the accuracy of simple approximations for E_{xc}. In the local density approximation (LDA),[20] it is approximated locally by that of the homogeneous electron gas with the same density. Later, the LDA has been improved by taking gradient corrections into account, in combination with exact constraints that E_{xc} must fulfill (generalized gradient approximation or GGA).[36] Although new functionals keep being developed in this manner, see for example Ref. [109], systematic improvements within the KS framework are difficult beyond a certain point.

The search for the exact KS potential, which exhibits interesting properties such as the famous derivative discontinuity,[30,31] is a worthwhile endeavor in its own right from a theoretical standpoint. Furthermore, high quality KS potentials can serve as a testing ground for lower level approximations. As the KS potential is easily visualizable, the differences can be intuitively interpreted and understood. Last not least, accurate KS potentials provide good starting points for various methods of many-body perturbation theory (MBPT).

In principle, quasi-exact KS potentials can be constructed from accurate densities obtained via quantum chemistry methods, as was done, for example, by Umrigar and Gonze.[110] This approach is, however, limited to very small systems due to its unfavorable scaling with respect to system size. Alternatively, it is also possible to take an energy functional from MBPT and map it to a KS potential. Through this procedure, which is known as the optimized effective potential (OEP) method, ever better approximations for v_{xc} can be found by including higher order terms in the perturbation series.

The OEP idea dates back to the 1950s, when Slater [15] constructed a local approximation for the Hartree-Fock potential by taking an orbital average. After further development of the exchange-only theory,[111,112] the framework was later generalized by Sham and Schlüter [6] and others.[113–115] Already in the 1980s, Godby *et al.*[7,8] pioneered the application of OEP from the random-phase approximation (RPA-OEP). They were able to prove that the derivative discontinuity plays a large role for the band gaps of semiconductors, which had been debated up to this point. Their findings were later confirmed by Grüning *et al.*[116,117] and extended to wide-gap systems. More recently, the RPA-OEP for small molecules was extensively studied by Hellgren *et al.*,[118–121] who have also investigated improvements beyond the RPA via the time-dependent DFT framework.[122,123] Similar studies were also performed by Bleiziffer *et al.*[124–126] The RPA-OEP exhibits several features that are expected from the exact exchange-correlation potential but are missing in the (semi-)local approximations. For example, it correctly decays as $1/r$ far away from finite systems such as atoms.[27,113] Moreover, it yields a good description of atomic shell oscillations[118] as well of the dissociation limit of closed-shell molecules.[119]

Due to its prohibitive computational cost, applications to the solid state have so far been limited to few systems. The most comprehensive study of the RPA-OEP for solids up to date was done by Klimeš and Kresse.[127] However, they did use a static approximation for the self-energy, the so-called quasiparticle approximation (QPA). The main focus of the current work is to drop this approximation in order to obtain KS potentials from self-consistent RPA-OEP. These results then serve as reference to determine the accuracy of the QPA.

The paper is organized as follows. In Sec. 5.2, we briefly recapitulate the OEP method and give the RPA-OEP expressions. The QPA is introduced, and we discuss its effects for simple model systems. In Sec. 5.3, key details of our implementation are presented. In Sec. 5.4, we show results from RPA-OEP calculations for 15 semiconductors and insulators. The effect of the QPA on band gaps and dielectric constants is investigated. The results are discussed in Sec. 5.5, and conclusions are drawn in Sec. 5.6. The current work is restricted to the case of non-spin-polarized electrons, spin is accounted for by inclusion of factors of two. Unless stated otherwise, Hartree units are used throughout the work.

5.2 Theory

5.2.1 The optimized effective potential method

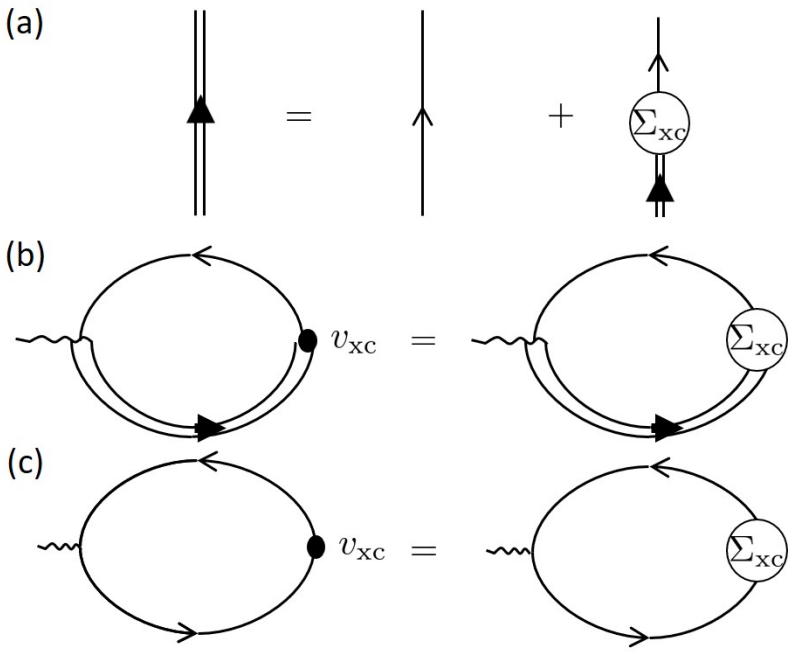

FIGURE 5.1: Diagrammatic representation[99,113] of (a) the Dyson equation, (b) the Sham-Schlüter equation, and (c) the linearized Sham-Schlüter equation. The self-energy Σ_{xc} is replaced by a local potential v_{xc} such that the density of the interacting system n is reproduced exactly (b), or up to first order in Σ_{xc} respectively (c).

We begin our discussion with a brief derivation of the Sham-Schlüter equation (SSE),[6,27] which provides the theoretical basis for the OEP method. The Dyson equation connects the interacting Green's function G to the non-interacting (Kohn-Sham)

Green's function G_0 and the (exchange-correlation part of the) self-energy Σ_{xc}[99]

$$G(\mathbf{r}_2,\mathbf{r}_1,\omega) = G_0(\mathbf{r}_2,\mathbf{r}_1,\omega) + \int \mathrm{d}\mathbf{r}_3 \int \mathrm{d}\mathbf{r}_4 G_0(\mathbf{r}_2,\mathbf{r}_3,\omega)\Sigma_{\mathrm{xc}}(\mathbf{r}_3,\mathbf{r}_4,\omega)G(\mathbf{r}_4,\mathbf{r}_1,\omega), \tag{5.1}$$

where the representation in terms of frequencies ω assumes time translation invariance. By closing the loops, i.e. by setting $\mathbf{r}_2 = \mathbf{r}_1$, summing over spin and integrating over frequencies, we obtain

$$\begin{aligned} &\underbrace{2\oint_{\mathcal{U}} \frac{\mathrm{d}\omega}{2\pi i} G(\mathbf{r}_1,\mathbf{r}_1,\omega)}_{n(\mathbf{r}_1)} = \\ &\underbrace{2\oint_{\mathcal{U}} \frac{\mathrm{d}\omega}{2\pi i} G_0(\mathbf{r}_1,\mathbf{r}_1,\omega)}_{n_0(\mathbf{r}_1)} + 2\oint_{\mathcal{U}} \frac{\mathrm{d}\omega}{2\pi i} G_0(\mathbf{r}_1,\mathbf{r}_3,\omega)\Sigma_{\mathrm{xc}}(\mathbf{r}_3,\mathbf{r}_4,\omega)G(\mathbf{r}_4,\mathbf{r}_1,\omega). \end{aligned} \tag{5.2}$$

Here, n and n_0 are the densities of the interacting system and non-interacting system, respectively, and $\oint_{\mathcal{U}}$ denotes a counterclockwise contour about the upper complex half plane. Now we replace Σ_{xc} by a local, frequency independent potential v_{xc}, and require that this reproduces n exactly,

$$\begin{aligned} n(\mathbf{r}_1) - n_0(\mathbf{r}_1) &= 2\int \mathrm{d}\mathbf{r}_3 \int \mathrm{d}\mathbf{r}_4 \oint_{\mathcal{U}} \frac{\mathrm{d}\omega}{2\pi i} G_0(\mathbf{r}_1,\mathbf{r}_3,\omega)\Sigma_{\mathrm{xc}}(\mathbf{r}_3,\mathbf{r}_4,\omega)G(\mathbf{r}_4,\mathbf{r}_1,\omega) \\ &\overset{!}{=} 2\int \mathrm{d}\mathbf{r}_3 \int \mathrm{d}\mathbf{r}_4 \oint_{\mathcal{U}} \frac{\mathrm{d}\omega}{2\pi i} G_0(\mathbf{r}_1,\mathbf{r}_3,\omega)v_{\mathrm{xc}}(\mathbf{r}_3)\delta(\mathbf{r}_3-\mathbf{r}_4)G(\mathbf{r}_4,\mathbf{r}_1,\omega). \end{aligned} \tag{5.3}$$

This result, the SSE, is depicted diagrammatically in Fig. 5.1. By virtue of the Hohenberg-Kohn theorems,[24] v_{xc} is, in fact, just the exact KS exchange-correlation potential, if no approximations for Σ_{xc} are made. Hence, v_{xc} is uniquely defined by the SSE (up to a constant). Furthermore, the ambiguity with respect to a constant shift can be lifted by the fact that the DFT chemical potential is correct.[8]

In practice, the OEP is often approximated by solving the linearized SSE,[8]

$$\int \mathrm{d}\mathbf{r}'\chi_0(\mathbf{r},\mathbf{r}')v_{\mathrm{xc}}(\mathbf{r}') = 2\int \mathrm{d}\mathbf{r}' \int \mathrm{d}\mathbf{r}'' \oint_{\mathcal{U}} \frac{\mathrm{d}\omega}{2\pi i} G_0(\mathbf{r},\mathbf{r}',\omega)\Sigma_{\mathrm{xc}}(\mathbf{r}',\mathbf{r}'',\omega)G_0(\mathbf{r}'',\mathbf{r},\omega), \tag{5.4}$$

which is obtained by replacing $G \to G_0$ in Eq. (5.3), and identifying the frequency integral in the last line as the static response function of the non-interacting system, symbolically $\chi_0 = G_0 G_0$. Since Eq. (5.4) is linear in Σ_{xc}, we can decompose v_{xc} into separate exchange and correlation parts

$$\begin{aligned} \Sigma_{\mathrm{xc}} &= \Sigma_{\mathrm{x}} + \Sigma_{\mathrm{c}} \\ v_{\mathrm{xc}}[\Sigma_{\mathrm{xc}}] &= v_{\mathrm{x}}[\Sigma_{\mathrm{x}}] + v_{\mathrm{c}}[\Sigma_{\mathrm{c}}]. \end{aligned} \tag{5.5}$$

For alternative derivations and more in-depth discussion of the OEP method, we refer to the reviews of Engel [27] and Kümmel and Kronik.[128]

We now turn to specific approximations for the self-energy Σ_{xc}. The exchange-only approximation (EXX-OEP),

$$\Sigma_{\mathrm{x}}(\mathbf{r},\mathbf{r}') = -\sum_i^{\mathrm{occ}} \frac{\phi_i(\mathbf{r})\phi_i^*(\mathbf{r}')}{|\mathbf{r}-\mathbf{r}'|}, \tag{5.6}$$

is the prototypical static approximation. Here, the frequency integral on the RHS of equation (5.4) can be performed analytically yielding

$$\begin{aligned}&\int \mathrm{d}\mathbf{r}_3 \chi_0(\mathbf{r},\mathbf{r}')v_\mathrm{x}(\mathbf{r}') = \\ &2\sum_i^{\mathrm{occ}}\sum_a^{\mathrm{unocc}} \int \mathrm{d}\mathbf{r}' \int \mathrm{d}\mathbf{r}'' \phi_a(\mathbf{r})\phi_a^*(\mathbf{r}')\Sigma_\mathrm{x}(\mathbf{r}',\mathbf{r}'')\phi_i(\mathbf{r}'')\phi_i^*(\mathbf{r})\frac{1}{\varepsilon_i-\varepsilon_a} + \mathrm{c.c.},\end{aligned} \tag{5.7}$$

where the ϕ_i and ε_i denote the orbitals of the non-interacting system and corresponding eigenvalues respectively. In RPA-OEP, the GW approximation[16,22,129] (more specifically, its one-shot or G_0W_0 version) for the self-energy is used,

$$\Sigma_\mathrm{xc}(\mathbf{r},\mathbf{r}',\omega) = -\oint_\mathcal{U} \frac{\mathrm{d}\omega'}{2\pi i} G_0(\mathbf{r},\mathbf{r}',\omega+\omega')W_0(\mathbf{r},\mathbf{r}',\omega'). \tag{5.8}$$

Here, W_0 is the screened Coulomb interaction using the random-phase approximation for the polarizability,

$$W_0 = V + \chi_0 V\chi_0 + \chi_0 V\chi_0 V\chi_0 + \ldots = V(1-\chi_0 V)^{-1}, \tag{5.9}$$

where V is the bare Coulomb potential. Fig. 5.2 shows the diagrammatic representation of these two approximations for the self-energy. In an orbital basis, the RPA-OEP equation reads

$$\begin{aligned}&2\sum_i^{\mathrm{occ}}\sum_a^{\mathrm{unocc}} \frac{\phi_i(\mathbf{r})\phi_a^*(\mathbf{r})v_{\mathrm{xc},ia}}{\varepsilon_i-\varepsilon_a} + \mathrm{c.c.} = \sum_{mn}^{\mathrm{all}} \phi_m(\mathbf{r})\phi_n^*(\mathbf{r})\rho_{\mathrm{xc},mn} + \mathrm{c.c.} \\ &\rho_{\mathrm{xc},mn} = 2\sum_{rs}^{\mathrm{all}} \oint_\mathcal{U} \frac{\mathrm{d}\omega}{2\pi i} G_{0,mr}(\omega)\Sigma_{\mathrm{xc},rs}(\omega)G_{0,sn}(\omega),\end{aligned} \tag{5.10}$$

where the respective matrix elements for any operator A are given by $A_{mn} = \langle m|A|n\rangle$. It is interesting to note that the RPA density matrix, $n_\mathrm{xc}(\mathbf{r},\mathbf{r}') = \sum_{mn}\phi_m(\mathbf{r})\phi_n^*(\mathbf{r}')\rho_{\mathrm{xc},mn}$, is inherently connected to the theory of RPA natural orbitals. That is, the matrix $\rho_{\mathrm{xc},mn}$ is per definition diagonal in the natural orbital basis, see Ref. [130] for further discussion. We also use the natural orbital basis in the present RPA-OEP implementation (compare Sec. 5.3).

Let us summarize briefly what we have achieved so far. We start from a MBPT energy functional that we want to map to an optimized effective potential (in our case exact exchange and RPA, respectively). An approximate MBPT functional corresponds to a subset of Feynman diagrams. Its variation with respect to the non-interacting Green's function yields a diagrammatic approximation for the self-energy (in our case the exchange-only and G_0W_0 approximation, respectively, compare also Fig. 5.2). The self-energy is then inserted into the linearized SSE, yielding the OEP. This OEP truly is the Kohn-Sham potential corresponding to the given energy functional. For a more rigorous discussion of this formalism, we refer to Hellgren and Barth.[118]

Historically, the RPA has been brought into the DFT framework via the adiabatic-connection formalism.[56,57] The expression for the exchange-correlation energy obtained in this way is formally equivalent to the diagrammatic expansion shown in Fig. 5.2. Following a general procedure,[6,131] it is also possible to re-derive the RPA-OEP equation (5.10) by taking the functional derivative, $v_\mathrm{xc}(\mathbf{r}) = \delta E_\mathrm{xc}/\delta n(\mathbf{r})$, and applying the chain rule (see Ref. [132]).

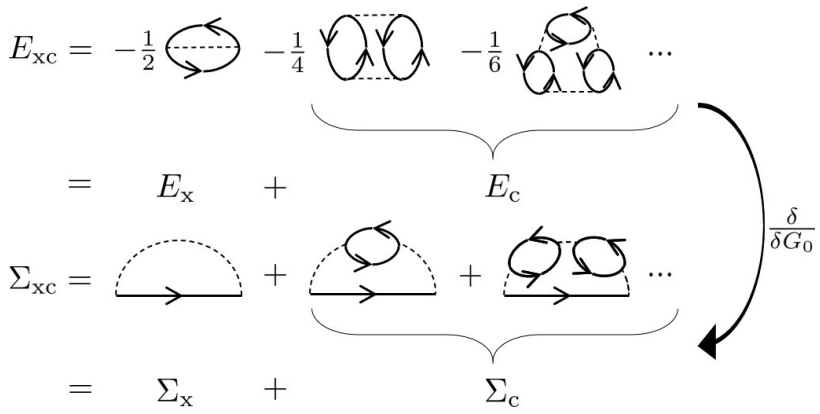

FIGURE 5.2: Diagrammatic representation of the RPA exchange-correlation energy. The self-energy in the G_0W_0 approximation is obtained by taking the functional derivative with respect to the non-interacting Green's function, $\delta E_{\mathrm{xc}}/\delta G_0 = \Sigma_{\mathrm{xc}}$.[118]

5.2.2 Quasiparticle approximation

Now that we have established the RPA-OEP framework, we discuss in the following an additional approximation, which is central to the current work.

The goal of the QPA, as first proposed by Casida,[114] is to find a static approximation $\Sigma_{\mathrm{xc}}(\omega) \approx \Sigma_{\mathrm{xc}}^{\mathrm{QPA}}$ for the self-energy. In the QP limit, we can assume that $\Sigma_{\mathrm{xc}}(\omega)$ is a slowly varying function of ω, and evaluate it at the QP energies ε_m. This simplifies the RPA-OEP equation (5.10), as one can perform the frequency integral on the RHS as in the exchange-only case. The resulting equation in an orbital basis is[114]

$$2\sum_{i}^{\text{occ.}}\sum_{a}^{\text{unocc.}} \phi_i(\mathbf{r})\phi_a^*(\mathbf{r})\frac{v_{\mathrm{xc},ia}}{\varepsilon_i - \varepsilon_a} + \text{c.c.} = 2\sum_{i}^{\text{occ.}}\sum_{a}^{\text{unocc.}} \phi_i(\mathbf{r})\phi_a^*(\mathbf{r})\frac{\Sigma_{\mathrm{xc},ia}^{\mathrm{QPA}}}{\varepsilon_i - \varepsilon_a} + \text{c.c.} \tag{5.11}$$

This is just the EXX-OEP equation with $\Sigma_{\mathrm{x}} \to \Sigma_{\mathrm{xc}}^{\mathrm{QPA}}$, compare Eq. (5.7). There is some ambiguity about how one should choose the non-diagonal elements of $\Sigma_{\mathrm{xc}}^{\mathrm{QPA}}$, which account for non-local effects.[114,133–135] Here, we follow Klimeš and Kresse [127] and choose the Hermitian form[134]

$$\Sigma_{\mathrm{xc},mn}^{\mathrm{QPA}} = \frac{1}{2}\left[\mathrm{Re}\Sigma_{\mathrm{xc},mn}(\varepsilon_m) + \mathrm{Re}\Sigma_{\mathrm{xc},mn}(\varepsilon_n)\right]. \tag{5.12}$$

It is interesting to note that Kotani *et al.*[133–136] used the QPA not as an approximation for the RPA-OEP potential, but rather to obtain a static, non-local potential,

$$V_{\mathrm{xc}}^{\mathrm{nl}} = \sum_{mn}^{\text{all}} |m\rangle\, \Sigma_{\mathrm{xc},mn}^{\mathrm{QPA}}\, \langle n|, \tag{5.13}$$

for self-consistent *GW* calculations. This approach is similar to the generalized OEP method of Jin *et al.*,[81] a detailed comparison of these methods is, however, beyond the scope of this paper. Here, we note only that if one neglects the off-diagonal elements completely, one obtains a local potential as given in Eq. (3.14) of Ref. [114], which is a generalized form of the Slater potential.[15]

Similar to the potential given in Eq. (5.13), a non-local, static approximation to the *GW* self-energy can be obtained by Hedin's COHSEX[22] (static Coulomb hole plus screened exchange). Like the QPA, COHSEX has been used as a non-local potential for self-consistent *GW*, achieving similar results.[137,138] The difference between those

two approximations is that in the QPA, the dynamical effects are neglected at the level of Σ_{xc}, whereas COHSEX neglects them already at the level of W.

5.2.3 The QPA in simple model systems

In order to shed some light on the physics behind the QPA, we investigate its effects in simple model systems. First, we calculate exchange-correlation energies for the homogeneous electron gas (HEG), and then we consider the effect of the QPA on the band gap of a simple flat band model.

For the HEG, spatial symmetry dictates that the OEP is a constant $v_{\text{xc,HEG}}$, which depends only on the density of the HEG n or equivalently the Wigner-Seitz radius $r_{\text{s}} = (3/4\pi n)^{1/3}$. Furthermore, it can be seen from the linearized SSE that v_{xc} is simply given by the self-energy evaluated at the Fermi edge[113]

$$v_{\text{xc,HEG}} = \Sigma_{\text{xc,HEG}}(k_{\text{F}}, k_{\text{F}}^2/2), \tag{5.14}$$

where $k_{\text{F}} = (\alpha r_{\text{s}})^{-1}$ is the Fermi wave vector of the HEG, with $\alpha = (4/9\pi)^{1/3}$. Any exchange-correlation potential for the HEG is related to the exchange-correlation energy per particle $\varepsilon_{\text{xc,HEG}}$ via the general relation

$$v_{\text{xc,HEG}} = \varepsilon_{\text{xc,HEG}} - \frac{r_{\text{s}}}{3}\frac{\mathrm{d}\varepsilon_{\text{xc,HEG}}}{\mathrm{d}r_{\text{s}}}. \tag{5.15}$$

For the exchange-only self-energy, one obtains the familiar Dirac expression $\varepsilon_{\text{x,HEG}} = -3/(4\pi\alpha r_{\text{s}})$, whereas the correlation part of the G_0W_0 energy is connected to the RPA correlation energy[120]

$$v_{\text{c,HEG}}^{G_0W_0} = \varepsilon_{\text{c,HEG}}^{\text{RPA}} - \frac{r_{\text{s}}}{3}\frac{\mathrm{d}\varepsilon_{\text{c,HEG}}^{\text{RPA}}}{\mathrm{d}r_{\text{s}}}. \tag{5.16}$$

We have used explicit labels here to emphasize that the random-phase approximation is constructed from the *non-interacting* quantities G_0 and W_0. For the HEG, the self-energy is diagonal in the momentum basis, hence $\Sigma_{\text{xc,HEG}}^{\text{QPA}}(k) = \Sigma_{\text{xc,HEG}}(k, \varepsilon_k)$. It is evident that the QPA gives the correct OEP per definition. In comparison, the COHSEX yields an OEP which is too negative,[22] see also Appendix D.

This exact relation for the OEP hides in some sense the drastic simplification that is made, when the self-energy as a function of frequency is crudely approximated as a constant. In reality, is has pronounced structure even for the HEG, especially near the plasmon frequency, see e.g. Hedin and Lundqvist.[16] Any static approximation corresponds to setting the renormalization factor $Z = (1 - \partial\text{Re}\Sigma/\partial\omega)^{-1}$ equal to 1. Clearly, all information about lifetimes and satellites is lost in this way. To demonstrate how the QPA can fail also for total energies, we have calculated exchange-correlation energies via the Galitskii-Migdal (GM) formalism,[99] that is we calculate the GM energy per particle[139]

$$\varepsilon_{\text{HEG}}^{\text{GM}} = \frac{1}{n}\int_0^\infty \frac{\mathrm{d}k}{(2\pi)^3} 4\pi k^2 \oint_{\mathcal{U}} \frac{\mathrm{d}\omega}{2\pi i}\left[2\varepsilon(k)G(k,\omega) + G(k,\omega)\Sigma_{\text{xc}}(k,\omega)\right], \tag{5.17}$$

where $\varepsilon(k) = k^2/2$ is the free electron parabola. The exchange-correlation energy per particle $\varepsilon_{\text{xc,HEG}}^{\text{GM}}$ is then defined as the difference between the above expression for the interacting and non-interacting HEG, i.e.

$$\varepsilon_{\text{xc,HEG}}^{\text{GM}} = \varepsilon_{\text{HEG}}^{\text{GM}} - 3k_{\text{F}}^2/10. \tag{5.18}$$

In general, Eq. (5.17) has to be evaluated self-consistently, where G, W and Σ_{xc} are updated via Hedin's GW equations. Only then do both expressions for the exchange-correlation energies, Eqs. (5.18) and (5.15), coincide[140] [in Eq. (5.15), $\varepsilon_{xc,HEG}$ is implicitly defined via the solution of the differential equation, see Hedin [22]]. For static approximations to the GW self-energy, $\Sigma_{xc}(\omega) \to \Sigma_{xc}^{static}$, there is no real self-consistency problem. The frequency integral in Eq. (5.17) can be performed analytically, and one obtains the simple expression (see chap. 10 of Ref. [99])

$$\varepsilon_{xc,HEG}^{static} = \frac{1}{n}\int_0^{k_F} \frac{dk}{(2\pi)^3} 4\pi k^2 \Sigma_{xc,HEG}^{static}(k). \tag{5.19}$$

This result can be intuitively understood, as a static interaction can only shift, but never smear the Fermi surface, since the QP lifetime is always infinite. For example, in the familiar exchange-only case, one obtains[16]

$$\Sigma_x(k) = \frac{k_F}{\pi}\left(1 + \frac{k_F^2 - k^2}{2kk_F}\ln\left|\frac{k_F + k}{k_F - k}\right|\right), \tag{5.20}$$

which yields once again the Dirac expression when inserted into Eq. (5.19). We have performed numerical calculations for Σ_{xc} in the COHSEX and QPA as well as in the fully-self consistent case (sc-GW). The procedure is detailed further in Appendix D, results are depicted in Fig. 5.3.

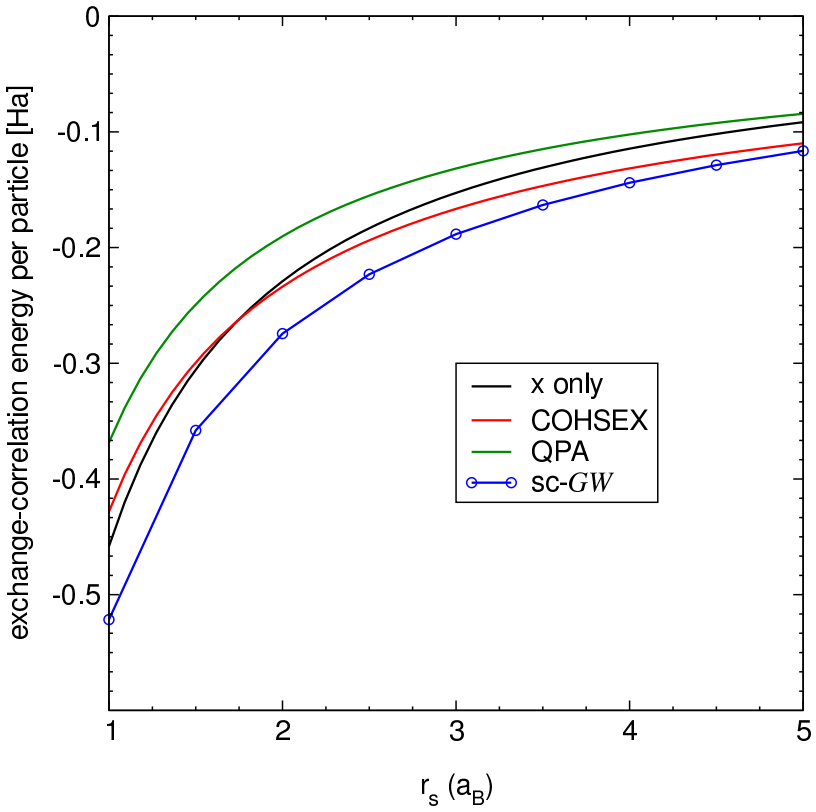

FIGURE 5.3: Exchange-correlation energies per particle for the HEG via the Galitskii-Migdal formula (5.18). Shown are different static approximations for the GW self-energy (x only, COHSEX, QPA) as well as the fully self-consistent case. For further discussion, see also Appendix D.

It can be seen that both static approximations, COHSEX and QPA, yield GM

exchange-correlation energies similar to the exchange-only case, that is, too positive when compared to sc-*GW*. We want to stress that the latter is indeed the most sound from a physical stand point, and any deviance must be interpreted as a failure of the static approximations. Furthermore, it was noted previously by Holm and Barth[139,140] that sc-*GW* is very close to the exact (QMC) data. Here, we find that the QPA performs even worse than COHSEX, which at least correctly predicts a negative contribution from correlation for metallic densities. As we discuss in Appendix D, the main failure of the QPA is that no QP weight is transferred from the QP peak to lower lying excitations (satellites).

After having discussed the QPA for the HEG, we now estimate its effect on the band gap of a semiconductor. To this purpose, we construct a simple flat band model, which allows us to derive a first-order estimate for the band-gap correction ΔE_g, i.e. the difference

$$\Delta E_\mathrm{g} = E_\mathrm{g}^\mathrm{QPA} - E_\mathrm{g}, \tag{5.21}$$

where E_g is the RPA-OEP band gap. This procedure is inspired by the work of Hanke and Sham,[141] who sought to build an analytical model for the G_0W_0 self-energy and the corresponding v_xc from RPA-OEP.

The assumptions of our model are as follows: (i) We approximate the system by two flat bands, one valence band and one conduction band (extreme tight-binding approximation). The bands have energies ε_v and ε_c respectively, and the OEP band gap is $E_\mathrm{g} = \varepsilon_c - \varepsilon_v$. Furthermore, the non-interacting Green's function is given by

$$G_0(\mathbf{r}, \mathbf{r}', \omega) = \frac{\phi_v(\mathbf{r})\phi_v^*(\mathbf{r}')}{\omega - \varepsilon_v - i\eta} + \frac{\phi_c(\mathbf{r})\phi_c^*(\mathbf{r}')}{\omega - \varepsilon_c + i\eta}, \tag{5.22}$$

where η is a positive infinitesimal.

(ii) We expand the self-energy as a function of frequency linearly around the QP energies, neglecting for a moment any energy dependence of the off-diagonal terms,

$$\begin{aligned}
\Sigma_{\mathrm{xc},vv}(\omega) &= \Sigma_{\mathrm{xc},vv}(\varepsilon_v) + (\omega - \varepsilon_v)\Sigma'_{vv}(\varepsilon_v) \\
\Sigma_{\mathrm{xc},cc}(\omega) &= \Sigma_{\mathrm{xc},cc}(\varepsilon_c) + (\omega - \varepsilon_c)\Sigma'_{cc}(\varepsilon_c) \\
\Sigma_{\mathrm{xc},vc} &= \Sigma^*_{\mathrm{xc},cv} = \Sigma^\mathrm{QPA}_{\mathrm{xc},vc},
\end{aligned} \tag{5.23}$$

where Σ' is connected to the Z-factor by

$$Z = \frac{1}{1 - \Sigma'}, \tag{5.24}$$

and is therefore negative as $Z < 1$. The QPA can be obtained by setting $\Sigma' \to 0$ in Eq. (5.23) and in the following expressions.

The second assumption implies that the effect of the QPA will be small in the sense $\Delta E_\mathrm{g}/E_\mathrm{g} \ll 1$. Within the limits of this approximation, we can solve the linear SSE in a one-shot fashion, neglecting the self-consistency requirement. Inserting assumption (i) in the OEP equation (5.10) and performing the contour integrals yields

$$-2\frac{\phi_v(\mathbf{r})\phi_c^*(\mathbf{r})v_{\mathrm{xc},vc}}{E_\mathrm{g}} + \mathrm{c.c.} = \left[-2\frac{\phi_v(\mathbf{r})\phi_c^*(\mathbf{r})\Sigma^\mathrm{QPA}_{\mathrm{xc},vc}}{E_\mathrm{g}} + 2\phi_v(\mathbf{r})\phi_v^*(\mathbf{r})\Sigma'_{vv}(\varepsilon_v)\right] + \mathrm{c.c.} \tag{5.25}$$

Comparing this result with Eq. (5.11), we see that only the pole in $\Sigma_{\mathrm{xc},vv}$ yields an extra term on the RHS, proportional to $E_\mathrm{g}\Sigma'_{vv}$. By inserting the completeness relation

$|v\rangle\langle v| + |c\rangle\langle c| = 1$, we find

$$\Delta v_{\mathrm{xc}}(\mathbf{r}) = \Delta v_{\mathrm{xc},vv} + E_{\mathrm{g}}\Sigma'_{vv}, \tag{5.26}$$

where we have defined $\Delta v_{\mathrm{xc}} = v_{\mathrm{xc}}^{\mathrm{QPA}} - v_{\mathrm{xc}}$. As $\Delta v_{\mathrm{xc}}(\mathbf{r})$ is constant, we see that here, the QPA amounts only to a rigid shift of both bands. Turning now to the influence of the off-diagonal terms [compare Eq. (5.12)], and proceeding as above, we find that valence and conduction band are further shifted by

$$\begin{aligned} \Delta v_{\mathrm{xc},vv} &= \frac{E_{\mathrm{g}}\Sigma'_{vv}(\varepsilon_v)}{2} \\ \Delta v_{\mathrm{xc},cc} &= \frac{E_{\mathrm{g}}\Sigma'_{cc}(\varepsilon_c)}{2}, \end{aligned} \tag{5.27}$$

where we have used that $\Sigma'(\varepsilon_v) \approx \Sigma'(\varepsilon_c)$ within the linear approximation. Using Eq. (5.24) to replace Σ' by the Z-factor, we obtain

$$\Delta E_{\mathrm{g}} = E_{\mathrm{g}}\frac{Z_c - Z_v}{2Z_cZ_v}. \tag{5.28}$$

Since Z_c is typically smaller than Z_v, the QPA opens the band gap. It is interesting that this term vanishes, if the Hermitian form (5.12) is replaced by the prescription of Casida,[114] where the non-diagonal terms are evaluated at occupied energies only. Finally, it is worth mentioning that the result (5.28) is not affected by a degeneracy neither of the conduction nor the valence band. Both sides of the OEP equation would be multiplied by a common factor, which than cancels out.

In summary, the QPA is a drastic approximation, which is generally unjustified except for states near the Fermi level. However, *for the purpose of the OEP*, it can yield satisfactory results. This is manifest in the exact result for the HEG (Eq. (5.14)), and the band gap correction (Eq. (5.28)) for our flat band model vanishes in the metallic limit. Further plausibility comes from the original derivation of Kotani *et al.*,[135] which is in spirit similar to that of the OEP equation. On the other hand, we can expect a failure of the QPA for both insulators and systems, where the exact treatment of the off-diagonal self-energy elements is important.

5.3 Computational details

In Sec. 5.3.1 we discuss how the self-consistency cycle is performed and describe details of our implementation in the PAW code `VASP` (Vienna *Ab Initio* Simulation Package).[104] To motivate the need for an efficient self-consistency scheme, we remark that a single RPA-OEP calculation as typically performed in this work takes up roughly 100-3000 core hours, as compared to 10-60 core seconds for standard GGA calculations.

5.3.1 Self-consistency cycle

As in any self-consistent scheme, a good starting point is important for fast convergence. The key trick is that a DFT potential (and the OEP is just that) usually converges faster with respect to the k-point mesh than other properties such as KS excitation energies. Hence, a good starting point for the OEP can by obtained from v_{xc} *on a sparser k-point mesh.* Small differences on a denser k-point mesh can than be added with few further iterations.

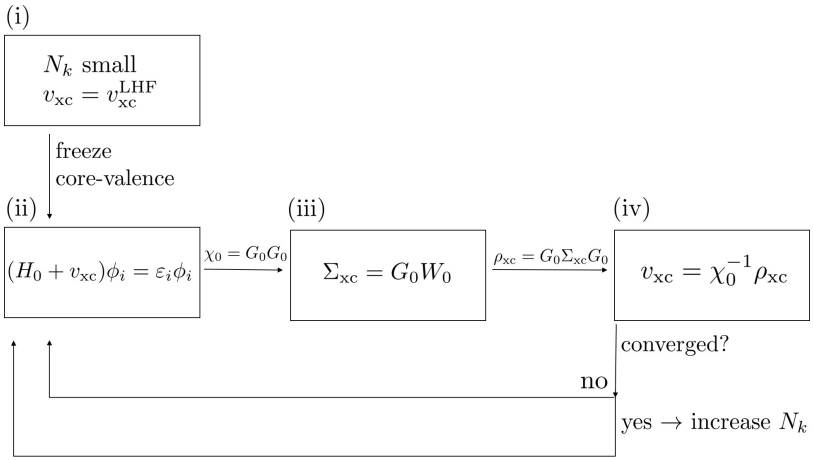

FIGURE 5.4: Schematic representation of the self-consistency scheme for RPA-OEP calculations.

The basic scheme is shown in Fig. 5.4. Starting with a sparse k-point grid, (i) we first perform a local Hartree-Fock[142] calculation (LHF, an approximation to EXX-OEP) to obtain a starting point for the RPA-OEP. Following Klimeš and Kresse,[127] LHF yields an approximation to the core-valence interaction that is kept frozen during the rest of the calculation. The LHF calculation is performed in a one-shot way on-top of DFT reference orbitals. Here, we use the GGA functional of Perdew, Burke and Ernzerhof[36](PBE). The subsequent OEP self-consistency cycle is detailed in steps (ii) - (iv). The KS Hamiltonian using the RPA-OEP (in the first step the LHF) exchange-correlation potential is diagonalized, yielding G_0, from which χ_0 and thereafter Σ_{xc} can be calculated. These steps parallel those of a routine G_0W_0 calculation, as detailed in Ref. [4]. Then, ρ_{xc} is evaluated in the natural orbital basis. The RPA-OEP potential is updated by letting χ_0^{-1} act on both sides of Eq. (5.10). In Appendix E, more details on our implementation of step (iv) are given. The OEP is inserted back in the KS equation (ii), and the loop (ii)-(iv) is repeated until some convergence criterion is met. Then, we switch to the denser k-point mesh and re-enter the self-consistency loop.

For QPA-RPA-OEP we use the implementation of Eq. (5.11) as presented in Ref. [127]. It slightly differs from the current implementation in the way that frequency integrations are performed in step (iii) and uses the Kohn-Sham rather than the natural orbital basis in step (iv). To enable a fair comparison, we have carefully converged both calculations with respect to the relevant parameters (number of frequency points and number of unoccupied bands) to 10 meV accuracy in the OEP band gaps.

Turning now to the performance of our self-consistency scheme, we find that switching from a Γ-centered $4 \times 4 \times 4$ k-point mesh to a Γ-centered $6 \times 6 \times 6$ k-point mesh, a single iteration is usually enough to converge the OEP band gaps within 10 meV. As a safety precaution, however, we always perform two iterations. The only approximation made is that the core-valence interaction terms are interpolated to the denser k-point mesh and that core-electrons are kept frozen at the level of the PBE reference.

Fig. 5.5 demonstrates this for the exemplary case of SiC. Clearly, the stated approximation is excellent, as both procedures converge towards nearly the same value (here within 2 meV, generally we found $\lesssim$ 10 meV accuracy, compare also Table

5.1). Furthermore, it can be seen that the pre-iteration procedure speeds up the self-consistency cycle on the more expensive $6 \times 6 \times 6$ k-point mesh, as a single iteration is enough to converge the band gap to 10 meV accuracy versus 6 iterations if starting directly from LHF.

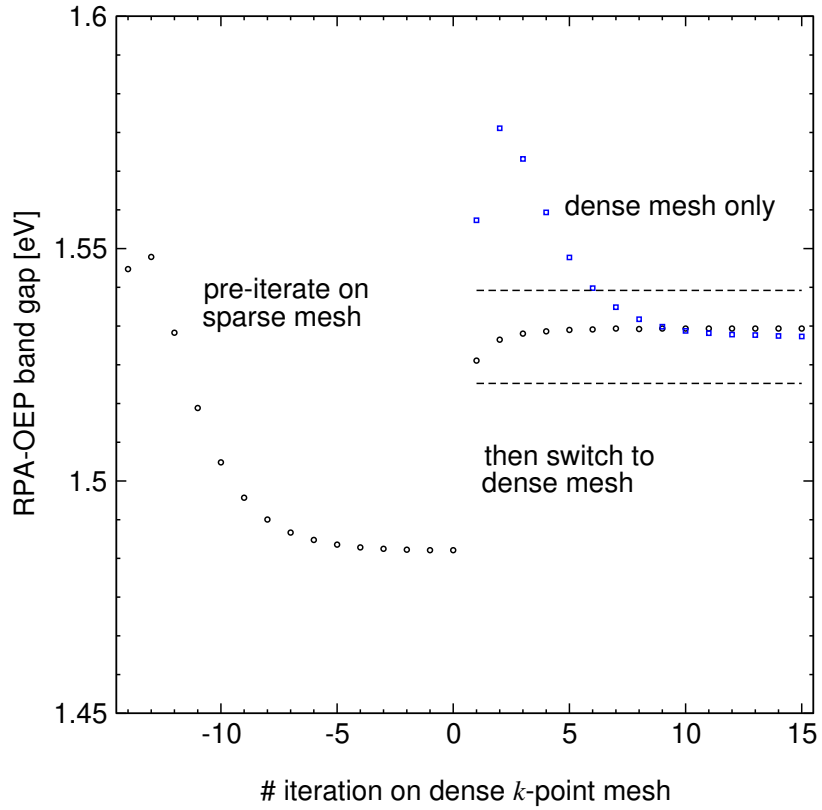

FIGURE 5.5: Convergence of the RPA-OEP band gap for SiC, with respect to the number of iterations in the self-consistency cycle. Squares: 15 iterations on a $6 \times 6 \times 6$ k-point mesh, starting from LHF. Circles: 15 iterations on a $4 \times 4 \times 4$ k-point mesh, then 15 further iterations on a $6 \times 6 \times 6$ k-point mesh. Dashed lines indicate a tolerance region of ± 10 meV.

5.4 Applications

5.4.1 Applied settings

In the present work, we consider 15 semiconductors and insulators listed in Table 5.2. Calculations are performed at the experimental lattice constant, where for materials that crystallize in the wurtzite structure under normal conditions[143] (GaN, ZnO, CdS), the zinc-blende structure was chosen to allow for comparison with previous calculations.

RPA-OEP calculations are done using the `VASP` code as described previously in Sec. 5.3. The plane wave cutoffs for the orbital basis $E_{\max}$ (`ENCUT` in `VASP`) are listed in Table 5.2. For the response function, we use a smaller cutoff $E^{\chi}_{\max} = E_{\max}/2$ (`ENCUTGW` in `VASP`). This is possible, as the convergence of the OEP tends to be better behaved with respect to $E^{\chi}_{\max}$ than single GW self-energies, which often require even an extrapolation towards infinite basis, see e.g. Ref. [86]. Better convergence for OEP is expected, since the OEP equation (5.10) takes essentially a self-energy average (the basis set incompleteness error also falls off as ${E^{\chi}_{\max}}^{-3/2}$, but with a different prefactor[127]). Nevertheless, the finite energy cutoff is the dominant error in

TABLE 5.1: RPA-OEP excitation energies for SiC from the valence band maximum at the Γ-point to the conduction band minimum at the indicated k-point (in eV). The first column shows results using a $4 \times 4 \times 4$ Γ-centered k-point mesh. The second column shows results for a $6 \times 6 \times 6$ mesh, and the third and fourth columns correspond to our interpolation method after 2 and 15 iterations on the dense mesh respectively, compare Fig. 5.5. The band gap as reported in the following tables is marked bold.

	$4 \times 4 \times 4$	$6 \times 6 \times 6$	interpolation method	
			2 iterations	15 iterations
Γ	6.501	6.505	6.512	6.515
L	5.606	5.628	5.633	5.635
X	1.485	1.531	**1.530**	1.533

TABLE 5.2: Chosen settings for the OEP calculations. Strukturbericht designations of the chosen crystal structures are listed in parenthesis. Short-hands _sv for the PAW potentials indicate treatment of the outermost s and p core states as valence. Moreover, short-hands _h and _nc indicate a very accurate treatment of high energy states. Orbital plane wave cutoffs $E_{\max}$ are given in eV. Values for the experimental lattice constant a_0 (in Å) are taken from Ref. [146], unless stated otherwise.

		PAW potentials	$E_{\max}$	a_0
C	(A4)	C_h_GW	742	3.567
Si	(A4)	Si_sv_GW	548	5.431
SiC	(B3)	Si_sv_GW C_h_GW	742	4.358
BN	(B3)	B_h N_h_GW	756	3.616
AlP	(B3)	Al_sv_GW P_sv_GW	553	5.463
AlAs	(B3)	Al_sv_GW As_sv_GW_nc	674	5.661
AlSb	(B3)	Al_sv_GW Sb_sv_GW_nc	607	6.136
GaN	(B3)	Ga_sv_GW_nc N_h_GW	802	4.531[143]
GaP	(B3)	Ga_sv_GW_nc P_sv_GW	802	5.451
InP	(B3)	In_sv_GW_nc P_sv_GW	604	5.869
InSb	(B3)	In_sv_GW_nc Sb_sv_GW_nc	607	6.479
ZnO	(B3)	Zn_sv_GW_nc O_h_GW	802	4.580[4]
ZnS	(B3)	Zn_sv_GW_nc S_GW_nc	802	5.409
CdS	(B3)	Cd_sv_GW_nc S_GW_nc	658	5.818
MgO	(B1)	Mg_sv_GW_nc O_h_GW	822	4.211

our calculations, typically underestimating the band gaps by up to 50 meV. The two RPA-OEP methods also differ slightly in details of the implementation, see Sec. 5.3. All in all, we estimate that the accuracy of the RPA-OEP band gaps is better than 100 meV. Nevertheless, we list them to higher precision, as the effect of the QPA, i.e. the differences ΔE_g, are estimated to be more accurate, within 50 meV.

EXX-OEP calculations are performed using the shift algorithm of Kümmel and Perdew[144,145] as presented in Ref. [127]. As unoccupied states are not required here, the EXX-OEP band gaps are more accurate, with errors well below 50 meV, and the dominant error is now related to the finite k-point mesh.

5.4.2 OEP band gaps

In Table 5.3, we report OEP excitation energies from the valence band maximum (VBM) at the Γ-point to the conduction band minimum (CBM) at the Γ, L, and X-point, respectively. For comparison, we also include Kohn-Sham excitation energies obtained using the PBE functional.We first note that our numerical results for EXX-OEP and QPA-RPA-OEP excitation energies are generally in good agreement with those of Klimeš and Kresse.[127] Slight differences for SiC, AlP, and AlAs are due to our use of more accurate pseudo-potentials for Si, P and As, respectively.

In the following, we discuss first general trends and thereafter quantitative results and specific materials. Generally, we observe the following order: PBE yields the smallest gaps, and EXX-OEP the largest. When screening in form of the QPA-RPA is taken into account, the gaps close substantially with respect to EXX-OEP. When the QPA is lifted, taking dynamical screening properly into account, the band gaps are further closed towards PBE. It is reassuring that similarly, the static COH-SEX approximation tends to overestimate band gaps.[129]

TABLE 5.3: Kohn-Sham excitation energies obtained with the PBE functional, EXX-OEP as well as RPA-OEP with and without the quasiparticle approximation (QPA, exact). The energy excitations between the VBM at the Γ-point and the CBM at the indicated *k*-point are given in eV. All calculations are performed self-consistently. Wherever InSb is predicted to be metallic, we report a negative band gap (see text).

		PBE	EXX	RPA	
				QPA	exact
C	Γ	5.60	6.21	6.04	5.75
	L	8.47	9.08	8.89	8.62
	X	4.76	5.42	5.00	4.89
Si	Γ	2.55	3.13	2.69	2.68
	L	1.53	2.32	1.69	1.64
	X	0.70	1.34	0.74	0.74
SiC	Γ	6.21	7.49	6.75	6.51
	L	5.41	6.38	5.81	5.63
	X	1.34	2.37	1.60	1.53
BN	Γ	8.82	9.80	9.49	9.12
	L	10.13	11.19	10.69	10.37
	X	4.46	5.57	4.92	4.70
AlP	Γ	3.27	4.35	3.60	3.50
	L	2.78	3.51	2.97	2.92
	X	1.57	2.26	1.70	1.71
AlAs	Γ	2.02	3.10	2.32	2.28
	L	2.13	2.86	2.32	2.31
	X	1.44	2.11	1.61	1.62
AlSb	Γ	1.59	2.49	1.73	1.73
	L	1.34	1.94	1.43	1.45
	X	1.22	1.73	1.29	1.34

Table 5.3, continued.

		PBE	EXX	RPA	
				QPA	exact
GaN	Γ	1.61	3.10	2.10	1.84
	L	4.52	5.81	4.93	4.67
	X	3.34	4.65	3.68	3.51
GaP	Γ	1.81	2.97	2.12	1.99
	L	1.66	2.45	1.82	1.76
	X	1.65	2.15	1.67	1.67
InP	Γ	0.69	1.68	0.84	0.79
	L	1.49	2.19	1.55	1.53
	X	1.77	2.26	1.76	1.77
InSb	Γ	-0.19	0.71	-0.16	-0.16
	L	0.54	1.11	0.53	0.54
	X	1.34	1.67	1.28	1.30
ZnO	Γ	0.68	2.90	1.46	1.20
	L	5.46	7.43	6.18	5.91
	X	5.27	7.52	5.99	5.77
ZnS	Γ	2.09	3.35	2.36	2.25
	L	3.30	4.34	3.53	3.46
	X	3.41	4.24	3.50	3.49
CdS	Γ	1.15	2.20	1.20	1.17
	L	3.02	3.87	3.04	3.04
	X	3.54	4.30	3.56	3.56
MgO	Γ	4.74	6.55	5.58	5.23
	L	7.91	9.71	8.66	8.36
	X	9.12	10.88	9.74	9.50

In summary, we obtain the following order for Kohn-Sham band gaps

$$\text{PBE} \leq \text{RPA-OEP} \leq \text{QPA-RPA-OEP} \ll \text{EXX-OEP}.$$

Moreover, we find that the effect of the QPA is stronger at the Γ-point than at the L-point and weakest at the X-point. This brings the dispersion of the RPA-OEP conduction bands closer to PBE.

Turning now to the discussion of specific systems, there are two groups of materials, where exact RPA-OEP differs most from QPA-RPA-OEP. (i) Large effects are seen for all insulators, where the indirect $\Gamma \rightarrow X$ gaps are closed by 0.1 eV (C), 0.2 eV (BN) and 0.35 eV (MgO) respectively. (ii) The band gaps are also much reduced in those materials, where the accurate treatment of the off-diagonal elements of Σ_{xc} is important.[135,147] Here, the direct $\Gamma \rightarrow \Gamma$ gaps are closed by 0.25 eV for both ZnO and GaN. The off-diagonal elements also play a large role for MgO,[147] which further explains why the effect is even stronger here than for the other insulators.

Generally, it can be observed that group (ii) is characterized by a large electronegativity difference of the constituents: compare the effects of the QPA for ZnO/ZnS,

GaN/GaP, the series C-BN-MgO, and note also that the QPA has small effects for the almost electroneutral systems AlP, AlAs and AlSb. Broadly speaking, the character of the VBM and the CBM is rather dissimilar in ionic systems. This is reflected in the difference between the Z-factors of the CBM and the VBM, which appears also in our model estimate for Δ_g, see Eq. (5.28). Similarly, it has been shown that for ionic systems, range-separated hybrid functionals can struggle to reproduce optical properties as calculated by more accurate MBPT methods,[*Chen2013, 148] even if the parameters of the hybrids are optimally tuned.[149] This underlines the importance of dynamical screening effects for ionic systems.

For AlSb, the QPA slightly closes the indirect band gap by 0.05 eV, in contradiction to the general trend. This effect is, however, within our estimated accuracy, and the dispersion is closer to PBE for exact RPA-OEP as is generally the case.

Finally, we want to comment briefly on the interesting case of InSb, which is predicted to be metallic by PBE as well as by both RPA-OEP schemes. Alongside the metallic phase, a band inversion occurs, i.e. the three-fold degenerate p bands (usually forming the top of the valence band) are then above the s band at the Γ-point. Per convention, the excitation energies are still reported with respect to the p bands, yielding a "negative band gap". We find that this negative band gap is virtually the same for PBE, RPA-OEP and QPA-RPA-OEP.

5.4.3 Band structures and potentials

To further substantiate the results of Sec. 5.4.2, we now discuss two representative systems, C and MgO, in greater detail. To this effect, we compare RPA-OEP band structures and KS potentials in real space to the respective PBE references. Starting with C, we find from the band structure shown in Fig. 5.6(a) that the valence bands of both RPA-OEP methods are very close to the PBE ones. The conduction bands from exact RPA-OEP resemble those from PBE, up to a rigid up-shift of about 150 meV, whereas the conduction bands from QPA-RPA-OEP exhibit broader dispersion and band width. Fig. 5.6(b) shows that this broader dispersion for QPA-RPA-OEP is less pronounced in MgO, where the band structures are close for all three methods, again up to rigid shifts of the conduction bands. Hence, it is difficult to draw general conclusions, except that for typical semiconductors and insulators as investigated in this work the PBE band structures are close to the exact RPA-OEP ones (up to a rigid shift of the conduction bands), compare also Table 5.3. This reaffirms the observations of Godby *et al.*,[7,8] then made with respect to LDA rather than PBE.

For the purpose of plotting the OEP potentials in real space, we redo the OEP calculations for C and MgO with an increased plane wave cutoff for the response function, $E^{\chi}_{\text{max}} = 2/3 E_{\text{max}}$. This has little effect on the band gaps, but helps to reduce numerical noise in the interstitial regions [for both C and MgO, the gaps open by $\lesssim 20$ meV, the effect on the differences ΔE_g, see Eq. (5.21), is negligible].

Fig. 5.7(a) shows total KS potentials for C from the two RPA-OEP methods as well as from PBE along the [111] direction (atom positions are indicated by small circles). The KS potential from QPA-RPA-OEP agrees well with that reported by Klimeš and Kresse.[127] Deeper KS potentials inside the PAW spheres in the current work are due to our use of a harder pseudo-potential. General features of the potentials are a well defined maximum at the center of the covalent bonds and fairly flat behavior in the interstitial regions.

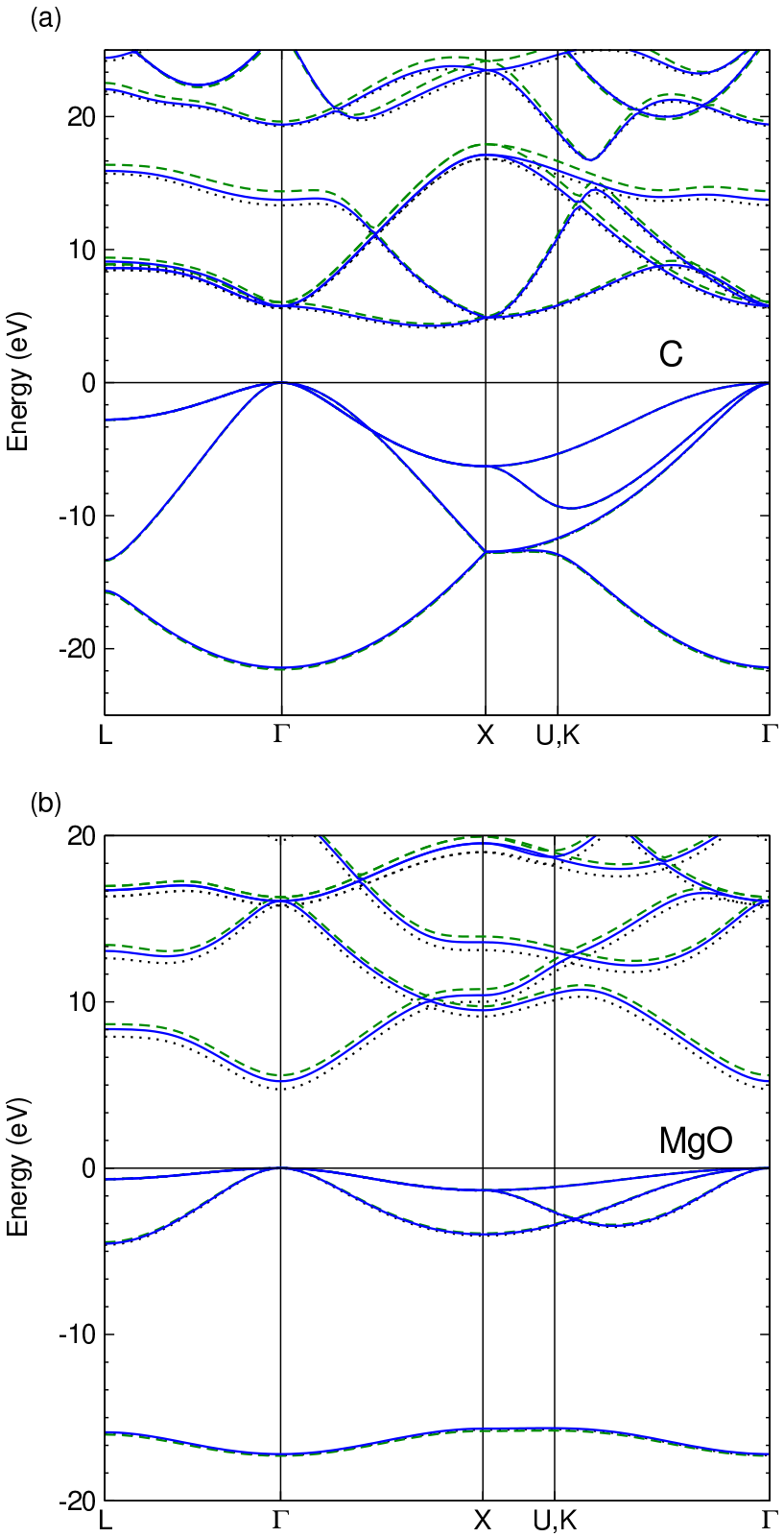

FIGURE 5.6: Kohn-Sham band structures for (a) C and (b) MgO. Dotted (black) lines represent PBE, dashed (green) lines QPA-RPA-OEP and solid (blue) lines exact RPA-OEP, respectively. Valence band maxima at the Γ-point have been aligned at zero.

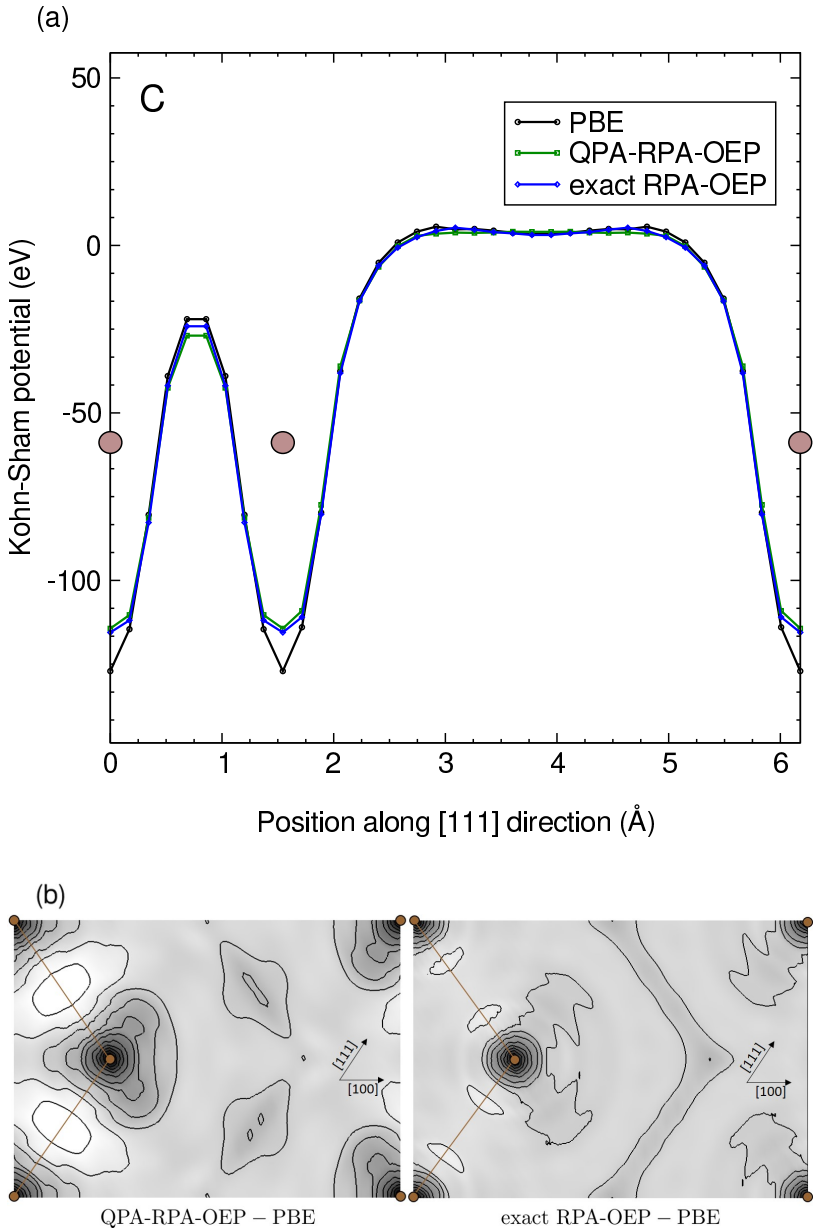

FIGURE 5.7: Comparison of the KS potentials $v_{\mathrm{KS}}(\mathbf{r})$ for C. The atom positions are indicated by small circles. (a) Total KS potentials along the [111] direction. Symbols indicate the finite real space grid, on which v_{KS} is evaluated. (b) Contour plots for the differences $v_{\mathrm{KS}}^{\mathrm{OEP}} - v_{\mathrm{KS}}^{\mathrm{PBE}}$ in the $(0\bar{1}1)$ plane. Contour lines are drawn in steps of 1.5 eV, lighter areas indicate that $v_{\mathrm{KS}}^{\mathrm{OEP}} < v_{\mathrm{KS}}^{\mathrm{PBE}}$. Left: QPA-RPA-OEP, right: exact RPA-OEP. Straight lines indicate covalent bonds between carbon atoms. The potential differences have been interpolated between real space grid points using cubic splines.[150]

A contour plot of the differences $v_{\mathrm{KS}}^{\mathrm{OEP}} - v_{\mathrm{KS}}^{\mathrm{PBE}}$ in the $(0\bar{1}1)$ plane is further shown in Fig. 5.7(b). For C, similar comparisons have been made already by previous authors,[8,127] albeit with respect to LDA rather than PBE. This difference, however, does not affect the following qualitative analysis. As in Refs. [8, 127], we observe that the RPA-OEP potentials are more attractive in the bonding regions, more so if dynamical screening is neglected in form of the QPA. Together with the fact that the potentials are fairly similar in the interstitial regions, this can explain the observed order for the band gaps.[8] That is, the gap opens as the valence states, which are concentrated around the bonds, get lowered in energy relative to the conduction states. Interestingly, Fig. 5.7(b) shows that the KS potential from exact RPA-OEP has noticeable angular structure near the anti-bonding regions, when compared to the more spherically symmetric PBE potential. This structure is absent in QPA-RPA-OEP, compare also respective figures in Refs. [8, 127].

Turning now to MgO, Fig. 5.8(a) shows the total KS potentials along the [100] direction. The PBE potential is relatively structureless and resembles a broad barrier between atomic potential wells. Both RPA-OEP methods significantly deviate from PBE in the vicinity of Mg atoms (light (orange) circles), the effect is again stronger in QPA-RPA-OEP. Contour plots of the potential differences in the (001) plane show distinct radial structures, see Fig. 5.8(b). Weaker, but more important, these "rings" exist also in the vicinity of O atoms (dark (red) circles), and have larger amplitudes in the static QPA-RPA-OEP. The KS potential from EXX-OEP shows similar radial structure that is even stronger (not shown). One is tempted to invoke the interpretation from above once again: relatively compact valence states get pulled down by the "white rings", whereas more delocalized conduction states are less effected by the oscillatory potential difference. Finally, as observed for C, we find that the exact RPA-OEP potential is less spherically symmetric around the atoms. However, the angular structure is not as pronounced here, since the rock-salt crystal structure constraints the potentials more strongly to spherical symmetry.

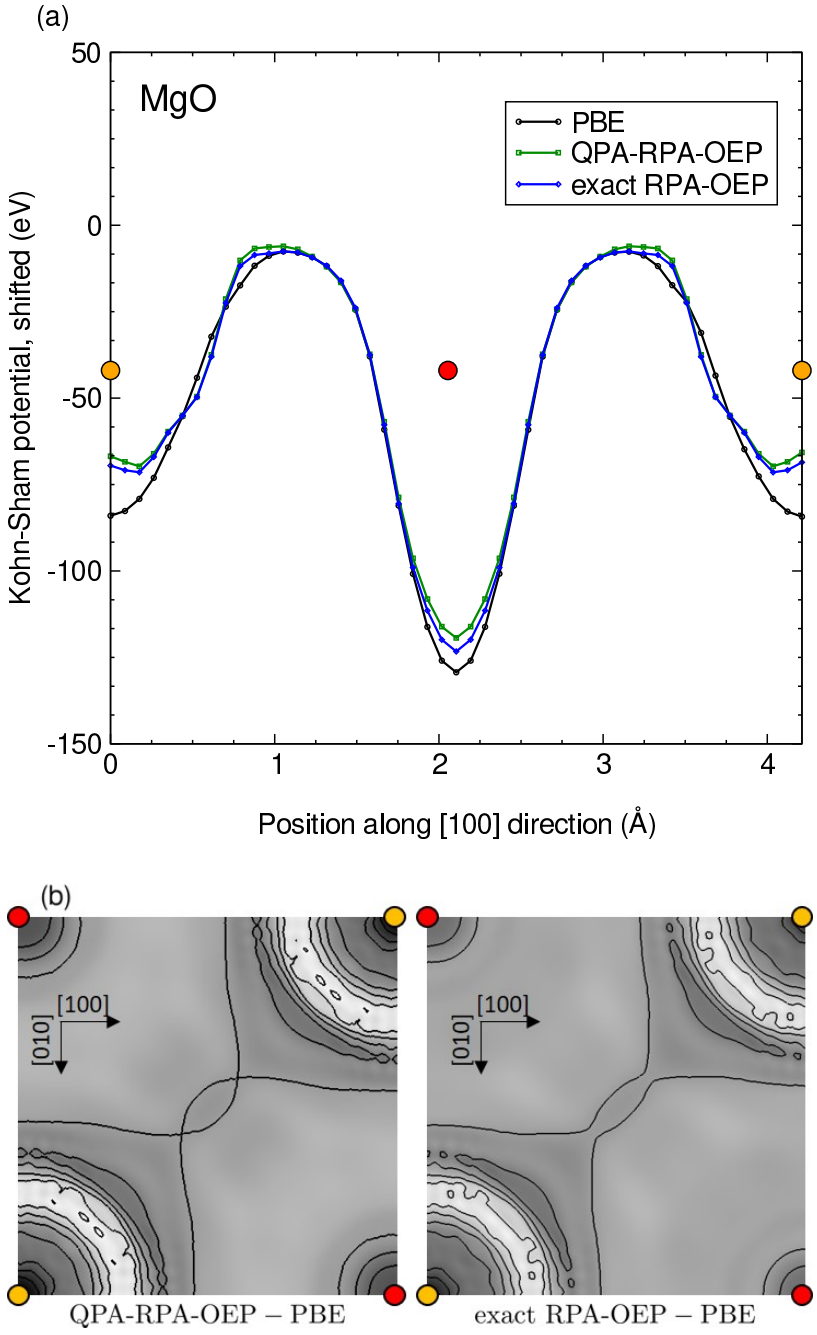

FIGURE 5.8: Comparison of the KS potentials $v_{\mathrm{KS}}(\mathbf{r})$ for MgO. The atom positions are indicated by light (orange) and dark (red) circles for Mg and O, respectively. For easier comparison, OEP potentials have been rigidly shifted to better fit PBE in the interstitial regions ($v_{\mathrm{KS}}^{\mathrm{OEP}}$ is only determined up to a constant). (a) Total KS potentials along the [100] direction. Symbols indicate the finite real space grid, on which v_{KS} is evaluated. (b) Contour plots for the differences $v_{\mathrm{KS}}^{\mathrm{OEP}} - v_{\mathrm{KS}}^{\mathrm{PBE}}$ in the (001) plane. Contour lines are drawn in steps of 3 eV, lighter areas indicate that $v_{\mathrm{KS}}^{\mathrm{OEP}} < v_{\mathrm{KS}}^{\mathrm{PBE}}$. Left: QPA-RPA-OEP, right: exact RPA-OEP. The potential differences have been interpolated between real space grid points using cubic splines.[150]

5.4.4 Dielectric constants from RPA-OEP

TABLE 5.4: Ion-clamped, macroscopic dielectric constants in the independent particle approximation obtained from PBE as well as RPA-OEP with and without the quasiparticle approximation (QPA, exact). The calculations use a $14 \times 14 \times 14$ Γ-centered k-point mesh. Experimental dielectric constants are taken from Ref. [147], unless stated otherwise. Footnotes indicate that experiments were performed at wurtzite crystal structure rather than zinc-blende. Mean relative errors (MRE) and mean absolute relative errors (MARE) are reported as well.

	PBE	RPA		expt.
		QPA	exact	
C	6.0	5.7	5.8	5.7
Si	13.5	12.9	13.1	11.9
SiC	7.2	6.8	7.0	6.5
BN	4.7	4.5	4.6	4.5
AlP	8.8	8.4	8.4	7.5
AlAs	9.9	9.3	9.3	8.2[143]
AlSb	12.2	11.7	11.6	10.2[143]
GaN	6.2	5.6	5.9	5.3[a]
GaP	10.9	10.4	10.6	9.1[143]
InP	11.3	11.0	11.1	10.9[143]
ZnO	5.4	4.2	4.5	3.7[a]
ZnS	6.3	6.0	6.1	5.1
CdS	6.4	6.4	6.4	5.3[a]
MgO	3.2	3.0	3.1	3.0
MRE	16%	9%	11%	
MARE	16%	9%	11%	

[a] wurtzite structure

In this section, we investigate the effect of the QPA on dielectric constants. The potentials from both RPA-OEP methods are used to calculate ion-clamped, macroscopic dielectric constants ϵ_∞,

$$\epsilon_\infty^{-1} = \lim_{\omega \to 0, \mathbf{q} \to 0} \epsilon^{-1}(\mathbf{q}, \mathbf{q}, \omega). \tag{5.29}$$

The dielectric constants are evaluated (i) from the independent particle response function χ_0, (ii) from the RPA response function, compare Eq. (5.9), and (iii) including vertex corrections in the form of local field effects. For the latter, one has to solve the Dyson-like equation

$$\chi = \chi_0 + \chi_0 (V + f_{\mathrm{xc}}) \chi. \tag{5.30}$$

The exchange-correlation kernel $f_{\mathrm{xc}} = \delta v_{\mathrm{xc}} / \delta n$ is approximated by its LDA version, for details of the calculations we refer to Ref. [151]. The results are collected in Tables 5.4-5.6, where the metallic InSb is excluded. For reference, we report also dielectric constants obtained from PBE. Where data for $\epsilon_\infty^{\mathrm{RPA}}$ is available, our dielectric constants from PBE agree well with those of Ref. [152]. Results for $\epsilon_\infty^{\mathrm{RPA}}$ from QPA-RPA-OEP are somewhat larger than those of Ref. [127]. This discrepancy, which is largest for Si (10.9 in Ref. [127] vs. our result of 11.6), can be traced back to better k-point convergence in the present work.

TABLE 5.5: Like Table 5.4, but with dielectric constants in the RPA.

	PBE	RPA		expt.
		QPA	exact	
C	5.5	5.3	5.4	5.7
Si	12.1	11.6	11.7	11.9
SiC	6.6	6.2	6.3	6.5
BN	4.4	4.1	4.2	4.5
AlP	7.6	7.2	7.3	7.5
AlAs	8.6	8.1	8.1	8.2[143]
AlSb	10.7	10.3	10.2	10.2[143]
GaN	5.7	5.2	5.5	5.3[a]
GaP	9.7	9.2	9.4	9.1[143]
InP	10.2	9.8	9.9	10.9[143]
ZnO	5.1	3.9	4.2	3.7[a]
ZnS	5.6	5.3	5.4	5.1
CdS	5.8	5.7	5.7	5.3[a]
MgO	3.0	2.8	2.9	3.0
MRE	5%	0%	0%	
MARE	7%	5%	5%	

[a] wurtzite structure

In the following, we once again comment first on general trends before discussing specific materials and comparing to experiment. Generally, we find that dielectric constants from PBE are the largest, followed by exact RPA-OEP and QPA-RPA-OEP. This is not surprising, as the dielectric constants are roughly inverse proportional to the band gap. Comparing results from the RPA-OEP methods, we find that the effect of the QPA is reduced compared to the band gaps. That is, the relative differences $\Delta\epsilon_\infty/\epsilon_\infty$ are somewhat smaller than the corresponding relative differences for the band gap, $\Delta E_g/E_g$. Similarly, it was reported in Ref. [152] that the discrepancy between different GW-methods is reduced for the dielectric constants. Comparing the different kernels for a given KS potential, we find that the dielectric constants in the independent particle approximation are generally the largest, those in RPA the smallest, and the vertex corrected ones in-between.

Comparing now to experiment, we find that the dielectric constants in the independent particle approximation are generally larger than the experimental ones. If screening in the RPA is taken into account, the dielectric constants from PBE are much reduced, but still larger than experiment. Agreement with experiment is now quite good for both RPA-OEP methods (MARE 5% each, no systematic errors can be discerned). Larger effects of the QPA are observed only for ZnO and GaN (the dielectric constant of MgO is quite small). If the LDA kernel is included, the dielectric constants are on average once again larger than the experimental ones, especially for PBE.

5.5 Discussion

In Sec. 5.4 we have presented results for band gaps and dielectric constants from both PBE and two RPA-OEP methods. In the following, we qualitatively discuss the approximations made and speculate on what exact Kohn-Sham theory would yield.

TABLE 5.6: Like Table 5.4, but with dielectric constants including vertex corrections via the LDA exchange-correlation kernel, see Eq. (5.30).

	PBE	RPA		expt.
		QPA	exact	
C	5.8	5.5	5.7	5.7
Si	12.8	12.3	12.4	11.9
SiC	6.9	6.5	6.7	6.5
BN	4.6	4.3	4.4	4.5
AlP	8.0	7.6	7.7	7.5
AlAs	9.2	8.6	8.6	8.2[143]
AlSb	11.4	10.9	10.8	10.2[143]
GaN	5.9	5.4	5.7	5.3[a]
GaP	10.2	9.7	9.9	9.1[143]
InP	10.7	10.3	10.4	10.9[143]
ZnO	5.3	4.1	4.4	3.7[a]
ZnS	5.8	5.5	5.6	5.1
CdS	6.0	6.0	6.0	5.3[a]
MgO	3.2	2.9	3.0	3.0
MRE	10%	3%	5%	
MARE	11%	5%	6%	

[a] wurtzite structure

Generally, the band gaps give more direct insight, whereas the interpretation of the dielectric constants is more difficult, as one has to disentangle approximations for the KS potential and the exchange-correlation kernel.

5.5.1 Band gaps

We first note that semi-local functionals like PBE have spurious self-interaction that delocalizes the orbitals and thus the exchange-correlation hole. Therefore, the eigenvalues are up-shifted compared to those of the exact KS potential. The effect is stronger for the more localized occupied orbitals, and it follows that the minimal gaps of (semi-)local functionals are generally too small. In fact, one can observe this trend quite consistently in small molecules, where an exact KS potential can be obtained as reference.[29] Unsurprisingly, the gaps are underestimated less by GGA than by LDA, as the self-interaction is even more severe for LDA.

RPA-OEP, on the other hand, differs from the true KS potential by neglecting diagrams corresponding to vertex corrections. The most important vertex corrections are (i) screened exchange diagrams (corrections to Σ_{xc}) and (ii) ladder diagrams (corrections to W). The screened exchange diagrams cancel the self-interaction error inherent to the RPA, thus including them opens the band gap. The ladder diagrams provide additional screening, which closes the band gap.

Previous work has shown that the ladder diagrams, albeit of higher order in the Coulomb interaction, are the most important corrections for ionization energies of both solids[146] and molecules.[153] Moreover, Kutepov[154,155] has found that the band gaps of solids are reduced by the inclusion of vertex corrections in self-consistent *GW* calculations. However, the picture is more complicated here as self-consistency introduces additional diagrams. Generally, one has to be careful in the comparison

of *GW* and OEP,[120] see also Sec. 5.2.3. More direct evidence is given by the results of Hellgren and Barth,[118] who have shown that the RPA-OEP excitation energies of atoms tend to be slightly larger than those of the exact KS potential. In any case, the exact balance of screened exchange diagrams and ladder diagrams is expected to be strongly system dependent, though.[146,153]

Nevertheless, we believe that for the solids considered in the present work *a good estimate for the true KS gap is probably in-between PBE and RPA-OEP*. This is satisfying insofar, as we can conclude that the exact RPA-OEP is thus closer to the true KS potential than QPA-RPA-OEP. We reiterate that also from a physical stand point, the exact RPA-OEP has to be considered the better theory, see Sec. 5.2.3. It is safer to say that for materials where PBE and both RPA-OEP methods are close, e.g. for Si, we can further conclude that all three methods yield decent approximations to the true KS gap. Moreover, we conjecture that the exact KS potential will also predict InSb to be metallic. Naturally, the fact that experiments yield a small, but finite fundamental band gap of 0.2 eV for InSb[143] does not indicate a failure of the KS formalism. Rather, this qualitative discrepancy underlines the importance of the derivative discontinuity, which has to be taken into account to enable comparison with experiment.

Finally, it is intuitively clear that a band inversion will occur alongside a negative band gap, if the derivative discontinuity can be approximated as a "scissors operator",[8] see Fig. 5.9. We have observed that the band inversion for InSb is incipient even in the first step of the self-consistency cycle. That is, the RPA natural orbitals (on-top of LHF) corresponding to the CBM show an occupancy much larger than zero, whereas those corresponding to the VBM are depleted (not shown). This is related to density fluctuations from the occupied Kohn-Sham orbitals into the unoccupied Kohn-Sham states. To achieve the corresponding charge density using a mean field method, the OEP potential needs to bring the conduction band down, eventually below the valence band. It is plausible that the band inversion will prevail even for the exact Kohn-Sham potential, given that these density fluctuations are described well enough by the RPA.

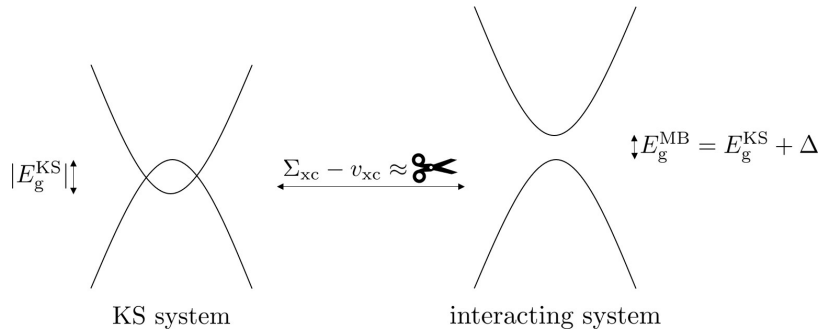

FIGURE 5.9: Comic illustrating the band inversion caused by the derivative discontinuity $\Delta = \langle \Sigma_{xc} - v_{xc} \rangle$. In the "scissors operator" approximation,[8] Δ simply rigidly shifts the conduction bands. If Δ is larger than the fundamental gap E_g^{MB}, the KS band gap E_g^{KS} is negative and a band inversion occurs alongside a metal-semiconductor phase transition.

5.5.2 Dielectric constants

Let us assume for the moment that (i) the KS potential of RPA-OEP is sufficiently accurate and (ii) other effects not included here such as electron-phonon coupling can be neglected. Then, the fact that the dielectric constants in the RPA are closer

to experiment than the ones including local field effects can be entirely attributed to poor performance of the LDA kernel. In fact, it has been shown that the local and static nature of the LDA kernel has some serious physical flaws, see for example Ref. [29]. This would further suggest that a more accurate kernel from MBPT would have to find once more a fine balance between vertex corrections in Σ_{xc} and W to improve upon the RPA. It is in fact gratifying that the dielectric constants in the random-phase approximation calculated using the self-consistent RPA-OEP potential and orbitals agree on average so well with experiment. It indicates that the – in itself closed – RPA-OEP scheme is, considering its simplicity, an astoundingly accurate approximation working well beyond its expectations.

Finally, it is interesting that the QPA-RPA-OEP seems to yield somewhat better agreement with experiment than exact RPA-OEP, if the LDA exchange-correlation kernel is included. The effect of the QPA is strongest for ZnO and GaN, where exact RPA-OEP yields dielectric constants that are too large. Thus, the better agreement with experiment here can be understood as an error cancellation effect, since the band gaps are (incorrectly) larger in the QPA. That is, error cancellation can occur if both dynamical screening and many-body vertex corrections are neglected. A similar phenomenon, the so-called "Z-factor cancellation",[135] has been previously discussed in the context of GW calculations.

5.6 Conclusion

We have obtained optimized effective potentials from the random-phase approximation for a test set of 15 semiconductors and insulators. The main goal of the present work was to study the role of dynamical screening effects in the form of the quasiparticle approximation. We have found that if this approximation is lifted, the band gaps are reduced towards PBE. Likely, this represents an improvement towards the true Kohn-Sham potential, as the RPA-OEP band gaps will be further reduced by the inclusion of ladder diagrams.

As can be understood from a simple flat band model, the effect of the quasiparticle approximation is largest for materials with strong ionic character, where the proper treatment of the off-diagonal self-energy matrix elements is important. Indeed, our calculations have shown that for these materials (here ZnO, GaN and MgO) the differences in the OEP band gaps can amount to several 100 meV. As an interesting side result, we have found that the symmetric prescription [see Eq. (5.12)] for the off-diagonal elements in the quasiparticle approximation is likely not optimal.

We have also used the exchange-correlation potentials from the RPA-OEP methods to calculate macroscopic, ion-clamped dielectric constants. In agreement with the trend for the band gaps, the dielectric constants are generally underestimated by the QPA. The effect is, however, somewhat reduced here. For both RPA-OEP methods, the dielectric constants in the RPA show generally good agreement with experiment, much better than dielectric constants from PBE. Interestingly, we found that the inclusion of vertex corrections in form of local field effects is detrimental for most materials. We have concluded that the exchange-correlation kernel in the LDA is not sophisticated enough, though.

Finally, from a technical point of view, we have demonstrated that the self-consistency cycle that is necessary for OEP can be sped up by pre-converging the exchange-correlation potential on a sparser k-point mesh.

Chapter 6

Machine learning density functionals from the random-phase approximation

Stefan Riemelmoser, Carla Verdi, Merzuk Kaltak, and Georg Kresse

Machine learning density functionals from the random-phase approximation

submitted to: The Journal of Chemical Theory and Computation (03.08.2023)
arxiv: https://doi.org/10.48550/arXiv.2308.00665
data repository: https://doi.org/10.25365/phaidra.418

Author contribution: Conception of the project, analytical derivations, code implementation (together with coworkes), numerical calculations (together with coworkers), first paper draft, paper editing and proofreading (together with coworkers)

Kohn-Sham density functional theory (DFT) is the standard method for first-principles calculations in computational chemistry and materials science. More accurate theories such as the random-phase approximation (RPA) are limited in application due to their large computational cost. Here, we construct a DFT substitute functional for the RPA using supervised and unsupervised machine learning (ML) techniques. Our ML-RPA model can be interpreted as a non-local extension to the standard gradient approximation. We train an ML-RPA functional for diamond surfaces and liquid water and show that ML-RPA can outperform the standard gradient functionals in terms of accuracy. Our work demonstrates how ML-RPA can extend the applicability of the RPA to larger system sizes, time scales and chemical spaces.

6.1 Introduction

For over half a century, generations of researchers have been looking to find ever better approximations for the elusive exchange-correlation (xc) functional of Kohn-Sham density functional theory (DFT).[49,156] The Hohenberg-Kohn theorems guarantee this exchange-correlation functional to be a universal functional of the electronic density n, in other words, there exists a map $n \mapsto E_{\mathrm{xc}}[n]$.[24] However, the exact functional is of complex non-local form and in general unknown. Common approximations for the exchange-correlation energy are built on the principle of nearsightedness:[25] in the local density approximation (LDA),[20] the exchange-correlation energy density is approximated to be locally that of a homogeneous electron gas with the same density.

To improve the accuracy of the approximation, one can add more non-local information by climbing up Jacob's ladder of DFT.[85] Next to the local density, one includes its gradient $|\nabla n|$ as ingredient to the exchange-correlation functional (generalized gradient approximation or GGA). Going beyond the GGA, more non-local information is added in the form of the kinetic energy density (meta-GGA), and fractions of exact exchange (hybrids). However, strictly speaking, most meta-GGA and hybrid functional approaches deviate from "pure" Kohn-Sham DFT, as the ingredients go beyond the electronic density alone.[46] A different route beyond GGA are non-local van der Waals (vdW) functionals,[42,157] which account for pair-wise dispersion interactions between densities $n(\mathbf{r})$ and $n(\mathbf{r}')$. As the ingredients are only the electronic density and its gradient at points $\mathbf{r}$ and $\mathbf{r}'$, the non-local vdW method stays within pure KS-DFT.

Given ingredients $\mathbf{X}$ for the exchange-correlation functional, one still has to find the actual functional form, that is the map $\mathbf{X} \mapsto E_{\mathrm{xc}}[\mathbf{X}]$. In the analytical approach developed by Perdew and others,[36,45,158] those maps are found by satisfying exact constraints. The empirical approach pursued by Becke and others[35,37,43,50] optimizes a small number of adjustable parameters to experimental data or higher level theory. Broadly speaking, the analytical functionals are more universally applicable, whereas the empirical approach can achieve higher accuracy for systems similar to the ones represented in their respective training sets.[156] This comes at the cost of worse performance for systems not represented by these training sets. For example, the widely used B3LYP functional,[44] whose parameters have been optimized for small main group molecules, performs well for main group chemistry but struggles when applied to extended systems[159] and transition metal chemistry.[160]

Recently, machine learning (ML) techniques have been taking the empirical approach to its extreme.[161–164] Not limited by human parametrizations, machine learning approaches can optimize the maps $\mathbf{X} \mapsto E_{\mathrm{xc}}[\mathbf{X}]$ using complicated non-linear functional forms. The first attempt of creating an ML density functional goes back to Tozer *et al.*,[165] an effort which culminated in the development of the HTCH functional (Hamprecht-Tozer-Cohen-Handy, a popular GGA functional).[166] The full potential of ML approaches has been demonstrated in pioneering work by Burke and coworkers, who showed that orbital-free density functionals can be learned from the full non-local density.[167,168] Their approach was later applied to standard Kohn-Sham DFT, enabling molecular dynamics simulations of single molecules with chemical accuracy.[162,169,170] Though this is very impressive, these ML-DFT functionals are tailor-made for this specific purpose and have to be retrained for every new molecule. A different approach was taken by Nagai *et al.*,[161] who complemented meta-GGA ingredients by a non-local density descriptor, achieving remarkable accuracy for a large molecular test set with training data from only three

molecules. For a broader discussion of different ML-DFT approaches, we refer also to the review of Schmidt *et al.*[171]

In the current work, we propose an approach to construct machine learned density functionals from the random-phase approximation (RPA, a high-level functional from the top of Jacob's ladder[85]). We adapt the power spectrum representation of atomic environments used for machine-learned force fields[172,173] (MLFF) to construct ingredients for ML-DFT. We show that these ingredients can be considered to be a non-local extension of GGA. In MLFF, data efficiency can be improved by training not only on energies alone but rather also on atomic forces.[174] Analogously, derivative information in DFT can be supplied via the exchange-correlation potentials,

$$v_{\mathrm{xc}}(\mathbf{r}) = \delta E_{\mathrm{xc}} / \delta n(\mathbf{r}). \tag{6.1}$$

However, obtaining accurate exchange-correlation potentials from beyond GGA functionals is generally difficult, and aside from the early work of Tozer *et al.*, this approach has only been applied to simple model systems.[175–177] Here, we supply such derivative information by using our recent implementation of the optimized effective potential method to obtain exchange-correlation potentials from the RPA.[10] We demonstrate our method by fitting ML-RPA to diamond and liquid water and show that it enables larger scale RPA calculations. ML-RPA achieves its speed-up via bypassing the optimized effective potential equation, substituting the complicated RPA exchange-correlation functional with pure KS-DFT. Further, our efficient plane-wave implementation brings the system size scaling of ML-RPA down to that of standard DFT. Finally, our approach enables self-consistent calculations, force and stress predictions, and even molecular dynamics simulations for molecules, solids and their surfaces. The rest of this paper is organized as follows. Sec. 6.2 introduces the ML-RPA formalism. In Sec. 6.3, we briefly discuss the optimized effective potential method and comment on the issue of electronic self-consistency. Results are presented in Sec. 6.4 and discussed in Sec. 6.5. Conclusion are drawn in Sec. 6.6.

6.2 ML-RPA formalism

6.2.1 Representation of the electronic density

We adapt the power spectrum representation of atomic environments[172] to electronic densities as follows. The electronic density around each real-space grid point $\mathbf{r}$ is expanded into radial basis functions ϕ_{nl} (described in App. F) times real spherical harmonics Y_l^m

$$n(\mathbf{r}+\mathbf{r}')f_{\mathrm{cut}}(r') = \sum_{nlm} c_{nlm}(\mathbf{r})\phi_{nl}(r')Y_l^m(\widehat{\mathbf{r}'}). \tag{6.2}$$

The cutoff function f_{cut} puts emphasis on nearby densities ($r' \leq R_{\mathrm{cut}}$), following Kohn's principle of nearsightedness.[25,178] Here, we use a cutoff radius of $R_{\mathrm{cut}} = 1.5$ Å.

The expansion coefficients c_{n00} are the equivalents of rotationally invariant two-body descriptors used in MLFF, thus we write $X_n^{(2)} = c_{n00}$. In the limit of small cutoffs R_{cut}, the $X_n^{(2)}$ reduce to the local density

$$X_n^{(2)}(\mathbf{r}) \propto n(\mathbf{r}) + \mathcal{O}(R_{\mathrm{cut}}^2) \quad \text{for } R_{\mathrm{cut}} \to 0, \tag{6.3}$$

as shown in App. F. It is interesting that the well-known weighted density approximation[179] can be viewed as the special case where only a single two-body descriptor is taken, compare also the non-local density descriptor introduced by Nagai *et al.*[161]

Further, angular information is accounted for by forming rotationally invariant combinations of the $l = 1$ expansion coefficients to construct additional density descriptors $X_n^{(3)}$, similar to the three-body descriptors in MLFF,

$$X_n^{(3)} = \frac{\sigma^{(3)}}{R_{\text{cut}}} \sqrt{c_{n1x}^2 + c_{n1y}^2 + c_{n1z}^2}. \tag{6.4}$$

Here, $\sigma^{(3)}$ is an ML hyperparameter that weighs the $X_n^{(3)}$ relative to the $X_n^{(2)}$.[180] For small cutoffs, the $X_n^{(3)}$ reduce to the local gradient

$$X_n^{(3)}(\mathbf{r}) \propto |\boldsymbol{\nabla} n(\mathbf{r})| + \mathcal{O}(R_{\text{cut}}^2) \quad \text{for } R_{\text{cut}} \to 0, \tag{6.5}$$

as demonstrated in App. F. In summary, an exchange-correlation functional with $X_n^{(2)}$ and $X_n^{(3)}$ as its ingredients can be considered as a *non-local extension of the generalized gradient approximation*. Here, we use 4 radial basis functions, thus in total we have $4 + 4 = 8$ density descriptors. A representation based on non-local convolutions of the electronic density has been previously suggested by Lei and Medford,[181] who also showed how the representation can be systematically completed by adding higher body-order descriptors. Likewise, representations of atomic environments for MLFF can be completed via moment tensor potentials[182] or the atomic cluster expansion.[183] Next to density convolutions proposed by Lei and Medford,[181] descriptors similar to ours have been used also in several other recent works, see Refs. [184–187]. A key distinction is that some of these works use density fitting to construct descriptors for the electronic density. As pointed out by Chen *et al.*,[188] the explicit dependence on chemical species makes those ML-DFT functionals less universal.

6.2.2 Machine learning scheme

The exchange-correlation energy for any GGA functional can be written as

$$E_{\text{xc}}^{\text{GGA}} = \int \mathrm{d}\mathbf{r}\, n(\mathbf{r}) \varepsilon_{\text{x,HEG}}[n(\mathbf{r})] F_{\text{xc}}[n(\mathbf{r}), |\boldsymbol{\nabla} n(\mathbf{r})|], \tag{6.6}$$

where $\varepsilon_{\text{x,HEG}}$ is the exchange energy density for the homogeneous electron gas of uniform density n, and F_{xc} is the enhancement factor. We use the same form as an ansatz for our ML-RPA model,

$$E_{\text{xc}}^{\text{ML-RPA}} = \int \mathrm{d}\mathbf{r}\, n(\mathbf{r}) \varepsilon_{\text{x,HEG}}[n(\mathbf{r})] F_{\text{xc}}^{\text{ML-RPA}}[\mathbf{X}(\mathbf{r})], \tag{6.7}$$

where $\mathbf{X}$ is a supervector containing the two- and three-body descriptors. The map $\mathbf{X}(\mathbf{r}) \mapsto F_{\text{xc}}^{\text{ML-RPA}}(\mathbf{r})$ is found by kernel regression using a Gaussian kernel,

$$F_{\text{xc}}^{\text{ML-RPA}}[\mathbf{X}(\mathbf{r})] = \sum_{i_B} w_{i_B} \exp\left\{ -\frac{[\mathbf{X}(\mathbf{r}) - \mathbf{X}^{i_B}]^2}{2\sigma^2} \right\}. \tag{6.8}$$

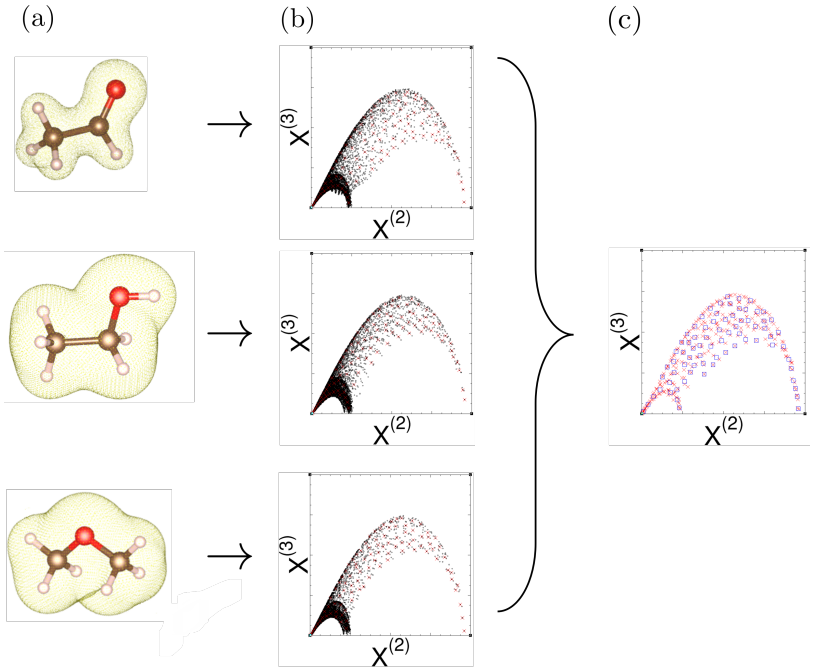

FIGURE 6.1: Data sparsification scheme for a training set consisting of three molecules, depicted in column (a). First, using the electronic density as input, we calculate the two-body descriptors $X_n^{(2)}(\mathbf{r})$ and three-body descriptors $X_n^{(3)}(\mathbf{r})$ at each real-space grid point [black dots in column (b)]. A single radial basis function is used here for visualization purposes. Next, a metric is introduced via the Gaussian kernel and representative density environments (red crosses) are chosen via k-means clustering for each training structure separately. The chosen points are concatenated and a second k-means layer selects the kernel control points $\mathbf{X}^{i_B}$ used in Eq. (6.8) [blue squares in column (c)]. For more details, see App. H.

Here, the kernel width σ is an ML hyperparameter, and the $\mathbf{X}^{i_B}$ are representative kernel control points chosen from the training data. The corresponding weights w_{i_B} are found by solving a linear regression problem. That is, the ML-RPA exchange-correlation energies and ML-RPA exchange-correlation potentials have to agree with exact RPA reference data in a least square sense. The ML-RPA exchange-correlation potentials are obtained by inserting the ansatz (6.7) into Eq. (6.1) and applying the chain rule, see App. G.

The exchange-correlation potentials provide derivative information for the ML fit as atomic forces do in MLFF, thus improving data efficiency. That is, instead of a single data point per structure for $E_{\mathrm{xc}}^{\mathrm{RPA}}$, we have additional data for $v_{\mathrm{xc}}^{\mathrm{RPA}}(\mathbf{r})$ on typically $\mathcal{O}(10^5) - \mathcal{O}(10^6)$ grid points $\mathbf{r}$. As this large amount of data cannot be handled by kernel methods, we have to employ data sparsification tools. Without loss of accuracy, the training data can be compressed dramatically by combining k-means clustering[189] with the metric induced by the Gaussian kernels (see App. H). This is illustrated in Fig. 6.1 using a single radial basis function, such that the descriptors can be easily visualized in 2D. Once training is complete, the computational cost of evaluating ML-RPA depends linearly on the number of kernel control points used. Further, efficient evaluation of the ML-RPA functional is achieved by extensive use of fast Fourier transforms. We find that ML-RPA is slower than standard GGA functionals by some prefactor for typical applications, but ML-RPA scales as $\mathcal{O}(N \log N)$ with system size N like GGA does.[190] In comparison, non-local vdW functionals can have the same system size scaling and similar computational cost as ML-RPA,[191] whereas exact RPA is several orders of magnitude slower and has at least $\mathcal{O}(N^3)$

scaling.[1,3]

6.3 Methods

6.3.1 Random-phase approximation

As the RPA includes information from unoccupied orbitals as ingredients, it sits on the fifth (highest) rung of Jacob's ladder. In the last two decades, the RPA has been successfully employed for a multitude of problems, see Refs. [52] and [55] for reviews. In particular, the RPA is considered a "gold standard" for first-principles surface studies[68,69,192] due to its seamless inclusion of vdW interactions next to the good description of covalent and metallic bonds. Combining exact exchange and a good description of dispersion interactions makes the RPA also suitable for water and ice.[62,64] The usual expression for the RPA exchange-correlation energy reads[57]

$$E_{\mathrm{xc}}^{\mathrm{RPA}} = \mathrm{Tr}[\ln(1 - \chi_0 V)], \tag{6.9}$$

where χ_0 is the Kohn-Sham response function, V is the Coulomb kernel, and we have used a symbolic notation for sake of brevity. As in standard Kohn-Sham DFT, one can obtain the exchange-correlation potential corresponding to the RPA exchange-correlation energy by taking the functional derivative with respect to the electronic density,

$$v_{\mathrm{xc}}^{\mathrm{RPA}}(\mathbf{r}) = \delta E_{\mathrm{xc}}^{\mathrm{RPA}} / \delta n(\mathbf{r}). \tag{6.10}$$

Plugging in Eq. (6.9) and using the chain rule, one can derive the so-called optimized effective potential (OEP) equation,[6,113,131,132] symbolically

$$\chi_0 v_{\mathrm{xc}} = G_0 \Sigma_{\mathrm{xc}}^{G_0 W_0} G_0, \tag{6.11}$$

where G_0 is the non-interacting (Kohn-Sham) Greens-function and $\Sigma_{\mathrm{xc}}^{G_0 W_0}$ is the self-energy in the $G_0 W_0$ approximation. For more details on the implementations of the RPA exchange-correlation energies and the RPA-OEP method, we refer to Refs. [1] and [10], respectively.

6.3.2 Electronic self-consistency

Even tough the RPA-OEP method allows in principle to perform RPA calculations self-consistently,[10] this procedure is seldom carried out due to the large computational overhead. A more common approach is to evaluate the RPA using orbitals from a semi-local DFT base functional ("RPA on-top of DFT", RPA@DFT).[65] Here, we calculate all RPA reference data using PBE as base functional (Perdew-Burke-Ernzerhof, a popular GGA functional[36]). That is, *RPA@PBE is the ground truth for ML-RPA*, and we denote this ground truth in the following as "exact RPA". Unless stated otherwise, all RPA calculations and ML-RPA calculations are thus performed non-self-consistently on-top of PBE orbitals. A ML substitute functional that reproduces only RPA@PBE would already be very useful, we reiterate that RPA@PBE is standard practice.

For the calculation of atomic forces, however, it is convenient to perform self-consistent calculations to avoid tedious non-Hellmann-Feynman terms. Wherever exact RPA reference forces are required, for instance for phonon calculations, we calculate such non-Hellmann-Feynman terms explicitly.[5] In contrast, ML-RPA can be simply run self-consistently like any semi-local density functional since the

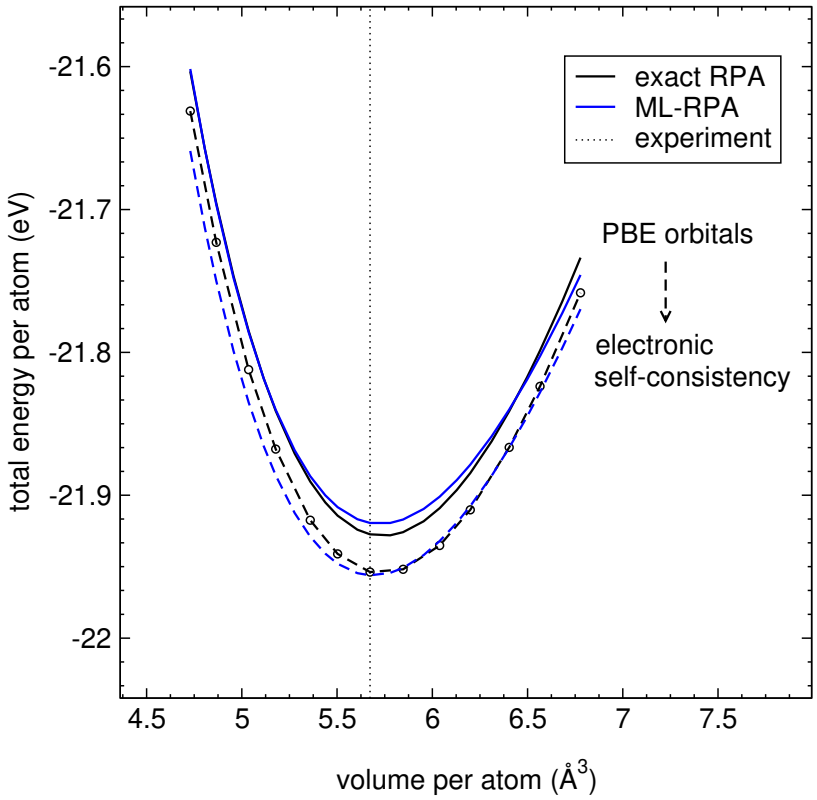

FIGURE 6.2: Energy-volume curves of bulk diamond obtained using exact RPA and ML-RPA. Full lines indicate calculations on-top of PBE orbitals, and dashed lines indicate self-consistent calculations. Self-consistent RPA reference energies are obtained using the RPA-OEP method. The dotted vertical line indicates the experimental equilibrium volume.[193]

exchange-correlation potential is readily available. As a validation, we used the computationally demanding RPA-OEP method to calculate the equilibrium volume of bulk diamond self-consistently. Fig. 6.2 shows that ML-RPA reproduces the RPA@PBE ground truth well (solid lines). Further, ML-RPA correctly predicts a small downward shift due to electronic self-consistency (dashed lines).

We would like to emphasize that this result is not obvious, as the training set covers only PBE densities. To this point, Snyder *et al.*[167] have reported early on that electronic self-consistency can grossly deteriorate the performance of ML-DFT functionals, as self-consistency leads the functional away from its training manifold. Likewise, we observed that earlier versions of ML-RPA became inaccurate when applied self-consistently. However, we find that the current ML-RPA is very stable and reliably converges to a tight energy threshold of 10^{-8} eV. Key hyperparameters in this regard are the cutoff radius ($R_{\text{cut}} = 1.5$ Å) and the Tikhonov regularization parameter ($t_{\text{SVD}} = 1.0 \times 10^{-9}$, see App. G). Even atomic densities can be used as starting points, tough preconverging with PBE typically speeds up the ML-RPA self-consistency cycle. Lastly, the ML-RPA stress tensor has also been implemented via finite differences, which is useful for example for volume relaxations and the training of machine learned force fields (see App. J).

6.3.3 Computational details

We use the PAW code `VASP` (Vienna *Ab Initio* Simulation Package),[104] adopting the C_GW, H_GW and O_GW pseudo-potentials. All DFT and RPA calculations are

performed spin-non-polarized. An energy cutoff of 600 eV is used for the plane-wave orbital basis set (`ENCUT` in VASP). For RPA calculations, a reduced cutoff of 400 eV is used to expand the response function χ_0 (`ENCUTGW` in `VASP`), using a cosine window to smoothen the cutoff of the Coulomb kernel.[9,65] Basis set incompleteness errors are discussed in App. I. The one-center PAW contributions to the RPA exchange-correlation energy are treated on the level of Hartree-Fock, consistently for RPA and ML-RPA calculations. The good agreement of *total energies* in Fig. 6.2, rather than relative energies only, demonstrates the consistency of the ML-RPA implementation. Similar agreement is observed for all materials, with fit errors around 1 meV/electron.

6.4 Results

6.4.1 Bulk diamond

We apply our ML scheme to create an RPA substitute functional for diamond and liquid water. Following a common MLFF practice,[178] bulk diamond training data are iteratively added from molecular dynamics (MD) simulations, using prior versions of the ML-RPA functional to create the MD trajectories. We pick 20 MD snapshots from the 8 atom supercell and 20 snapshots from the 16 atom supercell. The full ML-RPA training set is further detailed in App. I. The equilibrium lattice constant obtained by ML-RPA (3.582 Å) agrees well with the exact RPA value (3.581 Å).
Next, we calculate phonon dispersions using the finite displacement method.[194,195] Converged results are obtained in the large supercell limit, which is hard to achieve with exact RPA due to its unfavorable scaling behavior. Fig. 6.3 compares the ML-RPA phonon dispersions for different supercell sizes to exact RPA results. For contrast, phonon dispersions obtained using PBE are shown as well. For the 16 atom supercell [panel (a)], where training data are available, the ML-RPA phonon dispersion is generally in good agreement with exact RPA, though high-frequency modes are slightly underestimated. Exact RPA calculations for the larger 128 atom supercells validates the extrapolation ability of ML-RPA, as no training data are included for this supercell size. A prominent finite size effect is the closing of the gap near the K-point with respect to the smaller 16 atom cell. Further, the overbending of the LO modes reduces with increasing supercell size, which is most notable along Δ (Γ-X). These characteristic features are well reproduced with ML-RPA. The phonon dispersions obtained using exact RPA are overall in good agreement with experimental data,[193,196] whereas ML-RPA and PBE slightly underestimate the high-frequency modes.

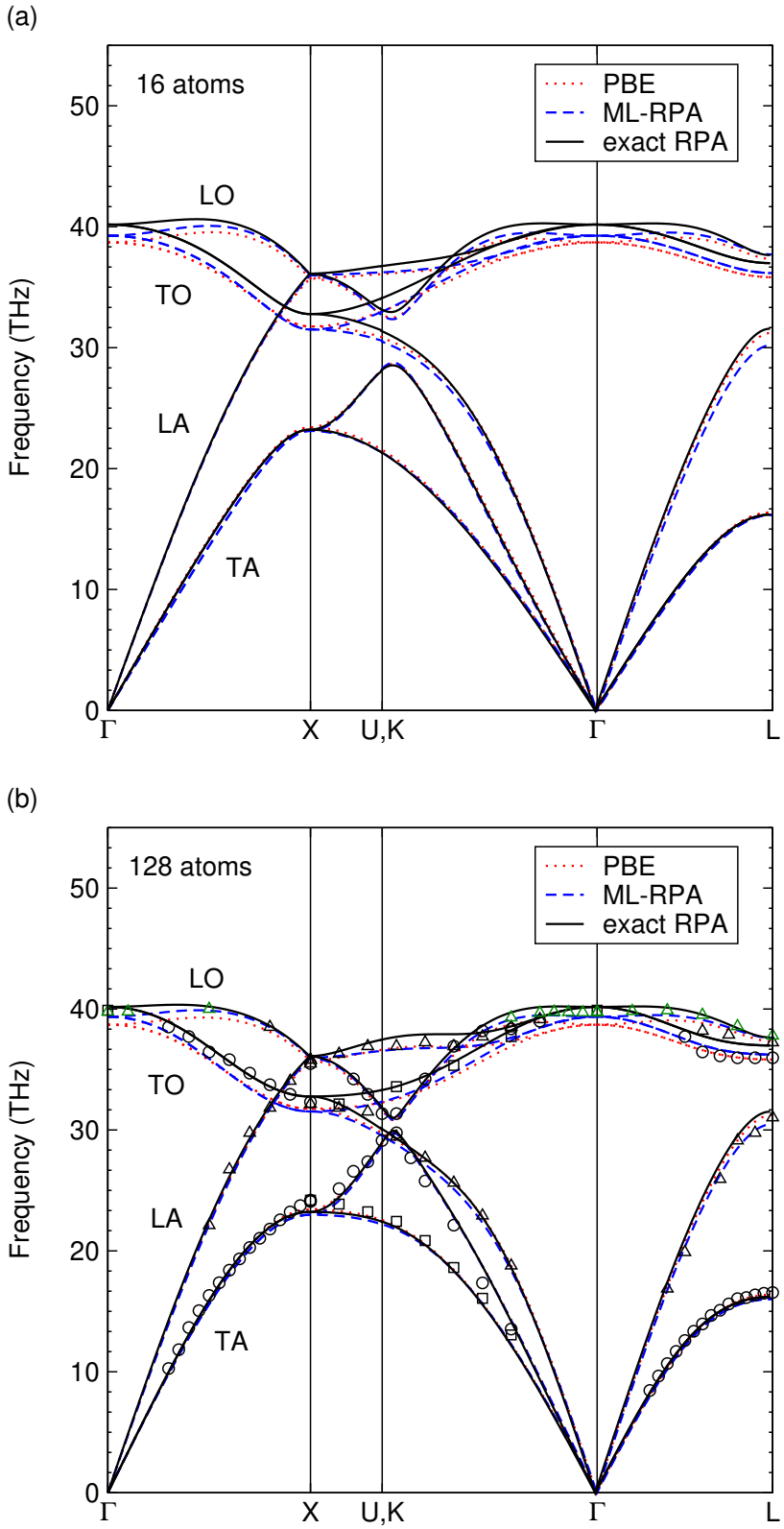

FIGURE 6.3: Phonon dispersion of diamond, calculated at the respective equilibrium lattice constants, using supercells containing (a) 16 atoms, (b) 128 atoms. Phonons obtained using exact RPA are represented as solid black lines, blue dashed lines represent ML-RPA. PBE calculations are also shown for comparison (red dotted lines). ML-RPA has training data only for the smaller supercell size [16 atoms, panel (a)]. Black and green symbols indicate experimental data from Refs. [193] and [196], respectively.

6.4.2 Diamond surfaces

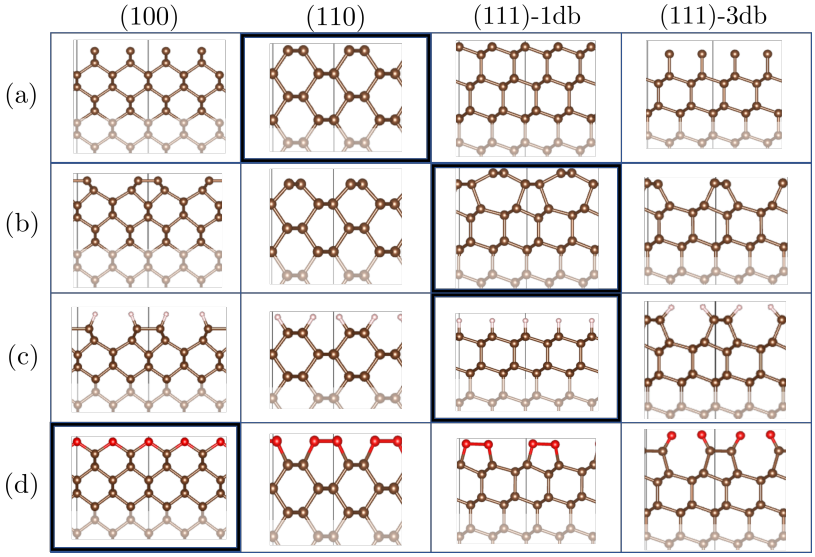

FIGURE 6.4: Side view of crystallographic diamond surfaces.[150] The 2×1 simulation cells are indicated by black vertical lines, and bulk regions are indicated by faded atoms. From top to bottom: (a) clean surfaces, (b) reconstructed surfaces, (c) hydrogenated surfaces (1 ML), (d) oxygenated surfaces (1 ML). Bold edges indicate the most stable orientation for a given surface termination as predicted by exact RPA. Whereas the (111)-1db surface dereconstructs upon the chemisorption of hydrogen and oxygen,[197] the (100) surface dereconstructs only upon the chemisorption of oxygen.[198] The (111)-3db surface retains the 2×1 geometry throughout,[199] and the (110) surface shows no 2×1 reconstruction at all.[200]

The advent of chemical vapor deposition (CVD) has encouraged detailed first-principles simulations of diamond surfaces. Specifically, the characterization of ideal crystallographic surfaces has proven useful for the theoretical understanding of CVD grown diamond.[201] When a diamond surface is cut, the outer surface layers can rearrange to partially eliminate the exposed dangling bonds, see Fig. 6.4. These reconstructions significantly change the properties of the surfaces. Further, important material properties such as electron affinity can be modified via chemisorption processes in a controlled fashion, the most important surface adsorbates being H and O.

The (100) surface is the most relevant crystallographic surface and has been thoroughly studied.[198,202] While the (111) surface has also received a lot of attention,[197,203] most studies neglect that there are two possible ways to cut this surface.[199,204] Namely, via the so-called glide and shuffle planes, one can expose (111) diamond surfaces with one dangling bond (1db) or three dangling bonds (3db) per surface atom, respectively. Even though the clean 1db surface is clearly more stable, 3db surfaces naturally occur in growth and etching processes. Finally, the (110) surface, which is difficult to prepare experimentally, has only recently been fully characterized.[205]

In the following, we calculate diamond surface energies of formation via

$$E_{\text{surf}} = (E - N_{\text{dia}} E_{\text{dia}} - N_{\text{H}} E_{\text{H}_2}/2 - N_{\text{O}} E_{\text{O}})/N_{\text{surf}}, \tag{6.12}$$

where E is the total energy of the surface, E_{dia} is the energy per atom of bulk diamond, E_{H_2} is the energy of the H_2 molecule, and E_{O} is calculated using the water

monomer as reference

$$E_O = E_{H_2O} - E_{H_2}. \tag{6.13}$$

Vibrational contributions to the formation energies due to zero-point motion are neglected. Diamond surface calculations are performed in 2×1 supercells using symmetric slabs. We use 18 surface layers for the (111)-1db surface and 16 layers for the rest. This assures convergence of the surface formation energies to better than 10 meV accuracy.[200,203] The surface geometries were obtained using the PBE functional, further details are given in App. I.

RPA formation energies of diamond surfaces are collected in Table 6.1. (100) and (111)-1db surfaces were included in training, whereas (110) and (111)-3db surfaces are left as independent tests for ML-RPA. For all surface terminations studied, ML-RPA correctly predicts the most stable surface orientation (underlined values). For example, of the clean surfaces (as cut), both RPA and ML-RPA predict the order (110) $<$ (111)-1db $<$ (100) $<$ (111)-3db, which can be qualitatively understood via coordination of the surface atoms.[203] Note that the (111)-3db surface becomes increasingly competitive with the (111)-1db surface as more dangling bonds are eliminated via reconstruction (-1 db) and chemisorption (-2 db for H, -3 db for O).

Including calculations of metastable surfaces (see App. I), we have assembled a database of 28 RPA surface formation energies in total. It is interesting to use these data as benchmark for other exchange-correlation functionals. Table 6.2 shows that all functionals including ML-RPA tend to predict smaller formation energies than exact RPA (negative mean relative errors). In terms of accuracy, ML-RPA performs very well, with a mean absolute error of 70 meV per surface atom. Surface energies predicted by the meta-GGA functional SCAN as well as the vdW functionals PBE+TS and SCAN+rVV10 are also in very good agreement with exact RPA, with mean absolute errors slightly larger than ML-RPA. Finally, we comment again on the stability of electronic self-consistancy. Going from ML-RPA@PBE to self-consistent ML-RPA, individual surface energies change by 60 meV per surface atom or less, and the mean absolute error of self-consistent ML-RPA (compared to exact RPA@PBE) is only 80 meV per surface atom. Thus, the accuracy of ML-RPA is not significantly diminished by electronic self-consistency.

TABLE 6.1: RPA energies of formation for diamond surfaces, calculated via Eq. (6.12) (in eV per surface atom). The most stable surface orientation for a given surface termination is underlined, and surfaces included in the ML-RPA training set are marked by asterisks. Surface calculations are performed in 2×1 supercells, with geometries illustrated in Fig. 6.4.

	(100)*		(110)		(111)-1db*		(111)-3db	
	exact	ML	exact	ML	exact	ML	exact	ML
clean	3.66	3.57	<u>2.09</u>	<u>1.95</u>	2.69	2.52	4.37	4.37
reconstructed	2.08	2.03	1.70	1.59	<u>1.41</u>	<u>1.34</u>	2.70	2.56
+H (1 ML)	0.20	0.11	-0.11	-0.12	<u>-0.19</u>	<u>-0.24</u>	0.17	0.11
+O (1 ML)	<u>1.99</u>	<u>1.91</u>	3.23	3.21	2.99	2.94	2.90	2.79

*included in the ML-RPA training set

TABLE 6.2: Surface formation energies from different exchange-correlation functionals compared to values from exact RPA. Mean signed error (MSE), mean absolute error (MAE) and maximum absolute error (MAX) are given in eV per surface atom. Averages are over 28 diamond surfaces of which 16 are in the ML-RPA training set, see Supplementary Section I.

	MSE	MAE	MAX
LDA	-0.06	0.14	0.34
PBEsol	-0.10	0.12	0.33
PBE	-0.19	0.19	0.39
RPBE	-0.23	0.24	0.44
PBE+TS	-0.01	0.08	0.25
RPBE+D3(BJ)	-0.09	0.12	0.48
optB88-vdW	-0.19	0.19	0.62
rev-vdW-DF2	-0.13	0.14	0.52
rVV10	-0.18	0.18	0.57
SCAN	-0.08	0.11	0.25
SCAN+rVV10	-0.03	0.10	0.24
ML-RPA	-0.07	0.07	0.18

6.4.3 Liquid water

Water with its many anomalies is both an important and challenging system for first-principles molecular dynamics simulations.[206] The role of the exchange-correlation functional for the description of liquid water and ice has been studied extensively.[62,63,207,208] This has made water an interesting target for several recent MLFF[64,209,210] and ML-DFT[163,185] approaches.
In particular, Yao and Kanai[64] used MLFF to perform RPA-level calculations for liquid water with the inclusion of nuclear quantum effects. They showed that the RPA can well reproduce experimental data for numerous water properties at different temperatures. Due to the small mass of the hydrogen atom, the oxygen-hydrogen radial distribution function (RDF) and especially the hydrogen-hydrogen RDF are significantly altered by nuclear quantum effects. Namely, classical MD predicts an oxygen-hydrogen RDF that is overstructured compared to experimental data, and even more so for the hydrogen-hydrogen RDF. In contrast, the oxygen-oxygen RDF is far less affected, especially for higher temperatures.

To perform calculations on liquid water, we add 32 liquid water structures containing 8 water molecules to the ML-RPA training set, as well as 39 structures using larger supercells (31 or 32 water molecules). The structures are again sampled from MD trajectories created by earlier ML-RPA versions. In addition, the ML-RPA training set contains 6 structures sampling the water monomer.

Accurate determination of the water RDFs require long MD simulations that are computationally expensive even without nuclear quantum corrections. Thus, we perform classical MDs using 64 water molecules and speed them up by combining ML-RPA with MLFF. That is, we train a machine learning force field "on-the-fly"[173,211] using the energies and forces predicted by ML-RPA. In order to obtain an RPA reference for the radial distribution function, we also train an MLFF directly on exact RPA energies and forces (RPA-MLFF). The RPA-MLFF training set contains all water structures from the ML-RPA training set plus 30 additional structures containing 32 molecules. To validate our machine learning force fields, we also trained

on-the-fly MLFFs for the vdW functionals RPBE+D3(BJ)[39,40] and PBE+TS.[38] Further details of the MLFF setups are given in App. J.

Fig 6.5 shows the oxygen-oxygen RDF, g_{OO}, and oxygen-hydrogen RDF, g_{OH}, at ambient conditions. First, we note that the RDFs obtained from PBE+TS and RPBE+D3(BJ) are in good agreement with respective literature results[214,215] (for PBE+TS, we compared the RDF at T = 330 K, not shown). The PBE+TS RDF is clearly overstructured compared to experimental data. The water structure is "too tetragonal", even more so when the TS vdW correction is not included, see Ref. [214]. The RPBE+D3(BJ) RDF is in better agreement with experiment, but is still somewhat overstructured. This is a specific effect of the Becke-Johnson (BJ) damping, that is. the RPBE+D3(0) RDF (using zero damping) is closer to experiment (see Ref. [215]). Next, the RDFs predicted by RPA-MLFF are less structured than the RPA references of Yao and Kanai, compare the first peaks and minima of both g_{OO} and g_{OH}. This discrepancy is possibly due to technical convergence of either RPA calculation, in particular, basis set incompleteness errors. The fact that RPA-MLFF closely reproduces the first experimental peak height of g_{OO} is arguably accidental, since nuclear quantum effects are not included. For g_{OH}, however, the result of Yao and Kanai is still more structured than experiment even with nuclear quantum effects included (see Fig. 1 in Ref. [64]), indicating that our RPA reference is potentially more accurate.

That said, overall both RPA reference results agree well with experimental data. Turning to the water structure predicted by ML-RPA, there are some clear discrepancies from both RPA references. The first peak of g_{OO} is smaller in height, and the second peak is completely missing. The g_{OH} predicted by ML-RPA is also somewhat less structured than the RPA references, but the overall agreement is better than for g_{OO}. Importantly, the discrepancies are mainly due to the actual ML-RPA density functional, since the on-the-fly MLFF is very accurate (see App. J). Specifically, atomic forces for all MLFFs trained here exhibit an root mean square error of roughly 30 meV Å^{-1}, whereas the respective force errors for liquid water due to ML-RPA are roughly 90 meV Å^{-1}. It is also important to point out that the RPA-MLFF is a single-purpose force field, trained specifically to simulate liquid water in the bulk (and the water monomer). In contrast, the ML-RPA functional is not limited in this way as will be demonstrated in the following section.

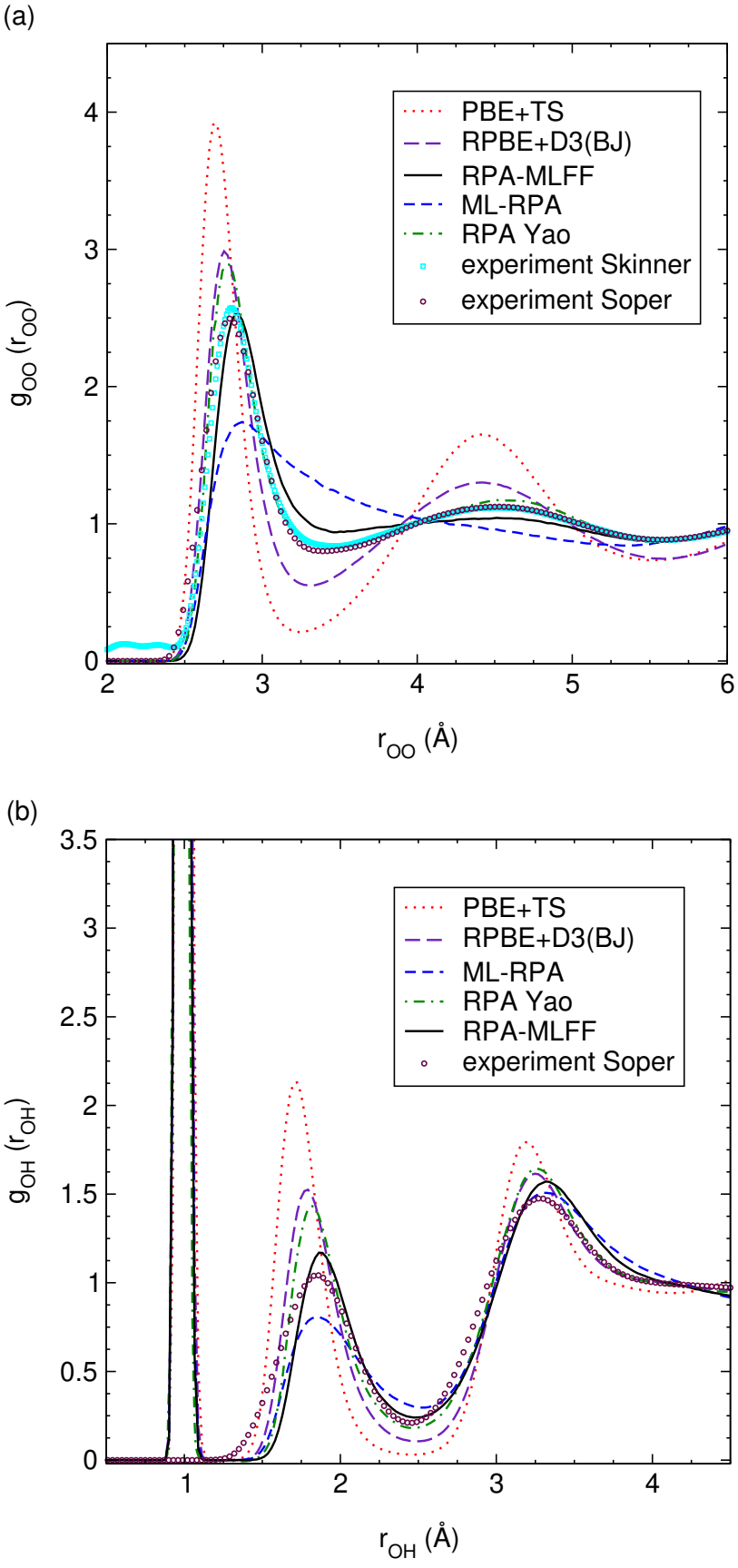

FIGURE 6.5: Partial radial distribution functions of liquid water at ambient conditions (T = 300 K, $\rho = 1$ g/cm^3), details of the MD simulations are given in App. J. (a) oxygen-oxygen radial distribution function, (b) oxygen-hydrogen radial distribution function. RPA results from Yao and Kanai are extracted from Ref. [64], experimental data are taken from Refs. [212, 213]. See text for a discussion of nuclear quantum effects.

6.4.4 Smaller water clusters

TABLE 6.3: Ground state properties of the H_2O dimer. Dimer binding energies, $E_b^{dim} = -E[(H_2O)_2] + 2E[H_2O]$, are given in eV. Equilibrium bond lengths d_{OO}^{dim} and d_{OH}^{dim} are given in Å. All calculations are performed fully self-consistently.

	E_b^{dim}	d_{OO}^{dim}	d_{OH}^{dim}
LDA	0.39	2.72	1.73
PBEsol	0.27	2.80	1.82
PBE	0.23	2.88	1.91
RPBE	0.17	3.02	2.04
PBE+TS	0.24	2.89	1.92
RPBE+D3(BJ)	0.21	2.94	1.97
optB88-vdW	0.22	2.90	1.93
rev-vdW-DF2	0.23	2.89	1.92
rVV10	0.25	2.88	1.90
SCAN	0.25	2.84	1.88
SCAN+rVV10	0.26	2.84	1.88
ML-RPA	0.18	3.07	2.10
RPA-MLFF	0.21	3.28	2.30
CCSD(T)[216]	0.22	2.91	1.96

An important H_2O benchmark is the performance for smaller water clusters.[207] Already the simple H_2O dimer gives a predictive measure of the strength of a hydrogen bond in liquid water. Table 6.3 shows that ML-RPA predicts a somewhat underbound dimer, consistent with the understructured liquid. Going to larger clusters, the water hexamers present a difficult challenge for DFT, as three-dimensional structures ("prism","cage","bag") compete energetically with two-dimensional ones ("book","chair","boat"). Fig. 6.6 shows that ML-RPA erroneously predicts two-dimensional structures to be most stable, as do all GGA functionals (see also App. K). LDA and the SCAN meta-GGA functional perform well in this regard, but overbind the dimer, compare Table 6.3. All vdW functionals tested give excellent results for both the dimer as well as the hexamers. This confirms the critical role that vdW interactions play for the structure of water.[207,209] Further, RPA-MLFF clearly fails for water clusters, but we reiterate that it has been trained only for liquid water in the bulk. The fact that RPA-MLFF extrapolates is substantiated by large Bayesian error predictions: compared to typical bulk water configurations, the maximum force Bayesian error is three times as large for the hexamers and five times as large for the dimer.

Finally, we investigated cubic ice, specifically, the I_c(a) proton-ordered ice phase as described in Ref. [62]. The equilibrium volume predicted by RPA-MLFF is 32.3 Å^3 per H_2O, in good agreement with the 32.6 Å^3 per H_2O obtained using exact RPA. The ML-RPA equilibrium volume is somewhat smaller (31.2 Å^3 per H_2O). For comparison, the equilibrium volumes predicted by PBE and PBE+TS are 30.2 Å^3 per H_2O and 30.0 Å^3 per H_2O, respectively. In summation, ML-RPA provides a consistent but somewhat inaccurate description of water and ice. The fact that ML-RPA misses the second g_{OO} maximum, underbinds the water dimer, and provides a PBE-like description of the water hexamers and cubic ice strongly

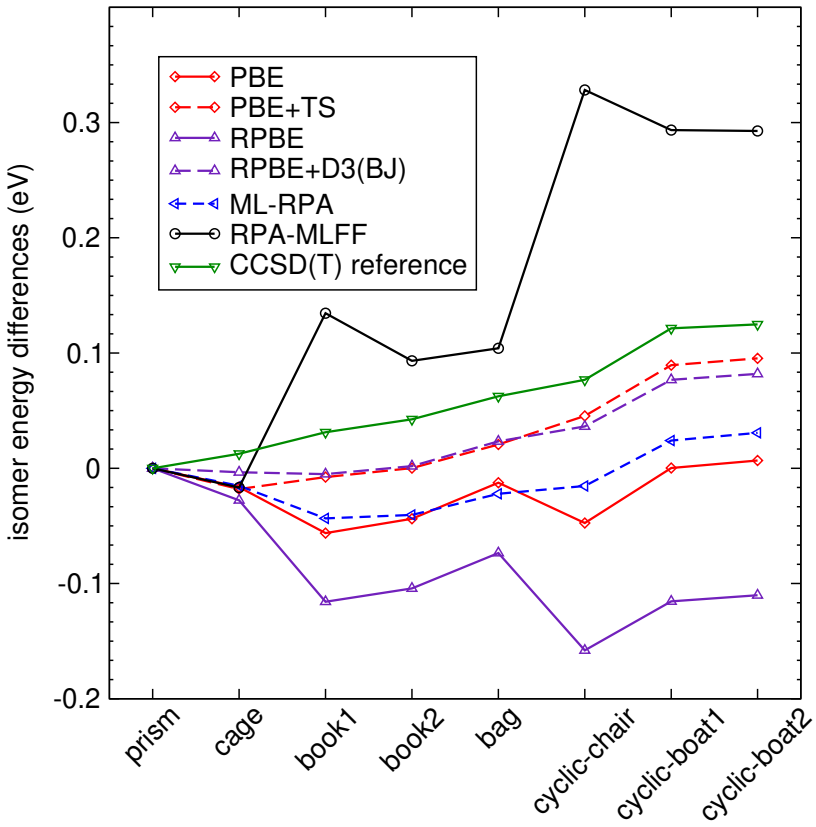

FIGURE 6.6: Binding energy differences of eight H_2O hexamers. Geometries and CCSD(T) reference data are taken from Ref. [217]. The vdW functionals PS+TS and RPBE+D3(BJ) largely correct the errors of their respective GGA base functionals, see also App. K. Lines drawn are only guides to the eye.

indicates that the current ML-RPA misses some crucial non-local interactions. This is likely connected to the rather small cutoff radius used here for ML-RPA ($R_{\text{cut}} = 1.5$ Å). However, increasing the cutoff is not beneficial for the current ML-RPA, our tests indicate that this diminishes ML-RPA accuracy (not shown).

6.4.5 Homogeneous electron gas

To challenge the extrapolation abilities of our ML-RPA functional, we apply it to the homogeneous electron gas (HEG). The HEG constitutes an "appropriate norm", that is an important theoretical limit that density functionals should fulfill. Due to symmetry, the HEG is completely characterized by the electron density n, or equivalently the Wigner-Seitz radius $r_s = (3/4\pi n)^{1/3}$. Starting with LDA, many successful exchange-correlation functionals are designed such that they describe the HEG exactly, but this is not the case for the present ML-RPA functional. It is important to point out that the ground truth here is the exchange-correlation energy per electron as given by exact RPA. As the RPA is itself an approximation, $\varepsilon_{\text{xc,HEG}}^{\text{RPA}}$ differs from the usual LDA which is based on exact numerical data from Quantum Monte Carlo calculations.[23] Figure 6.7 shows that ML-RPA for intermediate densities ($r_s \sim 2-5$) closely follows the exact RPA reference. Since this is the range of physical densities, ML-RPA seems to have learned the HEG indirectly from diamond and water data. Still, this excellent agreement comes somewhat surprising considering that no HEG data were explicitly added to the ML-RPA training set. Furthermore, for small densities ($r_s \gtrsim 5$), ML-RPA is slightly less accurate but still well behaved. Finally, for

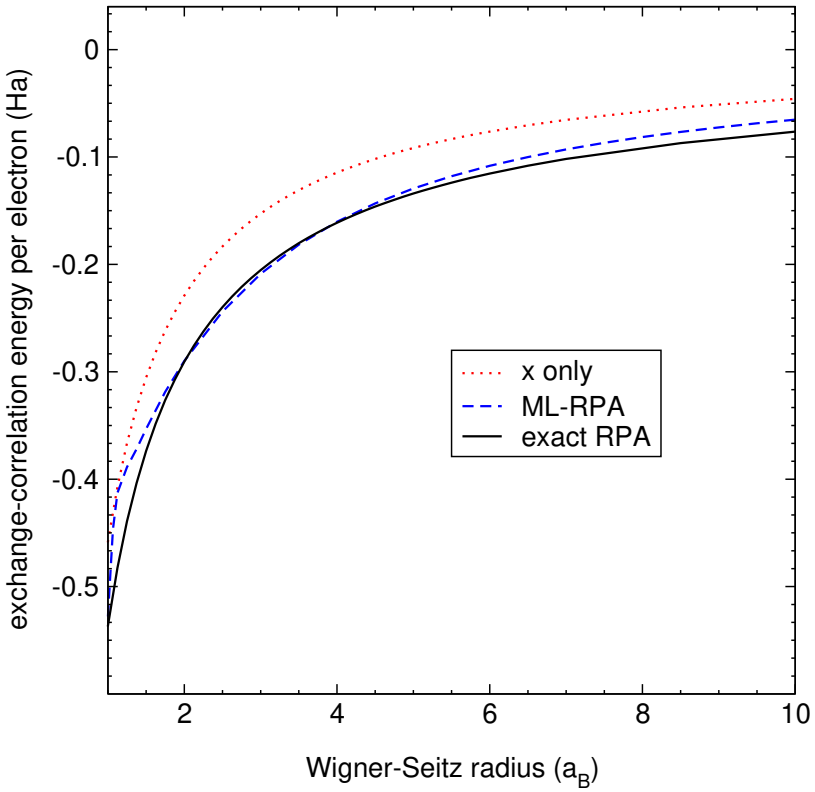

FIGURE 6.7: Application of ML-RPA to the homogeneous electron gas. Exact RPA results were taken from Ref. [9], the exchange only approximation $\varepsilon_{x,\mathrm{HEG}}$ is also shown for comparison. No HEG data were added to the ML-RPA training set.

large densities ($r_s \lesssim 2$), ML-RPA develops an unphysical kink. This indicates the presence of an "extrapolation hole", that is, the complete lack of training data can cause erratic behavior.

6.5 Discussion

The LDA and different GGA functionals differ in the strength of their respective enhancement factors. This results, for example, in the following trend for cohesive energies of solids

$$\text{LDA} > \text{PBEsol} > \text{PBE} > \text{RPBE}. \tag{6.14}$$

The same trend is also manifest for surface formation energies and molecular adsorption energies.[68] As different enhancement strengths fit better for different physical properties, this leads to a well-known trade-off for GGA functionals. This trade-off is visible also in the current study: LDA and PBEsol give better diamond surface energies (Table 6.2). PBE and RPBE perform better for the water dimer (Table 6.3), but the trend is reversed for the hexamer puzzle (App. K). This means that no GGA functional can give a completely satisfactory description of liquid water and ice, see also Ref. [207] for a more in-depth discussion. We have demonstrated that the non-local gradient approximation used in our ML-RPA model can overcome the GGA trade-off to some extend. While ML-RPA does not exceed a GGA-level description of liquid water, it clearly outperforms all GGA functionals for the diamond surface benchmark.

Traditional routes beyond GGA are metaGGA and hybrid functionals on the one hand, and vdW functionals on the other hand. The RPA itself can be considered as the "gold standard" of vdW functionals.[41] Different vdW functionals tested here generally outperform their respective semi-local DFT base functionals, though the improvement is not always consistent. For example, the rVV10 vdW correction slightly increases the surface energies of the pristine SCAN functional, achieving good agreement with exact RPA (Table 6.2, Ref. [192]). On the other hand, SCAN already slightly overbinds the water dimer and gives a somewhat overstructured liquid. Thus, it is plausible that additional binding in the form of rVV10 can only deteriorate the performance of SCAN for water (App. K, Ref. [218]). We reason that the rather small cutoff radius adapted here for ML-RPA is not sufficient to capture the full non-locality that is required for a complete description of liquid water (ML-RPA uses a cutoff radius of 1.5 Å, whereas RPA-MLFF uses a larger cutoff of 6.0 Å). However, simply increasing the cutoff radius is not an option with the current implementation and training database. We repeat that our tests show that a larger cutoff would diminish fit accuracy. Future work could instead focus on the construction of explicitly long-range descriptors as present in non-local vdW functionals or in recent extensions of MLFF frameworks.[219]

Finally, a common problem of ML techniques is extrapolation, that is, one can only expect good performance if applications are similar enough to the respective training sets. Here, this point was demonstrated by the poor performance of RPA-MLFF for water clusters (RPA-MLFF has been trained only for bulk water and the water monomer). In contrast, ML-RPA gives consistent if inaccurate predictions, though it has less water training data. We speculate that this is due to ML-RPA descriptors being much more compact, which makes extrapolation more manageable. Specifically, here we used 8 density descriptors for ML-RPA versus 408 atomic descriptors for RPA-MLFF (204 for both O and H). It is worth pointing out that this difference will be exacerbated when more chemical species have to be described at the same time. That is, the number of descriptors in MLFF schemes generally scales unfavorably with the number of chemical species, whereas the density descriptors used for ML-RPA do not depend explicitly on atom type. On the other side, RPA-MLFF is in the present implementation undeniable superior in terms of raw fit accuracy. ML-RPA and RPA-MLFF thus strike different balances between model flexibility and universality.

When pushed even further outside of its training set, however, ML-RPA eventually extrapolates as well as demonstrated for the homogeneous electron gas. The obvious but costly solution to the extrapolation problem is the construction of ever larger training databases. A more elegant alternative would be to enforce ML-RPA to obey known exact constraints. Exact constraints have been used in the past to construct successful functionals such as the SCAN functional ("Strongly constrained and appropriately normed").[158] Recently, there have been some promising efforts to incorporate exact constraints also into machine learned density functionals.[163,187,220,221]

6.6 Conclusion and Outlook

In this work we have machine learned a substitute density functional based on the random-phase approximation. The ingredients of ML-RPA are density descriptors constructed analogously to the two- and three-body descriptors used for machine learned force fields. These ingredients can be considered as non-local extensions of

the local density and its gradient. As a first application, we have constructed an ML-RPA functional for diamond and liquid water. We have demonstrated how such a functional can be used to enable RPA calculations at a larger scale. For a data set of 28 diamond surfaces, ML-RPA surpasses all tested GGA functionals in terms of accuracy and reaches the level of state-of-the-art vdW functionals. For liquid water, ML-RPA is less accurate and falls back to a GGA-level description, which we traced back to an insufficient description of non-local interactions.

Our ML-RPA scheme was demonstrated to learn fairly quickly from small amounts of exact RPA data, with the entire data base consisting of less than 200 structures. We credit this data efficiency to the inclusion of derivative information in the form of RPA exchange-correlation potentials, which are obtained via the optimized effective potential method. This is in close analogy to fitting atomic forces in MLFF. Generally, the tasks of machine learning atomic force fields and machine learning density functionals are closely related. We hope to see continued exchange of concepts and techniques, as we believe that both fields can benefit immensely from such a "cross-fertilization" of ideas.

Finally, our machine learning method using optimized effective potentials is general and not limited to the random-phase approximation. For example, beyond RPA theories can be constructed by including vertex correction to the screened Coulomb interaction and/or self energy. One can also envision to extract high accuracy exchange-correlation potentials from accurate coupled-cluster densities via Kohn-Sham inversion. Our method can also be applied to learn hybrid functionals, where large databases can be obtained more easily, thus facilitating large-scale hybrid functional simulations.

Part III

Summary

Chapter 7

Conclusion

In this thesis, we have developed methods that reduce the computational cost of RPA calculations. In a first approach, the short-range part of the RPA correlation energy is substituted either by an LDA functional, or taken into account implicitly via the squeezed Coulomb kernel. Both methods rely on homogeneous electron gas models and are based on the assumption that short-range effects are essentially local in nature. We have proven that the basis set correction methods can even become exact in the limit of large cutoffs. In a more ambitious second approach, the entire RPA exchange-correlation energy is substituted by a machine learned density functional. Here, a purely local theory (LDA) is clearly insufficient, and we thus constructed the ML-RPA model as a non-local extension of the GGA.

The essential approximation made by both approaches is some version of the nearsightedness principle. That is, even tough the ML-RPA functional is more sophisticated and contains some non-local information, it is clear that the ML-RPA descriptors are still incomplete. It is perhaps not surprising that either approach becomes less accurate when the assumption of nearsightedness is not valid. The examples of Pd and Kr demonstrate this for the basis set correction methods, and the example of water demonstrates this for ML-RPA, respectively. To improve the accuracy, future work should therefore focus on making the approaches less nearsighted by including further non-local information. That said, the nearsighted approaches work well already for materials such as C-diamond. The fact that ML-RPA reaches excellent accuracy for diamond surface energies is a particularly satisfying result. Future work could straightforwardly extend its application to different surface coverages and functional groups.

The computational cost of both the short-range LDA and ML-RPA functionals is orders of magnitude below that of the RPA, and the squeezed Coulomb kernel can be introduced essentially for free. Furthermore, it is also possible to combine the two approaches. On the one hand, the machine learned functionals could be trained only on the long-range RPA correlation energies. That is, even tough the machine learned density functionals are very fast in application, the creation of the training database is still time-consuming and here one could benefit from basis set correction. On the other hand, it is also possible to apply the machine learning scheme to substitute only the short-range RPA correlation to obtain a more accurate basis set correction.

Finally, we created two RPA benchmarks which can be used to test the accuracy of DFT functionals or assess the effects of beyond-RPA corrections. (i) We have calculated self-consistent RPA-OEP band gaps and dielectric constants for 15 semiconductors and insulators, and (ii) we have calculated RPA formation energies for 28 diamond surfaces. Moreover, we have assembled an ML-RPA training set for diamond, its surfaces and water containing over 150 RPA-OEP calculations. This database can be useful to compare the accuracy of different ML-DFT approaches.

Part IV

Appendices

Appendix A

Range-separated exchange

The exchange energy per particle of an HEG interacting via a long-range interaction V^{LR} is given as

$$\varepsilon_{\mathrm{x,HEG}}^{\mathrm{LR}}(r_\mathrm{s}) = -\Omega \int \frac{\mathrm{d}\mathbf{q}}{(2\pi)^3} V^{\mathrm{LR}}(|\mathbf{q}|) \int \frac{\mathrm{d}\mathbf{k}}{(2\pi)^3} \theta(k_\mathrm{F} - |\mathbf{k}+\mathbf{q}|)\theta(k_\mathrm{F} - |\mathbf{k}|) \tag{A.1}$$

The integration over $\mathbf{k}$ yields (compare derivation of Fetter and Walecka,[99] chap. 3)

$$\varepsilon_{\mathrm{x,HEG}}^{\mathrm{LR}}(r_\mathrm{s}) = -\frac{2k_\mathrm{F}^3}{\pi^2} \int_0^1 \mathrm{d}y\, y^2 V^{\mathrm{LR}}(y) \left(1 - \frac{3}{2}y + \frac{1}{2}y^3\right), \tag{A.2}$$

where $y = q/2k_\mathrm{F}$.

For the hard cutoff (4.9), we obtain Eq. (4.16), and for the error function (4.8) we recover the result of Savin [222]

$$\varepsilon_{\mathrm{x,HEG}}^{\mathrm{LR}}(\mu, r_\mathrm{s}) = -\frac{\mu}{\pi}\left[(2x - 4x^3)e^{-1/4x^2} - 3x + 4x^3 + \sqrt{\pi}\mathrm{erf}\left(\frac{1}{2x}\right)\right], \tag{A.3}$$

where $x = \mu/2k_\mathrm{F}$. For large μ, this can be expanded as

$$\varepsilon_{\mathrm{x,HEG}}^{\mathrm{LR}}(\mu, r_\mathrm{s}) = \varepsilon_\mathrm{x} + \frac{3}{16 r_\mathrm{s}^3 \mu^2} + \mathcal{O}\left(\frac{1}{\mu^4}\right). \tag{A.4}$$

By inserting this into equation (4.34), we obtain an expression for the LDA approximation to the short-range exchange energy

$$E_\mathrm{x}^{\mathrm{SR,LDA}}(\mu) = -\frac{\pi}{4\mu^2} \int \mathrm{d}\mathbf{r}\, n(\mathbf{r})^2 + \mathcal{O}\left(\frac{1}{\mu^4}\right). \tag{A.5}$$

Gill *et al.*[108] have shown that, up to leading order, this is also the expression for the exact short-range exchange, compare Eq. (4.35).

Appendix B

Short-range RPA energy for the HEG: approaching the full-range limit

Our derivation of the high Q_{cut}-limit of $\varepsilon_{\text{c,HEG}}^{\text{RPA,SR}}(Q_{\text{cut}})$ follows the study of Gulans.[87] The text-book equation for full-range expression reads[52]

$$\varepsilon_{\text{c,HEG}}^{\text{RPA}} = \frac{1}{n}\int \frac{\mathrm{d}q}{(2\pi)^3} 4\pi q^2 \int_0^\infty \frac{\mathrm{d}\omega}{2\pi} \left\{\ln\left[1-\chi_{0,\text{HEG}}(q,i\omega)V(q)\right] + \chi_{0,\text{HEG}}(q,i\omega)V(q)\right\}, \tag{B.1}$$

where $\chi_{0,\text{HEG}}(q,i\omega)$ is the Lindhard polarizibility for the HEG in terms of imaginary frequencies. The long-range version is obtained by replacing $V \to V^{\text{LR}}(Q_{\text{cut}})$ [see Eq. (4.9)], and $\varepsilon_{\text{c,HEG}}^{\text{RPA,SR}}(Q_{\text{cut}})$ is given by the difference between those. It is convenient to express $\chi_{0,\text{HEG}}$ in the closed form (see Ref. [223, chap. 4])

$$\chi_{0,\text{HEG}}(q,i\omega) = \frac{k_{\text{F}}^2}{\pi^2 q}\left[\Psi\left(\frac{i\omega}{qk_{\text{F}}} - \frac{q}{2k_{\text{F}}}\right) - \Psi\left(\frac{i\omega}{qk_{\text{F}}} + \frac{q}{2k_{\text{F}}}\right)\right], \tag{B.2}$$

where $\Psi(z)$ is defined as

$$\Psi(z) = \frac{z}{2} + \frac{1-z^2}{4}\ln\left(\frac{z+1}{z-1}\right). \tag{B.3}$$

Note that Gulans missed a factor of 2 in his expression for $\chi_{0,\text{HEG}}$, that accounts for summation over spin. This also affects his result for the *GW* basis set incompleteness error [compare Eq. (28) in Ref. [86]]. We introduce the dimensionless variables $y = q/2k_{\text{F}}$ and $t = 2\omega/q^2$ and use the series expansion

$$\Psi(z) \overset{|z|\to\infty}{=} \frac{1}{3z} + \frac{1}{15z^3} + \frac{1}{35z^5} + \mathcal{O}\left(\frac{1}{z^7}\right). \tag{B.4}$$

Hence, for large momentum transfers q we obtain

$$\chi_{0,\text{HEG}}(y,t) = -\frac{k_{\text{F}}}{2\pi^2 y^2}\left[\frac{2}{3}\frac{1}{1+t^2} + \frac{2}{15y^2}\frac{1-3t^2}{(1+t^2)^3} + \frac{2}{35y^4}\frac{1-10t^2+5t^4}{(1+t^2)^5} + \mathcal{O}\left(\frac{1}{y^6}\right)\right]. \tag{B.5}$$

In this limit, we may also use the Mercator expansion

$$\ln(1-x) = -x - \frac{x^2}{2} - \frac{x^3}{3} - \ldots \quad \text{for } x \to 0, \tag{B.6}$$

to decompose the RPA into its ring diagram components, compare Fig. 4.2. We proceed to evaluate the frequency integrations, starting with the direct MP2 part

$$\begin{aligned} &\int_0^\infty \frac{\mathrm{d}\omega}{2\pi} \frac{(\chi_{0,\mathrm{HEG}} V)^2 - (\chi_{0,\mathrm{HEG}} V^{\mathrm{LR}})^2}{2} = \\ &\frac{\theta(q-Q_{\mathrm{cut}})}{8\pi^2 y^6} \left[\frac{1}{9} + \frac{1}{90y^2} + \frac{1}{350y^4} + \mathcal{O}\left(\frac{1}{y^6}\right)\right]. \end{aligned} \tag{B.7}$$

After momentum integration, we find that the second order contribution to $\varepsilon_{\mathrm{c,HEG}}^{\mathrm{RPA,SR}}$ is given by

$$\begin{aligned} &\varepsilon_{\mathrm{c,HEG}}^{\mathrm{RPA,SR},(2)}(Q_{\mathrm{cut}}) = \\ &-\frac{1}{\pi}\left[\frac{1}{Q_{\mathrm{cut}}^3 r_{\mathrm{s}}^3} + \frac{6}{25\alpha^2 Q_{\mathrm{cut}}^5 r_{\mathrm{s}}^5} + \frac{216}{1225\alpha^4 Q_{\mathrm{cut}}^7 r_{\mathrm{s}}^7} + \mathcal{O}\left(\frac{1}{Q_{\mathrm{cut}}^9}\right)\right]. \end{aligned} \tag{B.8}$$

For contributions from the third order ring diagram, we evaluate

$$\int_0^\infty \frac{\mathrm{d}\omega}{2\pi} \frac{(\chi_{0,\mathrm{HEG}} V)^3 - (\chi_{0,\mathrm{HEG}} V^{\mathrm{LR}})^3}{3} = -\frac{\theta(q-Q_{\mathrm{cut}})}{432\pi^3 k_{\mathrm{F}} y^{10}} + \mathcal{O}\left(\frac{1}{y^{12}}\right), \tag{B.9}$$

and obtain for the short-range correlation energy per particle

$$\varepsilon_{\mathrm{c,HEG}}^{\mathrm{RPA,SR},(3)}(Q_{\mathrm{cut}}) = \frac{18}{7\pi Q_{\mathrm{cut}}^7 r_{\mathrm{s}}^6} + \mathcal{O}\left(\frac{1}{Q_{\mathrm{cut}}^9}\right). \tag{B.10}$$

Contributions of higher order diagrams are $\mathcal{O}(1/Q_{\mathrm{cut}}^9)$ as well. The last equation shows that the low-density scaling behavior starts to break down at $\mathcal{O}(1/Q_{\mathrm{cut}}^7)$ through the influence of higher order diagrams.

Appendix C

Fitting the short-range LDA functionals

As outlined in section 4.3, we fit the short-range LDA functionals using the form

$$\begin{aligned} \varepsilon_c^{\mathrm{RPA,SR}} &= A \frac{\ln\left(\frac{r_s + a_0 r_s^2 + a_1 r_s^3 + a_2 r_s^4}{1 + a_3 r_s + a_4 r_s^2 + a_5 r_s^3 + a_2 r_s^4}\right)}{1 + a_6 r_s + a_7 r_s^2} \\ A &= -\frac{\ln(2) - 1}{\pi^2}. \end{aligned} \tag{C.1}$$

In Tables C.1 and C.2, the fit parameters are given for selected range-separation parameters. Figs. C.1 and C.2 demonstrate the fits for the cosine window and the error function respectively.

TABLE C.1: Fit parameters for the cosine window. The Wigner-Seitz radius r_s is input in a_B, the short-range RPA energy per particle $\varepsilon_c^{\mathrm{RPA,SR}}$ is output in Ha.

	$Q_{\mathrm{cut}} = 2\ a_B^{-1}$	$Q_{\mathrm{cut}} = 3\ a_B^{-1}$	$Q_{\mathrm{cut}} = 4\ a_B^{-1}$
a_0	723.273	250.439	42.2121
a_1	-778.762	-458.185	-115.400
a_2	434.396	368.688	117.648
a_3	6985.71	2192.95	371.181
a_4	-2873.23	-1452.77	-347.389
a_5	251.151	295.871	124.814
a_6	0.958156	1.53924	1.88767
a_7	0.854852	2.67992	6.72314

TABLE C.2: Fit parameters for the error function. The Wigner-Seitz radius r_s is input in a_B, the short-range RPA energy per particle $\varepsilon_c^{\mathrm{RPA,SR}}$ is output in Ha.

	$\mu = 2\ a_B^{-1}$	$\mu = 3\ a_B^{-1}$	$\mu = 4\ a_B^{-1}$
a_0	60.2614	26.6952	56.7518
a_1	-50.7152	-38.9317	-113.350
a_2	141.086	138.271	523.105
a_3	728.749	439.932	703.130
a_4	722.861	458.791	1003.12
a_5	409.769	351.941	1002.40
a_6	2.26403	4.04404	5.21364
a_7	0.0416747	0.104055	0.157932

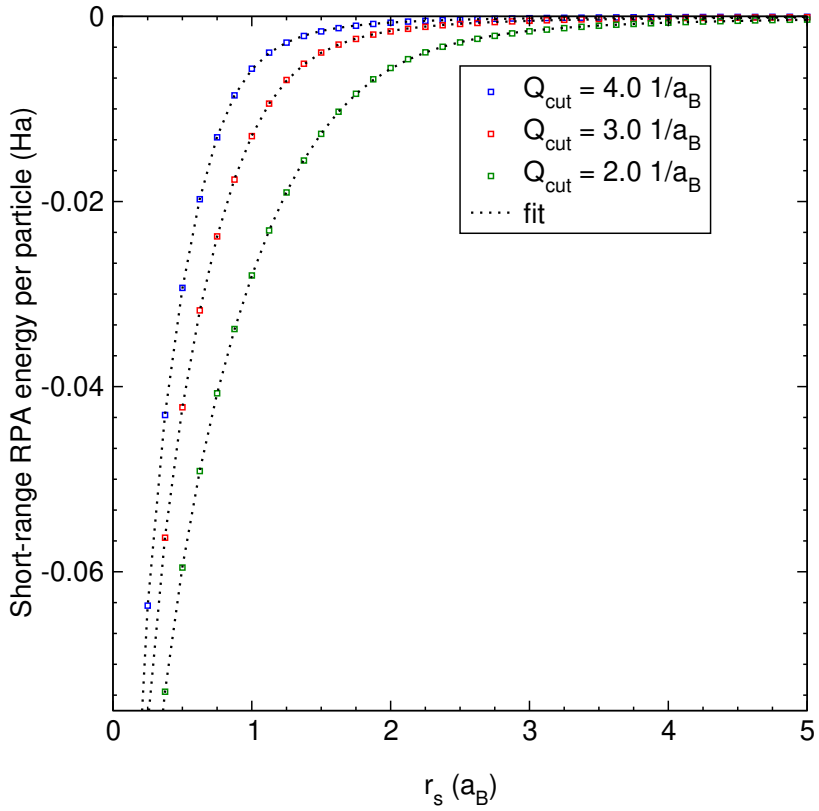

FIGURE C.1: Analytic representation of the short-range LDA functionals for the cosine window. Square symbols represent numerical data for different range-separation parameters, and dotted lines represent fits using Eq. (C.1).

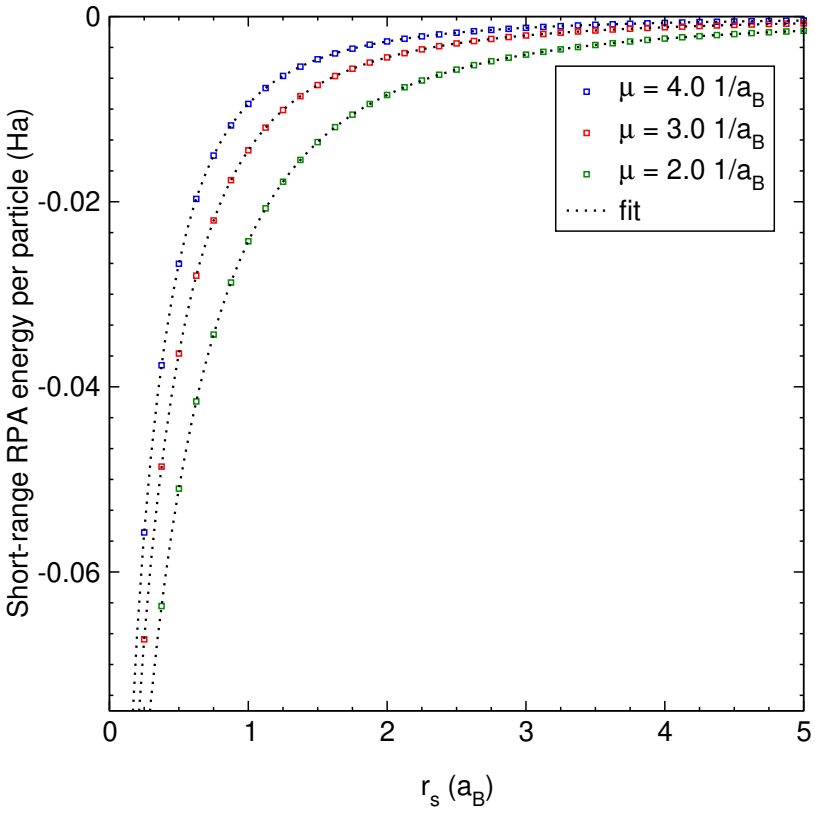

FIGURE C.2: Analytic representation of the short-range LDA functionals for the error function. Square symbols represent numerical data for different range-separation parameters, and dotted lines represent fits using Eq. (C.1).

Appendix D

GW correlation energies for the HEG

In the following, we discuss briefly our numerical calculations of *GW* correlation energies for the HEG. First, we describe the static QPA and COHSEX approximations and thereafter the fully self-consistent case.

The *GW* self-energy for the HEG is given by[16]

$$\Sigma_{\mathrm{xc,HEG}}(\mathbf{k},\omega) = -\oint_{\mathcal{U}} \frac{\mathrm{d}\nu}{2\pi i} \int \frac{\mathrm{d}\mathbf{q}}{(2\pi)^3} G(\mathbf{k}+\mathbf{q},\omega+\nu) W(\mathbf{q},\nu). \tag{D.1}$$

As discussed in Sec. 5.2.3, for static self-energies it is sufficient to consider the non-interacting G_0W_0 case, where the energy dispersion is given by $\varepsilon(k) = k^2/2$ and the chemical potential via $\mu = k_\mathrm{F}^2/2$ respectively. Following Hedin,[22] we split the screened interaction W in a static term and a dynamical remainder term

$$W(k,\nu) = \frac{V(k)}{\epsilon^{\mathrm{RPA}}_{\mathrm{HEG}}(k,0)} + V(k)\left[\frac{1}{\epsilon^{\mathrm{RPA}}_{\mathrm{HEG}}(k,\nu)} - \frac{1}{\epsilon^{\mathrm{RPA}}_{\mathrm{HEG}}(k,0)}\right], \tag{D.2}$$

where $\epsilon^{\mathrm{RPA}}_{\mathrm{HEG}} = (1-\chi_{0,\mathrm{HEG}}V)^{-1}$ is the Lindhard dielectric function and it is understood that the static interaction with the polarization cloud, $W_\mathrm{p}(\omega) = W(\omega = 0) - V$, is given by the average of infinitesimal positive and negative times[16]

$$W_\mathrm{p}(k,t) = W_\mathrm{p}(k)\left[\delta(t^+)/2 + \delta(t^-)/2\right]. \tag{D.3}$$

Then, performing the contour integral in Eq. (D.1) for the static parts yields the static Coulomb hole (COH) and screened exchange (SEX) terms, (see Hedin [22])

$$\begin{aligned}
\Sigma^{\mathrm{COH}}_{\mathrm{xc,HEG}}(k) =& \frac{1}{2}\int_0^\infty \frac{\mathrm{d}q}{(2\pi)^3} 4\pi q^2 V(q)\left[\frac{1}{\epsilon^{\mathrm{RPA}}_{\mathrm{HEG}}(q,0)} - 1\right] \\
\Sigma^{\mathrm{SEX}}_{\mathrm{xc,HEG}}(k) =& -\int_0^\infty \frac{\mathrm{d}q}{(2\pi)^3} 2\pi q^2 \int_{-1}^1 \mathrm{d}\xi \frac{V(q)}{\epsilon^{\mathrm{RPA}}_{\mathrm{HEG}}(q,0)} \theta(k_\mathrm{F}^2 - k^2 - q^2 - 2kq\xi),
\end{aligned} \tag{D.4}$$

The angular integral can be performed analytically using

$$\int_1^1 d\xi \theta(a - b\xi) = \left(\frac{a}{b} - 1\right)\theta(b-a) - \left(\frac{a}{b}+1\right)\theta(-b-a) + 2, \tag{D.5}$$

thus both terms can be easily evaluated by numerical integration. The COH term is dispersionless, since the interaction with the static Coulomb hole is local in space. The SEX term reduces to the bare exchange result (5.20) for $\epsilon^{\mathrm{RPA}}_{\mathrm{HEG}} \to 1$. To evaluate the dynamical remainder term, one can deform the contour as shown in Fig. D.1,

yielding

$$\begin{aligned}\Sigma^{\mathrm{c}}_{\mathrm{xc,HEG}}(k,\omega) =& \frac{1}{2}\int_0^\infty \frac{\mathrm{d}\nu}{2\pi}\int_0^\infty \frac{\mathrm{d}q}{(2\pi)^3}2\pi q^2\left[\frac{V(q)}{\epsilon^{\mathrm{RPA}}_{\mathrm{HEG}}(k,i\nu)} - \frac{V(q)}{\epsilon^{\mathrm{RPA}}_{\mathrm{HEG}}(q,0)}\right] \\ &\times \frac{1}{2kq}\ln\frac{(\omega - k^2/2 - q^2/2 - kq)^2 + \nu^2}{(\omega - k^2/2 - q^2/2 + kq)^2 + \nu^2} \\ \Sigma^{\mathrm{p}}_{\mathrm{xc,HEG}}(k,\omega) =& -\int_0^\infty \frac{\mathrm{d}q}{(2\pi)^3}2\pi q^2\int_{-1}^1 \mathrm{d}\xi\left[\frac{V(q)}{\epsilon^{\mathrm{RPA}}_{\mathrm{HEG}}(q,\omega)} - \frac{V(q)}{\epsilon^{\mathrm{RPA}}_{\mathrm{HEG}}(q,0)}\right] \\ &\times \left[\theta(2\omega - k^2 - q^2 - kq\xi) - \theta(k_{\mathrm{F}}^2 - k^2 - q^2 - kq\xi)\right],\end{aligned} \tag{D.6}$$

where $\Sigma^{\mathrm{c}}_{\mathrm{xc,HEG}}$ involves an integral along the imaginary frequency axis and we have used that the integrand is an even function of $i\nu$. Furthermore, $\Sigma^{\mathrm{p}}_{\mathrm{xc,HEG}}$ corresponds to a contribution from the poles of G. The QPA is obtained by setting $\omega = k^2/2$ in Eq. (D.6), hence

$$\Sigma^{\mathrm{QPA}}_{\mathrm{xc,HEG}}(k) = \Sigma^{\mathrm{COH}}_{\mathrm{xc,HEG}}(k) + \Sigma^{\mathrm{SEX}}_{\mathrm{xc,HEG}}(k) + \Sigma^{\mathrm{c}}_{\mathrm{xc,HEG}}(k, k^2/2) + \Sigma^{\mathrm{p}}_{\mathrm{xc,HEG}}(k, k^2/2). \tag{D.7}$$

Again, these integrals can be evaluated numerically with relative ease. Our results for $\Sigma_{\mathrm{xc,HEG}}(k_{\mathrm{F}}, k_{\mathrm{F}}^2/2)$ are in excellent agreement with those reported in Table III of Ref. [22]. Finally, the GW correlation energies for COHSEX and QPA are evaluated via Eq. (5.19). As was already discussed by Hedin,[22] the real part of $\Sigma^{\mathrm{p}}_{\mathrm{xc,HEG}}(k, k^2/2)$ vanishes at the Fermi edge and is also for other values of k numerically very small. The difference between QPA and COHSEX therefore stems mostly from $\Sigma^{\mathrm{c}}_{\mathrm{xc,HEG}}$, which is positive.

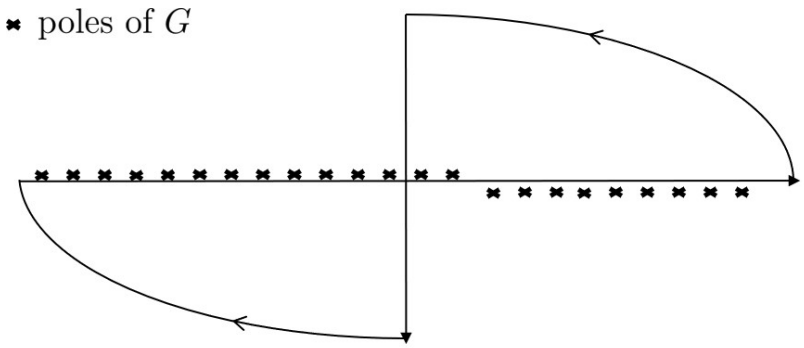

FIGURE D.1: Integration contour for the dynamical remainder term, compare Eq. (D.6), for $\omega < \mu$. The integral over imaginary frequencies corresponds to $\Sigma^{\mathrm{c}}_{\mathrm{xc}}$, the poles of G contribute to $\Sigma^{\mathrm{p}}_{\mathrm{xc}}$.

We now briefly discuss what changes in the case of self-consistent calculations. For the sake of clarity, we start with the GW_0 scheme, were only G is iterated to self-consistency. For this purpose, it is useful to consider the Galitskii-Migdal energy in the form[139]

$$\varepsilon^{\mathrm{GM}}_{\mathrm{xc,HEG}} = \frac{1}{n}\int_0^\infty \frac{\mathrm{d}k}{(2\pi)^3}4\pi k^2\int_0^\mu \frac{\mathrm{d}\omega}{2\pi}[\omega + \varepsilon(k)]A(k,\omega), \tag{D.8}$$

where $A(k,\omega)$ is the spectral function. In any static approximation, it is given by $\delta[\omega - \varepsilon(k) - \Sigma_{\mathrm{xc}}(k)]$, hence we recover Eq. (5.19). In reality, some spectral weight is transferred to a plasmon satellite. Furthermore, the peaks are spread out, owing

to the finite QP lifetime, which also implies a correlation part of the kinetic energy. However, it turns out that for the description of total energies only weight and position of the peaks, rather than their detailed structure, are of greater importance.[139] Therefore, we can assume a sharp QP peak at $\varepsilon(k) + \Sigma_{\mathrm{xc}}(k)$ and a sharp plasmon peak at $\varepsilon(k) + \Sigma_{\mathrm{xc}}(k) - \omega_{\mathrm{p}}$, respectively, where $\omega_{\mathrm{p}} = \sqrt{4\pi n}$ is the plasma frequency. In this approximation, the spectral function is thus given by

$$A(k,\omega) \approx Z\delta[\omega - \varepsilon(k) - \Sigma_{\mathrm{xc}}] + (1-Z)\{\delta[\omega - \varepsilon(k) - \Sigma_{\mathrm{xc}} + \omega_{\mathrm{p}}]\}. \tag{D.9}$$

By inserting this result into Eq. (D.8), we find that in the QPA, the exchange-correlation energies are reduced by

$$\varepsilon_{\mathrm{xc,HEG}}^{\mathrm{GM,QPA}} - \varepsilon_{\mathrm{xc,HEG}}^{\mathrm{GM}} \approx \frac{(1-Z)\omega_{\mathrm{p}}}{2}. \tag{D.10}$$

Comparing with GW_0 data from Holm and Barth,[139,140] we find that this simple formula is accurate to roughly 25% for metallic densities. In fully self-consistent GW calculations, the plasmon peak is very much spread out, which may cast doubt on the assumptions above. However, it turns out that the effect on total energies is again small.

For our self-consistent GW calculations, we use the GM routines of `VASP` as described in Ref. [224]. We find that the self-consistency loop converges rather quickly, and 5 iterations are typically enough to converge the GM energies up to 1 mHa. Such fully self-consistent GW calculations for the HEG were performed previously by Holm and Barth[139,140] as well as García-González and Godby,[225] and our exchange-correlation energies agree well with theirs (up to 1 mHa).

Appendix E

Numerical solution of the linearized Sham-Schlüter equation

In this section we describe in detail our implementation of step (iv) in the RPA-OEP self-consistency scheme, compare Fig. 5.4.

In the i-th iteration of the self-consistency cycle, we determine the difference between the effective exchange-correlation potential of the current and the previous iteration, $\Delta v_{\mathrm{xc}}^{(i)} = v_{\mathrm{xc}}^{(i)} - v_{\mathrm{xc}}^{(i-1)}$. Furthermore, the non-interacting Green's function of the previous iteration, $G_0^{(i-1)}(\omega) = [\omega - H_{\mathrm{KS}}^{(i-1)}]^{-1}$, belongs to the Kohn-Sham Hamiltonian $H_{\mathrm{KS}}^{(i-1)} = T + v_{\mathrm{ext}} + v_{\mathrm{H}} + v_{\mathrm{xc}}^{(i-1)}$. Then, $\Delta v_{\mathrm{xc}}^{(i)}$ is obtained from the linearized SSE (5.4) as follows. Writing Tr for the integration over $\mathbf{r}'$ and ω, Eq. (5.4) is rewritten into

$$0 = \mathrm{Tr}\left\{2G_0^{(i-1)}\left[\Sigma_{\mathrm{xc}}^{(i-1)} - v_{\mathrm{xc}}^{(i-1)}\right]G_0^{(i-1)}\right\}(\mathbf{r}). \tag{E.1}$$

Add a zero of the form $0 = H_{\mathrm{KS}}^{(i-1)} - H_{\mathrm{KS}}^{(i-1)}$ between the G_0W_0 self-energy and the exchange-correlation potential and separate the self-energy into an exchange and correlation term, $\Sigma_{\mathrm{xc}}^{(i-1)} = \Sigma_{\mathrm{x}}^{(i-1)} + \Sigma_{\mathrm{c}}^{(i-1)}$. This yields

$$\begin{aligned}&\mathrm{Tr}\left\{\chi_0^{(i-1)}\Delta v_{\mathrm{xc}}^{(i)}\right\}(\mathbf{r}) = \\ &\mathrm{Tr}\left\{2\left[H_{\mathrm{HF}}^{(i-1)} - H_{\mathrm{KS}}^{(i-1)}\right]G_0^{(i-1)}G_0^{(i-1)}\right\}(\mathbf{r}) + \mathrm{Tr}\left\{2G_0^{(i-1)}\Sigma_{\mathrm{c}}^{(i-1)}G_0^{(i-1)}\right\}(\mathbf{r}).\end{aligned} \tag{E.2}$$

The right hand side is evaluated in the basis of the Hartree-Fock Hamiltonian $H_{\mathrm{HF}}^{(i-1)} = T + v_{\mathrm{ext}} + v_{\mathrm{H}} + v_{\mathrm{x}}^{(i-1)}$ and diagonalized, yielding natural orbitals $\phi_\alpha^{(i-1)}$ and occupancies $f_\alpha^{(i-1)}$ for the i-th iteration. The corresponding natural orbital charge density,

$$\Delta\rho_{\mathrm{xc}}^{(i-1)}(\mathbf{r}) = \sum_{\alpha}^{\mathrm{all}} f_\alpha^{(i-1)}\phi_\alpha^{*(i-1)}(\mathbf{r})\phi_\alpha^{(i-1)}(\mathbf{r}), \tag{E.3}$$

is a valid spectral representation of the right hand side of Eq. (E.2) such that the linearized SSE reduces to

$$\int \mathrm{d}\mathbf{r}'\chi_0^{(i-1)}(\mathbf{r},\mathbf{r}')\Delta v_{\mathrm{xc}}^{(i)}(\mathbf{r}') = \Delta\rho_{\mathrm{xc}}^{(i-1)}(\mathbf{r}). \tag{E.4}$$

This equation is Fourier transformed to reciprocal space and solved for $\Delta v_{\mathrm{xc}}^{(i)}$. We follow Ref. [124] and use a cutoff $t_{\mathrm{SVD}} = 10^{-4}$ in the inversion of χ_0, which eliminates eigenmodes with eigenvalues smaller than t_{SVD}. Updating the Kohn-Sham Hamiltonian via $H_{\mathrm{KS}}^{(i)} = H_{\mathrm{KS}}^{(i-1)} + \Delta v_{\mathrm{xc}}^{(i)}$ completes one self-consistency loop.

Appendix F

Non-local density descriptors

In the following, we describe our density descriptors in more detail and comment on how they can be evaluated efficiently via the use of fast Fourier transforms (FFTs). We begin by expanding the electronic density around each grid point $\mathbf{r}$ [Eq. (6.2) in the main text]

$$n(\mathbf{r}+\mathbf{r}')f_{\text{cut}}(r') = \sum_{nlm} c_{nlm}(\mathbf{r})\phi_{nl}(r')Y_l^m(\widehat{\mathbf{r}'}). \tag{F.1}$$

For the cutoff function f_{cut}, we use the cosine cutoff proposed by Behler and Parrinello,[178]

$$f(r') = \begin{cases} \frac{1}{2}\left[1+\cos\left(\frac{\pi r'}{R_{\text{cut}}}\right)\right] & 0 \leq r' \leq R_{\text{cut}} \\ 0 & r \geq R_{\text{cut}}. \end{cases} \tag{F.2}$$

For radial basis functions ϕ_{nl}, we use spherical Bessel functions as in Ref. [173],

$$\phi_{nl}(r') = j_l(q_{nl}r'), \tag{F.3}$$

where the q_{nl} are chosen such that the basis functions vanish at $r' = R_{\text{cut}}$. Such spherical Bessel functions form a complete basis on the interval $[0, R_{\text{cut}}]$ and fulfill orthogonality relations of the kind

$$\int_0^{R_{\text{cut}}} \mathrm{d}r\; r^2 j_l(q_{nl}r) j_l(q_{n'l}r) = \delta_{nn'}A_{nl}. \tag{F.4}$$

For example, in the case of $l = 0$ one obtains

$$\phi_{n0}(r') = j_0(q_{n0}r') = \frac{\sin(q_{n0}r')}{q_{n0}r'}, \tag{F.5}$$

and demanding that $\sin(q_{n0}R_{\text{cut}}) = 0$ yields the simple expressions

$$\begin{aligned} q_{n0} &= \frac{n\pi}{R_{\text{cut}}} \\ A_{n0} &= \frac{R_{\text{cut}}^3}{2n^2\pi^2} \qquad n = 1, 2, \ldots \end{aligned} \tag{F.6}$$

Next, we calculate the expansion coefficients c_{nlm} using the orthogonality relations (F.4), as well as those for the Y_l^m,

$$\int d\Omega\; Y_l^m(\hat{\mathbf{r}})Y_{l'}^{m'}(\hat{\mathbf{r}}) = \delta_{ll'}\delta_{mm'}, \tag{F.7}$$

yielding

$$\begin{aligned} c_{nlm}(\mathbf{r}) &= \int_0^{R_{\text{cut}}} \mathrm{d}r' r'^2 \frac{\phi_{nl}(r') f_{\text{cut}}(r')}{A_{nl}} \int \mathrm{d}\Omega' Y_l^m(\widehat{\mathbf{r}'}) n(\mathbf{r}+\mathbf{r}') \\ &= \int_0^{R_{\text{cut}}} \mathrm{d}r' r'^2 \tilde{\phi}_{nl}(r') \int \mathrm{d}\Omega' Y_l^m(\widehat{\mathbf{r}'}) n(\mathbf{r}+\mathbf{r}'), \end{aligned} \tag{F.8}$$

where we have absorbed the coefficients A_{nl} and the cutoff function f_{cut} to define modified basis functions $\tilde{\phi}_{nl}$,

$$\tilde{\phi}_{nl}(r') = \frac{\phi_{nl}(r') f_{\text{cut}}(r')}{A_{nl}}. \tag{F.9}$$

Next, we combine the Fourier representation of the density

$$n(\mathbf{r}+\mathbf{r}') = \int \frac{\mathrm{d}\mathbf{q}}{(2\pi)^3} e^{i\mathbf{q}(\mathbf{r}+\mathbf{r}')} n(\mathbf{q}), \tag{F.10}$$

and the plane-wave expansion,[226]

$$e^{i\mathbf{q}\mathbf{r}'} = 4\pi \sum_{lm} i^l j_l(qr') Y_l^m(\widehat{\mathbf{q}}) Y_l^m(\widehat{\mathbf{r}'}), \tag{F.11}$$

to rewrite Eq. (F.8) as

$$c_{nlm}(\mathbf{r}) = 4\pi \int_0^{R_{\text{cut}}} \mathrm{d}r' r'^2 \tilde{\phi}_{nl}(r') \int \mathrm{d}\Omega' Y_l^m(\widehat{\mathbf{r}'}) \int \frac{\mathrm{d}\mathbf{q}}{(2\pi)^3} e^{i\mathbf{q}\mathbf{r}} n(\mathbf{q}) \sum_{l'm'} i^{l'} j_{l'}(qr') Y_{l'}^{m'}(\widehat{\mathbf{q}}) Y_{l'}^{m'}(\widehat{\mathbf{r}'}). \tag{F.12}$$

To simplify the equation above, we use the orthogonality relations of the Y_l^m [Eq. (F.7)] and define the spherical Bessel transform,

$$\begin{aligned} \tilde{\phi}_{nl}(q) &= 4\pi \int_0^{R_{\text{cut}}} \mathrm{d}r\, r'^2 j_l(qr') \tilde{\phi}_{ln}(r') \\ \leftrightarrow \tilde{\phi}_{nl}(r') &= \frac{1}{2\pi^2} \int \mathrm{d}q\, q^2 j_l(qr') \tilde{\phi}_{nl}(q), \end{aligned} \tag{F.13}$$

to finally arrive at the concise expression

$$c_{nlm}(\mathbf{r}) = i^l \int \frac{\mathrm{d}\mathbf{q}}{(2\pi)^3} e^{i\mathbf{q}\mathbf{r}} n(\mathbf{q}) \tilde{\phi}_{nl}(q) Y_l^m(\widehat{\mathbf{q}}). \tag{F.14}$$

This equation is evaluated numerically on an real-space grid,

$$c_{nlm}(\mathbf{r}) = i^l \sum_{\mathbf{q}} e^{i\mathbf{q}\mathbf{r}} n(\mathbf{q}) \tilde{\phi}_{nl}(q) Y_l^m(\widehat{\mathbf{q}}). \tag{F.15}$$

Thus, the coefficients $c_{nlm}(\mathbf{r})$ can be calculated *simultaneously for all real-space grid-points* via Fourier transform, and FFT achieves $\mathcal{N}_{\text{FFT}} \ln \mathcal{N}_{\text{FFT}}$ scaling with respect to the number of real-space grid points N_{FFT}.

To form descriptors for ML, one seeks rotationally invariant combinations of the coefficients c_{nlm}, as discussed by Bartok *et al.*[172] The c_{n00} are already rotationally invariant, following from the fact that $Y_0^0 = 1/\sqrt{4\pi}$ is scalar. This gives us the two-body descriptors, $X_n^{(2)} = c_{n00}$. Further rotational invariants can be formed as

follows[172,173]

$$p_{nn'l} = \sqrt{\frac{8\pi^2}{2l+1}} \sum_m c_{nlm} c_{n'lm}. \tag{F.16}$$

For $l = 1$, these rotational invariants can be understood as all possible dot products between vectors $\mathbf{c}_n = \{c_{n1x}, c_{n1y}, c_{n1z}\}$. That the $\mathbf{c}_n$ are vectors follows from the vector property of $\mathbf{Y}_1 = \{Y_1^x, Y_1^y, Y_1^z\}$ (we use the real spherical harmonics, where this vector property is clearly manifest)

$$\begin{aligned} Y_1^x &= \sqrt{\frac{3}{4\pi}} \frac{x}{\sqrt{x^2+y^2+z^2}} \\ Y_1^y &= \sqrt{\frac{3}{4\pi}} \frac{y}{\sqrt{x^2+y^2+z^2}} \\ Y_1^z &= \sqrt{\frac{3}{4\pi}} \frac{z}{\sqrt{x^2+y^2+z^2}}. \end{aligned} \tag{F.17}$$

To form three-body descriptors that have the same dimension as the $X_n^{(2)}$, we first form descriptors $X_{nn'l}^{(3)}$,

$$X_{nn'l}^{(3)} = \frac{\sigma^{(3)}}{R_{\text{cut}}} \frac{\sum_m c_{nlm} c_{n'lm}}{(\sum_m c_{nlm}^2)^{1/4} (\sum_m c_{n'lm}^2)^{1/4}}. \tag{F.18}$$

Next, we limit the $X_{nn'l}^{(3)}$ to $l = 1$ and neglect off-diagonal elements $n \neq n'$, obtaining the three-body descriptors $X_n^{(3)}$ [compare Eq. (6.4) in the main text]

$$\begin{aligned} X_n^{(3)} &= X_{nn'l}^{(3)} \delta_{nn'} \delta_{l1} \\ &= \frac{\sigma^{(3)}}{R_{\text{cut}}} \sqrt{c_{n1x}^2 + c_{n1y}^2 + c_{n1z}^2}. \end{aligned} \tag{F.19}$$

We have verified that this last approximation works well for the application to diamond and liquid water. Generally, however, the validity of the approximation depends on the concrete training set as well as on the radial basis functions used.[172] Here, we use four radial basis functions for both $l = 0$ and $l = 1$, thus we have in total $4 + 4 = 8$ density descriptors. Note that we use the weight factor $\sigma^{(3)}/R_{\text{cut}}$ in Eq. (F.18), rather than $(8\pi^2/3)^{1/4}$ which would correspond to $\sqrt{p_{nn1}}$. The possibility of using different weight factors for the three-body descriptors was also discussed in detail by Jinnouchi *et al.*[180]

F.1 Approaching GGA in the small cutoff limit

In Eqs. (6.3) and (6.5) in the main text, we have stated that in the limit of small cutoffs, the two-and three-body descriptors reduce to the local density and its gradient, respectively. A detailed proof of these limits is given in the following. For a small enough cutoff radius R_{cut}, the density inside the cutoff sphere varies little, assuming that the density is smooth enough. That means one can perform the gradient

expansion of the density[20] around $\mathbf{r}$

$$n(\mathbf{r}+\mathbf{r}') \approx n(\mathbf{r}) + r'_\alpha \nabla_\alpha n(\mathbf{r}) + \frac{1}{2} r'_\alpha r'_\beta \nabla_\alpha \nabla_\beta n(\mathbf{r}) + \frac{1}{6} r'_\alpha r'_\beta r'_\gamma \nabla_\alpha \nabla_\beta \nabla_\gamma n(\mathbf{r}) + ..., \tag{F.20}$$

where α, β and γ are Cartesian indices and we use the Einstein sum convention. The same limit can also be obtained for fixed cutoff radius by considering artificial weakly varying densities ($\nabla n \to 0$, in the extreme case, one obtains the homogeneous electron gas). In other words, the dimensionless expansion parameter is $r'\nabla n$, and that can be small when either r' or ∇n is fixed and the other one goes to zero.

We insert the gradient expansion (F.20) into the expression for the coefficients c_{nlm}, Eq. (F.8), yielding

$$\begin{aligned} c_{nlm}(\mathbf{r}) \approx & \int_0^{R_{\text{cut}}} \mathrm{d}r'\; r'^2 \tilde{\phi}_{nl}(r') \int \mathrm{d}\Omega'\; Y_l^m(\widehat{\mathbf{r}'}) \\ & \times \left[n(\mathbf{r}) + r'_\alpha \nabla_\alpha n(\mathbf{r}) + \frac{1}{2} r'_\alpha r'_\beta \nabla_\alpha \nabla_\beta n(\mathbf{r}) + \frac{1}{6} r'_\alpha r'_\beta r'_\gamma \nabla_\alpha \nabla_\beta \nabla_\gamma n(\mathbf{r}) + ... \right]. \end{aligned} \tag{F.21}$$

When evaluating the integral above, the first order term in the gradient expansion vanishes for $l = 0$. This is due to the anti-symmetry of the integrand. Likewise, the zeroth and second order terms vanish for $l = 1$. Thus, for the c_{n00} (two-body descriptors), Eq. (F.21) simplifies to

$$c_{n00}(\mathbf{r}) \approx \sqrt{4\pi} \int_0^{R_{\text{cut}}} \mathrm{d}r'\; r'^2 \tilde{\phi}_{n0}(r') n(\mathbf{r}) + \frac{\sqrt{4\pi}}{6} \int_0^{R_{\text{cut}}} \mathrm{d}r'\; r'^4 \tilde{\phi}_{n0}(r') \nabla^2 n(\mathbf{r}) + ..., \tag{F.22}$$

where we have used

$$\int \mathrm{d}\Omega'\; r'_\alpha r'_\beta = \frac{4\pi}{3} r'^2 \delta_{\alpha\beta}. \tag{F.23}$$

Further, the radial integrals give numerical constants, the first being independent of R_{cut}, and the second being proportional to R_{cut}^2 (this can be seen by performing a variable transform $x = r'/R_{\text{cut}}$). The two-body descriptors in the limit of small cutoffs therefore have the expansion [compare Eq. (6.3) in the main text]

$$X_n^{(2)}(\mathbf{r}) \propto n(\mathbf{r}) + \text{const} \times R_{\text{cut}}^2 \nabla^2 n(\mathbf{r}) + ... \tag{F.24}$$

Next, we use Eq. (F.21) to approximate the $l = 1$ coefficients $c_{n1\alpha}$,

$$\begin{aligned} c_{n1\alpha}(\mathbf{r}) &\approx \int_0^{R_{\text{cut}}} \mathrm{d}r'\; r'^2 \tilde{\phi}_{n1}(r') \int \mathrm{d}\Omega'\; Y_1^\alpha(\widehat{\mathbf{r}'}) \left[r'_\beta \nabla_\beta n(\mathbf{r}) + \frac{1}{6} r'_\beta r'_\gamma r'_\delta \nabla_\beta \nabla_\gamma \nabla_\delta n(\mathbf{r}) + ... \right] \\ &= \sqrt{\frac{3}{4\pi}} \int_0^{R_{\text{cut}}} \mathrm{d}r'\; r' \tilde{\phi}_{n1}(r') \int d\Omega'\; r'_\alpha \left[r'_\beta \nabla_\beta n(\mathbf{r}) + \frac{1}{6} r'_\beta r'_\gamma r'_\delta \nabla_\beta \nabla_\gamma \nabla_\delta n(\mathbf{r}) + ... \right], \end{aligned} \tag{F.25}$$

where in the second line we have plugged in Eq. (F.17) for the Y_1^α. To simplify this expression, we use Eq. (F.23) for leading order term and the identity

$$\int d\Omega' r'_\alpha r'_\beta r'_\gamma r'_\delta = \frac{4\pi}{15} r'^4 \left(\delta_{\alpha\beta}\delta_{\gamma\delta} + \delta_{\alpha\gamma}\delta_{\beta\delta} + \delta_{\alpha\delta}\delta_{\beta\gamma} \right) \tag{F.26}$$

for next-to-leading order term, yielding

$$
\begin{aligned}
&c_{n1\alpha}(\mathbf{r}) \approx \\
&\sqrt{\frac{3}{4\pi}}\left\{ \left[\int_0^{R_{\text{cut}}} \mathrm{d}r'\; r'^3 \tilde{\phi}_{n1}(r')\right] \nabla_\alpha n(\mathbf{r}) + \frac{1}{10}\left[\int_0^{R_{\text{cut}}} \mathrm{d}r'\; r'^5 \tilde{\phi}_{n1}(r')\right] \nabla_\alpha\nabla_\beta\nabla_\beta n(\mathbf{r}) + ...\right\} \\
&\propto R_{\text{cut}}\nabla_\alpha n(\mathbf{r}) + \text{const} \times R_{\text{cut}}^3 \nabla_\alpha\nabla_\beta\nabla_\beta n(\mathbf{r}) + ...
\end{aligned}
\tag{F.27}
$$

Next, we form the scalar products $c_{n1\alpha}c_{n'1\alpha}$ needed for the three-body descriptors. The leading order term in the expansion of these scalar products is proportional to the scalar product $\nabla_\alpha n(\mathbf{r})\nabla_\alpha n(\mathbf{r}) = |\boldsymbol{\nabla} n(\mathbf{r})|^2$, and the next-to-leading order term involves products of terms proportional to $\nabla_\alpha n(\mathbf{r})\nabla_\alpha\nabla_\beta\nabla_\beta n(\mathbf{r}) = \boldsymbol{\nabla} n(\mathbf{r}) \cdot \boldsymbol{\nabla}\nabla^2 n(\mathbf{r})$, thus

$$
c_{n1\alpha}(\mathbf{r})c_{n'1\alpha}(\mathbf{r}) \propto R_{\text{cut}}^2 |\boldsymbol{\nabla} n(\mathbf{r})|^2 + \text{const} \times R_{\text{cut}}^4 \boldsymbol{\nabla} n(\mathbf{r}) \cdot \boldsymbol{\nabla}\nabla^2 n(\mathbf{r}) + ... \tag{F.28}
$$

Inserting this result in the definition (F.18), we finally obtain

$$
X^{(3)}_{nn'1}(\mathbf{r}) \propto |\boldsymbol{\nabla} n(\mathbf{r})| + \mathcal{O}(R_{\text{cut}}^2) \quad \text{for } R_{\text{cut}} \to 0. \tag{F.29}
$$

As the three-body descriptors are simply the diagonal elements ($n = n'$) of the $X_{nn'1}$, this concludes the proof of the limit stated in Eq. (6.5) in the main text. Note that this limit extends also to the more general case of off-diagonal descriptors ($n \neq n'$).

Appendix G

Machine learning DFT via optimized effective potentials

In the following, we describe our ML scheme in more detail and discuss some challenges inherent to the use of optimized effective potentials (OEP). Further, we will derive analytic expression for the machine learned exchange-correlation potentials $v_{\mathrm{xc}}^{\mathrm{ML-RPA}}$ and show how they can be efficiently evaluated using FFTs.

We begin by briefly motivating our ML scheme via analogy to MLFF. The starting point for MLFF schemes is the atomic density,

$$n_{\mathrm{atom}}(\mathbf{r}) = \sum_{i}^{\mathrm{atoms}} \delta(\mathbf{r} - \mathbf{R}_i). \tag{G.1}$$

This atomic density is usually smoothed by replacing the delta function above by a Gaussian. The central assumption in MLFF is that the total energy can by decomposed into a sum of atomic energies ε_i, which depend on two- and three-body descriptors (collected in a supervector $\mathbf{X}_{\mathrm{atom}}$),

$$E = \sum_{i}^{\mathrm{atoms}} \varepsilon_i[\mathbf{X}_{\mathrm{atom}}(\mathbf{R}_i)]. \tag{G.2}$$

In DFT, the central quantity is the electronic density n. We do not apply smearing to n, as the electronic density is already a smooth object. Analogously to Eq. (G.2), one can formulate the assumption that the exchange-correlation energy can be written as an integral of energy densities depending on two- and three-body descriptors (supervector $\mathbf{X}$),

$$E_{\mathrm{xc}} = \int \mathrm{d}\mathbf{r}\, n(\mathbf{r}) \varepsilon_{\mathrm{xc}}[\mathbf{X}(\mathbf{r})]. \tag{G.3}$$

We further pull out a factor $\varepsilon_{\mathrm{x,HEG}}(\mathbf{r})$, such that the enhancement factor F_{xc} is approximated rather than $\varepsilon_{\mathrm{xc}}$. In other words, we use the LDA exchange as a baseline for ML-RPA, yielding the ansatz [Eq. (6.7) in the main text]

$$E_{\mathrm{xc}}^{\mathrm{ML-RPA}} = \int \mathrm{d}\mathbf{r}\, n(\mathbf{r}) \varepsilon_{\mathrm{x,HEG}}[n(\mathbf{r})] F_{\mathrm{xc}}^{\mathrm{ML-RPA}}[\mathbf{X}(\mathbf{r})]. \tag{G.4}$$

For the functional form of $F_{\mathrm{xc}}^{\mathrm{ML-RPA}}$, we use a Gaussian kernel [Eq. (6.8) in the main text]

$$F_{\mathrm{xc}}^{\mathrm{ML-RPA}}[\mathbf{X}(\mathbf{r})] = \sum_{i_B} w_{i_B} \exp\left\{ -\frac{[\mathbf{X}(\mathbf{r}) - \mathbf{X}^{i_B}]^2}{2\sigma^2} \right\}, \tag{G.5}$$

where the kernel width σ is an ML hyperparameter, the $\mathbf{X}^{i_B}$ are representative control

points and the w_{i_B} the corresponding weights. Combing Eqs. (G.4) and (G.5), we obtain

$$E_{\mathrm{xc}}^{\mathrm{ML-RPA}} = \int \mathrm{d}\mathbf{r}\, n(\mathbf{r})\varepsilon_{\mathrm{x,HEG}}[n(\mathbf{r})] \sum_{i_B} w_{i_B} \exp\left\{-\frac{[\mathbf{X}(\mathbf{r}) - \mathbf{X}^{i_B}]^2}{2\sigma^2}\right\}. \tag{G.6}$$

Evaluating the functional derivative, $v_{\mathrm{xc}}^{\mathrm{ML-RPA}} = \delta E_{\mathrm{xc}}^{\mathrm{ML-RPA}}/\delta n(\mathbf{r})$, yields a local term from the derivative of $n(\mathbf{r})\varepsilon_{\mathrm{x,HEG}}(\mathbf{r})$ and a non-local term which stems from the dependence of the descriptors $\mathbf{X}(\mathbf{r}')$ on the density $n(\mathbf{r})$

$$\begin{aligned} v_{\mathrm{xc}}^{\mathrm{ML-RPA}}(\mathbf{r}) &= \int \mathrm{d}\mathbf{r}' \frac{\delta}{\delta n(\mathbf{r})} \left\{n(\mathbf{r}')\varepsilon_{\mathrm{x,HEG}}[n(\mathbf{r}')]\right\} F_{\mathrm{xc}}^{\mathrm{ML-RPA}}(\mathbf{r}') \\ &\quad + \int \mathrm{d}\mathbf{r}' n(\mathbf{r}')\varepsilon_{\mathrm{x,HEG}}[n(\mathbf{r}')] \frac{\delta}{\delta n(\mathbf{r})} \left\{F_{\mathrm{xc}}^{\mathrm{ML-RPA}}[\mathbf{X}(\mathbf{r}')]\right\} \\ &= v_{\mathrm{xc,loc}}^{\mathrm{ML-RPA}}(\mathbf{r}) + v_{\mathrm{xc,nl}}^{\mathrm{ML-RPA}}. \end{aligned} \tag{G.7}$$

The local term is easily evaluated using $\delta n(\mathbf{r}')/\delta n(\mathbf{r}) = \delta(\mathbf{r} - \mathbf{r}')$, yielding

$$\begin{aligned} v_{\mathrm{xc,loc}}^{\mathrm{ML-RPA}}(\mathbf{r}) &= \frac{4}{3}\varepsilon_{\mathrm{x,HEG}}[n(\mathbf{r})] F_{\mathrm{xc}}^{\mathrm{ML-RPA}}[\mathbf{X}(\mathbf{r})] \\ &= \frac{4}{3}\varepsilon_{\mathrm{x,HEG}}[n(\mathbf{r})] \sum_{i_B} w_{i_B} \exp\left\{-\frac{[\mathbf{X}(\mathbf{r}) - \mathbf{X}^{i_B}]^2}{2\sigma^2}\right\}. \end{aligned} \tag{G.8}$$

The non-local term is more complicated, but we will show in the following that FFT can be employed once again for its efficient evaluation. Using Eq. (G.5) and applying the chain rule, we obtain

$$\begin{aligned} v_{\mathrm{xc,nl}}^{\mathrm{ML-RPA}}(\mathbf{r}) = \int \mathrm{d}\mathbf{r}' n(\mathbf{r}')\varepsilon_{\mathrm{x,HEG}}[n(\mathbf{r}')] \sum_{i_B} w_{i_B} \exp\left\{-\frac{[\mathbf{X}(\mathbf{r}') - \mathbf{X}^{i_B}]^2}{2\sigma^2}\right\} \\ \times \sum_{i}^{N_{\mathrm{des}}} \frac{-[X_i(\mathbf{r}') - \mathbf{X}^{i_B}]}{\sigma^2} \sum_{nml} \frac{\partial X_i(\mathbf{r}')}{\partial c_{nlm}(\mathbf{r}')} \frac{\delta c_{nlm}(\mathbf{r}')}{\delta n(\mathbf{r})}. \end{aligned} \tag{G.9}$$

As the descriptors $X_i(\mathbf{r}')$ depend on the expansion coefficients $c_{nlm}(\mathbf{r}')$ in a simple algebraic fashion, the complicated non-locality is thus due to the last term only. Inserting the expressions (F.13) and (F.10) yields

$$\begin{aligned} \frac{\delta c_{nlm}(\mathbf{r}')}{\delta n(\mathbf{r})} &= \frac{\delta}{\delta n(\mathbf{r})} i^l \int \frac{\mathrm{d}\mathbf{q}}{(2\pi)^3} e^{i\mathbf{q}\mathbf{r}'} \left[\int \mathrm{d}\mathbf{r}''\, e^{-i\mathbf{q}\mathbf{r}''} n(\mathbf{r}'')\right] \tilde{\phi}_{nl}(q) Y_l^m(\widehat{\mathbf{q}}) \\ &= i^l \int \frac{\mathrm{d}\mathbf{q}}{(2\pi)^3} \int \mathrm{d}\mathbf{r}''\, e^{i\mathbf{q}(\mathbf{r}'-\mathbf{r}'')} \delta(\mathbf{r} - \mathbf{r}'') \tilde{\phi}_{nl}(q) Y_l^m(\widehat{\mathbf{q}}) \\ &= i^l \int \frac{\mathrm{d}\mathbf{q}}{(2\pi)^3} e^{i\mathbf{q}(\mathbf{r}-\mathbf{r}')} \tilde{\phi}_{nl}(q) Y_l^m(-\widehat{\mathbf{q}}), \end{aligned} \tag{G.10}$$

where in the last line we have substituted $\mathbf{q} \mapsto -\mathbf{q}$. Next, we define the intermediate quantities η_{nlm}, which we evaluate numerically via FFT,

$$\begin{aligned} \eta_{nlm}(\mathbf{q}) = \frac{1}{N_{\mathrm{FFT}}} \sum_{\mathbf{r}'} e^{-i\mathbf{q}\mathbf{r}'} n(\mathbf{r}')\varepsilon_{\mathrm{x,HEG}}[n(\mathbf{r}')] \\ \times \sum_{i_B} w_{i_B} \exp\left\{\frac{-[\mathbf{X}(\mathbf{r}') - \mathbf{X}^{i_B}]^2}{2\sigma^2}\right\} \sum_{i}^{N_{\mathrm{des}}} \frac{-[X_i(\mathbf{r}') - \mathbf{X}^{i_B}]}{\sigma^2} \frac{\partial X_i(\mathbf{r}')}{\partial c_{nlm}(\mathbf{r}')}. \end{aligned} \tag{G.11}$$

With the help of the η_{nlm}, we can rewrite Eq. (G.9) in the compact form

$$v_{\mathrm{xc,nl}}^{\mathrm{ML-RPA}}(\mathbf{r}) = i^l \sum_{\mathbf{q}} e^{i\mathbf{q}\mathbf{r}} \sum_{nlm} \eta_{nlm}(\mathbf{q}) \tilde{\phi}_{nl}(q) Y_l^m(-\widehat{\mathbf{q}}), \tag{G.12}$$

which can be directly evaluated via FFT as well. In summary, Eqs. (G.11) and (G.12) allow us to evaluate the ML-RPA exchange-correlation potential on all real-space grid points $\mathbf{r}$ using a small number of FFTs. Thus, we have *avoided the evaluation of double integrals* by applying FFT throughout. Therefore, the overall computational cost of evaluating $v_{\mathrm{xc}}^{\mathrm{ML-RPA}}$ scales only as $\mathcal{O}(N_{\mathrm{FFT}} \ln N_{\mathrm{FFT}})$ rather than (N_{FFT}^2) with respect to the number of real-space grid points N_{FFT}.

A potential pitfall in using the OEP method for ML applications is the fact that $v_{\mathrm{xc}}^{\mathrm{RPA}}(\mathbf{r})$ is in practice determined only up to a constant shift. Inspired by the work of Nagai *et al.*,[175] we circumvent this problem by defining auxiliary exchange-correlation potentials $\tilde{v}_{\mathrm{xc}}^{\mathrm{RPA}}$,

$$\tilde{v}_{\mathrm{xc}}^{\mathrm{RPA}}(\mathbf{r}) = v_{\mathrm{xc}}^{\mathrm{RPA}}(\mathbf{r}) + \frac{E_{\mathrm{xc}}^{\mathrm{RPA}} - \int \mathrm{d}\mathbf{r}' n(\mathbf{r}') v_{\mathrm{xc}}^{\mathrm{RPA}}(\mathbf{r}')}{\int \mathrm{d}\mathbf{r}' n(\mathbf{r}')}. \tag{G.13}$$

Thus, the $\tilde{v}_{\mathrm{xc}}^{\mathrm{RPA}}$ are shifted with respect to the $v_{\mathrm{xc}}^{\mathrm{RPA}}$ such that they integrate to $E_{\mathrm{xc}}^{\mathrm{RPA}}$,

$$\int \mathrm{d}\mathbf{r}\, n(\mathbf{r}) \tilde{v}_{\mathrm{xc}}^{\mathrm{RPA}}(\mathbf{r}) \stackrel{!}{=} E_{\mathrm{xc}}^{\mathrm{RPA}}. \tag{G.14}$$

In fitting, we equate the auxiliary potentials with their ML-RPA analogs, $\tilde{v}_{\mathrm{xc}}^{\mathrm{ML-RPA}}$,

$$\tilde{v}_{\mathrm{xc}}^{\mathrm{ML-RPA}}(\mathbf{r}) = v_{\mathrm{xc}}^{\mathrm{ML-RPA}}(\mathbf{r}) + \frac{E_{\mathrm{xc}}^{\mathrm{ML-RPA}} - \int \mathrm{d}\mathbf{r}'\, n(\mathbf{r}') v_{\mathrm{xc}}^{\mathrm{ML-RPA}}(\mathbf{r}')}{\int \mathrm{d}\mathbf{r}'\, n(\mathbf{r}')}. \tag{G.15}$$

Thus, any information regarding absolute values of the OEP potentials is circumvented. Similar shifted exchange-correlation potentials occur also in the ML scheme of Tozer *et al.*,[227] the Becke-Johnson method[228] and the Levy-Zahariev formulation of DFT.[229] Here, however, the auxiliary potentials are used only as intermediate quantities for fitting, and once an ML-RPA functional has been learned, standard exchange-correlation potentials $v_{\mathrm{xc}}^{\mathrm{ML-RPA}}$ are extracted for applications.

To find the weights w_{i_B}, we fit to exchange-correlation energies and shifted exchange-correlation potentials at selected points $\mathbf{r}_k$ for all structures α contained in the training set. We demand that ML-RPA reproduces the reference data in a least square sense and apply appropriate weights, yielding the loss function

$$\begin{aligned}
\mathcal{L}_2 &= \frac{1}{N_{\mathrm{struct}}} \sum_{\alpha}^{N_{\mathrm{struct}}} c_E \mathcal{L}_{2,E}^{\alpha} + (1 - c_E) \mathcal{L}_{2,v}^{\alpha} \\
\mathcal{L}_{2,E}^{\alpha} &= \frac{1}{2} \frac{1}{N_e^{\alpha}} \left(E_{\mathrm{xc}}^{\mathrm{ML-RPA}} - E_{\mathrm{xc}}^{\mathrm{RPA}} \right)^2 \\
\mathcal{L}_{2,v}^{\alpha} &= \frac{1}{2} \frac{1}{N_e^{\alpha}} \frac{\Omega^{\alpha}}{N_{\mathrm{spars}}} \sum_{k}^{N_{\mathrm{spars}}} n(\mathbf{r}_k) \left[\tilde{v}_{\mathrm{xc}}^{\mathrm{ML-RPA}}(\mathbf{r}_k) - \tilde{v}_{\mathrm{xc}}^{\mathrm{RPA}}(\mathbf{r}_k) \right]^2.
\end{aligned} \tag{G.16}$$

Here we have introduced a dimensionless weight factor c_E, which allows us to balance exchange-correlation energies and potentials. Further, we normalize the loss with respect to system size via dividing by the number of electrons N_e^{α}. Likewise, a factor $\Omega^{\alpha} / N_{\mathrm{spars}}^{\alpha}$ is included for the exchange-correlation potentials, where Ω^{α} is

the volume of structure α. From Eq. (G.13) it is clear that the shifted exchange-correlation potentials depend linearly on the w_{i_B} just as the unshifted ones do. Thus, we can solve a system of linear equations that is obtained via minimization of the loss function (G.16) with respect to the w_{i_B},

$$\partial \mathcal{L}_2 / \partial w_{i_B} \stackrel{!}{=} 0 \rightarrow \sum_{i_B} \phi^{\alpha}_{j,i_B} w_{i_B} = y^{\alpha}_j. \tag{G.17}$$

Following Verdi *et al.*,[230] we regularize the solution of this linear problem via pseudo inverse of the design matrix ϕ, smoothly cutting off smaller singular values σ_i,

$$\sigma_i^{-1} \mapsto \frac{\sigma_i}{\sigma_i^2 + (t_{\mathrm{SVD}} \sigma_{\max})^2}, \tag{G.18}$$

where we multiply the Tikhonov parameter t_{SVD} by the largest singular value $\sigma_{\max}$. Thus, t_{SVD} is dimensionless and we can more easily compare numerical values of t_{SVD} for different databases. Finally, all ML-RPA hyperparameters are summarized in Table G.1.

TABLE G.1: Table of ML-RPA hyperparameters.

parameter	description	value
R_{cut}	cutoff radius	1.5 Å
N_{rad}	number of radial basis functions	4
N_{des}	number of density descriptors	4+4=8
σ	width of Gaussian kernel	3.0 eÅ^{-3}
$\sigma^{(3)}$	weight for three-body descriptors	1.0 Å
c_E	fit weight for xc-energies	0.999
t_{SVD}	Tikhonov regularization	1.0×10^{-9}

Appendix H

Data sparsification

To reduce computational cost, the exchange-correlation potential is fitted not on the entire real-space grid but rather at selected representative points $\mathbf{r}_k$. These points are represented as red crosses in Fig. 6.1 in the main text. For each individual structure α, we choose N_{spars} points via k-means sparsification. The k-means algorithm uses a metric that quantifies the similarity between density descriptors at points $\mathbf{r}$ and $\mathbf{r}'$. It is convenient to use the metric $d[\mathbf{X}(\mathbf{r}), \mathbf{X}(\mathbf{r}')]$ that is induced by the Gaussian kernel, $k[\mathbf{X}(\mathbf{r}), \mathbf{X}(\mathbf{r}')]$,

$$\begin{aligned} d[\mathbf{X}(\mathbf{r}), \mathbf{X}(\mathbf{r}')] &= k[\mathbf{X}(\mathbf{r}), \mathbf{X}(\mathbf{r})] + k[\mathbf{X}(\mathbf{r}'), \mathbf{X}(\mathbf{r}')] - 2k[\mathbf{X}(\mathbf{r}), \mathbf{X}(\mathbf{r}')] \\ &= 2 - \exp\left\{ -\frac{[\mathbf{X}(\mathbf{r}) - \mathbf{X}(\mathbf{r}')]^2}{2\sigma^2} \right\}. \end{aligned} \tag{H.1}$$

The k-means centers are initialized via farthest point sampling similar to Ref. [189]. In further iterations, the centers are updated as averages over all points belonging to their respective clusters as in the standard k-means algorithm. Those points are assigned to the clusters based again on the kernel induced metric.

Next, we combine the selected points from all structures and apply the sparsification again to choose the kernel control points $\mathbf{X}^{i_B}$, compare blue squares in Fig. 6.1 in the main text. An interesting technical detail is that the $\mathbf{r}_k$ are chosen as *actual real-space points* closest to k-means centers, where $v_{\text{xc}}^{\text{RPA}}(\mathbf{r})$ is available. For the selection of the $\mathbf{X}^{i_B}$, however, we find it beneficial to use *the k-means centers themselves*. That is, the chosen kernel control points correspond not to descriptors at actual real-space grid points, but rather optimized artificial ones. Integrals are evaluated on the entire real-space grid throughout.

In the following, we demonstrate numerically the efficiency of our sparsification scheme. First, we split the ML-RPA training set randomly (50:50) into a reduced training set and a validation set. Keeping one sparsification layer fixed and varying the number of k-means clusters in the other, we monitor the loss

$$\begin{aligned} \mathcal{L}_1{}' &= \frac{1}{N_{\text{struct}}} \sum_{\alpha}^{N_{\text{struct}}} c_E \mathcal{L}_{1,E}^{\alpha} + (1 - c_E) \mathcal{L}_{1,v}^{\alpha}{}' \\ \mathcal{L}_{1,E}^{\alpha} &= \frac{1}{N_e^{\alpha}} |E_{\text{xc}}^{\text{ML-RPA}} - E_{\text{xc}}^{\text{RPA}}| \\ \mathcal{L}_{1,v}^{\alpha}{}' &= \frac{1}{N_e^{\alpha}} \int \mathrm{d}\mathbf{r}\, n(\mathbf{r}) |\tilde{v}_{\text{xc}}^{\text{ML-RPA}}(\mathbf{r}) - \tilde{v}_{\text{xc}}^{\text{RPA}}(\mathbf{r})| \end{aligned} \tag{H.2}$$

for structures in the reduced training and validation sets. Note that the loss $\mathcal{L}_{1,v}^{\alpha}{}'$ includes the exchange-correlation potential *at all real-space grid points*, thus some amount of interpolation is required to minimize $\mathcal{L}_{1,v}^{\alpha}{}'$ even for structures α on which ML-RPA has been trained on. This means that $\mathcal{L}_{1,v}{}'$ is less prone to overfitting and

statistical error. Likewise, atomic forces in MLFF are known to be less prone to overfitting and statistical errors than energies. Fig. H.1 shows that in the first layer, we can downsample the number of real-space grid points per training structure (N_{spars}) from $\mathcal{O}(10^5) - \mathcal{O}(10^6)$ to a mere 100 without loosing significant fit accuracy. The second k-means layer inputs the combined $N_{\text{struct}} \times N_{\text{spars}}$ points from the first layer. Fig. H.2 shows that the number of kernel control points can be reduced by an additional factor of 4 without loss of accuracy. The other ML-RPA hyperparameters listed in Table G.1 were optimized in a similar fashion, minimizing validation set losses and monitoring the stability of electronic self-consistency.

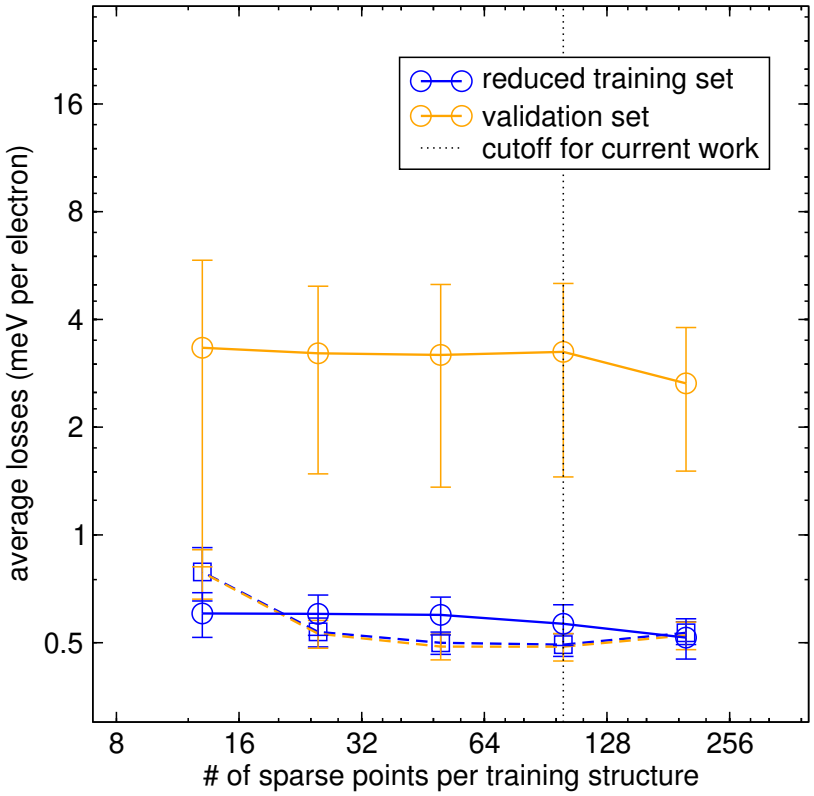

FIGURE H.1: Convergence of the ML-RPA fit with respect to N_{spars}, that is the number of sparse points kept by the first sparsification layer (second layer fixed). Note the log-log scale. Solid lines indicate losses for exchange-correlation energies [$c_E \mathcal{L}_E$ in Eq. (H.2)], and dashed lines indicate losses for exchange-correlation potentials [$(1 - c_E)\mathcal{L}'_v$ in Eq. (H.2)]. The losses are averaged losses over 10 random splittings (50:50).

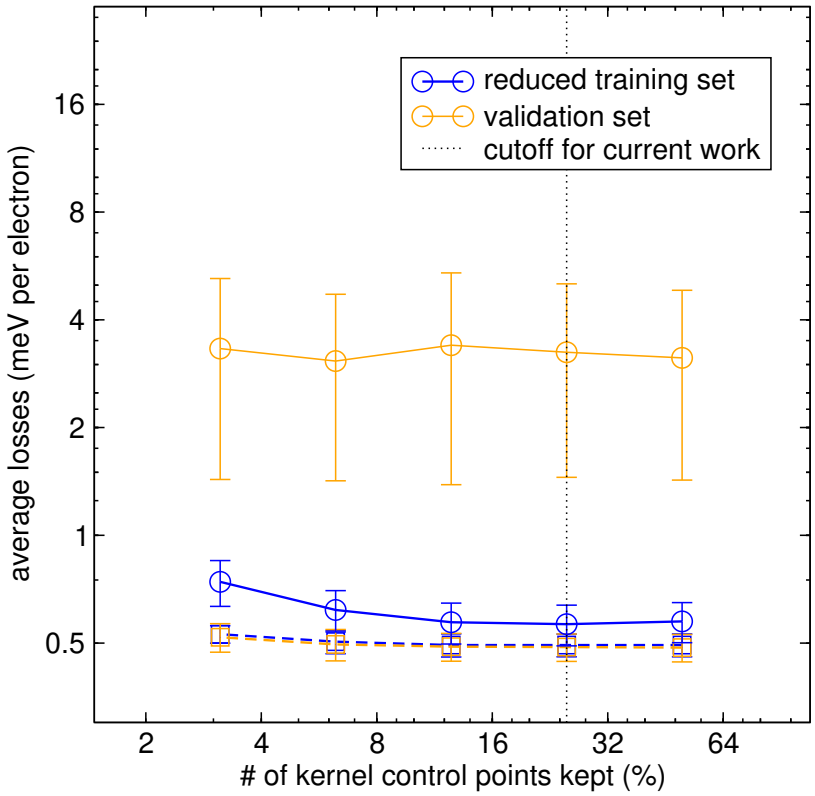

FIGURE H.2: Like Fig. H.1, but convergence with respect to the number of kernel control points kept by the second sparsification layer (first layer fixed).

Appendix I

ML-RPA training set

As a baseline, the ML-RPA training set contains 41 small molecules from the G2-2 database.[231] We include all non-spin-polarized molecules containing elements C, O and H except for CH_2, which does not posses a complete octet structure. We use experimental geometries where available, and otherwise geometries from accurate quantum chemistry calculations.[232] The molecules can be further classified as 20 hydrocarbons, 19 oxygen substituted hydrocarbons, and 2 inorganic molecules (H_2 and O_3). Thus, by including the G2 molecules we sample basic bonding motives and vacuum regions. To train ML-RPA for our specific applications, we supplement the training set with diamond and water structures, as discussed in the main text. Table I.1 and Fig. I.1 detail the ML-RPA fit errors with respect to the different training sub-groups.

TABLE I.1: Average training set losses calculated via Eq. (H.2) (in meV per electron) specified for different sub-groups of the ML-RPA training set. To compensate for the small amount of surface data, surfaces are included twice in the training set, giving them higher fit weight. The H_2O monomer at the experimental geometry is listed as a G2-molecule.

	$c_E\mathcal{L}_{1,E}$	$(1-c_E)\mathcal{L}_{1,v}{}'$
41 G2-molecules	0.73	0.30
40 bulk diamond structures	0.59	0.48
16 diamond surfaces (x2)	0.93	1.09
76 water structures	0.71	0.27
189 structures in total	0.73	0.46

I.1 Diamond surfaces

Table I.2 specifies the 28 diamond surfaces used to benchmark different DFT functionals (see Table 6.2 in the main text). These surfaces have been described in detail in past studies, we refer to the original references for more complete descriptions of the surface geometries.[197,199,200,204,205] In the following, we briefly comment on the interesting case of oxygenated (111) surfaces, where several (meta-)stable configurations exist that are close in energy. The least stable surface is the (111)-3db symmetric (1×1) oxygenated surface, while the most stable surface is the 2×1 reconstructed (111)-3db oxygenated chain surface, and the three oxygenated (111)-1db surfaces are in between. The (111)-3db oxygenated chain surface can be interpreted as clean (111)-1db surface adsorbing a monolayer of CO molecules, compare Fig. 6.4 in the main text. This is significant insofar as CO molecules have been reported to be the main desorption product in temperate-programmed desorption experiments

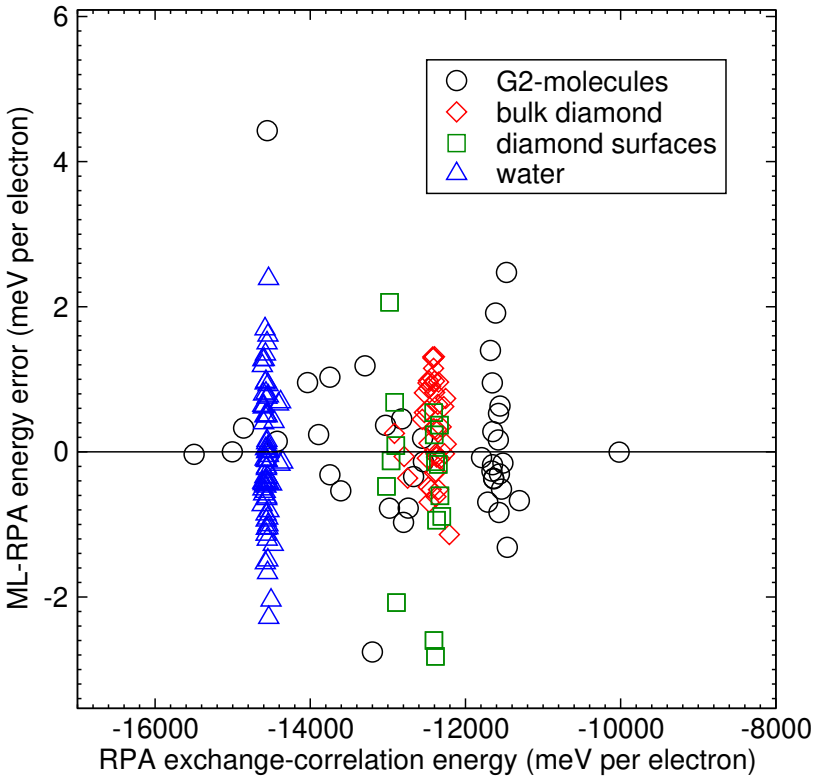

FIGURE I.1: ML-RPA energy fit error, $E_{\mathrm{xc}}^{\mathrm{ML-RPA}}/N_e - E_{\mathrm{xc}}^{\mathrm{RPA}}/N_e$. Symbols distinguish between different sub-groups of the training set. The data spread along the y-axis indicates that ML-RPA balances the fit well across the different sub-groups. Further, the spread along the x-axis shows that the G2-molecules contain very different chemical environments, whereas the other training data are more homogeneous. The H_2O monomer at the experimental geometry is listed as a G2-molecule.

on oxygenated (111) surfaces.[197] The C-O bond length of the oxygenated (111)-3db chain surface is calculated to be 1.20 Å (we use PBE geometries throughout). This clearly indicates strong double bonds, in comparison, the C-O bond lengths for the (111)-1db oxygenated surfaces are 1.20 Å (ketone) and 1.31 Å (on-top), as well as {1.43 Å, 1.44 Å} (peroxide). Out of the three oxygenated (111)-1db surfaces, exact RPA and ML-RPA predict the peroxide structure to be the most stable one, whereas PBE favors the on-top configuration. Otherwise, PBE, ML-RPA and exact RPA predict identical energy orderings throughout, see underlined values in Table I.2.

Finally, correlated methods such as RPA are known to converge slowly with respect to the basis set size.[83,86] To confirm the technical converge of our RPA calculations with respect to basis set, we extrapolate the RPA correlation energies with respect to the energy cutoff E_{max}^{χ} using the formula[9,65]

$$E_{\mathrm{c}}^{\mathrm{RPA}}(E_{\mathrm{max}}^{\chi}) = E_{\mathrm{c}}^{\mathrm{RPA}}(E_{\mathrm{max}}^{\chi} = \infty) + \frac{\mathrm{const}}{{E_{\mathrm{max}}^{\chi}}^{3/2}}. \tag{I.1}$$

Table I.2 shows that the extrapolated formation energies are slightly larger than our "exact RPA" values, which form the ground truth for ML-RPA. The agreement between "exact" and extrapolated RPA formation energies is 40 meV or better throughout.

The basis set incompleteness error also causes a slight underbinding of bulk diamond. The extrapolated values for the equlibrium lattice constant is 3.572 Å, whereas "exact RPA" predicts 3.581 Å.

TABLE I.2: List of the 28 diamond surfaces used for our surface energy benchmark (see Table 6.2 in the main text). The first column defines the surface symmetry and stoichiometry (corresponding to the chemisorption of 1 ML hydrogen for hydrogenated surfaces, and 1 ML oxygen for oxygenated surfaces). The second column describes the geometry of the surface termination and quotes literature references, where the surfaces are characterized. Further columns show surface formation energies [see Eq. (6.12) in the main text] that are given in eV per surface atom. "Exact RPA" is the ground truth for ML-RPA, and basis set extrapolated RPA formation energies are obtained using Eq. (I.1). Formation energies calculated with the PBE functional are also listed for comparison. All (100) and (111)-1db surfaces are included in the ML-RPA training set, all (110) and (111)-3db surfaces are out-of training. Underlined values correspond to the most stable configurations for a given a surface termination and orientation.

		PBE	RPA		
			extrap.	exact	ML
(100)*					
1×1	bulk terminated, as cut[202]	3.49	3.70	3.66	3.57
1×1	bulk terminated, relaxed[202]	3.36	3.62	3.59	3.51
1×1:H	bulk terminated, on-top[202]	0.90	1.21	1.21	1.16
1×1:O	bulk terminated, ketone[198]	2.29	2.38	2.38	2.39
1×1:O	bulk terminated, ether[198]	<u>1.97</u>	<u>2.03</u>	<u>1.99</u>	<u>1.91</u>
2×1	dimer[198]	<u>1.89</u>	<u>2.08</u>	<u>2.08</u>	<u>2.03</u>
2×1:2H	dimer, on-top[198]	<u>0.01</u>	<u>0.20</u>	<u>0.20</u>	<u>0.11</u>
2×1:2O	dimer, bridge[204]	3.45	3.50	3.48	3.40
(110)					
1×1	bulk terminated, as cut[200]	1.90	2.11	2.09	1.95
1×1	bulk terminated, relaxed[200]	<u>1.45</u>	<u>1.69</u>	<u>1.70</u>	<u>1.59</u>
1×1:H	bulk terminated, on-top[200]	<u>-0.23</u>	<u>-0.12</u>	<u>-0.11</u>	<u>-0.12</u>
1×1:O	bulk terminated, on-top†	3.38	3.61	3.60	3.58

*included in the ML-RPA training set

†similar to the hydrogenated (110) surface, the calculated C-O bond length is 1.36 Å.

Table I.2, continued.

		PBE	RPA		
			extrap.	exact	ML
(111)-1db*					
1×1	bulk terminated, as cut[203]	2.46	2.71	2.69	2.52
1×1	bulk terminated, relaxed[203]	1.94	2.30	2.29	2.12
1×1:H	bulk terminated, on-top[203]	-0.34	-0.19	-0.19	-0.24
1×1:O	bulk terminated, on-top[197]	2.84	3.19	3.19	2.99
2×1:2O	bulk terminated (distorted), peroxide[197]	2.99	3.02	2.99	2.94
2×1	Pandey chain[203]	1.18	1.43	1.41	1.34
2×1:2H	Pandey chain, on-top[203]	0.31	0.49	0.47	0.40
2×1:2O	Pandey chain, ketone[197]	2.94	3.08	3.09	2.99
(111)-3db					
1×1	bulk terminated, as cut[199]	4.27	4.41	4.37	4.37
1×1	bulk terminated, relaxed[199]	4.26	4.41	4.37	4.37
1×1:H	bulk terminated, on-top[199]	3.01	3.38	3.36	3.43
1×1:O	bulk terminated, ketone[204]	3.50	3.92	3.90	3.87
2×1	Seiwatz chain[199]	2.44	2.71	2.70	2.56
2×1:2H	Seiwatz chain, on-top[199]	0.00	0.17	0.17	0.11
2×1:2O	Seiwatz chain, ketone[204]	2.67	2.91	2.90	2.79

*included in the ML-RPA training set

Appendix J

Machine learning force fields for liquid water

RPA-MLFF is trained directly on total energies and forces from RPA calculations. Since RPA force calculations are very expensive, we use a cheaper RPA setup here. Specifically, an energy cutoff of 500 eV is used for the plane-wave basis sets expanding both the orbitals and the response function (ML-RPA ground truth calculations use 600 eV and 400 eV, respectively). Our tests, however, indicate that this difference has only minor effects on the predicted liquid water RDFs. The RPA-MLFF training data set consists 107 water structures containing 32 molecules or less. We use a compact hyperparameter setup that has shown to enable an efficient and accurate MLFF training for liquid water.[233] In particular, the radial and angular descriptors are separated as described in Ref. [180], and the angular descriptors are truncated at angular momentum number $l = 2$. Further, the radial descriptors use a cutoff of 6.0 Å and 8 radial basis functions, whereas the angular descriptors use a smaller cutoff of 4.0 Å and only 6 radial basis functions. For a general description of the MLFF scheme see also Refs. [211] and [173]. The RPA-MLFF training set errors are given in Table J.1.

The MLFF used to speed up ML-RPA uses the same descriptors as RPA-MLFF, but is trained on-the-fly[173,211] at fixed volume using a temperature ramp from 270 K to 370 K and a supercell containing 64 water molecules. In this way, a training set of around 400 structures is created. Thus, the combination of ML-RPA and MLFF allows for significantly more MLFF ground truth calculations, since ML-RPA is orders of magnitude cheaper than exact RPA. Moreover, the stresses predicted by ML-RPA can be seamlessly included in the MLFF training, whereas this would not be as easily possible for RPA-MLFF (RPA stress tensors can be included via finite differences,[234] but this is very expensive). The MLFFs for PBE+TS and RPBE+D3(BJ) are also trained on-the-fly, fit accuracy being similar to ML-RPA (see Table J.1).

The production run which produced the RDFs shown in Fig. 6.5 in the main text used 200000 MD steps with a time step of 1.5 fs. To increase sampling efficiency, the mass of the hydrogen atom was increased by a factor 8 (this does not affect static properties such as the RDF). For PBE+TS, which diffuses very weakly at 300 K, we further increased the supercell size to 512 water molecules, and increased the length of the MD run by a factor 3. Next, we define an independent test set of 10 liquid water snapshots sampled from the RPA-MLFF production run (64 water molecules). A low test set energy root means square error (RMSE) of 1.6 meV per atom demonstrates (i) that the ambient conditions used are well covered by the RPA-MLFF training set, (ii) that RPA-MLFF is able to extrapolate to the slightly larger simulation cell (64 water molecules). We also use this test set to evaluate the on-the-fly MLFFs, and the test set energy RMSEs are excellent (0.4 meV per atom for ML-RPA, 0.6 meV per atom for PBE+TS, and 0.5 meV per atom for RPBE+D3(BJ), respectively).

TABLE J.1: Training set errors (root means square error, RMSE) for the MLFFs trained for liquid water. Energy RMSEs are given in meV per atom, force RMSEs are given in meV $Å^{-1}$, and stress RMSEs are given in kbar.

	structures	energy	force	stress
RPA-MLFF	107	0.6	27.0	—
ML-RPA-MLFF	389	0.4	29.9	0.26
PBE+TS-MLFF	490	0.3	31.7	0.21
RPBE+D3(BJ)-MLFF	521	0.3	30.5	0.21

Appendix K

Water hexamer benchmark

Figs. K.1 and K.2 detail the water hexamer benchmark for various semi-local and vdW functionals, respectively. The vdW corrected PBE+TS and RPBE+D3 functionals well improve over their respective GGA base functionals, whereas SCAN+rVV10 performs slightly worse than the pristine SCAN functional.

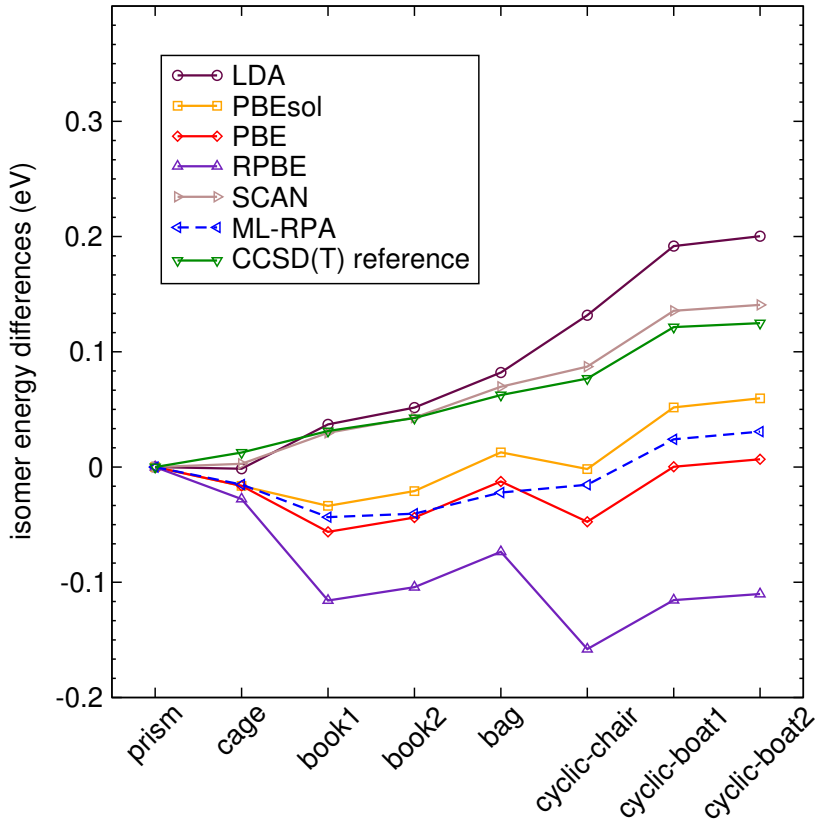

FIGURE K.1: Binding energies differences of eight hexamers as in Fig. 6.6 in the main text. ML-RPA results are compared to various semi-local density functionals. Lines drawn are only guides to the eye.

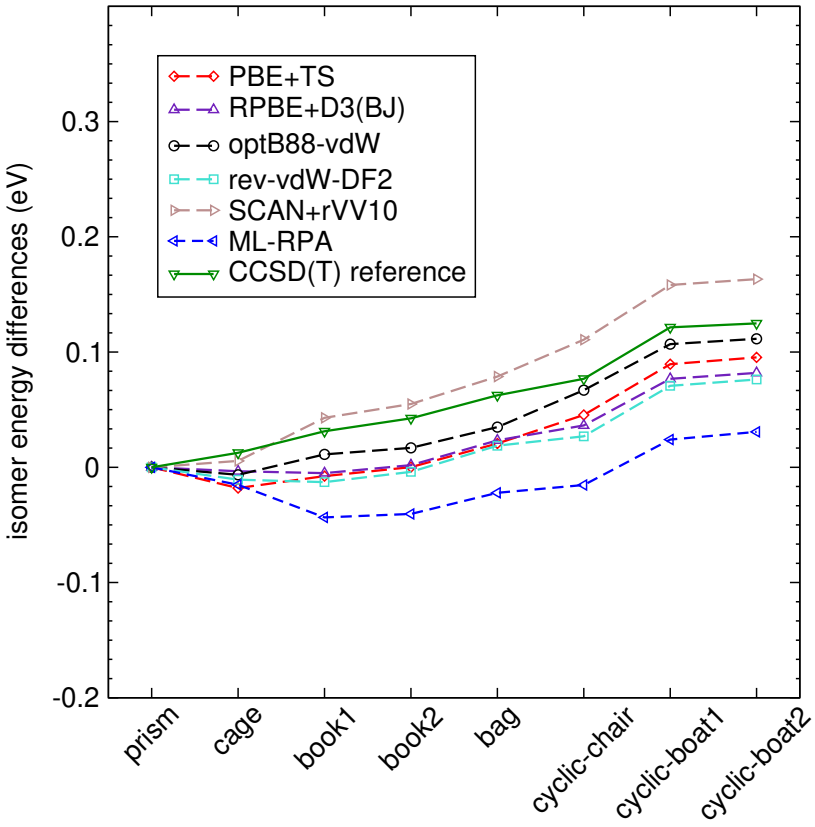

FIGURE K.2: Like Fig. K.1, but for various vdW functionals.

Bibliography

[1] M. Kaltak, J. Klimeš, and G. Kresse, "Low scaling algorithms for the random phase approximation: imaginary time and Laplace transformations", J. Chem. Theory Comput. **10**, 2498–2507 (2014).

[2] M. Kaltak, J. Klimeš, and G. Kresse, "Cubic scaling algorithm for the random phase approximation: self-interstitials and vacancies in Si", Phys. Rev. B **90**, 054115 (2014).

[3] H. N. Rojas, R. W. Godby, and R. J. Needs, "Space-time method for *ab initio* calculations of self-energies and dielectric response functions of solids", Phys. Rev. Lett. **74**, 1827–1830 (1995).

[4] P. Liu, M. Kaltak, J. Klimeš, and G. Kresse, "Cubic scaling *GW*: towards fast quasiparticle calculations", Phys. Rev. B **94**, 165109 (2016).

[5] B. Ramberger, T. Schäfer, and G. Kresse, "Analytic interatomic forces in the random phase approximation", Phys. Rev. Lett. **118**, 106403 (2017).

[6] L. J. Sham and M. Schlüter, "Density-functional theory of the energy gap", Phys. Rev. Lett. **51**, 1888–1891 (1983).

[7] R. W. Godby, M. Schlüter, and L. J. Sham, "Accurate exchange-correlation potential for silicon and its discontinuity on addition of an electron", Phys. Rev. Lett. **56**, 2415–2418 (1986).

[8] R. W. Godby, M. Schlüter, and L. J. Sham, "Self-energy operators and exchange-correlation potentials in semiconductors", Phys. Rev. B **37**, 10159–10175 (1988).

[9] S. Riemelmoser, M. Kaltak, and G. Kresse, "Plane wave basis set correction methods for RPA correlation energies", J. Chem. Phys. **152**, 134103 (2020).

[10] S. Riemelmoser, M. Kaltak, and G. Kresse, "Optimized effective potentials from the random-phase approximation: accuracy of the quasiparticle approximation", J. Chem. Phys. **154**, 154103 (2021).

[11] S. Riemelmoser, C. Verdi, M. Kaltak, and G. Kresse, "Machine learning density functionals from the random-phase approximation", `https://doi.org/10.48550/arXiv.2308.00665` (2023).

[12] A. D. Becke, "Perspective: fifty years of density-functional theory in chemical physics", J. Chem. Phys. **140**, 18A301 (2014).

[13] R. O. Jones, "Density functional theory: its origins, rise to prominence, and future", Rev. Mod. Phys. **87**, 897–923 (2015).

[14] R. M. Martin, *Electronic structure, Basic theory and practical methods* (Cambridge University Press, 2004), 648 pp.

[15] J. C. Slater, "A simplification of the Hartree-Fock method", Phys. Rev. **81**, 385–390 (1951).

[16] L. Hedin and S. Lundqvist, "Effects of electron-electron and electron-phonon interactions on the one-electron states of solids", in *Solid state physics*, Vol. 23, edited by F. Seitz, D. Turnbull, and H. Ehrenreich (Academic Press, 1970), pp. 1 –181.

[17]N. W. Ashcroft and D. N. Mermin, *Solid state physics* (Holt, Rinehart and Winston, 1976), 826 pp.

[18]J. P. Perdew and S. Kurth, "Density functionals for non-relativistic coulomb systems in the new century", in *A primer in density functional theory*, edited by C. Fiolhais, F. Nogueira, and M. A. L. Marques (Springer, 2003), pp. 1–55.

[19]T. Kato, "On the eigenfunctions of many-particle systems in quantum mechanics", Commun. Pure Appl. Math. **10**, 151–177 (1957).

[20]W. Kohn and L. J. Sham, "Self-consistent equations including exchange and correlation effects", Phys. Rev. **140**, A1133–A1138 (1965).

[21]P. Nozières and D. Pines, "Correlation energy of a free electron gas", Phys. Rev. **111**, 442–454 (1958).

[22]L. Hedin, "New method for calculating the one-particle Green's function with application to the electron-gas problem", Phys. Rev. **139**, A796–A823 (1965).

[23]D. M. Ceperley and B. J. Alder, "Ground state of the electron gas by a stochastic method", Phys. Rev. Lett. **45**, 566–569 (1980).

[24]P. Hohenberg and W. Kohn, "Inhomogeneous electron gas", Phys. Rev. **136**, B864–B871 (1964).

[25]W. Kohn, "Nobel lecture: electronic structure of matter—wave functions and density functionals", Rev. Mod. Phys. **71**, 1253–1266 (1999).

[26]R. O. Jones and O. Gunnarsson, "The density functional formalism, its applications and prospects", Rev. Mod. Phys. **61**, 689–746 (1989).

[27]E. Engel, "Orbital-dependent functionals for the exchange-correlation energy: a third generation of density functionals", in *A primer in density functional theory*, edited by C. Fiolhais, F. Nogueira, and M. A. L. Marques (Springer, 2003), pp. 56–122.

[28]A. J. Cohen, P. Mori-Sánchez, and W. Yang, "Insights into current limitations of density functional theory", Science **321**, 792–794 (2008).

[29]E. J. Baerends, O. V. Gritsenko, and R. van Meer, "The Kohn–Sham gap, the fundamental gap and the optical gap: the physical meaning of occupied and virtual Kohn–Sham orbital energies", Phys. Chem. Chem. Phys. **15**, 16408–16425 (2013).

[30]J. P. Perdew, R. G. Parr, M. Levy, and J. L. Balduz, "Density-functional theory for fractional particle number: derivative discontinuities of the energy", Phys. Rev. Lett. **49**, 1691–1694 (1982).

[31]J. P. Perdew and M. Levy, "Physical content of the exact Kohn-Sham orbital energies: band gaps and derivative discontinuities", Phys. Rev. Lett. **51**, 1884–1887 (1983).

[32]D. C. Langreth and J. P. Perdew, "Theory of nonuniform electronic systems. i. analysis of the gradient approximation and a generalization that works", Physical Review B **21**, 5469–5493 (1980).

[33]D. C. Langreth and M. J. Mehl, "Beyond the local-density approximation in calculations of ground-state electronic properties", Phys. Rev. B **28**, 1809–1834 (1983), Erratum, **29**, 2310, (1984).

[34]J. P. Perdew and Y. Wang, "Accurate and simple density functional for the electronic exchange energy: generalized gradient approximation", Phys. Rev. B **33**, 8800–8802 (1986).

[35]A. D. Becke, "Density-functional exchange-energy approximation with correct asymptotic behavior", Phys. Rev. A **38**, 3098–3100 (1988).

[36]J. P. Perdew, K. Burke, and M. Ernzerhof, "Generalized gradient approximation made simple", Phys. Rev. Lett. **77**, 3865–3868 (1996), Erratum, **78**, 1396, (1997).

[37]C. Lee, W. Yang, and R. G. Parr, "Development of the colle-salvetti correlation-energy formula into a functional of the electron density", Phys. Rev. B **37**, 785–789 (1988).

[38]A. Tkatchenko and M. Scheffler, "Accurate molecular van der Waals interactions from ground-state electron density and free-atom reference data", Phys. Rev. Lett. **102**, 073005 (2009).

[39]S. Grimme, J. Antony, S. Ehrlich, and H. Krieg, "A consistent and accurate *ab initio* parametrization of density functional dispersion correction (DFT-D) for the 94 elements H-Pu", J. Chem. Phys. **132**, 154104 (2010).

[40]S. Grimme, S. Ehrlich, and L. Goerigk, "Effect of the damping function in dispersion corrected density functional theory", J. Comput. Chem. **32**, 1456–1465 (2011).

[41]J. Klimeš and A. Michaelides, "Perspective: advances and challenges in treating van der Waals dispersion forces in density functional theory", J. Chem. Phys. **137**, 120901 (2012).

[42]K. Berland, V. R. Cooper, K. Lee, E. Schröder, T Thonhauser, P. Hyldgaard, and B. I. Lundqvist, "van der Waals forces in density functional theory: a review of the vdW-DF method", Rep. Prog. Phys. **78**, 066501 (2015).

[43]A. D. Becke, "Density-functional thermochemistry. III. the role of exact exchange", J. Chem. Phys. **98**, 5648–5652 (1993).

[44]P. J. Stephens, F. J. Devlin, C. F. Chabalowski, and M. J. Frisch, "*Ab initio* calculation of vibrational absorption and circular dichroism spectra using density functional force fields", J. Phys. Chem. **98**, 11623–11627 (1994).

[45]J. P. Perdew, M. Ernzerhof, and K. Burke, "Rationale for mixing exact exchange with density functional approximations", J. Chem. Phys. **105**, 9982–9985 (1996).

[46]A. Seidl, A. Görling, P. Vogl, J. A. Majewski, and M. Levy, "Generalized Kohn-Sham schemes and the band-gap problem", Phys. Rev. B **53**, 3764–3774 (1996).

[47]J. Heyd, G. E. Scuseria, and M. Ernzerhof, "Hybrid functionals based on a screened Coulomb potential", J. Chem. Phys. **118**, 8207–8215 (2003), Erratum, **124**, 219906, (2006).

[48]C. A. Rozzi, D. Varsano, A. Marini, E. K. U. Gross, and A. Rubio, "Exact Coulomb cutoff technique for supercell calculations", Phys. Rev. B **73**, 205119 (2006).

[49]K. Burke, "Perspective on density functional theory", J. Chem. Phys. **136**, 150901 (2012).

[50]Y. Zhao and D. G. Truhlar, "The M06 suite of density functionals for main group thermochemistry, thermochemical kinetics, noncovalent interactions, excited states, and transition elements: two new functionals and systematic testing of four M06-class functionals and 12 other functionals", Theor. Chem. Acc. **120**, 215–241 (2007).

[51]J.-D. Chai and M. Head-Gordon, "Long-range corrected hybrid density functionals with damped atom–atom dispersion corrections", Phys. Chem. Chem. Phys. **10**, 6615 (2008).

[52]X. Ren, P. Rinke, C. Joas, and M. Scheffler, "Random-phase approximation and its applications in computational chemistry and materials science", J. Mater. Sci. **47**, 7447–7471 (2012).

[53]T. Olsen, C. E. Patrick, J. E. Bates, A. Ruzsinszky, and K. S. Thygesen, "Beyond the RPA and GW methods with adiabatic xc-kernels for accurate ground state and quasiparticle energies", npj Comput. Mater. **5**, 106 (2019).

[54]J. Harl, "The linear response function in density functional theory: optical spectra and improved description of the electron correlation", PhD thesis (Universität Wien, 2008).

[55]H. Eshuis, J. E. Bates, and F. Furche, "Electron correlation methods based on the random phase approximation", Theor. Chem. Acc. **131**, 1–18 (2012).

[56]D. Langreth and J. Perdew, "The exchange-correlation energy of a metallic surface", Solid State Commun. **17**, 1425 –1429 (1975).

[57]D. C. Langreth and J. P. Perdew, "Exchange-correlation energy of a metallic surface: wave-vector analysis", Phys. Rev. B **15**, 2884–2901 (1977).

[58]H. Eshuis and F. Furche, "Basis set convergence of molecular correlation energy differences within the random phase approximation", J. Chem. Phys. **136**, 084105 (2012).

[59]J. Harl and G. Kresse, "Cohesive energy curves for noble gas solids calculated by adiabatic connection fluctuation-dissipation theory", Phys. Rev. B **77**, 045136 (2008).

[60]S. Lebègue, J. Harl, T. Gould, J. G. Ángyán, G. Kresse, and J. F. Dobson, "Cohesive properties and asymptotics of the dispersion interaction in graphite by the random phase approximation", Phys. Rev. Lett. **105**, 196401 (2010).

[61]T. Björkman, A. Gulans, A. V. Krasheninnikov, and R. M. Nieminen, "Van der waals bonding in layered compounds from advanced density-functional first-principles calculations", Phys. Rev. Lett. **108**, 235502 (2012).

[62]M. Macher, J. Klimeš, C. Franchini, and G. Kresse, "The random phase approximation applied to ice", J. Chem. Phys. **140**, 084502 (2014).

[63]M. Del Ben, J. Hutter, and J. VandeVondele, "Probing the structural and dynamical properties of liquid water with models including non-local electron correlation", J. Chem. Phys. **143**, 054506 (2015).

[64]Y. Yao and Y. Kanai, "Nuclear quantum effect and its temperature dependence in liquid water from random phase approximation via artificial neural network", J. Phys. Chem. Lett. **12**, 6354–6362 (2021).

[65]J. Harl, L. Schimka, and G. Kresse, "Assessing the quality of the random phase approximation for lattice constants and atomization energies of solids", Phys. Rev. B **81**, 115126 (2010).

[66]L. Schimka, R. Gaudoin, J. Klimeš, M. Marsman, and G. Kresse, "Lattice constants and cohesive energies of alkali, alkaline-earth, and transition metals: random phase approximation and density functional theory results", Phys. Rev. B **87**, 214102 (2013).

[67]G. P. Chen, V. K. Voora, M. M. Agee, S. G. Balasubramani, and F. Furche, "Random-phase approximation methods", Annual Review of Physical Chemistry **68**, 421–445 (2017).

[68]L. Schimka, J. Harl, A. Stroppa, A. Grüneis, M. Marsman, F. Mittendorfer, and G. Kresse, "Accurate surface and adsorption energies from many-body perturbation theory", Nat. Mater. **9**, 741–744 (2010).

[69]J. G. Brandenburg, A. Zen, M. Fitzner, B. Ramberger, G. Kresse, T. Tsatsoulis, A. Grüneis, A. Michaelides, and D. Alfè, "Physisorption of water on graphene: subchemical accuracy from many-body electronic structure methods", J. Phys. Chem. Lett. **10**, 358–368 (2019).

[70]A. Ruzsinszky, J. P. Perdew, and G. I. Csonka, "The RPA atomization energy puzzle", J. Chem. Theory Comput. **6**, 127–134 (2009).

[71]Z. Yan, J. P. Perdew, and S. Kurth, "Density functional for short-range correlation: accuracy of the random-phase approximation for isoelectronic energy changes", Phys. Rev. B **61**, 16430–16439 (2000), Erratum, **81**, 169902, (2010).

[72]J. Toulouse, I. C. Gerber, G. Jansen, A. Savin, and J. G. Ángyán, "Adiabatic-connection fluctuation-dissipation density-functional theory based on range separation", Phys. Rev. Lett. **102**, 096404 (2009).

[73]J. Toulouse, W. Zhu, J. G. Ángyán, and A. Savin, "Range-separated density-functional theory with the random-phase approximation: detailed formalism and illustrative applications", Phys. Rev. A **82**, 032502 (2010).

[74]B. G. Janesko, T. M. Henderson, and G. E. Scuseria, "Long-range-corrected hybrids including random phase approximation correlation", J. Chem. Phys. **130**, 081105 (2009).

[75]B. G. Janesko and G. E. Scuseria, "The role of the reference state in long-range random phase approximation correlation", J. Chem. Phys. **131**, 154106 (2009), Erratum, **138**, 019901, (2013).

[76]B. G. Janesko, T. M. Henderson, and G. E. Scuseria, "Long-range-corrected hybrid density functionals including random phase approximation correlation: application to noncovalent interactions", J. Chem. Phys. **131**, 034110 (2009), Erratum, **133**, 179901, (2010).

[77]A. Grüneis, M. Marsman, J. Harl, L. Schimka, and G. Kresse, "Making the random phase approximation to electronic correlation accurate", J. Chem. Phys. **131**, 154115 (2009).

[78]F. Furche and T. Van Voorhis, "Fluctuation-dissipation theorem density-functional theory", J. Chem. Phys. **122**, 164106 (2005).

[79]T. Olsen and K. S. Thygesen, "Beyond the random phase approximation: improved description of short-range correlation by a renormalized adiabatic local density approximation", Phys. Rev. B **88**, 115131 (2013).

[80]X. Ren, A. Tkatchenko, P. Rinke, and M. Scheffler, "Beyond the random-phase approximation for the electron correlation energy: the importance of single excitations", Phys. Rev. Lett. **106**, 153003 (2011).

[81]Y. Jin, D. Zhang, Z. Chen, N. Q. Su, and W. Yang, "Generalized optimized effective potential for orbital functionals and self-consistent calculation of random phase approximations", J. Phys. Chem. Lett. **8**, 4746–4751 (2017).

[82]J. Klimeš, M. Kaltak, E. Maggio, and G. Kresse, "Singles correlation energy contributions in solids", J. Chem. Phys. **143**, 102816 (2015).

[83]F. Furche, "Molecular tests of the random phase approximation to the exchange-correlation energy functional", Phys. Rev. B **64**, 195120 (2001).

[84]D. Pines, *Theory of quantum liquids: normal fermi liquids (advanced books classics)* (Westview Press, 1989).

[85]J. P. Perdew and K. Schmidt, "Jacob's ladder of density functional approximations for the exchange-correlation energy", AIP Conf. Proc. **577**, 1–20 (2001).

[86]J. Klimeš, M. Kaltak, and G. Kresse, "Predictive *GW* calculations using plane waves and pseudopotentials", Phys. Rev. B **90**, 075125 (2014).

[87]A. Gulans, "Towards numerically accurate many-body perturbation theory: short-range correlation effects", J. Chem. Phys. **141**, 164127 (2014).

[88]T. Helgaker, P. Jorgensen, and J. Olsen, *Molecular electronic-structure theory* (John Wiley & Sons, 2014).

[89]J. Toulouse, F. Colonna, and A. Savin, "Long-range–short-range separation of the electron-electron interaction in density-functional theory", Phys. Rev. A **70**, 062505 (2004).

[90]F. Bruneval, "Range-separated approach to the RPA correlation applied to the van der Waals bond and to diffusion of defects", Phys. Rev. Lett. **108**, 256403 (2012).

[91]W. Yang, "Generalized adiabatic connection in density functional theory", J. Chem. Phys. **109**, 10107–10110 (1998).

[92]J. Toulouse, F. Colonna, and A. Savin, "Short-range exchange and correlation energy density functionals: beyond the local-density approximation", J. Chem. Phys. **122**, 014110 (2005).

[93]S. Paziani, S. Moroni, P. Gori-Giorgi, and G. B. Bachelet, "Local-spin-density functional for multideterminant density functional theory", Phys. Rev. B **73**, 155111 (2006).

[94]U von Barth and L Hedin, "A local exchange-correlation potential for the spin polarized case. i", J. Phys. C: Solid State Phys. **5**, 1629 (1972).

[95]K. Burke, J. P. Perdew, and D. C. Langreth, "Is the local density approximation exact for short wavelength fluctuations?", Phys. Rev. Lett. **73**, 1283–1286 (1994).

[96]J. Paier, B. G. Janesko, T. M. Henderson, G. E. Scuseria, A. Grüneis, and G. Kresse, "Hybrid functionals including random phase approximation correlation and second-order screened exchange", J. Chem. Phys. **132**, 094103 (2010), Erratum, **133**, 179902, (2010).

[97]E. Maggio and G. Kresse, "Correlation energy for the homogeneous electron gas: exact Bethe-Salpeter solution and an approximate evaluation", Phys. Rev. B **93**, 235113 (2016).

[98]K. Burke, J. P. Perdew, and M. Ernzerhof, "Why semilocal functionals work: accuracy of the on-top pair density and importance of system averaging", J. Chem. Phys. **109**, 3760–3771 (1998).

[99]A. L. Fetter and J. D. Walecka, *Quantum theory of many-particle systems (dover books on physics)* (Dover Publications, 2003).

[100]V. Heine, "The pseudopotential concept", in *Solid state physics*, Vol. 24 (Elsevier BV, 1970), pp. 1–36.

[101]M. Gell-Mann and K. A. Brueckner, "Correlation energy of an electron gas at high density", Phys. Rev. **106**, 364–368 (1957).

[102]L. Schimka, J. Harl, and G. Kresse, "Improved hybrid functional for solids: the HSEsol functional", J. Chem. Phys. **134**, 024116 (2011).

[103]K. Rościszewski, B. Paulus, P. Fulde, and H. Stoll, "*Ab initio* coupled-cluster calculations for the fcc and hcp structures of rare-gas solids", Phys. Rev. B **62**, 5482–5488 (2000).

[104]G. Kresse and J. Furthmüller, "Efficient iterative schemes for *ab initio* total-energy calculations using a plane-wave basis set", Phys. Rev. B **54**, 11169–11186 (1996).

[105]P.-F. Loos, B. Pradines, A. Scemama, J. Toulouse, and E. Giner, "A density-based basis-set correction for wave function theory", J. Phys. Chem. Lett. **10**, 2931–2937 (2019).

[106]J. Paier, R. Hirschl, M. Marsman, and G. Kresse, "The Perdew–Burke–Ernzerhof exchange-correlation functional applied to the G2-1 test set using a plane-wave basis set", J. Chem. Phys. **122**, 234102 (2005).

[107]J. G. Ángyán, I. Gerber, and M. Marsman, "Spherical harmonic expansion of short-range screened Coulomb interactions", J. Phys. A: Math. Gen. **39**, 8613–8630 (2006).

[108]P. M. W. Gill, R. D. Adamson, and J. A. Pople, "Coulomb-attenuated exchange energy density functionals", Mol. Phys. **88**, 1005–1009 (1996).

[109]Z.-h. Yang, H. Peng, J. Sun, and J. P. Perdew, "More realistic band gaps from meta-generalized gradient approximations: only in a generalized Kohn-Sham scheme", Phys. Rev. B **93**, 205205 (2016).

[110]C. J. Umrigar and X. Gonze, "Accurate exchange-correlation potentials and total-energy components for the helium isoelectronic series", Phys. Rev. A **50**, 3827–3837 (1994).

[111]R. T. Sharp and G. K. Horton, "A variational approach to the unipotential many-electron problem", Phys. Rev. **90**, 317–317 (1953).

[112]J. D. Talman and W. F. Shadwick, "Optimized effective atomic central potential", Phys. Rev. A **14**, 36–40 (1976).

[113]L. J. Sham, "Exchange and correlation in density-functional theory", Phys. Rev. B **32**, 3876–3882 (1985).

[114]M. E. Casida, "Generalization of the optimized-effective-potential model to include electron correlation: a variational derivation of the Sham-Schlüter equation for the exact exchange-correlation potential", Phys. Rev. A **51**, 2005–2013 (1995).

[115]U. von Barth, N. E. Dahlen, R. van Leeuwen, and G. Stefanucci, "Conserving approximations in time-dependent density functional theory", Phys. Rev. B **72**, 235109 (2005).

[116]M. Grüning, A. Marini, and A. Rubio, "Density functionals from many-body perturbation theory: the band gap for semiconductors and insulators", J. Chem. Phys. **124**, 154108 (2006).

[117]M. Grüning, A. Marini, and A. Rubio, "Effect of spatial nonlocality on the density functional band gap", Phys. Rev. B **74**, 161103 (2006).

[118]M. Hellgren and U. von Barth, "Correlation potential in density functional theory at the GWA level: spherical atoms", Phys. Rev. B **76**, 075107 (2007).

[119]M. Hellgren, D. R. Rohr, and E. K. U. Gross, "Correlation potentials for molecular bond dissociation within the self-consistent random phase approximation", J. Chem. Phys. **136**, 034106 (2012).

[120]F. Caruso, D. R. Rohr, M. Hellgren, X. Ren, P. Rinke, A. Rubio, and M. Scheffler, "Bond breaking and bond formation: how electron correlation is captured in many-body perturbation theory and density-functional theory", Phys. Rev. Lett. **110**, 146403 (2013).

[121]M. Hellgren, F. Caruso, D. R. Rohr, X. Ren, A. Rubio, M. Scheffler, and P. Rinke, "Static correlation and electron localization in molecular dimers from the self-consistent RPA and *GW* approximation", Phys. Rev. B **91**, 165110 (2015).

[122]M. Hellgren and U. von Barth, "Linear density response function within the time-dependent exact-exchange approximation", Phys. Rev. B **78**, 115107 (2008).

[123]M. Hellgren and U. von Barth, "Correlation energy functional and potential from time-dependent exact-exchange theory", J. Chem. Phys. **132**, 044101 (2010).

[124]P. Bleiziffer, A. Heßelmann, and A. Görling, "Efficient self-consistent treatment of electron correlation within the random phase approximation", J. Chem. Phys. **139**, 084113 (2013).

[125]P. Bleiziffer, A. Heßelmann, C. J. Umrigar, and A. Görling, "Influence of the exchange-correlation potential in methods based on time-dependent density-functional theory", Phys. Rev. A **88**, 042513 (2013).

[126]P. Bleiziffer, M. Krug, and A. Görling, "Self-consistent Kohn-Sham method based on the adiabatic-connection fluctuation-dissipation theorem and the exact-exchange kernel", J. Chem. Phys. **142**, 244108 (2015).

[127]J. Klimeš and G. Kresse, "Kohn-Sham band gaps and potentials of solids from the optimised effective potential method within the random phase approximation", J. Chem. Phys. **140**, 054516 (2014).

[128]S. Kümmel and L. Kronik, "Orbital-dependent density functionals: theory and applications", Rev. Mod. Phys. **80**, 3–60 (2008).

[129]M. S. Hybertsen and S. G. Louie, "Electron correlation in semiconductors and insulators: band gaps and quasiparticle energies", Phys. Rev. B **34**, 5390–5413 (1986).

[130]B. Ramberger, Z. Sukurma, T. Schäfer, and G. Kresse, "RPA natural orbitals and their application to post-Hartree-Fock electronic structure methods", J. Chem. Phys. **151**, 214106 (2019).

[131]A. Görling and M. Levy, "Exact Kohn-Sham scheme based on perturbation theory", Phys. Rev. A **50**, 196–204 (1994).

[132]Y. M. Niquet, M. Fuchs, and X. Gonze, "Exchange-correlation potentials in the adiabatic connection fluctuation-dissipation framework", Phys. Rev. A **68**, 032507 (2003).

[133]S. V. Faleev, M. van Schilfgaarde, and T. Kotani, "All-electron self-consistent *GW* approximation: application to Si, MnO, and NiO", Phys. Rev. Lett. **93**, 126406 (2004).

[134]M. van Schilfgaarde, T. Kotani, and S. Faleev, "Quasiparticle self-consistent *GW* theory", Phys. Rev. Lett. **96**, 226402 (2006).

[135]T. Kotani, M. van Schilfgaarde, and S. V. Faleev, "Quasiparticle self-consistent *GW* method: a basis for the independent-particle approximation", Phys. Rev. B **76**, 165106 (2007).

[136]T. Kotani, M. van Schilfgaarde, S. V. Faleev, and A. Chantis, "Quasiparticle self-consistent *GW* method: a short summary", J. Phys.: Condens. Matter **19**, 365236 (2007).

[137]F. Bruneval, N. Vast, and L. Reining, "Effect of self-consistency on quasiparticles in solids", Phys. Rev. B **74**, 045102 (2006).

[138]F. Bruneval and M. Gatti, "Quasiparticle self-consistent *GW* method for the spectral properties of complex materials", in *First principles approaches to spectroscopic properties of complex materials* (Springer, 2014), pp. 99–135.

[139]B. Holm and U. von Barth, "Fully self-consistent *GW* self-energy of the electron gas", Phys. Rev. B **57**, 2108–2117 (1998).

[140]B. Holm, "Total energies from *GW* calculations", Phys. Rev. Lett. **83**, 788–791 (1999).

[141]W. Hanke and L. J. Sham, "Density-functional theory in insulators: analytical model for Σ_{xc}, v_{xc}, and the gap correction", Phys. Rev. B **38**, 13361–13370 (1988).

[142]F. Della Sala and A. Görling, "Efficient localized Hartree–Fock methods as effective exact-exchange Kohn–Sham methods for molecules", J. Chem. Phys. **115**, 5718–5732 (2001).

[143]O. Madelung, *Semiconductors: data handbook* (Springer Berlin Heidelberg, 2004).

[144]S. Kümmel and J. P. Perdew, "Simple iterative construction of the optimized effective potential for orbital functionals, including exact exchange", Phys. Rev. Lett. **90**, 043004 (2003).

[145]S. Kümmel and J. P. Perdew, "Optimized effective potential made simple: orbital functionals, orbital shifts, and the exact Kohn-Sham exchange potential", Phys. Rev. B **68**, 035103 (2003).

[146]A. Grüneis, G. Kresse, Y. Hinuma, and F. Oba, "Ionization potentials of solids: the importance of vertex corrections", Phys. Rev. Lett. **112**, 096401 (2014).

[147]M. Shishkin, M. Marsman, and G. Kresse, "Accurate quasiparticle spectra from self-consistent *GW* calculations with vertex corrections", Phys. Rev. Lett. **99**, 246403 (2007).

[148]W. Chen and A. Pasquarello, "Band-edge levels in semiconductors and insulators: hybrid density functional theory versus many-body perturbation theory", Phys. Rev. B **86**, 035134 (2012).

[149]A. Tal, P. Liu, G. Kresse, and A. Pasquarello, "Accurate optical spectra through time-dependent density functional theory based on screening-dependent hybrid functionals", Phys. Rev. Research **2**, 032019 (2020).

[150]K. Momma and F. Izumi, "*VESTA3* for three-dimensional visualization of crystal, volumetric and morphology data", J. Appl. Crystallogr. **44**, 1272–1276 (2011).

[151]M. Gajdoš, K. Hummer, G. Kresse, J. Furthmüller, and F. Bechstedt, "Linear optical properties in the projector-augmented wave methodology", Phys. Rev. B **73**, 045112 (2006).

[152]M. Shishkin and G. Kresse, "Self-consistent *GW* calculations for semiconductors and insulators", Phys. Rev. B **75**, 235102 (2007).

[153]E. Maggio and G. Kresse, "*GW* vertex corrected calculations for molecular systems", J. Chem. Theory Comput. **13**, 4765–4778 (2017).

[154]A. L. Kutepov, "Electronic structure of Na, K, Si, and LiF from self-consistent solution of Hedin's equations including vertex corrections", Phys. Rev. B **94**, 155101 (2016).

[155]A. L. Kutepov, "Self-consistent solution of Hedin's equations: semiconductors and insulators", Phys. Rev. B **95**, 195120 (2017).

[156]M. G. Medvedev, I. S. Bushmarinov, J. Sun, J. P. Perdew, and K. A. Lyssenko, "Density functional theory is straying from the path toward the exact functional", Science **355**, 49–52 (2017).

[157]M. Dion, H. Rydberg, E. Schröder, D. C. Langreth, and B. I. Lundqvist, "Van der Waals density functional for general geometries", Phys. Rev. Lett. **92**, 246401 (2004), Erratum, **95**, 109902, (2005).

[158]J. Sun, A. Ruzsinszky, and J. P. Perdew, "Strongly constrained and appropriately normed semilocal density functional", Phys. Rev. Lett. **115**, 036402 (2015).

[159]J. Paier, M. Marsman, and G. Kresse, "Why does the B3LYP hybrid functional fail for metals?", J. Chem. Phys. **127**, 024103 (2007).

[160]C. J. Cramer and D. G. Truhlar, "Density functional theory for transition metals and transition metal chemistry", Phys. Chem. Chem. Phys. **11**, 10757 (2009).

[161]R. Nagai, R. Akashi, and O. Sugino, "Completing density functional theory by machine learning hidden messages from molecules", npj Comput. Mater. **6**, 1–8 (2020).

[162]M. Bogojeski, L. Vogt-Maranto, M. E. Tuckerman, K.-R. Müller, and K. Burke, "Quantum chemical accuracy from density functional approximations via machine learning", Nat. Commun. **11**, 1–11 (2020).

[163]S. Dick and M. Fernandez-Serra, "Highly accurate and constrained density functional obtained with differentiable programming", Phys. Rev. B **104**, l161109 (2021).

[164]J. Kirkpatrick, B. McMorrow, D. H. P. Turban, A. L. Gaunt, J. S. Spencer, A. G. D. G. Matthews, A. Obika, L. Thiry, M. Fortunato, D. Pfau, L. R. Castellanos, S. Petersen, A. W. R. Nelson, P. Kohli, P. Mori-Sánchez, D. Hassabis, and A. J. Cohen, "Pushing the frontiers of density functionals by solving the fractional electron problem", Science **374**, 1385–1389 (2021).

[165]D. J. Tozer, V. E. Ingamells, and N. C. Handy, "Exchange-correlation potentials", J. Chem. Phys. **105**, 9200–9213 (1996).

[166]F. A. Hamprecht, A. J. Cohen, D. J. Tozer, and N. C. Handy, "Development and assessment of new exchange-correlation functionals", J. Chem. Phys. **109**, 6264–6271 (1998).

[167]J. C. Snyder, M. Rupp, K. Hansen, K.-R. Müller, and K. Burke, "Finding density functionals with machine learning", Phys. Rev. Lett. **108**, 253002 (2012).

[168]L. Li, J. C. Snyder, I. M. Pelaschier, J. Huang, U.-N. Niranjan, P. Duncan, M. Rupp, K.-R. Müller, and K. Burke, "Understanding machine-learned density functionals", Int. J. Quantum Chem. **116**, 819–833 (2015).

[169]F. Brockherde, L. Vogt, L. Li, M. E. Tuckerman, K. Burke, and K.-R. Müller, "Bypassing the Kohn-Sham equations with machine learning", Nat. Commun. **8**, 1–10 (2017).

[170]B. Kalita, L. Li, R. J. McCarty, and K. Burke, "Learning to approximate density functionals", Acc. Chem. Res. **54**, 818–826 (2021).

[171]J. Schmidt, M. R. G. Marques, S. Botti, and M. A. L. Marques, "Recent advances and applications of machine learning in solid-state materials science", npj Comput. Mater. **5**, 1–36 (2019).

[172]A. P. Bartók, R. Kondor, and G. Csányi, "On representing chemical environments", Phys. Rev. B **87**, 184115 (2013), Erratum, **87**, 219902, (2013); Erratum, **96**, 019902, (2017).

[173]R. Jinnouchi, F. Karsai, and G. Kresse, "On-the-fly machine learning force field generation: application to melting points", Phys. Rev. B **100**, 014105 (2019).

[174]S. Chmiela, A. Tkatchenko, H. E. Sauceda, I. Poltavsky, K. T. Schütt, and K.-R. Müller, "Machine learning of accurate energy-conserving molecular force fields", Sci. Adv. **3**, e1603015 (2017).

[175]R. Nagai, R. Akashi, S. Sasaki, and S. Tsuneyuki, "Neural-network Kohn-Sham exchange-correlation potential and its out-of-training transferability", J. Chem. Phys. **148**, 241737 (2018).

[176]Y. Zhou, J. Wu, S. Chen, and G. Chen, "Toward the exact exchange–correlation potential: a three-dimensional convolutional neural network construct", J. Phys. Chem. Lett. **10**, 7264–7269 (2019).

[177]J. Schmidt, C. L. Benavides-Riveros, and M. A. L. Marques, "Machine learning the physical nonlocal exchange–correlation functional of density-functional theory", J. Phys. Chem. Lett. **10**, 6425–6431 (2019).

[178]J. Behler and M. Parrinello, "Generalized neural-network representation of high-dimensional potential-energy surfaces", Phys. Rev. Lett. **98**, 146401 (2007).

[179]O. Gunnarsson, M. Jonson, and B. I. Lundqvist, "Descriptions of exchange and correlation effects in inhomogeneous electron systems", Phys. Rev. B **20**, 3136–3164 (1979).

[180]R. Jinnouchi, F. Karsai, C. Verdi, R. Asahi, and G. Kresse, "Descriptors representing two- and three-body atomic distributions and their effects on the accuracy of machine-learned inter-atomic potentials", J. Chem. Phys. **152**, 234102 (2020).

[181]X. Lei and A. J. Medford, "Design and analysis of machine learning exchange-correlation functionals via rotationally invariant convolutional descriptors", Phys. Rev. Materials **3**, 063801 (2019).

[182]A. V. Shapeev, "Moment tensor potentials: a class of systematically improvable interatomic potentials", Multiscale Model Sim **14**, 1153–1173 (2016).

[183]R. Drautz, "Atomic cluster expansion for accurate and transferable interatomic potentials", Phys. Rev. B **99**, 014104 (2019), Erratum, **99**, 249901, (2019).

[184]A. Grisafi, A. Fabrizio, B. Meyer, D. M. Wilkins, C. Corminboeuf, and M. Ceriotti, "Transferable machine-learning model of the electron density", ACS Cent. Sci. **5**, 57–64 (2018).

[185]J. T. Margraf and K. Reuter, "Pure non-local machine-learned density functional theory for electron correlation", Nat. Commun. **12**, 1–7 (2021).

[186]S. Dick and M. Fernandez-Serra, "Machine learning accurate exchange and correlation functionals of the electronic density", Nat. Commun. **11**, 1–10 (2020).

[187]K. Bystrom and B. Kozinsky, "CIDER: an expressive, nonlocal feature set for machine learning density functionals with exact constraints", J. Chem. Theory Comput. **18**, 2180–2192 (2022).

[188]Y. Chen, L. Zhang, H. Wang, and W. E, "DeePKS: a comprehensive data-driven approach toward chemically accurate density functional theory", J. Chem. Theory Comput. **17**, 170–181 (2020).

[189]D. Arthur and S. Vassilvitskii, *K-means++: the advantages of careful seeding*, Technical Report 2006-13 (Stanford InfoLab, 2006).

[190]J. A. White and D. M. Bird, "Implementation of gradient-corrected exchange-correlation potentials in Car-Parrinello total-energy calculations", Phys. Rev. B **50**, 4954–4957 (1994).

[191]G. Román-Pérez and J. M. Soler, "Efficient implementation of a van der Waals density functional: application to double-wall carbon nanotubes", Phys. Rev. Lett. **103**, 096102 (2009).

[192]A. Patra, J. E. Bates, J. Sun, and J. P. Perdew, "Properties of real metallic surfaces: effects of density functional semilocality and van der Waals nonlocality", Proc. Natl. Acad. Sci. **114**, E9188–E9196 (2017).

[193]J. L. Warren, J. L. Yarnell, G. Dolling, and R. A. Cowley, "Lattice dynamics of diamond", Phys. Rev. **158**, 805–808 (1967).

[194]G Kresse, J Furthmüller, and J Hafner, "*Ab initio* force constant approach to phonon dispersion relations of diamond and graphite", Europhys. Lett. **32**, 729–734 (1995).

[195]M. Engel, M. Marsman, C. Franchini, and G. Kresse, "Electron-phonon interactions using the projector augmented-wave method and Wannier functions", Phys. Rev. B **101**, 184302 (2020).

[196]J. Kulda, H. Kainzmaier, D. Strauch, B. Dorner, M. Lorenzen, and M. Krisch, "Overbending of the longitudinal optical phonon branch in diamond as evidenced by inelastic neutron and x-ray scattering", Phys. Rev. B **66**, 241202 (2002).

[197]K. P. Loh, X. N. Xie, S. W. Yang, and J. C. Zheng, "Oxygen adsorption on (111)-oriented diamond: a study with ultraviolet photoelectron spectroscopy, temperature-programmed desorption, and periodic density functional theory", J. Phys. Chem. B **106**, 5230–5240 (2002).

[198]S. J. Sque, R. Jones, and P. R. Briddon, "Structure, electronics, and interaction of hydrogen and oxygen on diamond surfaces", Phys. Rev. B **73**, 085313 (2006).

[199]G. Kern, J. Hafner, and G. Kresse, "Atomic and electronic structure of diamond (111) surfaces II. (2×1) and $(\sqrt{3} \times \sqrt{3})$ reconstructions of the clean and hydrogen-covered three dangling-bond surfaces", Surf. Sci. **366**, 464–482 (1996).

[200]G. Kern and J. Hafner, "***Ab initio*** calculations of the atomic and electronic structure of clean and hydrogenated diamond (110) surfaces", Phys. Rev. B **56**, 4203–4210 (1997).

[201]J. Ristein, "Surface science of diamond: familiar and amazing", Surf. Sci. **600**, 3677–3689 (2006).

[202]J. Furthmüller, J. Hafner, and G. Kresse, "Dimer reconstruction and electronic surface states on clean and hydrogenated diamond (100) surfaces", Phys. Rev. B **53**, 7334–7351 (1996).

[203]G. Kern, J. Hafner, and G. Kresse, "Atomic and electronic structure of diamond (111) surfaces i. reconstruction and hydrogen-induced de-reconstruction of the one dangling-bond surface", Surf. Sci. **366**, 445–463 (1996).

[204]X. Zheng and P. Smith, "The stable configurations for oxygen chemisorption on the diamond (100) and (111) surfaces", Surf. Sci. **262**, 219–234 (1992).

[205]S. Chaudhuri, S. J. Hall, B. P. Klein, M. Walker, A. J. Logsdail, J. V. Macpherson, and R. J. Maurer, "Coexistence of carbonyl and ether groups on oxygen-terminated (110)-oriented diamond surfaces", Communications Materials **3**, 1–9 (2022).

[206]E. Brini, C. J. Fennell, M. Fernandez-Serra, B. Hribar-Lee, M. Lukšič, and K. A. Dill, "How water's properties are encoded in its molecular structure and energies", Chem. Rev. **117**, 12385–12414 (2017).

[207]M. J. Gillan, D. Alfè, and A. Michaelides, "Perspective: how good is DFT for water?", J. Chem. Phys. **144**, 130901 (2016).

[208]M. Chen, H.-Y. Ko, R. C. Remsing, M. F. C. Andrade, B. Santra, Z. Sun, A. Selloni, R. Car, M. L. Klein, J. P. Perdew, and X. Wu, "Ab initio theory and modeling of water", Proc. Natl. Acad. Sci. **114**, 10846–10851 (2017).

[209]T. Morawietz, A. Singraber, C. Dellago, and J. Behler, "How van der Waals interactions determine the unique properties of water", Proc. Natl. Acad. Sci. **113**, 8368–8373 (2016).

[210]S. Dasgupta, E. Lambros, J. P. Perdew, and F. Paesani, "Elevating density functional theory to chemical accuracy for water simulations through a density-corrected many-body formalism", Nat. Commun. **12**, 1–12 (2021).

[211]R. Jinnouchi, J. Lahnsteiner, F. Karsai, G. Kresse, and M. Bokdam, "Phase transitions of hybrid perovskites simulated by machine-learning force fields trained on the fly with Bayesian inference", Phys. Rev. Lett. **122**, 225701 (2019).

[212]L. B. Skinner, C. Huang, D. Schlesinger, L. G. M. Pettersson, A. Nilsson, and C. J. Benmore, "Benchmark oxygen-oxygen pair-distribution function of ambient water from x-ray diffraction measurements with a wide Q-range", J. Chem. Phys. **138**, 074506 (2013).

[213]A. K. Soper, "The radial distribution functions of water as derived from radiation total scattering experiments: is there anything we can say for sure?", ISRN Physical Chemistry **2013**, 1–67 (2013).

[214]L. Zheng, M. Chen, Z. Sun, H.-Y. Ko, B. Santra, P. Dhuvad, and X. Wu, "Structural, electronic, and dynamical properties of liquid water by *ab initio* molecular dynamics based on SCAN functional within the canonical ensemble", J. Chem. Phys. **148**, 10.1063/1.5023611 (2018).

[215]S. Sakong, K. Forster-Tonigold, and A. Groß, "The structure of water at a Pt(111) electrode and the potential of zero charge studied from first principles", The Journal of Chemical Physics **144**, 194701 (2016).

[216]J. R. Lane, "CCSDTQ optimized geometry of water dimer", J. Chem. Theory Comput. **9**, 316–323 (2012).

[217]S. K. Reddy, S. C. Straight, P. Bajaj, C. H. Pham, M. Riera, D. R. Moberg, M. A. Morales, C. Knight, A. W. Götz, and F. Paesani, "On the accuracy of the MB-pol many-body potential for water: interaction energies, vibrational frequencies, and classical thermodynamic and dynamical properties from clusters to liquid water and ice", J. Chem. Phys. **145**, 194504 (2016).

[218]J. Wiktor, F. Ambrosio, and A. Pasquarello, "Note: assessment of the SCAN+rVV10 functional for the structure of liquid water", J. Chem. Phys. **147**, 216101 (2017).

[219]A. Grisafi and M. Ceriotti, "Incorporating long-range physics in atomic-scale machine learning", J. Chem. Phys. **151**, 10.1063/1.5128375 (2019).

[220]J. Hollingsworth, T. E. Baker, and K. Burke, "Can exact conditions improve machine-learned density functionals?", J. Chem. Phys. **148**, 241743 (2018).

[221]R. Nagai, R. Akashi, and O. Sugino, "Machine-learning-based exchange correlation functional with physical asymptotic constraints", Phys. Rev. Research **4**, 013106 (2022).

[222]A. Savin, "On degeneracy, near-degeneracy and density functional theory", in *Recent developments and applications of modern density functional theory*, Vol. 4, edited by J. Seminario, Theoretical and Computational Chemistry (Elsevier, 1996), pp. 327 –357.

[223]G. V. Gabriele Giuliani, *Quantum theory of the electron liquid* (Cambridge University Press, Mar. 1, 2008), 800 pp.

[224]M. Kaltak and G. Kresse, "Minimax isometry method: a compressive sensing approach for Matsubara summation in many-body perturbation theory", Phys. Rev. B **101**, 205145 (2020).

[225]P. García-González and R. W. Godby, "Self-consistent calculation of total energies of the electron gas using many-body perturbation theory", Phys. Rev. B **63**, 075112 (2001).

[226]G. B. Arfken and H. J. Weber, *Mathematical methods for physicists*, 1999.

[227]D. J. Tozer and N. C. Handy, "The development of new exchange-correlation functionals", J. Chem. Phys. **108**, 2545–2555 (1998).

[228]A. D. Becke and E. R. Johnson, "A simple effective potential for exchange", J. Chem. Phys. **124**, 221101 (2006).

[229]M. Levy and F. Zahariev, "Ground-state energy as a simple sum of orbital energies in Kohn-Sham theory: a shift in perspective through a shift in potential", Phys. Rev. Lett. **113**, 113002 (2014).

[230]C. Verdi, F. Karsai, P. Liu, R. Jinnouchi, and G. Kresse, "Thermal transport and phase transitions of zirconia by on-the-fly machine-learned interatomic potentials", npj Comput. Mater. **7**, 1–9 (2021).

[231]L. A. Curtiss, K. Raghavachari, P. C. Redfern, and J. A. Pople, "Assessment of Gaussian-2 and density functional theories for the computation of enthalpies of formation", J. Chem. Phys. **106**, 1063–1079 (1997).

[232]R. Johnson, *Computational chemistry comparison and benchmark database, NIST standard reference database 101*, 2002.

[233]R. Jinnouchi, S. Minami, F. Karsai, C. Verdi, and G. Kresse, "Proton transport in perfluorinated ionomer simulated by machine-learned interatomic potential", J. Phys. Chem. Lett. **14**, 3581–3588 (2023).

[234]P. Liu, C. Verdi, F. Karsai, and G. Kresse, "Phase transitions of zirconia: machine-learned force fields beyond density functional theory", Phys. Rev. B **105**, l060102 (2022).

Curriculum Vitae

University education

2018-ongoing	**University of Vienna** PhD student, thesis: "Density functional theory for the random-phase approximation" Supervisor: Univ.-Prof. Dipl.Ing. Dr. Georg Kresse
August 2017	graduation with distinction
2011-2017	**University of Vienna** studies of physics, master's thesis: "Norm conserving pseudo-potentials for the Coulomb interaction" Supervisor: Univ.-Prof. Dipl.Ing. Dr. Georg Kresse

Research interests

- Density functional theory
- Many-body perturbation theory: RPA, *GW*
- Machine learning

Awards and certificates

2012-2015	Merit scholarships according to the Studienförderungsgesetz awarded by the Austrian Ministry of Science, Research and Economy
2011	Cambridge certificate in Advanced English (CAE)

Teaching experience

2022-2023	Co-supervision of a master's project (topic: metal vacancies)
2014-2016	Student tutor (scientific computing, mathematics for physicists)

Publication list

Publications

- Riemelmoser, S., Verdi, C., Kaltak, M., & Kresse, G. (2023). Machine learning density functionals from the random-phase approximation. *arXiv preprint* arXiv:2308.00665.
- Riemelmoser, S., Kaltak, M., & Kresse, G. (2021). Optimized effective potentials from the random-phase approximation: Accuracy of the quasiparticle approximation. *The Journal of Chemical Physics, 154*(15), 154103.
- Riemelmoser, S., Kaltak, M., & Kresse, G. (2020). Plane wave basis set correction methods for RPA correlation energies. *The Journal of Chemical Physics, 152*(13), 134103.

Contributed talks

- Riemelmoser, S., Verdi, C., Kaltak, M., & Kresse, G. (2022). Machine learning density functionals from the random-phase approximation. *Psi-k conference* (Lausanne, Switzerland)
- Riemelmoser, S., Verdi, C., Kaltak, M., & Kresse, G. (2022). Machine learning density functionals from the random-phase approximation. *APS march meeting* (Chicago, USA)
- Riemelmoser, S., Kaltak, M., & Kresse, G. (2021) Plane wave basis set correction methods for GW self-energies. *GW goes large scale workshop* (Helsinki, Finland)

Posters

- Riemelmoser, S., Kaltak, M., & Kresse, G. (2021) RPA-OEP for solids. *Total energy and force methods conference* (Trieste, Italy)
- Riemelmoser, S., Kaltak, M., & Kresse, G. (2019) Range-separated density functional theory. *Autumn school for correlated electrons* (Jülich, Germany)
- Riemelmoser, S., Kaltak, M., & Kresse, G. (2019) Range-separated density functional theory. *CECAM 50 conference* (Lausanne, Switzerland)